IN-DEPTH STUDY OF PLANE WAVE-BLOCKAGE INTERACTION AND ANALYSIS OF HIGH FREQUENCY WAVES BEHAVIOUR IN WATER-FILLED PIPE SYSTEMS

by

MOEZ LOUATI

A Thesis Submitted to
The Hong Kong University of Science and Technology
in Partial Fulfilment of the Requirements for
the Degree of Doctor of Philosophy
in Civil Engineering

August 2016, Hong Kong

Authorization

I hereby declare that I am the sole author of the thesis.

I authorize the Hong Kong University of Science and Technology to lend this thesis to other institutions or individuals for the purpose of scholarly research.

I further authorize the Hong Kong University of Science and Technology to reproduce the thesis by photocopying or by other means, in total or in part, at the request of other institutions or individuals for the purpose of scholarly research.

_____

MOEZ LOUATI

17 August 2016

In-Depth Study of Plane Wave-Blockage Interaction and Analysis of High Frequency Waves Behaviour in Water-Filled Pipe Systems

by

MOEZ LOUATI

This is to certify that I have examined the above PhD thesis
and have found that it is complete and satisfactory in all respects,
and that any and all revisions required by
the thesis examination committee have been made.

_____

Prof. Mohamed S. GHIDAOUI (Supervisor)

_____

Prof. Hong K. LO (Head department)

Department of Civil and Environmental Engineering

17 August 2016

ACKNOWLEDGEMENTS

I am grateful to God for the good health and wellbeing that were necessary to complete this thesis.

Special thanks to my supervisor Prof. Mohamed S. GHIDAOUI for providing me his valuable advice and knowledge which led to the accomplishement of this work. I also would like to thank him for his immense patience in hearing sometimes inexhaustible questions, which stimulated and reinforced my philosophical logic and broadened my knowledge. With his challenges and support my confidence grew and stretched my own capabilities, allowing me to complete this work.

I would also like to express my sincere gratitude to Prof. Bruno BRUNONE and Prof. Silvia MENICONI for their supervision and support in designing and carrying out difficult experimental tests for this work at the Water Engineering Laboratory, University of Perugia-Italy. Thanks go also to their team members Prof. Marco FERRANTE, Enrico, Caterina, Elisa, Claudio and Emanuele for the warm and comfortable atmosphere they created around me during my stay in Perugia.

My special appreciation to the members of the thesis examination committee, Prof. Hanif M. CHAUDHRY, Prof. Daniel P. PALOMAR, Prof. Joseph H.W. LEE, Prof. Ilias G. DIMITRAKOPOULOS and Prof. Ross D. MURCH for their valuable insights and comments.

Prof. William G. GRAY and Dr. Duncan McInnis also contributed some invaluable advice during my PhD qualifying exam.

Nothing I could say would be enough to express my love, gratefulness and thanks to my entire family and close friends and especially my dear parents and lovely wife for their continual support, encouragement and patience. Thank you enormously!

This study is supported by the Hong Kong Research Grant Council (projects 612712 & 612713 & T21-602/15R) and by the Postgraduate Studentship.

Last, but not least, I particularly thank my high-school physics teacher Mr. Faiçal FRIKHA who implanted the love of physics in me and set me on this path.

TABLE OF CONTENTS

LIST OF FIGURES

LIST OF TABLES

In-Depth Study of Plane Wave-Blockage Interaction and Analysis of High Frequency Waves Behaviour in Water-Filled Pipe Systems

by MOEZ LOUATI

Department of Civil and Environmental Engineering

The Hong Kong University of Science and Technology

Abstract

Water supply systems (WSS) experience blockages during their life time due to physical and/or chemical processes (e.g. material deposition, tubercles (rust), scales, plaque, bio-fouling and inadvertently throttled inline valves, and air intrusion). Such blockages result in wastage of energy and financial resources, reduction in carrying capacity, and increased potential for contamination. This research investigates the physics of wave-blockage interaction in WSS by analytical, numerical and experimental means. Both shallow blockages (*i.e.*, blockages with small radial protrusion) and severe blockages (*i.e.*, blockages with large radial protrusion) are studied. The principle of action invariance shows that $w_m E_m$ is conserved for small blockages implying $\Delta w_m / w_m = -\Delta E_m / E_m$, where w_m and E_m are the eigenfrequency and total energy of the m^{th} mode and Δw_m and ΔE_m its eigenfrequency and energy shift due to the blockage. The change in energy is shown to be equal to the work of the radiation pressure during the formation of the blockage. In addition, it is found that a small blockage reduces the potential energy, but increases the kinetic energy of all modes. For a severe blockage, the pipe system is decoupled into two independent subsystems: a subsystem that involves the blockage and another that involves the intact pipe section. The decoupling is lost when the blockage length is such that the fundamental frequencies of the two subsystems are close or equal, resulting in resonance which means that waves within the subsystem involving the blockage are able to penetrate (transmit) to the second subsystem and vice-versa. It is shown that the assumption of small blockage is applicable when the

blockage occupies 30% of the crossectional area. The assumption of severe blockage is applicable when the blockage occupies 30% of the crossectional area or larger provided that the decoupling assumption is valid. When the blockage and the remainder of the pipe system are coupled, perturbation theory is successfully used to derive a simple frequency relation for the case of a blockage with large radial extent. This study also reveals that Bragg's resonance plays a key role where the wave-blockage interaction is minimal for certain frequencies and maximal for others. The spacing between consecutive Bragg's resonance frequencies, where maximal interaction occurs, scales as the wavespeed divided by the blockage length. Therefore, a wideband frequency of the transient generator is required to capture the signature of a short blockage. However, the use of high frequency waves (HFW) excites radial and azimuthal waves and renders the classical one-dimensional water-hammer (WH) theory invalid. Unlike classical WH theory, the resulting wave field is highly dispersive. Therefore, this thesis examines and reviews the behaviour of HFW in water-filled pipes and how they interact with blockages. As a result, a high-order numerical scheme has been developed and tested. The results show the strong effects of multi-paths on the propagation of high HFW in WSS and highlight that such waves, althgouh provide the required resolution, have a low range of detectability. Thus, a double pronged approach, where low frequency waves are used for reconnaissance and HFW are used for the localization is desirable in the future.

LIST OF SYMBOLS

There are too many variables in this thesis for it to be possible to give each one a unique notation. Whereas some variable notations are used throughout the thesis, others are duplicated and have different meanings in different Chapters. For this reason, the notion list below is be given for each chapter alone. The duplicated variables are redefined within the text to avoid any confusion.

Chapter 1

a	acoustic wave speed in water (m s^{-1})
A_0	cross sectional area of intact pipe (m^2)
A_1	cross sectional area of pipe 1 (m^2)
A_2	cross sectional area of pipe 2 (m^2)
A_3	cross sectional area of pipe 3 (m^2)
$F_{dis}\left(w_m, l_2, l_3, \alpha\right)$	dispersion function (-)
l_1	length of pipe 1 (m)
l_2	length of pipe 2 (m)
l_3	length of pipe 3 (m)
m	number of the fundamental (resonant) mode (-)
w_m	eigenfrequency of the m^{th} fundamental (resonant) mode (rad Hz)
w_m^{mes}	m^{th} measured eigenfrequency (rad Hz)

Greek letters

α	area ratio between blocked and intact cross sectional areas (-)

Chapter 2

a	wave speed in water-filled pipe (m s^{-1})
a_c	wave speed in the open channel (ms^{-1})
A	initial cross sectional area (m^2)
A_0	cross-sectional area of the intact pipe (m^2)
A_{in}	inward area of the control volume (m^2)
A_{out}	outward area of the control volume (m^2)
dA	infinitesimal change in area (m^2)
$d\rho$	infinitesimal change in density (kg m^3)
E	total energy of the fluid in the pipe system (J)
E_s	energy losses due to the viscosity (J)
E_n^T	total energy of the n^{th} mode (J)
E_{Fn}	energy flux (i.e. power) of the n^{th} mode (J s^{-1})
E_n	total energy per unit wavelength of the n^{th} mode (J)
E_{tr}, E_{ref} and E_{in}	transmitted, reflected and incident energy, respectively (J)
f	the frequency (Hz)
f_n	cut-off frequency of the n-th mode (Hz)
$\overline{f}$	Darcy-Weisbach friction factor (-)
F	vector flux along x-direction (-)
F_{ext}	external forces (J)
F_{shear}	shear force (J)
F_p	pressure force (J)
F_g	gravity force (J)
F_p^{side}	pressure force on converging or diverging pipe walls (J)
g	standard gravitational acceleration
G	vector flux along r-direction (-)
h	unsteady pressure head (m)

h_m^0	m^{th} pressure harmonic (m)
h_m^{amp}	amplitude of pressure head harmonic (m)
H	instantaneous pressure head (m)
$\overline{H}$	mean pressure head (m)
J_0 and Y_0	zeroth order Bessel's function of first and second kind, respectively (-)
$J_1(r)$	first order Bessel's function of first kind (-)
k	wavenumber (rad m^{-1})
k_m^0	m^{th} wavenumber of intact pipe (rad m^{-1})
k_{rn}	radial wavenumber of the n^{th} mode (rad m^{-1})
k_{xn}	axial wavenumber of the n^{th} mode (rad m^{-1})
k_{xn}	axial wavenumber of the n^{th} mode (rad m^{-1})
K_e	equivalent bulk modulus (Pa)
K_f	bulk modulus of the fluid (Pa)
K_s	bulk modulus of the pipe walls elasticity (Pa)
l^*	characteristic length scales (m)
L	pipe length (m)
M_{ch}	Mach number (-)
$\overline{M}_{in}$	the rate of mass entering the control volume (kg s^{-1})
$\overline{M}_{out}$	the rate of mass exiting the control volume (kg s^{-1})
n	radial mode number (-)
n_r	reflected mode number (-)
n_t	transmitted modes number (-)
$\vec{n}$	unit normal vector to the control volume area (-)
P	pressure (Pa).
P_{in}	incident pressure wave $x = \infty$ (Pa)
P_{ref}	reflected pressure wave from discontinity (Pa)
P_{tr}	transmitted pressure wave (Pa)

q	unsteady discharge ($m^3\ s^{-1}$)
q_m^0	m^{th} flow discharge harmonic ($m^3\ s^{-1}$)
q_m^{amp}	amplitudes = flow discharge harmonic ($m^3\ s^{-1}$)
Q	instantaneous flow discharge ($m^3\ s^{-1}$)
Q_0	initial steady state flow rate ($m^3 s^{-1}$)
$\overline{Q}$	mean discharge ($m^3\ s^{-1}$)
R	pipe radius (m)
R_e	Reynolds number (-)
S	vecotor of source terms (-)
t	time (s)
t_p	one (or multiple) wave period(s) (s)
t_w	characteristic time scales (s)
T	kinetic energy (J)
T_{nm}	transmission matrice (-)
T_{rn}	radial kinetic energy of the n^{th} mode (J)
T_n	kinetic energy of the n^{th} mode (J)
T_{xn}	axial kinetic energy of the n^{th} mode (J)
U	potential energy (J)
U_c	vector of conservative variables (-)
U_n	potential energy of the n^{th} mode (J)
V_0	initial steady state velocity (ms^{-1})
V_r	velocity component in r-directions ($m\ s^{-1}$)
V_{rn}	radial velocity of the n^{th} mode ($m\ s^{-1}$)
V_x	velocity component in x- direction ($m\ s^{-1}$)
V_{xn}	axial velocity of the n^{th} mode ($m\ s^{-1}$)
V_{gn}	group velocity of the n^{th} mode ($m\ s^{-1}$)
V^*	characteristic velocity scales ($m\ s^{-1}$)

V_m^0	m^{th} flow velocity harmonic (m s^{-1})
w	angular frequency (rad Hz)
w_m^0	m^{th} eigenfrequency (rad Hz)
W_r	work done at lateral boundaries are, the and the (J s^{-1})
W_x	work done at the axial boundaries (J s^{-1})
x	axial coordinate (m)

Greek letters

α_{rn}	n^{th} zero of the first order Bessel's function of first kind (-)
β	averaging cofficient (-)
γ_n	n-th pressure amplitude of the right going wave (Pa)
δ_{nj}	Kronecker delta function (-)
ΔV	change in velocity induced by the wave (m s^{-1})
ΔP	change in pressure (Pa)
ΔA_c	change in area after transient in the channel (m^2)
ΔA	change in pipe area (m^2)
ΔQ	change in flow rate induced by the wave (m^3 s^{-1})
Δt	change in time (s)
$\Delta \rho$	change in water density (kg m^{-3})
θ_{kn}	propagation angle of the n-th mode
λ_n	wavelength of the n^{th} mode (m)
μ, $\bar{\mu}$	dynamic viscosity second viscosity the fluid (Pa s)
ν	kinematic viscosity (m^2 s^{-1})
ρ	water density (kg m^{-3})
ρ^*	characteristic density scales (kg m^{-3})
τ	shear stress between the fluid and the conduit walls (Pa)
τ_{rr} , τ_{xx} , $\tau_{\theta\theta}$ and τ_{rx}	components of the stress tensor (Pa)
υ_n	phase velocity of the n^{th} mode (m s^{-1})

Υ_{nm}	reflection matrice (-)
φ_n	*n*-th pressure amplitude of the left going wave (Pa)
Ω	control volume (m^3)

Chapter 3

b	scheme order of accuracy (-)
b_0	reference scheme order of accuracy (-)
C^- , C^+	Riemann Invariants (-)
E_{Fn}	energy flux of the n^{th} mode ($J\ s^{-1}$)
f	frequency (Hz)
f_c	central frequency (Hz)
F	radial flux (-)
F^{1D}	one dimensional splitted flux along the radial direction (-)
G	axial flux (-)
G^{1D}	one dimensional splitted flux along the axial direction (-)
i	radial coordinate in the numerical domain (-)
j	axial coordinate in the numerical domain(-)
J_F	Jacobian matrix with respect to F (-)
J_G	Jacobian matrix with respect to G (-)
L	length of the pipe (m)
L_G, L_F	left eigenvectors matrices (-)
N_{bc}	number of fictitious cells added for boundary conditions (-)
N_R	number of discrete finite volumes along the axial direction (-)
N_S	number of discretized FV per central wavelength (-)
N_X	number of discrete finite volumes along the axial direction (-)
P	pressure (Pa)
P_{Jou}	Joukowsky pressure (Pa)
P_n	pressure of the n^{th} radial mode (Pa)

P_{res}	pressure at the reservoir (P)
P_s	pressure induced by the generated source (Pa)
R	pipe radius (m)
r	radial coordinate (m)
S	vecotor of source terms (-)
t	time (s)
t_{wave}	duration of the generated transient wave (s)
T_b^{CPU}	fitted CPU time function (s)
U_c	vector of conservative variables (-)
U_F	1st updat of U along the radial direction(-)
U_r^{1D}	one dimensional splitted vector of conservative variables along the radial direction (-)
U_x^{1D}	one dimensional splitted vector of conservative variables along the axial direction (-)
$\overline{\overline{U}}$	second splitting update of U (-)
$\overline{U}$	vector of averaged conservative variables in a cell (-)
x	axial coordinate (m)

Greek letters

Γ_b	constant defining the CPU time at very low NR (s)
Δt	numerical time step (s)
Δx	axial length of the discrete finite volume (m)
Δr	radial length of the discrete finite volume (m)
Δ^+	forward jump (-)
Δ^-	backward jump (-)
ε	a very small number to avoid singularity (-)
ρ^*	Riemann solution for density (kg m^{-3})
$(\rho V_x)^*$	Riemann solution for axial momentum (kg s^{-1} m^{-2})
$(\rho V_r)^*$	Riemann solution for radial momentum (kg s^{-1} m^{-2})
$\bar{\tau}_b$	rate at which the CPU time increases (-)

χ	norm function used to obtain the numerical scheme accuracy (-)
$\overline{\psi}_x^{1D}, \overline{\psi}_r^{1D}$	characteristic variables (-)
ϖ	vector variable of reconstructed data (-)
$\Omega_{i,j}$	volume of the discrete finite volume at i,j (m^2)
$\Im_i$	slope limiter along the radial direction (-)
$\Im_j$	slope limiter along the axial direction (-)

Chapter 4

a	acoustic wave speed ($m\ s^{-1}$)
A_0	cross sectional area of intact pipe (m^2)
A_j	the area of the j^{th} pipe (m^2)
$A(x)$	cross sectional area function of the conduit (m^2)
k	wavenumber (rad m^{-1})
k_m	wavenumber of the m^{th} mode (rad m^{-1})
l_b	length of the blockage (m)
l_j	length of the j^{th} pipe (m)
p_0	the amplitude of the incident wave (Pa)
p_j^{tr} and p_j^{ref}	transmitted and reflected wave amplitude in pipe number j (Pa)
$p(x,w)$	pressure wave function in the frequency domain (Pa)
P_1	transmitted pressure wave in region 1 (Pa)
P_3^I and P_3^R	incident and reflected pressure wave in pipe region 3 (Pa)
w	angular frequency (rad Hz)
w_c	central frequency (rad s^{-1})
$w_{\overline{m}}^R$	$\overline{m}^{th}$ Bragg resonance frequency of maximum reflections (rad s^{-1})
$w_{\overline{m}}^T$	$\overline{m}^{th}$ Bragg resonance frequency of total transmission (rad s^{-1})
x	axial coordinate (m)

Greek letters

α	area ratio between blocked and intact cross sectional areas (-)
α_{1b}	area ratio for single blockage case (-)
β	coefficient that controls the frequency bandwidth (rad)
λ	wavelength (m)

Chapters 5 & 6

a	acoustic wave speed in water (ms^{-1})
A_0	cross sectional area of intact pipe (m^2)
A_0	cross sectional area of intact pipe (m^2)
A_1	cross sectional area of pipe 1 (m^2)
A_2	cross sectional area of pipe 2 (m^2)
A_3	cross sectional area of pipe 3 (m^2)
D_1	diameter of pipe 1 (m)
D_2	diameter of pipe 2 (m)
D_3	diameter of pipe 3 (m)
D_H	determinant of the Hessian matrix (-)
D_v	diameter of the electro-valve (m)
E	otal energy per unit length ($J\ m^{-1}$)
$\mathrm{err}(m)$	dimensiolness error in zero shift position at mode m (-)
$F_{dis}(w_m, l_2, l_3, \alpha)$	dispersion function (-)
g	acceleration due to gravity ($m\ s^{-2}$)
H	instantaneous pressure head (m)
$\overline{H}$	mean pressure head (m)
h	unsteady pressure head induced by the wave (m)
h_m^0	m^{th} pressure head harmonic of intact pipe system (m)
$\bar{h}_m$	m^{th} dimensionless pressure head harmonic (m)

h_m^{amp}	m^{th} maximum complex amplitude of pressure head (m)
k	wavenumber (rad m^{-1})
$k_m^{\max}$	m^{th} wavenumber at maximum shift (rad m^{-1})
k_m^s	m^{th} wavenumber when $\alpha = 0$ (rad m^{-1})
L	whole pipe length (m)
l_1	length of pipe 1 (m)
l_2	length of pipe 2 (m)
l_3	length of pipe 2 (m)
m	mode number for pipe system of length L (-)
m_1	mode number for subsystem 1 (-)
m_2	mode number for subsystem 2 (-)
N	number of blockages (-)
P	pressure (Pa)
P_c	characteristic pressure difference scale (Pa)
Q	instantaneous flow discharge (m^3 s^{-1})
$\overline{Q}$	mean discharge (m^3 s^{-1})
q	unsteady discharge due to wave (m^3 s^{-1})
$\bar{q}_m$	m^{th} dimensionless discharge (-)
q_m^{amp}	m^{th} maximum complex amplitude of flow discharge (m^3 s^{-1})
q_m^0	m^{th} flow discharge harmonic of intact pipe system (m^3 s^{-1})
T	kinetic energy per unit length (J m^{-1})
$\overline{T}$	normalized kinetic energy (-)
t	time (s)
$\overline{U}$	normalized potential energy (-)
U	potential energy per unit length (J m^{-1})
V	unsteady flow velocity induced by the wave (m s^{-1})
w	angular frequency (rad s^{-1})
w_m	m^{th} resonant frequencies in the blocked pipe case (rad s^{-1})

$w_m^{s_1}$	m^{th} eigenfrequency of uncoupled subsystem 1 ($\alpha = 0$) (rad s^{-1})
$w_m^{s_2}$	m^{th} eigenfrequency of uncoupled subsystem 2 ($\alpha = 0$) (rad s^{-1})
w_m^{s}	m^{th} eigenfrequency when $\alpha = 0$ (rad s^{-1})
w_m^{mes}	m^{th} measured eigenfrequency (rad Hz)
w_m^0	m^{th} resonant frequencies in the intact pipe case (rad s^{-1})
w_H	natural frequency of Helmholtz resonator (rad s^{-1})
$w_{\overline{m}}^R$	$\overline{m}^{\text{th}}$ Bragg resonance frequency of maximum reflections (rad s^{-1})
$w_{\overline{m}}^T$	$\overline{m}^{\text{th}}$ Bragg resonance frequency of total transmission (rad s^{-1})
x	axial coordinate (m)
Z	impedance (Pa m^{-3} s^{-1})

Greek letters

α	area ratio between blocked and intact areas (-)
ΔE	energy change due to cross sectional area variation (J m^{-1})
$\overline{\Delta E}$	integrated energy change over the pipe domain (J)
ΔT_m	change in kinetic energy at the m^{th} mode due to the blockage (J m^{-3})
ΔU_m	change in potebtial energy at the m^{th} mode due to the blockage (J m^{-3})
Δw_m	m^{th} eigenfrequency shift (rad s^{-1})
$\Delta w_m^{\max}$	maximum m^{th} eigenfrequency shift (rad s^{-1})
$\overline{\Delta w_m}$	m^{th} integrated eigenfrequency shift over the pipe domain (rad s^{-1})
δk	small perturbation in wave number (rad m^{-1})
δw	small perturbation in eigenfrequency (rad s^{-1})
η_1	l_1 / L dimensionless length (-)
η_2	l_2 / L dimensionless length (-)
η_3	l_3 / L dimensionless length (-)
Θ	defined function (-)

λ	probing wavelength (m)
τ	τ^{th} zero shift position at a given m mode(-)

Chapter 7

a	acoustic wave speed in water (ms^{-1})
B	integration constant (Pa)
D	pipe diameter (m)
D_s	source diameter (m)
E_{Fn}	energy flux of the n^{th} mode ($J\ s^{-1}$)
E_v	total energy dissipation ($J\ m^{-1}$)
E_n	total energy per unit wavelength of the n^{th} mode ($J\ m^{-1}$)
E_T	the total injected energy from the source ($J\ m^{-1}$)
f	frequency (Hz)
f_1	cut-off frequency of the first mode (Hz)
f_2	cut-off frequency of the second mode (Hz)
f_c	central frequency (Hz)
f_v	friction factor (-)
J_0	Bessel function of order 0 (-)
k	wavenumber ($rad\ m^{-1}$)
k_{rn}	radial wavenumber of the n^{th} mode ($rad\ m^{-1}$)
k_{xn}	axial wavenumber of the n^{th} mode ($rad\ m^{-1}$)
L	length of the pipe (m)
n	mode number (-)
n_h	the highest excited radial mode number (m)
P	pressure (Pa)
P_0	initial pressure in the pipe (Pa)
P_F	transient pressure at the source (Pa)
P_n	pressure of the n^{th} mode (Pa)
P_s	pressure amplitude of the generated source (Pa)

R	radius of the pipe (m)
r	radial coordinate (m)
t	time (s)
t_p	time period (s)
t_{wave}	duration of the generated transient wave (s)
t^{mes}	measurement time (s)
t_n^s	spreading time of the energy flux of the *n*-th high mode at x_n^s, (s)
t_n^E	time at which the *n*-th mode energy reaches a measurement location x_n^{mes} (s)
V	average water speed along the pipe (m s^{-1})
V_n	phase velocity of the n^{th} mode (m s^{-1})
V_r	radial velocity (m s^{-1})
V_{rn}	radial velocity of the n^{th} mode (m s^{-1})
V_x	axial velocity (m s^{-1})
V_{xn}	axial velocity of the n^{th} mode (m s^{-1})
V_{gn}	group velocity of the n^{th} mode (m s^{-1})
$V_{gn}^{\max}$	maximum group velocity of the *n*-th excited high mode (m s^{-1})
$V_{gn}^{\min}$	minimum group velocity of the *n*-th excited high mode (m s^{-1})
w	andgular frequency (rad s^{-1})
x	axial coordinate (m)
x_n^r	Propagation range of the *n*-th high mode with repect to the plane mode (m)
x^{mes}	measurement location away from the source and (m)
x_n^s	position at which the *n*-th mode is separated from all other excited modes (m)
x_n^c	Propagation range of the *n*-th high mode with repect to the plane mode (m) at the pipe centreline (m)

Greek letters

α_{rn}	n^{th} zero of Bessel function of order 1 (-)

λ_n	wavelength of the n^{th} mode (m)
θ	azimuthal coordinate (rad)
θ_{kn}	propagation angle of the *n*-th mode (rad)
θ_{kn}^{c}	propagation angle of the *n*-th mode at the central frequency (rad)
ν	kinematic viscosity of wate ($m^2\ s^{-1}$)
ρ	density ($kg\ m^{-3}$)
ς_n	viscous dissipation rate of the *n*-th mode (-)
φ_n	*n*-th pressure amplitude of the left going wave (Pa)
υ_n	phase velocity of the n^{th} mode ($m\ s^{-1}$)
Ψ_n	ratio of MEA between the *n*-th high mode and M0 measured at the location x_n^s (-)

Abbreviations

1D	One dimensional
2D	Two dimensional
3D	Three dimensional
CBC	Characteristic boundary condition
CPU	Computational
DFT	Discrete Fourrier transform
ENO	Essentially Non-Oscillatory
FV	Finite volume
HFW	High frequency waves
M0	Plane wave mode
M1	First high mode
M2	Second high mode
MEA	Maximum energy amplitude
MPA	Maximum pressure amplitude
PML	Perfectly matched layer

Re	Real part
RPR	Reservoir-pipe-valve
RPV	Reservoir-pipe-valve
TBDDM	Transient-based defect detection methods
TVD	Total variation diminishing
VPV	Valve-pipe-valve
WENO	Weighted Essentially Non-Oscillatory

CHAPTER 1

INTRODUCTION AND LITERATURE REVIEW

"*So startling would his results appear to the uninitiated that until they learned the process by which he had arrived at them they might well consider him as a necromancer*"

Dr. Watson, speaking about Sherlock Holmes
A Study in Scarlet

1.1. Blockages in Water Supply systems

Current water supply systems (WSS) around the world are wasteful with numerous malfunctioning devices and undetected faults including blockages, leakages, etc, all leading to poorly performing systems and increased risk of water contamination. Worldwide, the water losses are estimated around at 40% and the associated percentage of energy wasted in them is even higher ([18], [17]). A critical need for massive and costly WSS upgrades has been reported by many countries in the world. For example, Hong Kong has committed to a HK$ 22 billion program of WSS rehabilitation and replacement with the aim of curbing the water losses from about 30% to just below 20%. Since 2009, the US has planned to spend more than US$ 300 billion on WSS over 20 years ([3], [4], and [20]).

One of the major factors of inefficiency in WSS is that they often experience blockages during their life time due to physical and/or chemical processes (e.g. material deposition, tubercles (rust), scales, plaque, bio-fouling and inadvertently throttled inline valves, and air intrusion). The build-up of blockages on the inside of a pipe wall often begins in the form of increased roughness (see Figure 1.1) with small amplitude, growing with time, and

eventually block a sizeable portion of the pipe's cross sectional area (see Figures 1.2 and 1.3). Such blockages result in wastage of energy and financial resources, reduction in carrying capacity, and increased potential for contamination. In addition, the flows in severely blocked pipes can become throttled to large degree resulting in flow redistribution, and reduction of the overall system's redundancy (reliability), and overpressure of some pipes in the system, thereby, leading to increased leaks. Whether for engineered or natural conduits, it is of paramount importance to detect blockages so that they are dealt with in a timely manner. Clearly, it would be highly desirable if blockages could be detected at an early enough stage so that problems, damage and waste incurred by large blockages can be minimized.

Figure 1.1 Increased roughness in pipe ([116])

Figure 1.2 Partially blocked pipe ([40])

Figure 1.3 Severely blocked pipe ([128])

1.2. Acoustic waves for imaging the internal shape of vocal tracts and musical instruments

The approach of using a measured pressure trace to infer the internal shape of a conduit is a mainstay of the field of acoustic phonetics (e.g. [112], [41], [89], [91], [92] and [120]). In particular, it is found that the eigenfrequencies of a bounded pipe system vary with the cross sectional area of the conduit, where this dependence is used to formulate algorithms for the reconstruction of the cross sectional area function of human vocal tract system. Similar approach is also used to acoustically image and study the properties of musical instruments (e.g. [53], [26] and [114]). More recently, this approach is being used for blockage detection in WSS (e.g. [32], [119], [10], [134], [73] [88], [85], [97] and [111]).

Schroeder ([112]) shows that the Ehrenfest theorem ([37]) can be used to formulate an algorithm for determining the geometry of the vocal tract from measured values of the eigenfrequencies of the acoustic pressure wave. Essentially, the Ehrenfest theorem states that the change in the eigenfrequencies is related to the change in energy such that $w_m E_m$ remaines constant for small variations in the cross sectional area, where w_m and E_m are the eigenfrequency and total energy of the m^{th} resonant mode. The derivation of this approach is given in the work by Fant ([41]) for vocal tract application and it is used in Chapter 5 for shallow blockages (*i.e.* blockages with small radial protrusion) in water-filled pipe systems. Schroeder's approach formed the basis for other works (e.g. [56] and [98]).

Based on Webster's horn equation ([136]) and perturbation theory, Mermelstein ([89]) showed that the eigenfrequency shift of the m^{th} pressure mode is directly linked to the amplitude of the m^{th} term in the Fourier series expansion of the cross sectional area function of the conduit with respect to longitudinal distance.

Sondhi and Gopinath ([117]) used the impulse response measured at the human lips to determine the vocal-tract shape. In a later work, Sondhi and Resnick ([118]) provide the measurement techniques and numerical procedures used for continuous speech synthesized from direct measurements of the area functions. A comprehensive review of vocal tract reconstruction techniques can be found in Milenkovic ([91]) and ([92]). In addition, the textbook by Stevens ([120]) provides an excellent overview of acoustic phonetics.

The impulse response method is also used to study the sound propagation in musical instruments. Some of the early works on this topic are by Goodwin ([53]) and Deane ([26]) where they discussed the relations between the geometry and acoustics of brass instruments using acoustic pulse reflectometry. Recent advances in the use of pulse reflectometry for bore reconstruction of brass instruments can be found in Sharp et al. ([114]).

Domis ([27]) found that the presence of a blockage in a pipe shifts the eigenfrequencies of the pipe system, and used this knowledge to detect an early forming blockage in a cooling system wrapper of sodium-cooled fast nuclear reactors. In a follow-up paper ([28]), Domis showed through experimental investigation that the position and size of the blockage could be determined from the eigenfrequency shift using the transfer function.

Qunli and Frick ([105]) considered the case of a shallow blockage located at the boundary of a pipe system and determined a simple harmonic equation for the eigenfrequency shift. They show that the blockage location is related to the periodicity pattern of the shift and its size is related the shift amplitude. Following the works by Schroeder ([112]) and Mermelstein ([89]) for vocal tract area reconstruction, Qunli and Frick ([106]) used perturbation theory and Fourier decomposition for the case of interior blockages in pipe systems. They obtained an area function that depends on the eigenfrequency shift at the odd and even resonant modes. This requires the use of two different boundary condition setups: one being symmetric (e.g. Valve-pipe-valve (VPV) system) and the other asymmetric (e.g. Reservoir-pipe-valve (RPV) system).

De Salis and Oldham ([25]) showed that it is suficient to study a symmetric or asymmetric pipe system making use of the anti-resonant frequencies shifts which were identified using maximum length sequence (MLS) techniques.

1.3. Acoustic waves for imaging the internal shape of water pipes: Blockage detection in WSS

Commercially available techniques for diagnosis of WSS are predominantly targeted at leakage detection. For example, noise correlation techniques ([62]), Sahara system ([129]),

smart ball ([48]) etc ([104]) are all leakage detection technologies. One exception is the closed-circuit television (CCTV) which can be used for both leakage and blockage detection. However, CCTV is expensive, time consuming and intrusive and best suited for newly installed pipes.

TBDDM is a promising general approach for blockage detection and overall pipe wall condition assessment.

Duan et al. ([32]) developed a blockage detection methodology that does not require knowledge of the eigenfrequencies of the intact pipe system. Their technique uses inverse optimization methods (e.g. genetic algorithm) to find the blockage geometry and location that best satisfies the dispersion relation of the blocked pipe system. Duan et al. ([32]) generalized their technique for multi-blockages. This approach is discussed in more details in the next section. It is noted that the technique of using inverse transient methods for condition assessment of WSS dates back to the work of Liggett and Chen ([77]). This technique is often referred to as Transient-Based Defect Detection Method (TBDDM).

Similar to the work by Qunli and Frick ([105]), Duan et al. ([35]) applied Taylor expansion to the dispersion relation of the blocked pipe system for shallow blockages and found a simple frequency-shift equation. This simplified blockage detection model is limited to cases where blockages occupy about 30% of the pipe area or less. This simple frequency-shift formula is further investigated in Chapter 6 of this thesis.

Brunone et al. ([10]) show that discrete and extended blockages have significantly different impact on the system's response. While Mohapatra et al. ([97]) found that extended blockages shift the eigenfrequencies of the system, Sattar et al. ([111]) and Lee et al. ([73]) found that discrete blockages (short blockages along the axial extent) damp the amplitude of pressure frequency response signals and impose an oscillatory pattern of resonant pressure frequency peaks. They showed that this pattern could be related to the location and size of the blockage.

Wang et al. ([134]) show that a discrete blockage in a pipe system introduces damping to the transient signal and developed a technique for locating and sizing discrete blockages based on this damping.

Meniconi et al. ([88]) use wavelet analysis techniques to indentify the blockage reflection signature in a pressure signal and determined the blockage location with prior knowledge of the wave speed information. A hybrid wavelet-frequency shift aproach is used by Meniconi et al. ([88]) for blockage detection, where wavelet analysis is used to locate the blockage while the frequency shift is used to identify the radial and longitidunal dimensions of the blockage. The hybrid approach is found to be superior than the individual approaches. The effect of visco-elasticity of a pipe on extended blockage detection is investigated in Duan et al. ([30]) and Meniconi et al. ([85]). Massari et. al ([83]) applied a stochastic successive linear estimator algorithm on the time domain response signal to provide statistically the best unbiased estimations of the diameter distribution due to partial blockages in a pipe system and to quantify the uncertainty associated with these estimations.

Recently Tolstoy ([125]) applied acoustic waves monitoring for blockage detection in pipe and used the match field processing (MFP) technique to detect and locate the blockage. She concluded that "(1) near blockages show stronger effects than far ones, (2) bigger blockages show stronger effects than weaker ones, and (3) multiple blockages appear to be dominated by the nearest effects leaving far blockages still unseen. Additional work such as other, non-linear processors and additional receivers may improve this last situation.''

1.4. Problem statement

It is clear from the above literature survey that that the focus of past research in WSS is on the inverse problem where mathematical relations that link the measured transient wave to the cross sectional area of the pipe were formulated and algorithms for how these relationships could be used to infer blockages were proposed. While this research direction is promising and has led to proof of concept under idealized laboratory settings, there are a

number of unresolved issues. For example, there is neither a proof that the inverse problem, which relates the unknown blockage properties to the measured eigenfrequencies, has a unique solution nor is there a technique to find it, if it even exists. In fact, current solutions of this inverse problem require that the number of blockages is known a priori which is unrealistic in practice. In addition, the computational time needed to solve the inverse problem grows exponentially with the number of blockages. Moreover, the physics of why blockages shift eigenfrequrencies, why some eigenfrequencies are shifted more than another and why some eigenfrequencies experience positive shift while others experience negative shift is not yet clear, and has only been partially discussed in the past (e.g. [39] and [120]). The two problems addressed in this thesis are introduced below.

1.4.1. Problem 1: solution of the blockage detection problem

Consider a reservoir-pipe-valve (RPV) system as shown in Figure 1.4, the blocked pipe system is modelled as the junction of three pipes in series with different diameters (see Figure 1.4). The three pipes are defined as pipe 1 with length l_1 and cross sectional area $A_1 = A_0$, pipe 2 with length l_2 and cross sectional area $A_2 < A_0$ and pipe 3 with length l_3 and cross sectional area $A_3 = A_0$ where A_0 is the intact cross sectional area. The frequency response function (FRF) of the RPV system could be measured by generating a transient signal at the valve (e.g. opening and closing the valve rapidly). Figure 1.5 compares the FRF of the blocked RPV system (Figure 1.4) and the FRF of an intact RPV system (*i.e.* with no blockage). Figure 1.5 shows the eigenfrequency shifting effect due to the presence of a blockage in the pipe system.

The dispersion relation of the blocked RPV (Figure 1.4) that governs the eigenfrequency variation is given by El-Rahed and Wagner ([39]) and Duan et al. ([32]) as :

$$\begin{aligned} F_{dis}(w_m, l_2, l_3, \alpha) &= \cos(w_m l_1/a)\sin(w_m l_2/a)\sin(w_m l_3/a) \\ &-\alpha\cos(w_m l_1/a)\cos(w_m l_2/a)\cos(w_m l_3/a) \\ &+\alpha\sin(w_m l_1/a)\cos(w_m l_2/a)\sin(w_m l_3/a) \\ &+\alpha^2\sin(w_m l_1/a)\sin(w_m l_2/a)\cos(w_m l_3/a) = 0 \end{aligned} \tag{1.1}$$

where $\alpha = A_2 / A_0$ is the cross sectional area ratio between blocked area and the intact area, w_m is the eigenfrequency of the m^{th} fundamental (resonant) mode, and a is the acoustic wave speed in water. Duan et al. ([32]) has generalized the dispersion relation (Eq. (1.1)) for general multi-blockage cases in bounded pipe system. For blockage localization, Duan et al. ([32]) used inverse optimization techniques, such as the genetic algorithm, to minimize the following equation

$$\sum_m \left| F_{dis}\left(w_m^{mes}, l_2, l_3, \alpha\right) \right| = \min \tag{1.2}$$

where w_m^{mes} is the m^{th} measured eigenfrequency (see Figure 1.5). Such techniques require a search on all possible combinations of $\{ l_2, l_3, \alpha \}$ which gives a very large search domain. Figure 1.5 gives a 3D plot of the objective function in Eq. (1.2) variation with length l_2 and l_3 for a fixed area ratio α = 0.2. Figure 1.5 shows that the eigenfrequency function admits many minima and is very complex for optimization problems. One objective of this thesis is to gain an understanding of the eigenfrequency shift mechanism induced by wave-blockage interaction that would help in reducing the search domain for the inverse optimization techniques. This is necessary if the dispersion relation (e.g. Eq. (1.1)) is to become a viable approach for identifying blockages in fluid lines.

Figure 1.4 A single blockage in a Reservoir-pipe-valve system (bounded system)

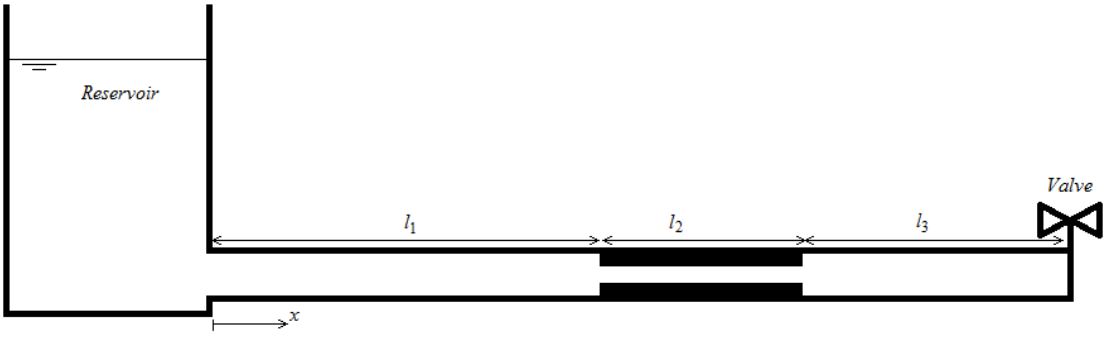

Figure 1.5 A single blockage in a Reservoir-pipe-valve system

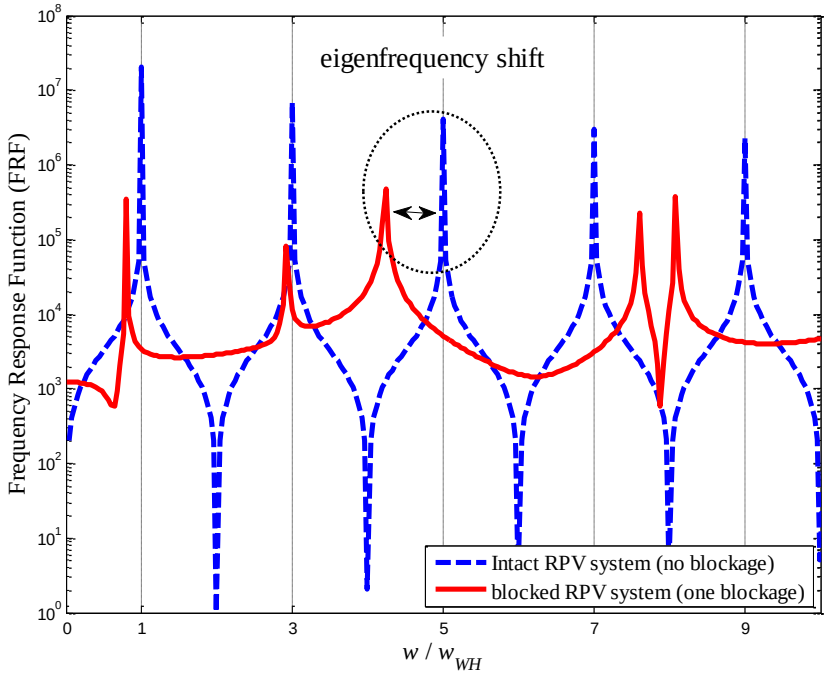

Figure 1.6 Objective function in Eq. (1.2) variation with length l_2 and l_3 for a fixed area ratio α = 0.2 using the first 10 eigenfrequencies.

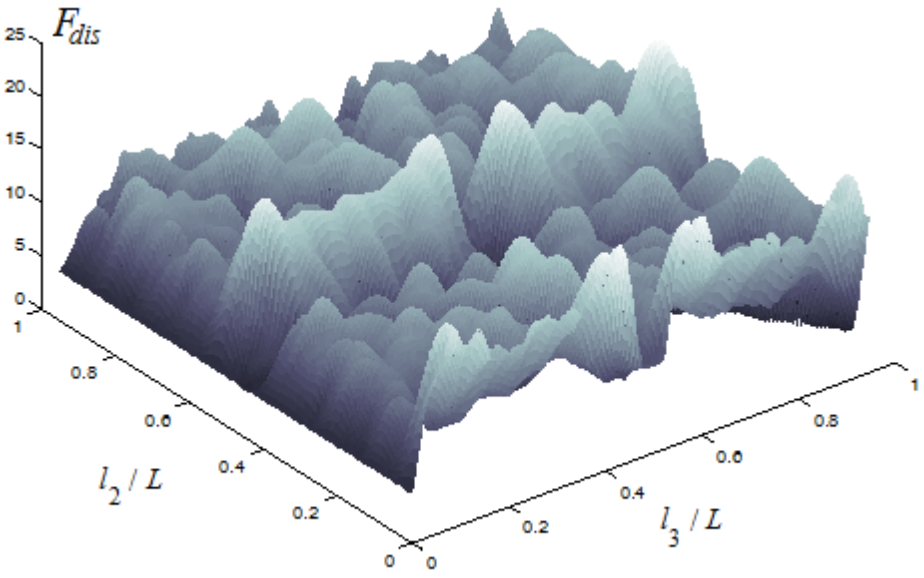

1.4.2. Problem 2: resolution of blockage detection

Although not well analyzed, there is an implicit recognition in the literature (e.g. [71] and [32], [79]) that signals with wide frequency bandwidth (FBW) are most suitable for defect detection. Lee et al. ([71]) recently demonstrated the importance of input signal FBW on pipe condition assessment through analytical, numerical and experimental means. The majority of transient wave generator technologies used in TBDDM are based on rapid valve closures (e.g. [88], [73], and [119]) or pump operation (e.g. [87]). The signals induced by valve-type generators induce significant loss of water, their signals are too crude, the reflections cannot be distinguished from normal system noise and their resolution is too low for localized defects. For example, the so-called rapid valve closure often takes about 0.05s to complete. As a result, the wave front is spread over a physical length of about 20 m along the pipe and cannot emphasize the effects of leaks and discrete blockages since their length scale is generally smaller than this wave front ([140]).

Wave theory is widely used to probe and characterize various media and to convey information in various applications (e.g., non-destructive material testing, medical diagnostics, and underwater communications), where it is well known that the higher frequency of the waves the better is the resolution. Unsurprisingly, similar conclusions are found for TBDDM ([71], [79]). In fact, transient waves used for TBDDM cannot resolve scales that are smaller than a/f, where a is the wave speed and f is the frequency. For example, Allen et al. ([2]) simulated a sudden burst and reported that it could only be located to within ± 45m (*i.e.* 90m range) even though the sensor was only 20 m away from the fault. The wave resolution in this case was $a/f \sim 900/10 \sim 90$ m. Similarly, a simulated burst in Hong Kong could only be located to within ± 42 m ([60]), and the wave resolution in this case was $a/f \sim 1200/10 \sim 90$m. In addition, Meniconi et al. ([87]) conducted field investigation in the city of Milan (Italy) and reported that leaks could only be located to within 800m ([87]). Their wave resolution in this case was $a/f \sim 900/1 \sim 900$m.

Moreover, Duan et al. ([32]) reported that the more measured eigenfrequencies included into the objective function (Eq. (1.2)), the better is the accuracy given by the inverse optimization technique. This is natural given that higher frequencies (*i.e.*, shorter wavelengths) provide

higher resolution in defect detection and are better at localizing multi-defects with multi-scales.

However, the use of high frequency waves (HFW) excites radial and azimuthal waves and renders the classical one-dimensional water-hammer (WH) theory invalid. This work studies the behaviour of HFW in water-filled pipes and how they interact with blockage.

1.5. Objectives and organization of the thesis

The objective of this thesis is to shed greater light on the forward problem of wave-blockage interaction in WSS under a wide range of frequencies. In particular,

(i) The eigenfrequency shift mechanism induced by wave-blockage interaction is investigated theoretically, numerically and experimentally. The underlying physics of the eigenfrequency shift is clarified.
(ii) HFW in water-filled pipe and how they interact with blockages is investigated

This research is motivated by the fact that only if this forward problem is understood can one hope to address the issues that arise in connection with its inversion.

This thesis consists of eight chapters which are organized as follows. Following this introduction,

Chapter 2 introduces the governing equations relevant to this thesis. The phenemona of water-hammer is elucidated by drawing an analogy between surge waves in open channels and surge waves in pipes. The Joukowsky equation and the full one dimensional water-hammer equations are introduced. Then, the harmonic solution for 1D water-hammer in an intact pipe is derived. The two dimensional water-hammer wave equations are then introduced and their analytical solution for an inviscid fluid is given.

Chapter 3 gives details of the two-dimensional (2D) Riemann solver (RS)-based finite volume (FV) numerical schemes developed and used in this work. The Riemann problem and solution are illustrated. In addition, the MUSCL-Hancock approach used to obtain second-order accuracy in space and time is described, and details of the WENO reconstruction method for higher-order accuracy are given. Moreover, the numerical test cases and the boundary conditions are introduced. Then, the schemes' accuracy, stability, convergence and robustness are analyzed and discussed.

Chapter 4 uses analytical and numerical methods to study the processes of transmission and reflection of a pressure wave in a one dimensional unbounded pipe system. The existence of Bragg-type resonance in conduits where wave reflections are enhanced at certain frequency bands and wave transmissions are enhanced at other frequency bands are established. The Bragg resonce conditions are derived. The effect of Bragg resonance for the case of multi-blockages is discussed.

Chapter 5 studies the eigenfrequency shift mechanism caused by the presence of a blockage at the boundary of a bounded pipe system (e.g. reservoir-pipe-valve system). First, the chapter discusses the case of shallow blockages (*i.e.*, blockages with small radial protrusion) where it is shown that the eigenfrequency shift is governed by Ehrenfest theorem. The relation between the work of the radiation pressure and eigenfrequency shift for shallow blockages is derived. Second, the case of severe blockages (*i.e.*, blockages with large radial protrusion) is analyzed where it is shown that the pipe system decouples into independent subsystems: a subsystem that involves the blockage and another that involves the intact pipe sections. Third, the case of moderate blockage is dicussed.

Chapter 6 studies the eigenfrequency shift mechanism for the case of interior blockage and shows how this mechanism is related to (i) the Bragg-type resonance introduced in Chapter 4 and (ii) the simple blocked pipe system in Chapter 5. The mechanisms causing zero, positive and negative eigenfrequency shifst are described for shallow as well as severe and moderate blockage cases. Moreover, experimental tests are conducted to validate the eigenfrequency shift mechanism and the Bragg resonance effect.

Chapter 7 studies numerically the behaviour of HFW (non-plane and dispersive waves) in water-filled pipe. The dispersion behaviour of HFW under resonating probing source (*i.e.* the injected FBW contains the cut-off frequencies of high modes) and non-resonating probing source (*i.e.* the injected FBW does not contain any cut-off frequency) are discussed. Particularly, the effect of multi-path on the energy propagation and dissipation is analyzed, and the effect of the energy radial distribution and mode separation is emphasized. Furthermore, the scattering behaviour of HFW due to the presence of a blockage in a conduit is investigated.

Chapter 8 gives an overall summary of the work done in this research and recommends possible future work.

1.6. Publication list

The following is the list of publications produced during this research.

Journal papers:

Louati M, and Ghidaoui M.S. (2016). ”In-depth study of the eigenfrequency shift mechanism due to variation in the cross sectional area of a conduit”, *Journal of Hydraulic Research*. Submitted. Under review.

Louati M, and Ghidaoui M.S. (2016). ”On the behavior of high frequency acoustic waves in pressurized fluid in a conduit”, *Journal of Hydraulic Research*. Submitted. Under review.

Louati M, and Ghidaoui M.S. (2016). ”Range of propagation of high frequency acoustic waves in pipe”, *Journal of Hydraulic Research*. Submitted. Under review.

Louati M, and Ghidaoui M.S. (2016). ”In-depth Study of eigenfrequency shift mechanism due to an interior blockage in a pipe”, *Journal of Hydraulic Engineering*. To be Submitted.

Louati M, and Ghidaoui M.S. (2016). ”Bragg-type resonance in blocked pipe system and its effect on the eigenfrequency shift”, *Journal of Hydraulic Engineering*. To be Submitted.

Louati M, Meniconi M, Ghidaoui M.S. and Brunone B (2016). ”Experimental validation of the effect of Bragg-type resonance and eigenfrequency shift mechanism in blocked pipe system”, *Journal of Hydraulic Engineering*. To be Submitted.

Louati M, and Ghidaoui M.S. (2016). ”The need of high order numerical scheme for modeling high frequency acoustic waves in water-filled pipe”, *Computer & Fluids*. To be Submitted.

Louati M, Meniconi M, Ghidaoui M.S. and Brunone B. ”The use of Bragg resonnace and eigenfrequency shift information for blockage detection in pipes”, *Journal of Hydraulic Engineering*. In progress.

Louati M, and Ghidaoui M.S. ” On the scattering behavior of high frequency acoustic waves due to blockages in pipes”, *Journal of Hydraulic Research*. In progress.

Conference papers:

Louati, M. (2013).“On wave-defect interaction in pressurized conduits.”Proceedings of the 35th IAHR Congress, Chengdu-China.

Louati M, and Ghidaoui M.S. (2015). ”Wave-blockage interaction in pipes”, *36th IAHR World Congress* 2015, June 28- July 3, The Hague, The Netherlands.

Louati M, and Ghidaoui M.S. (2015). ”On the behavior of high frequency waves in pressurized conduits”, *12th International Conference-Pressure* Surges 2015, Nov 18-20, Dublin, Ireland.

Louati M, Luo J, Ghidaoui M.S. and Xu K. (2016). ”Numerical study of high frequency acoustic waves in water-filled conduits”, *13th ICMMES* 2016, July 18- 22, Hamburg, Germany. Accepted.

Louati M, and Ghidaoui M.S. (2016). ”Study of the eigenfrequency shift mechanism due to an interior blockage in a pipe”, *20th Congress of the IAHR APD* 2016, August 29- 31, Colombo, Sri Lanka. Accepted.

Louati M, and Ghidaoui M.S. (2017). ”On the scattering behavior of high frequency acoustic waves due to blockage in pressurized water-filled pipe”, *37th IAHR World Congress* 2017, August 13- 18, Kuala Lumpur, Malaysia. To be submitted.

CHAPTER 2

GOVERNING EQUATIONS

2.1. Introduction

The aim of this chapter is to introduce the low frequency and high frequency water-hammer models and their key analytical solutions. The study of water hammer (WH) (or transient) waves in pipe flow has been undertaken since the middle of the nineteenth century ([13]). WH arises in a wide range of application such as water distribution systems, the oil industry, power-plants, defect detections, etc. The majority of existing WH models are one-dimensional (1D) and assume that the pressure does not vary with radius and that the radial velocity is negligible compared to the axial velocity ([50]). Such models are the mainstays of WH analysis and pipe-network design. In the last two decades, quasi-2D models were developed with the aim of examining the validity of existing unsteady friction expressions and guiding the development of new ones (e.g. [38], [102], [103], [115], [130] and [141]). Again, these models assume that the pressure is not a function of radius.

Theoretically, the assumption that the pressure is not a function of radius is valid provided that the frequency of the WH is of the order of a/D or smaller, where a is the wave speed and D is the pipe diameter ([108]). Taking typical values of a (~1000 m/s) and D (~0.1 to 0.5 m) shows that the classical WH models are valid if the frequency, f, is of the order of 2 to 10 kHz or smaller. In the past, this condition and, by implication, the classical WH theory has never been challenged because WH waves are generated by mechanical devices such valves and pumps whose frequency is far below 1 kHz.

2.2. One dimensional water hammer equations

2.2.1. Water-Hammer wave

An analogy between a transient flow in an open channel and a transient flow in a pipe is useful for water-hammer wave behaviour ([50]). Figure 2.1 shows a transient in an open channel generated by a sudden and complete closure at a downstream gate, while Figure 2.2 shows a transient in a pipe generated by a sudden and complete closure of a valve of the downstream end. The initial steady state flow rate (Q_0) and velocity (V_0) are assumed to be the same in both the channel and the pipe. Therefore, the initial cross sectional area of the flow in the channel (A) is the same as that of the pipe.

Applying mass balance for the case of sudden gate closure, gives:

$$\rho\Delta Q\Delta t = \rho\Delta A_c a_c \Delta t \quad \text{or} \quad a_c = \frac{\Delta Q}{\Delta A_c} = \frac{\Delta V}{\Delta A_c / A} \tag{2.1}$$

where a_c is the wave speed in the open channel, ρ is the density, t is time; Δt is the change in time; and ΔA_c is the change in area after transient in the channel, ΔQ and ΔV are the change in flow and velocity within the transient time Δt. For the case of sudden valve closure in pressurized pipe, the mass balance dictates

$$\rho\Delta Q\Delta t = (\Delta\rho + \rho)(\Delta A + A)a\Delta t - \rho A a\Delta t \approx (A\Delta\rho + \rho\Delta A)a\Delta t \tag{2.2}$$

where a is the wave speed in the pipe, $\Delta\rho$ is the change in density; and ΔA is the change in pipe area. Equation (2.2) leads to

$$a = \frac{\rho\Delta Q}{(A\Delta\rho + \rho\Delta A)} = \frac{\Delta V}{\frac{\Delta A}{A} + \frac{\Delta\rho}{\rho}} \tag{2.3}$$

Clearly, the mass stored due to a change in pipe area, ΔA, and water density, $\Delta\rho$, is much smaller than the mass stored in a channel due to a change in water depth. That is

$$\frac{\Delta A}{A} + \frac{\Delta\rho}{\rho} << \frac{\Delta A_c}{A} \quad \text{or} \quad a >> a_c \tag{2.4}$$

Figure 2.1 Sudden gate closure

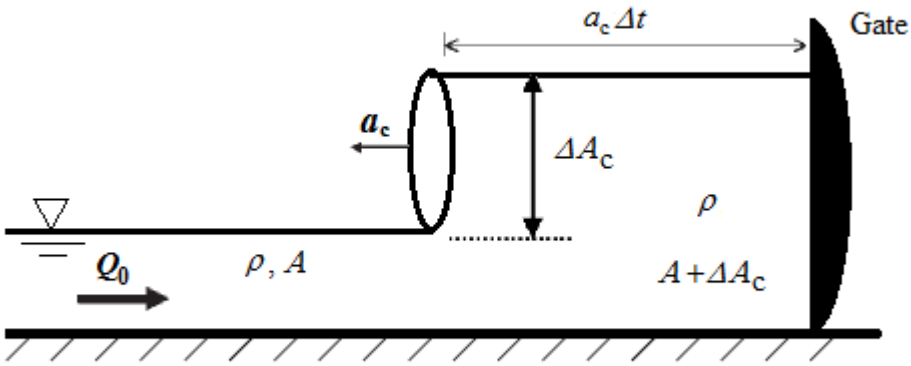

Figure 2.2 Sudden valve closure

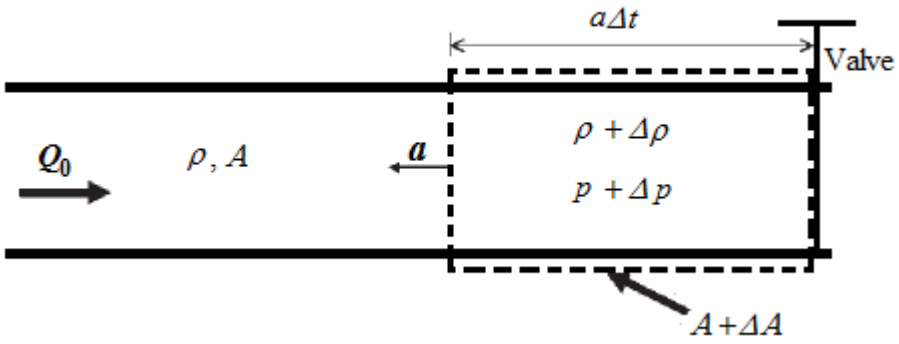

2.2.2. Fundamental equation of water hammer: Joukowsky relation

The first fundamental relation for estimating the magnitude of these so-called water-hammer pressures was formulated by Joukowsky in 1898 ([50]). In his formulation, Joukowsky applied the mass and momentum principles to one-dimensional flow in a pipe and assumed that the fluid and pipe are homogenous and that the effects of friction are negligible. Adopting Joukowsky's assumptions and assuming that the control volumes in Figure 2.3 is

moving with the wave front, the equations governing the unsteady flow problem can be formulated using steady state theory.

Figure 2.3 Control volume moving with the wave front a pipe flow system

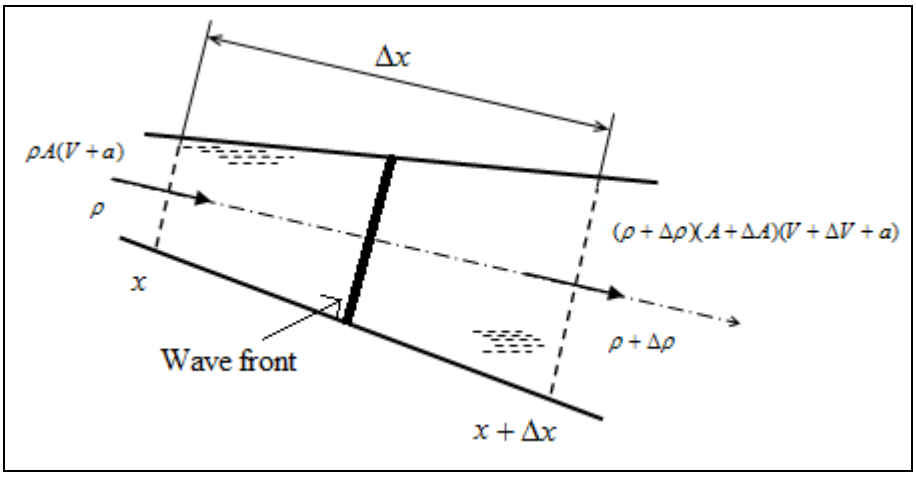

Applying the steady mass conservation equation gives

$$\overline{M}_{in} = \overline{M}_{out} \rightarrow \rho A(V+a) = (\rho+\Delta\rho)(A+\Delta A)(V+\Delta V+a) \tag{2.5}$$

where $\overline{M}_{in}$ is the rate of mass influx in the control volume; $\overline{M}_{out}$ is the rate of mass outflow from the control volume; ρ = density; A=cross-sectional area; a=acoustic wave speed; V=cross-sectional average velocity; ΔV, $\Delta\rho$ and ΔA= wave-induced change in velocity, density and area, respectively. The above continuity Eq. (2.5) can be rewritten as follows:

$$\frac{\Delta\rho}{\rho}+\frac{\Delta A}{A}+\frac{\Delta A\Delta\rho}{A\rho}=-\frac{\Delta V}{V+\Delta V+a} \tag{2.6}$$

Applying the momentum principle to the control volume in Figure 2.3 and neglecting the shear force, gravity force and the pressure force on converging or diverging side, gives

$$\sum Fx = PA-(P+\Delta P)(A+\Delta A)=\overline{M}\left\{(V+\Delta V+a)-(V+a)\right\}=\overline{M}\Delta V \tag{2.7}$$

Using the continuity Eq. (2.5), Eq. (2.7) becomes

$$PA-\left(P+\Delta P\right)\left(A+\Delta A\right)=\rho A\left(V+a\right)\Delta V \tag{2.8}$$

where P is the pressure and ΔP is the pressure difference. In typical water hammer applications, the fluid (water) is only slightly compressible and the pipe is only slightly deformable. That is $\Delta A\Delta\rho$ / $A\rho$ << ΔA / A << 1 and $\Delta A\Delta\rho$ / $A\rho$ << $\Delta\rho$ / ρ << 1. In addition and as it will be shown later, for most water hammer application the Mach number is very low (a >> V); thus, Eqs. (2.8) and (2.6) become

$$\Delta P=-\rho a\Delta V \tag{2.9}$$

In general, the momentum Eq. (2.9) is called the fundamental equation of water hammer or the *Joukowsky equation (relation)*, in honour to the person who was the first to derive it. The Joukowsky relation and its formulation constitute the ideal starting point for introducing and elucidating water-hammer phenomena to the novice. In addition, this relation is useful for obtaining a first approximation of the transient response of a pipe system. Essentially, the Joukowsky equation is used to estimate the head rise in a pipe for a given change in velocity. However, this equation can neither resolve the dynamics of transient waves in pipe systems and how these waves interact with the various hydraulic and control devices nor estimate the effects of wall shear on water-hammer waves.

Inserting Eq. (2.9) into Eq. (2.3) gives

$$\rho a^2=\frac{\Delta P}{\frac{\left(\rho\Delta A+A\Delta\rho\right)}{\rho A}} \tag{2.10}$$

Although $\Delta\rho$ / ρ and ΔA / A are small, their presence in Eq. (2.10) is essential and provides the essence to the wave nature of water-hammer flows; in particular, these terms provide the mechanism of mass storage by fluid compressibility and pipe elasticity. Therefore, neglecting these terms by assuming incompressible fluid and rigid pipe walls, result in *rigid water hammer theory* and an infinite wave speed. Indeed, although $\Delta\rho$ / ρ and ΔA / A are small they must be maintained in the continuity equation to balance the equally small but physically important term of $\Delta V/a$.

2.2.3. State Equations

Taking the limit of infinitesimal change, Eq. (2.10) leads to the following state equation

$$\rho a^2 = \frac{dP}{\frac{d(\rho A)}{\rho A}} = \frac{dP}{\frac{dA}{A} + \frac{d\rho}{\rho}} \tag{2.11}$$

which could be expressed in terms of bulk modulus of the fluid (K_f) and the bulk modulus of the pipe walls elasticity (K_s) as follows ([50]):

$$\frac{1}{\rho a^2} = \frac{1}{K_e} = \frac{\frac{d\rho}{\rho} + \frac{dA}{A}}{dP} = \frac{1}{K_f} + \frac{1}{K_s} \tag{2.12}$$

where

$$\frac{dP}{d\rho} = \frac{K_f}{\rho} \quad ; \quad \frac{AdP}{\rho dA} = \frac{K_s}{\rho} \tag{2.13}$$

and K_e is an equivalent bulk modulus corresponding to an equivalent bulk strain ($d\rho/\rho + dA/A$) of the fluid-pipe system induced by a change in pressure dP. From Eq. (2.12), it is clear that the state equation at the two limits: (i) rigid pipe and compressible flow and (ii) flexible pipe and incompressible flow, becomes

$$\frac{dP}{d\rho} = a^2 = \frac{K_f}{\rho} \text{ and } \frac{AdP}{\rho dA} = a^2 = \frac{K_s}{\rho} \tag{2.14}$$

respectively. If the change in cross sectional area is neglected (*i.e.* rigid pipe), Eq. (2.12) becomes

$$\frac{dP}{d\rho} = a^2 \tag{2.15}$$

2.2.4. Importance of compressibility in rapid varying flow

In reality, all fluids are compressible. However, since some fluids are only slightly compressible, they are usually assumed incompressible. Water is a slightly compressible-type of fluid that is usually assumed incompressible in most hydraulic application except few but very important cases. For instance, in most ocean, and shallow water application, water is assumed incompressible. But in pipe flow, compressibility becomes very important for water hammer (transient) assessment. To understand the assumption limits, Newton' second law is used to illustrate a simple example as follows

$$Force = Mass \times \frac{\Delta V}{\Delta t} \tag{2.16}$$

where V is velocity and t is time. Taking the force to be the pressure difference force between two distinct points, Eq. (2.16) becomes

$$A\Delta P = Mass \times \frac{\Delta V}{\Delta t} \tag{2.17}$$

When Δt goes to zero (*i.e.* very rapid change), the left hand side of Eq (2.17) becomes very large. Since ΔP is fixed and the area A, even if it is variable, cannot take very large value, then the only way to get around this singularity is to take into account the compressibility of the fluid for which the *Mass* can be written as follows

$$Mass = \rho A a \Delta t \tag{2.18}$$

Inserting Eq. (2.18) into Eq. (2.17) gives

$$\Delta P = \rho a \Delta V \tag{2.19}$$

which corresponds to the Joukowsky relation (Eq. ((2.9))).

2.2.5. 1D water hammer equation

2.2.5.1. Continuity Equation

Considering the pipe flow system given in Figure 2.4, the continuity equation is given by

$$\frac{\partial}{\partial t}\int_{\Omega}\rho d\Omega = -\int_{A_{in}}\rho(\vec{V}\cdot\vec{n})dA - \int_{A_{out}}\rho(\vec{V}\cdot\vec{n})dA \tag{2.20}$$

where Ω is the control volume; $\vec{n}$ is unit normal vector to the control volume area; A_{in} and A_{out} are the inward and outward areas of the control volume, respectively. Equation (2.20) gives

$$\frac{\partial}{\partial t}(\rho A\Delta x) = \frac{\partial}{\partial t}(\rho A)\Delta x = (\rho AV)_x - (\rho AV)_{x+\Delta x} \tag{2.21}$$

Figure 2.4 Control volume for mass conservation

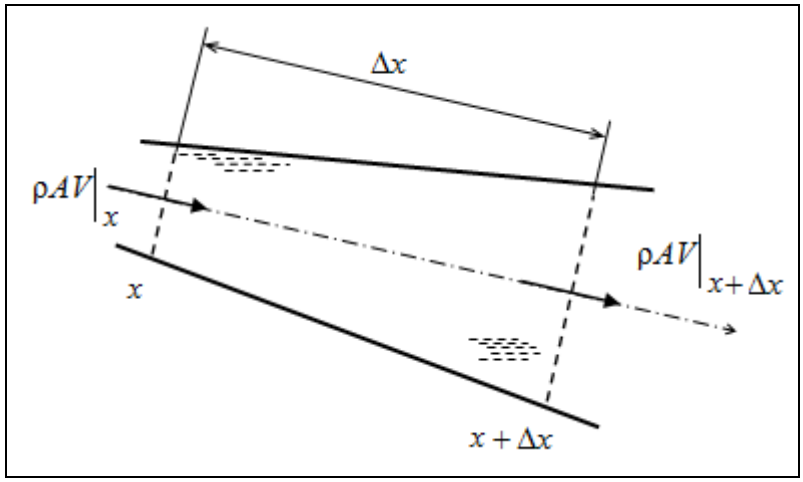

Dividing Eq. (2.21) by Δx and taking the limit when Δx goes to zero, yields

$$\frac{\partial}{\partial t}(\rho A) + \frac{\partial}{\partial x}(\rho AV) = 0 \tag{2.22}$$

In non-conservative form, Eq. (2.22) becomes

$$\rho\frac{\partial A}{\partial t}+A\frac{\partial \rho}{\partial t}+\rho A\frac{\partial V}{\partial x}+V\left[A\frac{\partial \rho}{\partial x}+\rho\frac{\partial A}{\partial x}\right]=0 \tag{2.23}$$

Using the total derivative, Eq. (2.23) gives

$$\frac{1}{\rho}\frac{d\rho}{dt}+\frac{1}{A}\frac{dA}{dt}+\frac{\partial V}{\partial x}=0 \tag{2.24}$$

Equation (2.24) can be written in term of pressure as follows

$$\frac{1}{\rho}\frac{d\rho}{dP}\frac{dP}{dt}+\frac{1}{A}\frac{dA}{dP}\frac{dP}{dt}+\frac{\partial V}{\partial x}=0 \tag{2.25}$$

Using the state equations (Eq. (2.14)), Eq. (2.25) becomes

$$\left(\frac{1}{K_f}+\frac{1}{K_s}\right)\frac{dP}{dt}+\frac{\partial V}{\partial x}=\frac{1}{K_e}\frac{dP}{dt}+\frac{\partial V}{\partial x}=0 \tag{2.26}$$

where K_e is the equivalent bulk modulus of the fluid-pipe system.

2.2.5.2. <u>Momentum Equation</u>

Considering the control volume given in Figure 2.5, the momentum equation is given by

$$\frac{\partial}{\partial t}\int_{\Omega}\rho V d\Omega=\Sigma F_{ext}-\int_{A_{in}}\rho V\left(\vec{V}\cdot\vec{n}\right)dA-\int_{A_{out}}\rho V\left(\vec{V}\cdot\vec{n}\right)dA \tag{2.27}$$

where F_{ext} are the external forces. For a fix control volume, Eq. (2.27) becomes

$$\frac{\partial}{\partial t}\left(\rho VA\right)\Delta x=\Sigma F_{ext}+\left(\rho A\beta V^2\right)_x-\left(\rho A\beta V^2\right)_{x+\Delta x} \tag{2.28}$$

Where β is defined as

$$\beta=\frac{1}{\rho V^2 A}\int_A \rho V^2 dA \tag{2.29}$$

β is usually assumed to be equal to 1 for water hammer models. This assumption could fail for certain unsteady flows where β can be very large ([50]). The one dimensional water hammer model in this work assumes β = 1.

Figure 2.5 Control volume for momentum conservation

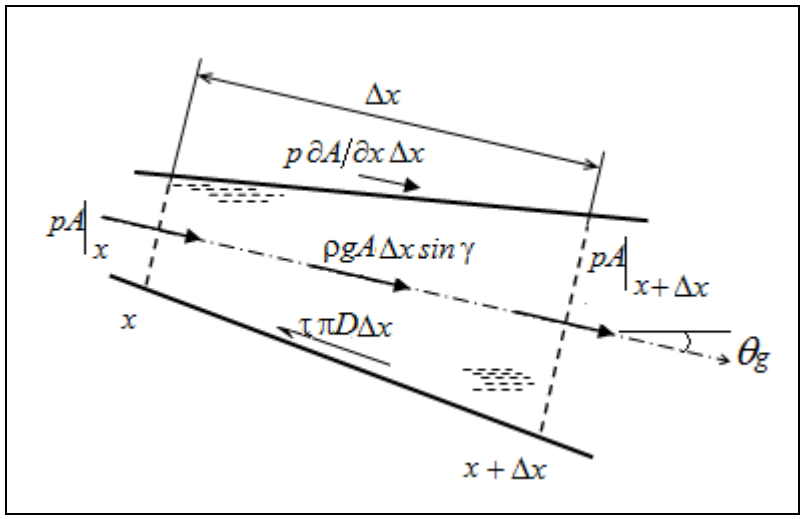

The external forces to the control volume are (see Figure 2.5):

i. Pressure forces at the sections x and $x+\Delta x$:

$$F_p = PA\big|_x - PA\big|_{x+\Delta x} \tag{2.30}$$

ii. Pressure force on converging or diverging side:

$$F_p^{\ side} = P\frac{\partial A}{\partial x}\Delta x \tag{2.31}$$

iii. Gravity force:

$$F_g = \rho g A \Delta x \sin\left(\theta_g\right) \tag{2.32}$$

where g is the standard gravitational acceleration.

iv. Shear force:

$$F_{shear} = \tau \int_0^{2\pi} \int_x^{x+\Delta x} R d\theta dx = \tau \pi D \Delta x \tag{2.33}$$

where τ is the shear stress between the fluid and the conduit walls which can be approximated by Darcy-Weisbach equation

$$\tau = \frac{\rho \overline{f} |V| V}{8} = \frac{\rho \overline{f}}{8A^2} Q^2 \tag{2.34}$$

where $\overline{f}$ is the Darcy-Weisbach friction factor; V and Q are the flow velocity and discharge, respectively. Using the Eqs. (2.30)-(2.33) and dividing Eq. (2.28) by Δx and taking the limit when Δx goes to zero, give

$$\frac{\partial}{\partial t}(\rho VA) + \frac{\partial}{\partial x}\left(\rho AV^2\right) = -A\frac{\partial P}{\partial x} + \rho gA \sin\left(\theta_g\right) - \tau \pi D \tag{2.35}$$

In non-conservative form and using the continuity equation (Eq. (2.22)), Eq. (2.35) becomes

$$\frac{dV}{dt} + \frac{1}{\rho}\frac{\partial P}{\partial x} = +g \sin\left(\theta_g\right) - \frac{4\tau}{\rho D} \tag{2.36}$$

The slope term is usually either small and can be dropped or combined with the pressure term. Recalling the continuity Eq. (2.26) with Eq. (2.36) gives the *1D water hammer equations*

$$\begin{cases} \dfrac{\partial P}{\partial t} + V\dfrac{\partial P}{\partial x} + K_e \dfrac{\partial V}{\partial x} = 0 \\ \dfrac{\partial V}{\partial t} + V\dfrac{\partial V}{\partial x} + \dfrac{1}{\rho}\dfrac{\partial P}{\partial x} = -\dfrac{4\tau}{\rho D} \end{cases} \tag{2.37}$$

2.2.5.3. Simplified Equations

Applying dimensional analysis to each term in Eq. (2.37) gives

$$\begin{cases} \dfrac{\partial p}{\partial t} \approx \dfrac{\rho^* a V^*}{t_w} \\ V\dfrac{\partial P}{\partial x} \approx \dfrac{\rho^* a V^{*2}}{l^*} \\ K_e \dfrac{\partial V}{\partial x} \approx \rho^* a^2 \dfrac{V^*}{l^*} \end{cases} ; \quad \begin{cases} \dfrac{\partial V}{\partial t} \approx \dfrac{V^*}{t_w} \\ V\dfrac{\partial V}{\partial x} \approx \dfrac{V^{*2}}{l^*} \\ \dfrac{1}{\rho}\dfrac{\partial P}{\partial x} \approx \dfrac{1}{\rho^*}\dfrac{\rho^* a V^*}{l^*} = \dfrac{a V^*}{l^*} \\ \dfrac{4\tau}{\rho D} \approx \nu \dfrac{V^*}{l^{*2}} \end{cases} \tag{2.38}$$

where ρ^* , V^* , l^*, $t_w = l^*/a$ are the characteristic density, velocity, length and time scales, respectively. Therefore, Eq. (2.84) is equivalent to

$$\begin{cases} \dfrac{\rho^* a V^*}{l^*/a} + \dfrac{\rho^* a V^{*2}}{l^*} + \rho^* a^2 \dfrac{V^*}{l^*} = 0 \\ \dfrac{V^*}{l^*/a} + \dfrac{V^{*2}}{l^*} + \dfrac{a V^*}{l^*} = -\nu \dfrac{V^*}{l^{*2}} \end{cases} \Leftrightarrow \begin{cases} 1 + M_{ch} + 1 = 0 \\ 1 + M_{ch} + 1 = -\dfrac{M_{ch}}{R_e} \end{cases} \tag{2.39}$$

where $M_{ch} = V^*/a$ is the mach number and it is usually of the order of 10^{-3} in water hammer flows; and $R_e = l^* V^*/\nu$ is the Reynolds number which usually about 10^6 in water supply pipe flow except at the boundary layer where the flow becomes laminar. Thus, the convective terms can be neglected and the system of Eq. (2.37) becomes

$$\begin{cases} \dfrac{\partial P}{\partial t} + \rho a^2 \dfrac{\partial V}{\partial x} = 0 \\ \dfrac{\partial V}{\partial t} + \dfrac{1}{\rho}\dfrac{\partial P}{\partial x} = -\dfrac{4\tau}{\rho D} \end{cases} \tag{2.40}$$

These equations are called the classical 1D water hammer equation.

Moreover, the slope term is usually either small and can be dropped or combined with the pressure term. Neglecting the slope term and using the Darcy-Weisbach equation (Eq. (2.34)) to approximate the shear stress, Eq. (2.40) becomes

$$\begin{cases} \dfrac{\partial P}{\partial t} + \rho a^2 \dfrac{\partial V}{\partial x} = 0 \\ \dfrac{\partial V}{\partial t} + \dfrac{1}{\rho}\dfrac{\partial P}{\partial x} = -\dfrac{\overline{f}\,|V|V}{2D} \end{cases} \tag{2.41}$$

It is common practice in hydraulic engineering to compute pressures in the pipeline in terms of the piezometric head H above a specified datum and use the discharge, Q, as the second variable instead of the velocity V. The pressure P and the discharge Q maybe written as

$$P = \rho g H \quad ; \quad Q = AV \tag{2.42}$$

Assuming that the fluid is slightly compressible and that the conduit walls are slightly deformable, the variations of ρ and A due to the change of the inside pressure could be neglected. However, these variations of ρ and A are taken indirectly into account by considering the wave speed to have finite speed (see Eq. (2.10)). Consequently, substituting Eq. (2.42) into Eq. (2.41) gives

$$\begin{cases} \dfrac{\partial H}{\partial t} + \dfrac{a^2}{gA}\dfrac{\partial Q}{\partial x} = 0 \\ \dfrac{\partial Q}{\partial t} + gA\dfrac{\partial H}{\partial x} = -\dfrac{f\,|Q|Q}{2DA} \end{cases} \tag{2.43}$$

and for frictionless system, becomes

$$\begin{cases} \dfrac{\partial H}{\partial t} + \dfrac{a^2}{gA}\dfrac{\partial Q}{\partial x} = 0 \\ \dfrac{\partial Q}{\partial t} + gA\dfrac{\partial H}{\partial x} = 0 \end{cases} \tag{2.44}$$

To obtain the steady state equations, the time derivatives in Eq. (2.43) are taken to zero. This gives

$$\begin{cases} \Delta Q = 0 \\ \Delta H = \dfrac{f\,\Delta x Q^2}{2gDA^2} \end{cases} \tag{2.45}$$

2.3. Harmonic solution for 1D intact pipe flow

The one dimensional water-hammer equations for inviscid flow in a single intact pipe case are given by (Eq. (2.44)) ([13])

$$\begin{cases} \dfrac{\partial H}{\partial t} + \dfrac{a^2}{gA_0}\dfrac{\partial Q}{\partial x} = 0 \\ \dfrac{\partial Q}{\partial t} + gA_0\dfrac{\partial H}{\partial x} = 0 \end{cases} \tag{2.46}$$

where Q is the instantaneous flow discharge, H is the instantaneous pressure head, g is the acceleration due to gravity, A_0 is the cross-sectional area of the intact pipe, a is the acoustic wave speed, x is the distance along the pipe line and t is the time. In steady-oscillatory flow, Q and H could be divided into steady and unsteady parts as follow

$$\begin{cases} Q = \overline{Q} + q \\ H = \overline{H} + h \end{cases} \tag{2.47}$$

where $\overline{Q}$ and $\overline{H}$ are the mean discharge and pressure head, respectively, and q and h are the unsteady discharge and pressure head parts. In what follows, q and h will be referred simply as discharge (flow rate) and pressure head, respectively. Substituting Eq. (2.47) into Eq. (2.46) gives

$$\begin{cases} \dfrac{\partial h}{\partial t} + \dfrac{a^2}{gA_0}\dfrac{\partial q}{\partial x} = 0 \\ \dfrac{\partial q}{\partial t} + gA_0\dfrac{\partial h}{\partial x} = 0 \end{cases} \tag{2.48}$$

Differentiating the continuity equation with t and the momentum equation with x, Eq. (2.48) leads to the following wave equation

$$\frac{\partial^2 h}{\partial t^2} - a^2\frac{\partial^2 h}{\partial x^2} = 0 \tag{2.49}$$

Assuming that q and h are harmonics in time, the solution to Eq. (2.49) is

$$h = \left[C_1 \exp\left(-ikx\right) + C_2 \exp\left(ikx\right) \right] \exp\left(iwt\right) \tag{2.50}$$

where $k = w/a$ is the wavenumber with w being the angular frequency and a is the acoustic wave speed in water, C_1 and C_2 are complex constants that depend on the boundary conditions (BCs), and $i = \sqrt{-1}$. The pressure head and discharge solution for an intact symmetric pipe system such as Valve-Pipe-Valve (VPV) system (see Figure 2.6) and for an anti-symmetric pipe system such as reservoir-pipe-valve (RPV) system (see Figure 2.7) are governed by ([13])

$$\begin{cases} h_m^0\left(x, k_m^0\right) = 2C\cos\left(k_m^0 x\right) = h_m^{\text{amp}} \cos\left(k_m^0 x\right) \\ q_m^0\left(x, k_m^0\right) = -2i\dfrac{g}{a} A_0 C \sin\left(k_m^0 x\right) = q_m^{\text{amp}} \cos\left(k_m^0 x\right) \end{cases} \tag{2.51}$$

and

$$\begin{cases} h_m^0\left(x, k_m^0\right) = 2iC\sin\left(k_m^0 x\right) = h_m^{\text{amp}} \sin\left(k_m^0 x\right) \\ q_m^0\left(x, k_m^0\right) = -2\dfrac{g}{a} A_0 C \cos\left(k_m^0 x\right) = q_m^{\text{amp}} \cos\left(k_m^0 x\right) \end{cases} \tag{2.52}$$

where m is the mode number of the natural resonant frequencies (eigenfrequencies); k_m^0 is the m^{th} wavenumber; h_m^0 and $q_m^0 = A_0 V_m^0$ are the m^{th} pressure head and flow discharge harmonics, respectively, with V_m^0 the m^{th} flow velocity harmonic; h_m^{amp} and q_m^{amp} are the amplitudes of maximum pressure head and flow discharge harmonics, respectively; C is a complex constant of integration; The dispersion relationships that govern the natural resonant frequencies (eigenfrequencies) for intact VPV system and RPV system can be obtained by imposing the velocity to be zero at $x=L$ (at the valve) as follow

VPV system: $$\sin\left(kL\right) = 0 \quad \Leftrightarrow \quad w_m^0 = ak_m^0 = 2\pi\left(\left(2m\right)\frac{a}{4L}\right) \;\; ; \;\; m = 1, 2, 3... \tag{2.53}$$

and

RPV system: $$\cos\left(kL\right) = 0 \quad \Leftrightarrow \quad w_m^0 = ak_m^0 = 2\pi\left[\left(2m-1\right)\frac{a}{4L}\right] \;\; ; \;\; m = 1, 2, 3... \tag{2.54}$$

respectively. Where w_m^0 is the m^{th} eigenfrequency; with the superscript "0" refers to intact pipe; L is the total length of an intact pipe. Inserting the m^{th} eigenfrequency in the pressure head and flow velocity solution gives the m^{th} mode solution. In linear wave theory, the summation of all the mode solutions gives the overall solution of the pressure and flow velocity as follows

$$\begin{cases} h = \sum_m h_m^0 \\ q = \sum_m q_m^0 \end{cases} \tag{2.55}$$

Figure 2.6 Valve-pipe-valve (VPV) system

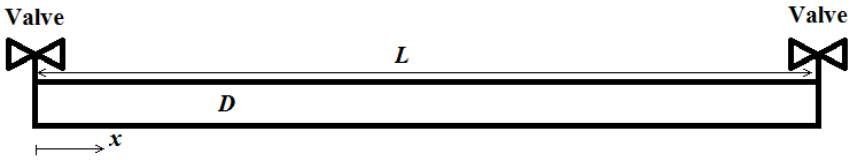

Figure 2.7 Reservoir-pipe-valve (RPV) system

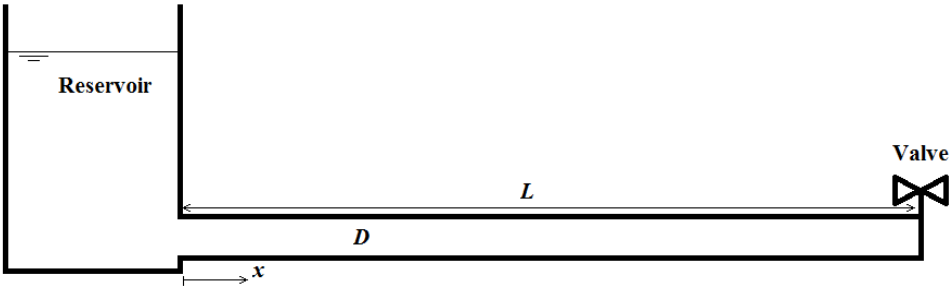

The mode solution in pipe system depends on the boundary conditions where for example Eq. (2.53) gives the even modes and Eq. (2.54) gives the odd modes. These modes solution are also often referred as standing waves or harmonics. Figure 2.8 gives the pressure head and the velocity harmonic along x/L of the 2nd mode (m=2) for an intact Reservoir-Pipe-Valve system (Eq. (2.52)).

Figure 2.8 Pressure head and velocity harmonics of an intact RPV system at the 2nd mode (m = 2).

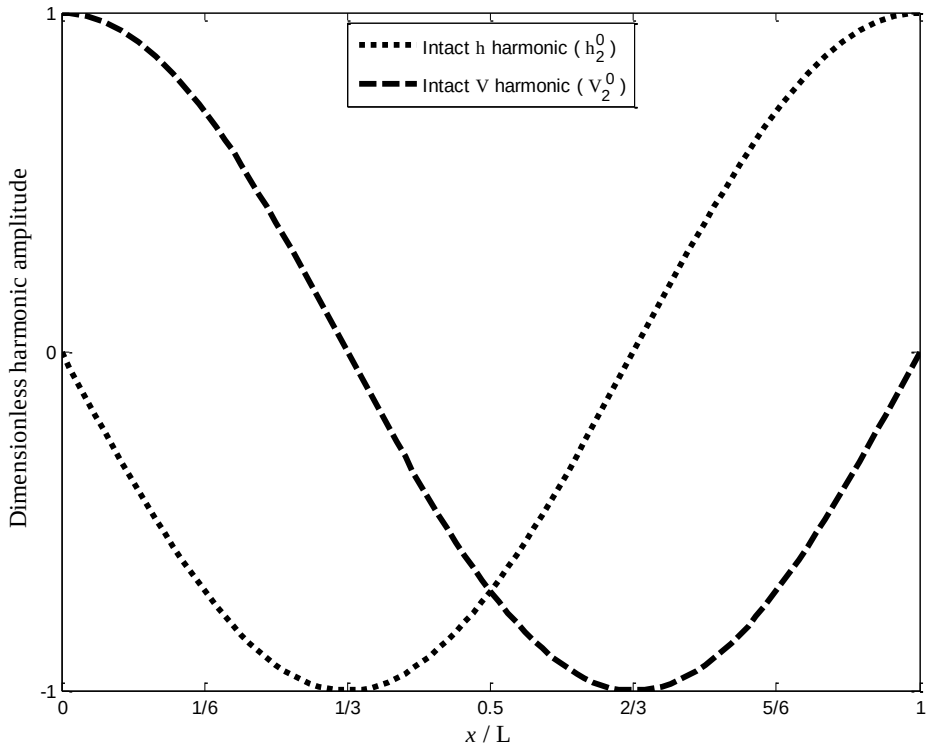

2.4. Two dimensional axi-symetric Navier-Stokes equation for unsteady flow in cylindrical pipe

Let x and r denote the axial and radial coordinates; t is the time; V_x and V_r denote the velocity components in x- and r-directions (Figure 2.9), respectively; and ρ, and P denote the fluid density and the pressure, respectively. The 2D axi-symmetric Navier-Stokes equations for a compressible Newtonian fluid in cylindrical coordinate are ([50]):

$$\frac{\partial U_c}{\partial t}+\frac{\partial F}{\partial r}+\frac{\partial G}{\partial x}=S \tag{2.56}$$

where

$$U_c=\begin{pmatrix}\rho\\ \rho V_r\\ \rho V_x\end{pmatrix}\quad;\quad F=\begin{pmatrix}\rho V_r\\ \rho V_r^2+P\\ \rho V_r V_x\end{pmatrix}\quad;\quad G=\begin{pmatrix}\rho V_x\\ \rho V_r V_x\\ \rho V_x^2+P\end{pmatrix} \tag{2.57}$$

$$S=\begin{pmatrix}-\dfrac{\rho V_r}{r}\\ \dfrac{\partial \tau_{rr}}{\partial r}+\dfrac{\partial \tau_{rx}}{\partial x}+\dfrac{1}{r}\left(\tau_{rr}-\tau_{\theta\theta}-\rho V_r^2\right)\\ \dfrac{\partial \tau_{rx}}{\partial r}+\dfrac{\partial \tau_{xx}}{\partial x}+\dfrac{1}{r}\left(\tau_{rx}-\rho V_r V_x\right)\end{pmatrix} \tag{2.58}$$

In Eq. (2.58), τ_{rr}, τ_{xx}, $\tau_{\theta\theta}$ and τ_{rx} denote the components of the stress tensor given by

$$\begin{cases}\tau_{rr}=(2\mu+\lambda)\dfrac{\partial V_r}{\partial r}+\lambda\left(\dfrac{V_r}{r}+\dfrac{\partial V_x}{\partial x}\right)\quad;\quad \tau_{xx}=(2\mu+\lambda)\dfrac{\partial V_x}{\partial x}+\lambda\left(\dfrac{V_r}{r}+\dfrac{\partial V_r}{\partial r}\right)\\ \tau_{\theta\theta}=(2\mu+\lambda)\dfrac{V_r}{r}+\lambda\left(\dfrac{\partial V_r}{\partial r}+\dfrac{\partial V_x}{\partial x}\right)\quad;\quad \tau_{rx}=\mu\left(\dfrac{\partial V_r}{\partial x}+\dfrac{\partial V_x}{\partial r}\right)\end{cases} \tag{2.59}$$

where $\bar{\mu} = -2\mu/3$ with μ denotes the dynamic viscosity of the fluid. In each line of the right hand side of Eq. (2.58), the last terms represent the extra terms due to the cylindrical coordinate formulation.

Notice that in the Eqs. (2.56) and (2.57), the energy equation is not included. This is because the fluid considered in this work (water) is not sensitive to temperature change because of its high heat capacity. Although the process of water-filled pipe flow is adiabatic, it is usually assumed that the process is isothermal. For this reason, the energy equation is not solved and the pressure is related to the density using the isentropic and isothermal state equation for an infinitely rigid conduit given by ([50]).

$$\frac{\partial P}{\partial \rho} = a^2 \tag{2.60}$$

where a is the acoustic wave speed. Equation (2.60) is for rigid pipe and in this case a is about 1440m/s. However, for simplicity in this work, a is taken equal to1000m/s although Eq. (2.60) is used.

Figure 2.9 Sketch of a pipe showing the coordinate system

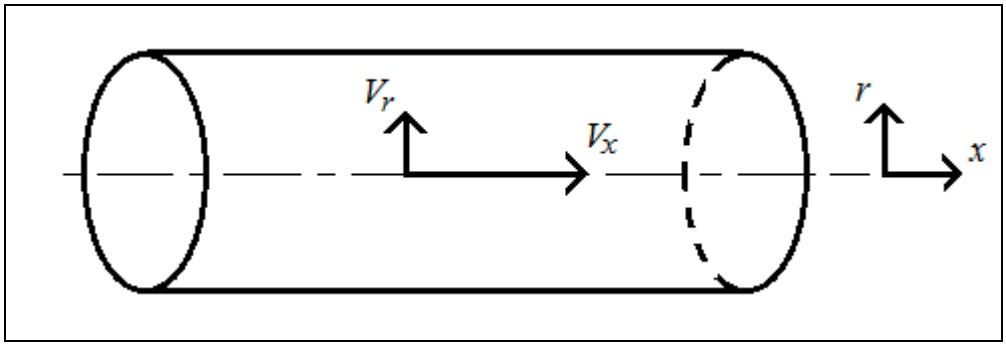

2.5. Eenergy equation for the 2D inviscid Navier-Stokes equations in cylindrical coordinate system

Assuming the viscous terms are negligible, Eq. (2.56) becomes:

$$\frac{\partial \rho}{\partial t}+\frac{\partial \rho V_r}{\partial r}+\frac{\partial \rho V_x}{\partial x}=-\frac{\rho V_r}{r} \tag{2.61}$$

$$\frac{\partial \rho V_r}{\partial t}+\frac{\partial\left(\rho V_r{}^2+P\right)}{\partial r}+\frac{\partial \rho V_x V_r}{\partial x}=-\frac{\rho V_r{}^2}{r} \tag{2.62}$$

$$\frac{\partial \rho V_x}{\partial t}+\frac{\partial \rho V_x V_r}{\partial r}+\frac{\partial\left(\rho V_x{}^2+P\right)}{\partial x}=-\frac{\rho V_x V_r}{r} \tag{2.63}$$

Multiplying Eq. (2.61) by P/ρ gives :

$$\begin{aligned}&\frac{P}{\rho}\times\left(\frac{\partial \rho}{\partial t}+\frac{\partial \rho V_r}{\partial r}+\frac{\partial \rho V_x}{\partial x}\right)=\frac{P}{\rho}\times\left[\frac{\partial \rho}{\partial t}+V_r\frac{\partial \rho}{\partial r}+V_x\frac{\partial \rho}{\partial x}+\rho\left(\frac{\partial V_r}{\partial r}+\frac{\partial V_x}{\partial x}\right)\right]=\\&\frac{P}{\rho}\frac{d\rho}{dt}+P\frac{\partial V_r}{\partial r}+P\frac{\partial V_x}{\partial x}=-\frac{PV_r}{r}\end{aligned} \tag{2.64}$$

Using the following state equation for rigid pipe (Eq. (2.60)):

$$\frac{dP}{d\rho}=a^2=\frac{K_f}{\rho} \tag{2.65}$$

Equation (2.64) and Eq. (2.65) give

$$\frac{1}{K_f}\frac{d\left(P^2/2\right)}{dt}+P\frac{\partial V_r}{\partial r}+P\frac{\partial V_x}{\partial x}=-\frac{PV_r}{r} \tag{2.66}$$

Multiplying Eq. (2.62) by V_r gives :

$$V_r\left(\frac{\partial \rho V_r}{\partial t}+\frac{\partial\left(\rho V_r^{\,2}+P\right)}{\partial r}+\frac{\partial \rho V_x V_r}{\partial x}\right)= V_r\left[\begin{array}{l} V_r\left(\frac{\partial \rho}{\partial t}+\frac{\partial\left(\rho V_r\right)}{\partial r}+\frac{\partial \rho V_x}{\partial x}\right) \\ +\rho\left(\frac{\partial V_r}{\partial t}+V_r\frac{\partial V_r}{\partial r}+V_x\frac{\partial V_r}{\partial x}\right)+\frac{\partial P}{\partial r}\end{array}\right]=-\frac{\rho V_r^{\,3}}{r} \tag{2.67}$$

Using the Eq. (2.61), Eq. (2.67) becomes

$$\begin{aligned}&\rho\left(\frac{\partial\left(V_r^{\,2}/2\right)}{\partial t}+V_r\frac{\partial\left(V_r^{\,2}/2\right)_r}{\partial r}+V_x\frac{\partial\left(V_r^{\,2}/2\right)}{\partial x}\right)+V_r\frac{\partial P}{\partial r}\\&=\rho\frac{d\left(V_r^{\,2}/2\right)}{dt}+\frac{\partial\left(PV_r\right)}{\partial r}-P\frac{\partial V_r}{\partial r}=0\end{aligned} \tag{2.68}$$

Similarly, multiplying Eq. (2.63) by V_x gives:

$$\rho\frac{d\left(V_x^{\,2}/2\right)}{dt}+\frac{\partial\left(PV_x\right)}{\partial x}-P\frac{\partial V_x}{\partial x}=0\,. \tag{2.69}$$

The sum of Eqs. (2.66), (2.68) and (2.69) gives the energy equation as follows

$$\frac{1}{K_f}\frac{d\left(P^2/2\right)}{dt}+\rho\frac{d\left(V_r^{\,2}/2\right)}{dt}+\rho\frac{d\left(V_x^{\,2}/2\right)}{dt}+\frac{\partial\left(PV_r\right)}{\partial r}+\frac{\partial\left(PV_x\right)}{\partial x}=-V_r\frac{P}{r} \tag{2.70}$$

The three terms on the left hand side of the Eq. (2.70) can be written as

$$\begin{aligned}&\frac{1}{K_f}\frac{d\left(P^2/2\right)}{dt}+\rho\frac{d\left(V_r^{\,2}/2\right)}{dt}+\rho\frac{d\left(V_x^{\,2}/2\right)}{dt}\\&=\frac{P}{\rho}\frac{d\rho}{dt}+\frac{d\left(\rho V_r^{\,2}/2\right)}{dt}-\frac{d\left(\rho V_x^{\,2}/2\right)}{dt}-\frac{V_r^{\,2}}{2}\frac{d\rho}{dt}-\frac{V_x^{\,2}}{2}\frac{d\rho}{dt}\end{aligned} \tag{2.71}$$

Since $P/\rho\sim a^2$ and for most water hammer application $a >> V_r$, and $a >> V_x$, therefore, $P/\rho >> V_r^{\,2}/2$ and $P/\rho >> V_x^{\,2}/2$. Hence, Eq. (2.70) becomes

$$\frac{d}{dt}\left(\frac{P^2}{2K_f}+\frac{\rho V_r^{\,2}}{2}+\frac{\rho V_x^{\,2}}{2}\right)+\frac{1}{r}\frac{\partial\left(rPV_r\right)}{\partial r}+\frac{\partial\left(PV_x\right)}{\partial x}=0 \tag{2.72}$$

Although V_r is usually very small in water hammer application, the last term in Eq. (2.70) is not neglected because, near the vicinity of a blockage in a pipe, the radial velocity could be significant.

Multiplying Eq. (2.72) by $2\pi rdrdx$ and integrating over the volume and with respect to time give

$$\begin{aligned}&\int_0^t\frac{d}{dt}\left[\int_0^R\int_0^L\left(\frac{P^2}{2K_f}+\frac{\rho V_r^{\,2}}{2}+\frac{\rho V_x^{\,2}}{2}\right)2\pi rdrdx\right]dt \;+\\&\int_0^t\int_0^R\int_0^L\frac{\partial\left(rPV_r\right)}{\partial r}2\pi drdxdt \;+\; \int_0^t\int_0^R\int_0^L\frac{\partial\left(PV_x\right)}{\partial x}2\pi rdrdxdt=0\end{aligned} \tag{2.73}$$

$$\Rightarrow E\left(t\right)-E\left(0\right)+\int_0^t W_r dt+\int_0^t W_x dt=0 \tag{2.74}$$

$$\Rightarrow\frac{E\left(t\right)+\int_0^t W_r dt+\int_0^t W_x dt}{E\left(0\right)}=1 \tag{2.75}$$

where E, W_x and W_r are the total energy of the fluid in the pipe system, the work done at the axial boundaries and the work done at lateral boundaries, respectively. These terms are defined as

$$E=\int_0^R\int_0^L\left(\frac{P^2}{2K_f}+\frac{\rho V_r^{\,2}}{2}+\frac{\rho V_x^{\,2}}{2}\right)2\pi rdrdx\,, \tag{2.76}$$

$$W_x=\int_0^R\int_0^L\frac{\partial\left(PV_x\right)}{\partial x}2\pi rdrdx \tag{2.77}$$

and

$$W_r = \int_0^R \int_0^L \frac{\partial \left(rPV_r \right)}{\partial r} 2\pi dr dx \,, \tag{2.78}$$

respectively. Equation (2.76) could be split into two parts: kinetic energy T and potential energy U as follows

$$T = \int_0^R \int_0^L \left(\frac{\rho V_r^{\,2}}{2} + \frac{\rho V_x^{\,2}}{2} \right) 2\pi r dr dx \tag{2.79}$$

$$U = \int_0^R \int_0^L \left(\frac{P^2}{2K} \right) 2\pi r dr dx \tag{2.80}$$

If viscous terms are included, there will be energy losses (E_s) due to the viscosity, and the general form of Eq. (2.75) becomes

$$\frac{E(t) + \int_0^t W_r dt + \int_0^t W_x dt - \int_0^t E_s dt}{E(0)} = 1 \tag{2.81}$$

2.6. 2D wave solution for the case of inviscid pipe flow

In this section, the classical axi-symmetric wave solutions in a pipe, widely studied in duct acoustics, are briefly reviewed.

2.6.1. Wave equation

Consider the pipe system shown in Figure 2.9. The continuity equation (Eq. (2.61)) in a general compact form is given by

$$\frac{\partial \rho}{\partial t} + \nabla \cdot \left(\rho \vec{V} \right) = 0 \tag{2.82}$$

where $\vec{V} = \left[V_x, V_r \right]^{tr}$ is the velocity vector and ∇ is the nabla operator. Using the state equation (Eq. (2.60)), the first term on the left hand side of Eq. (2.82) becomes

$$\frac{\partial \rho}{\partial t} = \frac{\partial \rho}{\partial P} \frac{\partial P}{\partial t} = \frac{1}{a^2} \frac{\partial P}{\partial t} \tag{2.83}$$

Therefore, Eq. (2.82) becomes

$$\frac{1}{a^2} \frac{\partial P}{\partial t} + \nabla \cdot \left(\rho \vec{V} \right) = \frac{1}{a^2} \frac{\partial P}{\partial t} + \rho \nabla \cdot \left(\vec{V} \right) + \vec{V} \cdot \nabla \left(\rho \right) = 0 \tag{2.84}$$

Applying dimensional analysis to each term in Eq. (2.84) gives

$$\begin{cases} \dfrac{1}{a^2} \dfrac{\partial p}{\partial t} \approx \dfrac{1}{a^2} \dfrac{\rho^* a V^*}{t_w} \\ \rho \nabla \cdot \left(\vec{V} \right) \approx \dfrac{\rho^* V^*}{l^*} \\ \vec{V} \cdot \nabla \left(\rho \right) = V \dfrac{\nabla P}{a^2} \approx \dfrac{\rho^* a V^{*2}}{l^* a^2} \\ \text{where } \; t_w = \dfrac{l^*}{a} \end{cases} \tag{2.85}$$

where ρ^* , V^* , l^*, $t_w = l^*/a$ are the characteristic density, velocity, length and time scales, respectively. Therefore, Eq. (2.84) is equivalent to

$$\frac{\rho^* V^*}{l^*} + \frac{\rho^* V}{l^*} + \frac{\rho^* V^* V^*}{l^* a} = 0 \Leftrightarrow \quad 1+1+M_{ch} = 0 \tag{2.86}$$

where $M_{ch} = V^*/a$ is the mach number and it is usually of the order of 10^{-3} in water hammer flows. This shows that the convective term could be neglected and Eq. (2.84) becomes

$$\boxed{\frac{1}{a^2}\frac{\partial P}{\partial t} + \rho \nabla \cdot \left(\vec{V}\right) = 0} \tag{2.87}$$

The momentum equations (Eqs. (2.62) and (2.63)) in a simplified compact form are

$$\frac{\partial \vec{V}}{\partial t} + \left(\vec{V} \cdot \nabla\right)\vec{V} = -\frac{1}{\rho}\nabla P + \nu \nabla^2 \left(\vec{V}\right) + F_g \tag{2.88}$$

where ν is the kinematic viscosity. Applying dimensional analysis to each term in Eq. (2.88) gives

$$\begin{cases} \dfrac{\partial \vec{V}}{\partial t} \approx \dfrac{V^*}{t_w} \\ \left(\vec{V} \cdot \nabla\right)\vec{V} \approx \dfrac{V^* V^*}{l^*} \\ \dfrac{1}{\rho}\nabla P \approx \dfrac{1}{\rho}\dfrac{\rho^* a V^*}{l^*} \\ \nu \nabla^2 \left(\vec{V}\right) \approx \nu \dfrac{V^*}{l^{*2}} \end{cases} \tag{2.89}$$

Therefore, Eq. (2.88) is equivalent to

$$1 + M = 1 + \frac{M_{ch}}{\mathrm{R_e}} + \frac{l^*}{a V^*} F_g \tag{2.90}$$

where $\mathrm{R_e} = l^* V^*/\nu$ is the Reynolds number. Neglecting the effect of gravity, Eq. (2.90) becomes

$$\Rightarrow 1+M_{ch}=1+\frac{M_{ch}}{\mathrm{R_e}} \tag{2.91}$$

Pipe flow are usually turbulent flows (e.g. $V\approx 0.5-1\mathrm{m/s}$; $L\approx D\approx 0.01\mathrm{m\ to\ 1m}$; $\nu\approx 10^{-6}\mathrm{m^2/s}\ \Rightarrow \mathrm{R_e}\approx 5000$ to 10^6) except near the boundaries where the flow is laminar (e.g. non slip condition at the pipe wall leading to very low velocity). If one is not resolving the flow at the boundary layer scale, Eq. (2.91) shows that the viscous terms and the convective term could be neglected. Finally, neglecting:

i. Nonlinear terms: $\left(\vec{V}\cdot\nabla\right)\vec{V}$

ii. Body Forces: F_g

iii. Viscous effect: $\nu\nabla^2\left(\vec{V}\right)$

Equation (2.88) becomes

$$\boxed{\frac{\partial V}{\partial t}=-\frac{1}{\rho}\nabla P} \tag{2.92}$$

The wave equation could be obtained in terms of pressure by differentiating Eq. (2.87) with time and differentiating Eq. (2.92) with space which give

$$\boxed{\frac{\partial^2 P}{\partial t^2}-a^2\nabla^2 P=0} \tag{2.93}$$

2.6.2. Solution of the wave equation (Eq. (2.93))

Assuming separable solution (method of separation of variable) and that the wave is harmonic in time, the pressure is given by

$$P=\exp\left(-iwt\right)f_x\left(x\right)f_r\left(r\right) \tag{2.94}$$

where f_r and f_x are pressure functions depending only on r and only on x, respectively; $w=2\pi f$ is the angular frequency with f is the frequency; $i=\sqrt{-1}$. Inserting Eq. (2.94) into Eq. (2.93) gives

$$\nabla^2 \left(f_x f_r \right) + \frac{w^2}{a^2} \left(f_x f_r \right) = 0 \tag{2.95}$$

$$\Rightarrow \left(\nabla_r^2 + \frac{\partial^2}{\partial x^2} \right) \left(f_x f_r \right) + k^2 f_x f_r = 0 \tag{2.96}$$

$$\Rightarrow f_x \nabla_r^2 \left(f_r \right) + f_r \frac{\partial^2 f_x}{\partial x^2} + k^2 f_x f_r = 0 \tag{2.97}$$

$$\Rightarrow -\frac{\nabla_r^2 \left(f_r \right)}{f_r} = \frac{1}{f_x} \frac{d^2 f_x}{dx^2} + k^2 = \text{constant} = k_r^2 \tag{2.98}$$

where $k = w/a$ is the wavenumber. First, solving for f_r, Eq. (2.98) gives

$$-\frac{\nabla_r^2 \left(f_r \right)}{f_r} = k_r^2 \quad \Rightarrow \quad \frac{\partial^2 f_r}{\partial r^2} + \frac{1}{r} \frac{\partial f_r}{\partial r} + k_r^2 f_r = 0 \tag{2.99}$$

$$\Rightarrow r^2 \frac{\partial^2 f_r}{\partial r^2} + r \frac{\partial f_r}{\partial r} + r^2 k_r^2 f_r = 0 \tag{2.100}$$

Using the following change of variable

$$r^* = r k_r \quad ; \quad \frac{\partial}{\partial r} = \frac{\partial}{\partial r^*} \frac{\partial r^*}{\partial r} = k_r \frac{\partial}{\partial r^*} \tag{2.101}$$

Equation (2.100) becomes

$$\left(\frac{r^*}{k_r} \right)^2 k_r^2 \frac{\partial^2 f_r}{\partial r^{*2}} + \frac{r^*}{k_r} k_r \frac{\partial f_r}{\partial r^*} + \left(\frac{r^*}{k_r} \right)^2 k_r^2 f_r = 0 \tag{2.102}$$

$$\Rightarrow \left(r^* \right)^2 \frac{\partial^2 f_r}{\partial r^{*2}} + r^* \frac{\partial f_r}{\partial r^*} + \left(r^* \right)^2 f_r = 0 \tag{2.103}$$

Equation (2.103) is the Bessel's equation and its solution is

$$f_r \left(r, k_r \right) = \overline{C_1} J_0 \left(r k_r \right) + \overline{C_2} Y_0 \left(r k_r \right) \tag{2.104}$$

where J_0 and Y_0 are the zeroth order Bessel's function of first and second kind, respectively (Figure 2.10); and $\overline{C_1}$ and $\overline{C_2}$ are constants. The constant $\overline{C_2}$ must be equal to zero ($\overline{C_2}$ = 0) so that the solution remains finite (*i.e.* physical) at r^*= 0. Therefore, Eq. (2.104) becomes

$$f_r(r,k_r) = C_1 J_0(rk_r) \tag{2.105}$$

Figure 2.10 Bessel functions

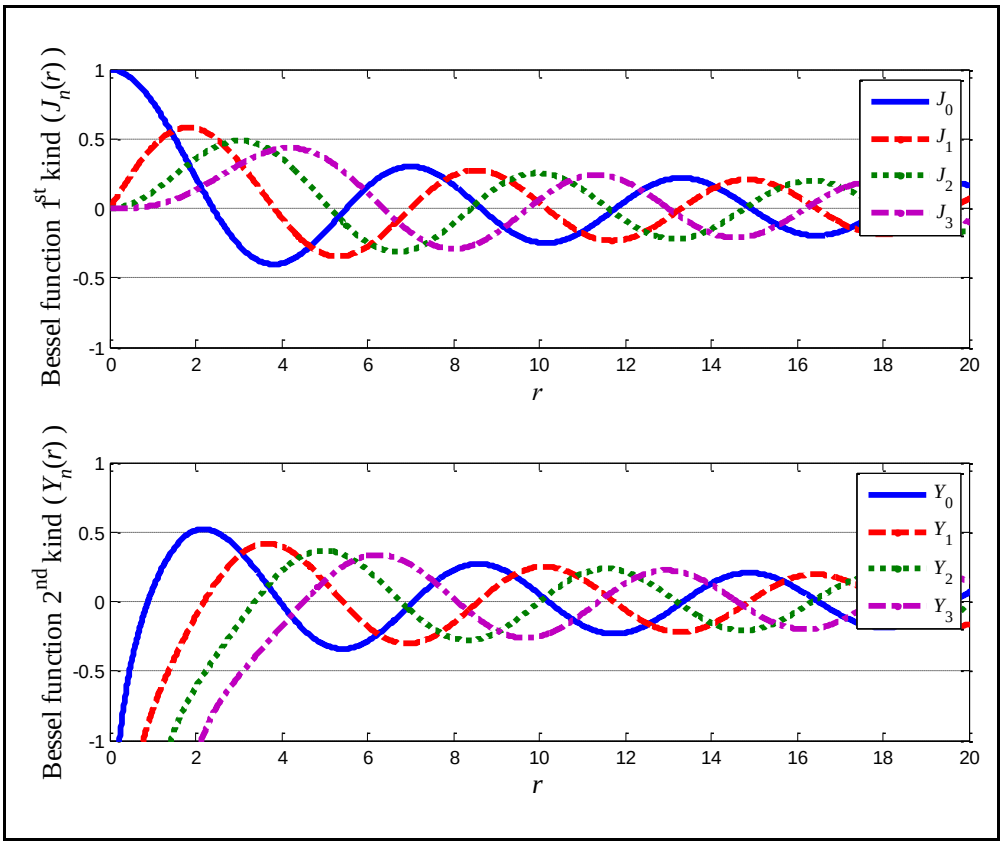

(a) Top **Bessel's functions of first kind**

(b) Bottom **Bessel's functions of second kind**

Since normal wall velocity is zero, then

$$\left.\frac{\partial P}{\partial r}\right|_{r=R} = \left.\frac{\partial f_r}{\partial r}\right|_{r=R} = 0 \;\Rightarrow\; \frac{\partial J_0}{\partial r}(Rk_r) = 0 \;\Rightarrow\; J_1(Rk_r) = 0 \tag{2.106}$$

where $J_1(r) = -\partial J_0 / \partial r$ is first order Bessel's function of first kind; R is the pipe radius. J_1 has multiple zeros which are

$$\alpha_{rn} = Rk_{rn} = 0 \; ; \; 3.8317 \; ; \; 7.01559 \; ; \; 10.17347 \; ; ... \tag{2.107}$$

where $n \equiv n^{\text{th}}$ zero of J_1. Therefore, the solution in Eq. (2.105) becomes

$$\boxed{f_{rn}(r, k_{rn}) = C_{1n} J_0(rk_{rn})} \tag{2.108}$$

Solving for f_x, Eq. (2.98) gives

$$\frac{d^2 f_x}{dx^2} + \left[k^2 - k_{rn}^2 \right] f_x = 0 \tag{2.109}$$

which has the following solution

$$f_x = \varphi \exp\left(i\sqrt{k^2 - k_{rn}^2}\; x \right) + \gamma \exp\left(-i\sqrt{k^2 - k_{rn}^2}\; x \right) \tag{2.110}$$

where φ and γ are complex constants. Combining Eq. (2.108) and Eq. (2.110) leads to the solution of the pressure for a single mode n

$$\boxed{P_n = \left\{ \varphi_n \exp\left(i\sqrt{k^2 - k_{rn}^2}\; x \right) + \gamma_n \exp\left(-i\sqrt{k^2 - k_{rn}^2}\; x \right) \right\} \exp(-iwt)\, J_0(rk_{rn})} \tag{2.111}$$

and the total pressure is given by

$$P = \sum_n P_n \tag{2.112}$$

The zeroth mode wave (n = 0 and α_{r0} = 0) is:

$$P_0 = \varphi_0 \exp(ikx - iwt) + \gamma_0 \exp(-ikx - iwt) \tag{2.113}$$

which is the classical one-dimensional (1D) WH solution and will be referred to as M0 hereafter. Further detailed 2D solution and three dimensional (3D) solution could be found in [108].

2.6.3. Cut-off frequencies

Considering only one direction of the wave, then Eq. (2.111) gives

$$\boxed{P_n = \varphi_n \exp\left(i\sqrt{k^2 - k_{rn}^2}\; x\right)\exp\left(-iwt\right) J_0\left(rk_{rn}\right)} \tag{2.114}$$

Equation (2.114) shows that if $k^2 > k_{rn}^2$ then $\sqrt{k^2 - k_{rn}^2}$ is real, and therefore, the waves are propagating. However, if $k^2 < k_{rn}^2$ then $\sqrt{k^2 - k_{rn}^2}$ is imaginary, and therefore, the waves are evanescent. This specifies the condition on the frequency (cut-off frequency) for which a high mode is either propagating or not. For example, the first high mode (n = 1), hereafter referred to as M1, is excited and propagating under the following condition

$$k^2 \geq k_{r1}^2 \;\Rightarrow\; \frac{w}{a} \geq k_{r1} \approx \frac{\alpha_{r1}}{R} \;\Rightarrow\; f \geq f_1 = \frac{\alpha_{r1}}{\pi}\frac{a}{D} \tag{2.115}$$

where $f_1 = \frac{\alpha_{r1}}{\pi}\frac{a}{D}$ is the cut-off frequency of the first high mode; and $\alpha_{r1} \approx 3.83$ is the second zero of J_1. The cut-off frequency of the second (n = 2) high mode, hereafter referred to as M2, is

$$f \geq f_2 = \frac{\alpha_{r2}}{\pi}\frac{a}{D} \approx \frac{7.01}{\pi}\frac{a}{D} \tag{2.116}$$

The cut-off frequency of the n^{th} high mode is

$$f \geq f_n = \frac{\alpha_{rn}}{\pi}\frac{a}{D} \tag{2.117}$$

2.6.4. Dispersion curves, phase velocity and group velocity

The dispersion relation is given by

$$k_{xn} = \sqrt{(w/a)^2 - k_{rn}^2} \tag{2.118}$$

From Eq. (2.114), the phase velocity (obtained from the phase of the solution) is

$$\upsilon_n = \frac{w}{k_{xn}} = \frac{w}{\sqrt{(w/a)^2 - k_{rn}^2}} = \frac{a}{\sqrt{1 - \frac{k_{rn}^2}{k^2}}} \geq a \tag{2.119}$$

and the group velocity, at which the energy propagates, is(using Eq. (2.118))

$$V_{gn} = \frac{dw}{dk_x} = \frac{d\left[a\sqrt{k_{xn}^2 - k_r^2}\right]}{dk_{xn}} = \frac{ak_{xn}}{k} = \frac{a\sqrt{(w/a)^2 - k_{rn}^2}}{\frac{w}{a}} = \frac{a^2}{\upsilon_n} \leq a \tag{2.120}$$

The group velocity (Eq. (2.120)) variation with frequency for the first four modes is given in Figure 2.11. For $n > 0$, Eq. (2.120) and Figure 2.11 reveals that the group velocity is smaller than the WH wave speed a. The fact that the energy propagates at a speed slower than a is due to the fact that modes with $n > 0$ do not travel parallel to the pipe axis; instead, they take a zigzag-type path ([108]). Figure 2.12 provides a sketch of the path of different wave modes where the direction of the waves are dictated by the following wavenumber vector relation

$$\vec{k} = k_{rn}\vec{i} + k_{xn}\vec{j}\,. \tag{2.121}$$

where $\vec{i}$ and $\vec{j}$ are unit vectors along r and x directions, respectively. The speed along each path is given by the phase velocity (Eq. (2.119)) which shows that higher wave modes travel faster, but take longer path. The zigzag-type of path is dictated from Eq. (2.121) where the direction of the wave is normal to the wave front (see Figure 2.12). High frequency waves will propagate along a diagonal direction with a certain angle (θ_{kn}) from the pipe centreline when $k_{rn} \neq 0$ in Eq. (2.121). Only M0 waves travels in straight path along the pipe for which $k_{r0} = 0$ in Eq. (2.121). The fact that different wave modes acquire different paths is referred to as multipath process and is the reason why high frequency waves are dispersive. The angle of propagation θ_{kn} is defined as follows

$$\theta_{kn} = \tan^{-1}\left(\frac{k_{rn}}{k_{xn}}\right) = \tan^{-1}\left(\frac{k_{rn}}{\sqrt{(w/a)^2 - k_{rn}^2}}\right). \qquad (2.122)$$

and its variation with frequency for the first three high modes is given in Figure 2.13. Figure 2.13 shows that at the cut-off frequencies, θ_{kn} becomes 90 degrees. Therefore waves at cut-off frequencies are standing waves and do not propagate along the pipe. Waves propagating at frequencies near (but not at) the cut-off frequencies, their angle of propagation is slightly less than 90 degrees , hence, they propagate along the pipe but take very long path. On the other hand, Figure 2.13 shows that the farther away the wave frequency is from the cut-off, the smaller is its angle of propagation, and therefore, the shorter is its path. The high mode behaviour and multi-path effect will be discussed further in Chapter 7.

Figure 2.11 Dimensionless group velocity variation with frequency for the first four modes (*a*=1000 m/s).

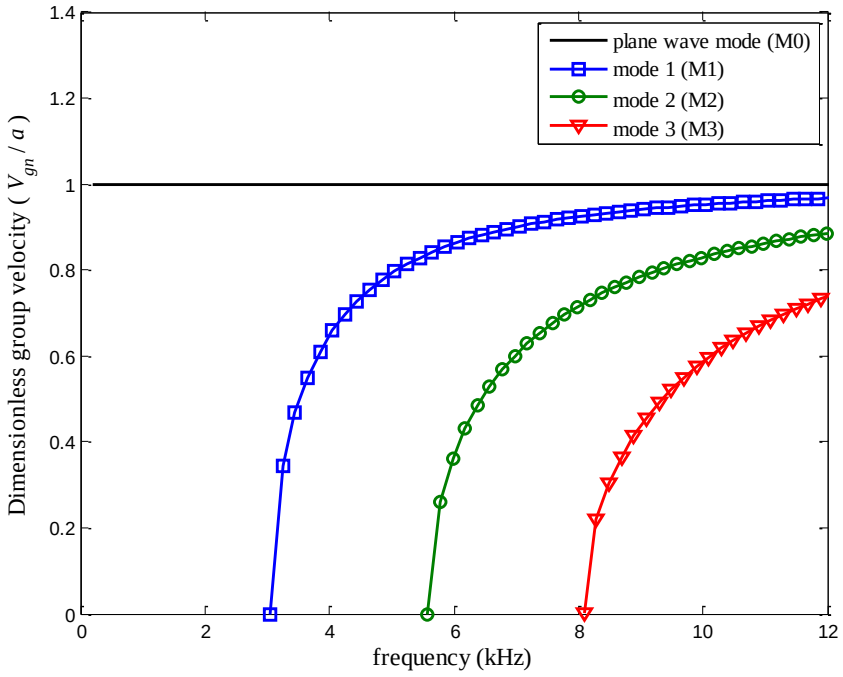

Figure 2.12 Descriptive sketch of multipath effect (Zigzag-type of path) in axi-symetric pipe flow

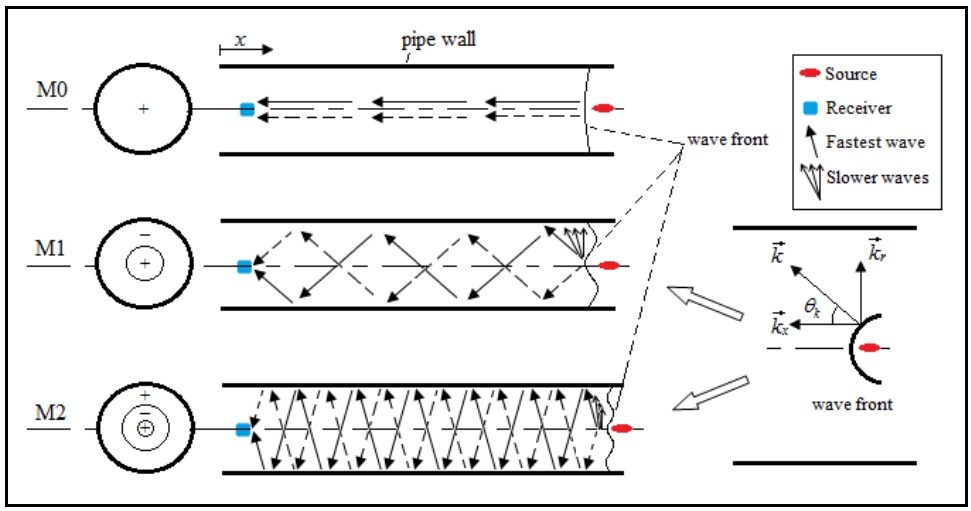

Figure 2.13 Variation of the propagation angle (Eq. (2.122)) with frequency for the first four modes

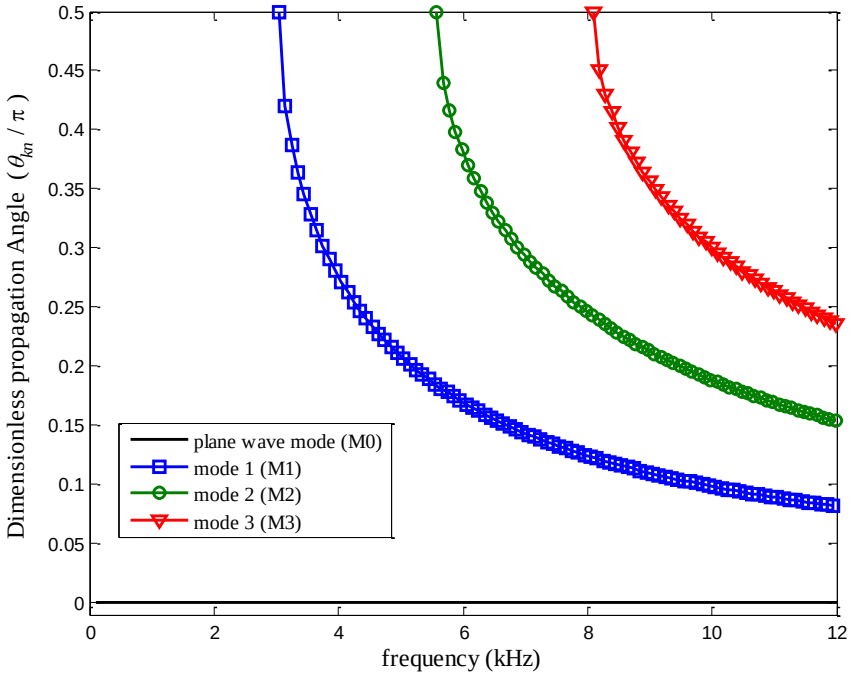

2.6.5. Energy and Energy flux

Considering only the incident wave (Eq. (2.114)) and using the momentum equation (Eq. (2.93)), the pressure and velocities at the n^{th} mode are

$$P_n = \varphi_n \cos\left(k_{xn}\ x - wt\right) J_0\left(rk_{rn}\right) \tag{2.123}$$

$$V_{xn} = \frac{k_{xn}}{\rho w}\varphi_n \cos\left(k_{xn}x - wt\right) J_0\left(rk_{rn}\right) \tag{2.124}$$

$$V_{rn} = \frac{k_{rn}}{\rho w}\varphi_n \sin\left(k_{xn}x - wt\right) J_1\left(rk_{rn}\right) \tag{2.125}$$

where the following formulas ([63]) are used

$$\begin{cases} \dfrac{d}{dr}\left[r^n J_n\left(r\right)\right] = r^n J_{n-1}\left(r\right) \\ J_{-n}\left(r\right) = \left(-1\right)^n J_n\left(r\right) \end{cases} \tag{2.126}$$

2.6.5.1. <u>Kinetic energy</u>

The kinetic energy of the n^{th} mode could be obtained as follows

$$T_n = T_{xn} + T_{rn} = \int_0^{2\pi}\int_0^R\int_0^{\lambda_n} \frac{1}{2}\rho\left(V_{xn}^2 + V_{rn}^2\right) r\,dr\,dx\,d\theta \tag{2.127}$$

where

$$T_{xn} = \int_0^{2\pi}\int_0^R\int_0^{\lambda_n} \frac{1}{2}\rho\left(V_{xn}^2\right) r\,dr\,dx\,d\theta = \frac{\pi k_{xn}^2 \varphi_n^2}{\rho w^2}\int_0^{\lambda_n} \cos^2\left(k_{xn}x - wt\right) dx \int_0^R J_0^2\left(k_{rn}r\right) r\,dr \tag{2.128}$$

$$\Rightarrow T_{xn} = \frac{\pi k_{xn}^2 \varphi_n^2 R^2 \lambda_n}{4\rho w^2} J_0^2\left(\alpha_{rn}\right) = \frac{k_{xn}^2 \varphi_n^2 A \lambda_n}{4\rho w^2} J_0^2\left(\alpha_{rn}\right) \tag{2.129}$$

and

$$T_{rn} = \int_0^{2\pi}\int_0^{R}\int_0^{\lambda_n} \frac{1}{2}\rho\left(V_{xn}^2\right) r dr dx d\theta = \frac{\pi k_{rn}^2 \varphi_n^2}{\rho w^2}\int_0^{\lambda_n} \sin^2\left(k_{xn}x - wt\right) dx \int_0^{R} J_1^2\left(k_{rn}r\right) r dr \qquad (2.130)$$

$$T_{rn} = \frac{\pi k_{rn}^2 \varphi_n^2 R^2 \lambda_n}{4\rho w^2} J_0^2\left(\alpha_{rn}\right) = \frac{k_{rn}^2 \varphi_n^2 A \lambda_n}{4\rho w^2} J_0^2\left(\alpha_{rn}\right) \qquad (2.131)$$

Therefore (using Eq. (2.118)),

$$T_n = \frac{\pi \varphi_n^2 R^2 \lambda_n}{4\rho a^2} J_0^2\left(\alpha_{rn}\right) = \frac{\varphi_n^2 A \lambda_n}{4\rho a^2} J_0^2\left(\alpha_{rn}\right) \qquad (2.132)$$

2.6.5.2. Potential Energy

The potential energy of the n^{th} mode is

$$U_n = \int_0^{2\pi}\int_0^{R}\int_0^{\lambda_n} \left(\frac{P_n^2}{2\rho a^2}\right) r dr dx d\theta = \frac{\pi \varphi_n^2}{\rho a^2}\int_0^{\lambda_n} \cos^2\left(k_{xn}x - wt\right) dx \int_0^{R} J_0^2\left(k_{rn}r\right) r dr \qquad (2.133)$$

$$\Rightarrow U_n = \frac{\pi \varphi_n^2 R^2 \lambda_n}{4\rho a^2} J_0^2\left(\alpha_{rn}\right) = \frac{\varphi_n^2 A \lambda_n}{4\rho a^2} J_0^2\left(\alpha_{rn}\right) \qquad (2.134)$$

2.6.5.3. Total energy

Using Eqs. (2.132) and (2.134), the total energy of the n^{th} mode is

$$E_n^T = T_n + U_n = \frac{\varphi_n^2 A \lambda_n}{2\rho a^2} J_0^2\left(\alpha_{rn}\right) \qquad (2.135)$$

and the total energy per unit wavelength of the n^{th} mode is

$$E_n = \frac{E_n^T}{\lambda_n} = \frac{\pi \varphi_n^2 R^2}{2\rho a^2} J_0^2\left(\alpha_{rn}\right) = \frac{\varphi_n^2 A}{2\rho a^2} J_0^2\left(\alpha_{rn}\right) \qquad (2.136)$$

2.6.5.4. Energy Flux

The energy flux (*i.e.* power) is obtained as follow

$$
\begin{aligned}
E_{Fn} &= \frac{1}{t_p}\int_0^{2\pi}\int_0^{R}\int_0^{t_p}\left(P_n \cdot V_{xn}\right) r\,dr\,d\theta\,dt \\
&= \frac{2\pi\varphi_n^2 k_{xn}}{t_p \rho w}\left[\int_0^{t_p}\cos^2\left(k_{xn}x - wt\right)dt\right]\left[\int_0^{R} J_0^2\left(k_{rn}r\right) r\,dr\right] \\
&= \frac{2\pi\varphi_n^2 k_{xn}}{t_p \rho w}\left[\frac{t_p}{2}\right]\left[\frac{R^2}{2} J_0^2\left(k_{rn}R\right)\right]
\end{aligned}
\tag{2.137}
$$

$$
\Rightarrow E_{Fn} = \frac{\pi\varphi_n^2 R^2 k_{xn}}{2\rho w} J_0^2\left(\alpha_{rn}\right) = \underbrace{\frac{\varphi_n^2 A}{2\rho a^2} J_0^2\left(\alpha_{rn}\right)}_{=E_n} a^2 \underbrace{\frac{k_{xn}}{w}}_{=V_{gn}} \tag{2.138}
$$

$$
\Rightarrow E_{Fn} = E_n \cdot V_{gn} \tag{2.139}
$$

where, in this case, $t_p = 2\pi/w$.

2.7. Summary

This chapter introduces the governing equations relevant to this thesis. The phenemona of water-hammer is elucidated by drawing an analogy between surge waves in open channels and surge waves in pipes. The harmonic solution for 1D water-hammer in an intact pipe is derived. The 2D water-hammer wave equations are introduced and their analytical solution for an inviscid fluid is given.

CHAPTER 3

NUMERICAL SCHEMES

3.1. Introduction

In this thesis, the behaviour of high frequency waves (HFW) in water pipe system is studied numerically in Chapter 7. This chapter gives details of the numerical schemes used for modeling HFW in water pipe system.

To the authors' best knowledge, the only numerical work that used a complete 2D model for pressurized water pipe system, where the radial variation of pressure is included, is by Mitra and Rouleau ([96]) where they employed an implicit numerical scheme based on matrix factorization. They used the finite difference method (FDM) for space discretization and a three backward point approach for time marching. A predictor-corrector technique was used to sweep along the axial and radial direction simultaneously. They reported that radial waves are only important in the vicinity of devices (e.g., valves) and singularities. However, their test cases were limited to relatively low frequencies because their scheme was very dissipative and dispersive. Moreover, their scheme was very time consuming and therefore, their study was limited to very short pipe lengths (a multiple of few diameter length).

HFW are dispersive and their physical dispersion must be accurately modelled; therefore, numerical dispersion must be minimized. For this reason, finite difference methods (FDM) (such as Lax-Wendroff schemes) should be avoided due to their dispersive behaviour ([58]). Even though point-wise schemes such as the finite element method (FEM) ([57]) could be used and they have an advantage in handling boundary conditions, the finite volume (FV) method is usually preferred for the great advantage provided by its conservation ability.

The two main families of FV methods are the Godunov-type schemes (GTS) ([127]) and Gas Kinetic schemes (GKS) ([139], [15]). The GTS are based on the Riemann solver (RS) solution to evaluate the numerical fluxes at the cell interface, while GKS are based on the solution of the Boltzmann equation. A comparison between the two FV families ([76]) showed that the main advantages of GKS over the GTS are (i) its ability in evaluating the inviscid and viscous parts together in a single flux evaluation (no splitting operator needed) (ii) and a straightforward and robust technique for upgrading the scheme for a high order of accuracy in multi-dimensional cases, based on simple Taylor expansions (no flux evaluation at Gaussian quadrature points are needed) ([139], [82]). However, these advantages are beneficial only when solving nonlinear system and shock-capturing problems. This is not the case for water-hammer problems because they are weakly nonlinear and only involve jump discontinuities. Moreover, GKS are about three times slower than GTS based on the approximate Riemann solver ([76]). For these reasons, GTS are preferred in this work.

Although many GTS have been developed, showing great accuracy and robustness ([127]), most of those schemes are usually tested and applied in gas dynamic applications ([127]). Therefore in this work, a two-dimensional (2D) FV numerical scheme based on the Riemann solver ([127]) is developed for water-hammer flow application and its robustness and accuracy is tested for modelling HFW in water-filled pipe flow.

In a finite volume (FV) discretized numerical domain, these high frequency waves leads to severe jumps at the cell interface. Despite the absence of shock waves in water-filled unsteady flow, such severe jumps still require delicate techniques to conserve the physical characteristics of the propagating waves and to avoid numerical anomalies ([100]). An appropriate dissipation mechanism is important since it controls the stability of the scheme versus the clarity of the results. The dissipation mechanism in FV GTS is complex and depends on the grid resolution, flux evolution and the projection stage ([138]).

In the last few decades, the need for high-order (>2) numerical schemes (e.g. [101], [82], [75], [132], [126], [16], [64], [54] and [135]) has been extensively recognized in many engineering applications, such as vortex-dominated flows, acoustic and aeroacoustic noise predictions and LES/DNS computations for complex configurations. Since the current work

considers simple and not very complex flow (e.g. no turbulent flow, single pipe), only second and third orders of accuracy are considered. The second order accuracy in space and time is achieved by using the Monotone Upstream-centred Scheme for Conservation Laws (MUSCL) Hancock approach ([127]), for its good accuracy and robustness. Whereas the third order scheme is achieved using the weighted essentially non-oscillatory (WENO) reconstruction ([64]). The viscous terms, when included, are discretized using a second order finite difference central scheme ([58]), and the classical third order Runge-Kutta (RK) method is used for time marching ([58]).

3.2. Numerical schemes

The developed numerical scheme solves the two dimensional axi-symmetric Navier stokes equations (Eqs. (2.56)-(2.60)) for unsteady and compressible flow in water-filled pipe (Figure 2.9). The physical domain is discretized into a numerical domain (Figure 3.1) containing N_R and N_X ($N_R \times N_X$) finite volumes along the radial and axial directions, respectively. Given that the pipe system is assumed axi-symmetric, only half domain of the pipe is considered ($0 \le r \le R$) where $R = D/2$ is the pipe radius and D is the pipe diameter. Since the numerical scheme used is based on FV formulation, it is instructive to illustrate the FV discretization (Figure 3.1) of Eq. (2.56) by integrating it over time and space. The S term on the right hand side of Eq. (2.56) will be evaluated using operator splitting, and therefore, the integration here only covers the inviscid part as follows

$$\begin{aligned} \overline{U}_{i,j}^{t+\Delta t} &= \overline{U}_{i,j}^{t} + \frac{1}{\Delta r \Delta x} \int_{0}^{\Delta t} \int_{-\frac{1}{2}\Delta x}^{+\frac{1}{2}\Delta x} \left(F_{i-1/2}(t,x) - F_{i+1/2}(t,x) \right) dx dt \\ &+ \frac{1}{\Delta r \Delta x} \int_{0}^{\Delta t} \int_{-\frac{1}{2}\Delta r}^{+\frac{1}{2}\Delta r} \left(G_{j-1/2}(t,r) - G_{j+1/2}(t,r) \right) dr dt \end{aligned} \qquad (3.1)$$

where

$$\begin{cases} U_{i,j} = U_c\left(r_i, x_j\right) \\ \overline{U}_{i,j} = \dfrac{1}{\Delta r \Delta x} \displaystyle\int_{r_{i-1/2}}^{r_{i+1/2}} \int_{x_{j-1/2}}^{x_{j+1/2}} U_c \; dxdr \\ F_{i+1/2}\left(t,x\right) = F\left(t, r_i + \tfrac{1}{2}\Delta r, x\right) \\ G_{j+1/2}\left(t,x\right) = F\left(t, r, x_j + \tfrac{1}{2}\Delta x\right) \end{cases} ; \quad \begin{cases} \Omega_{i,j} = \left[r_{i-\frac{1}{2}}, r_{i+\frac{1}{2}}\right] \times \left[x_{j-\frac{1}{2}}, x_{j+\frac{1}{2}}\right] \\ i = 1 \ldots N_R \\ j = 1 \ldots N_X \end{cases} ; \qquad (3.2)$$

Δr , Δx and Δt are the radial, axial and time discretization step sizes, respectively. Equation (3.1) shows that at each time level $t + \Delta t$, at least four fluxes need to be computed namely $F_{i-1/2}$, $F_{i+1/2}$, $G_{j-1/2}$ and $G_{j+1/2}$ at the corresponding cell interfaces $\left(r_i - \frac{1}{2}\Delta r, x\right)$, $\left(r_i + \frac{1}{2}\Delta r, x\right)$, $\left(r, x_j - \frac{1}{2}\Delta x\right)$ and $\left(r, x_j + \frac{1}{2}\Delta x\right)$, respectively. The solution of Riemann problem is used to evaluate those fluxes (see Figure 3.2) at the cell interfaces.

Figure 3.1 Discretized space: numerical mesh

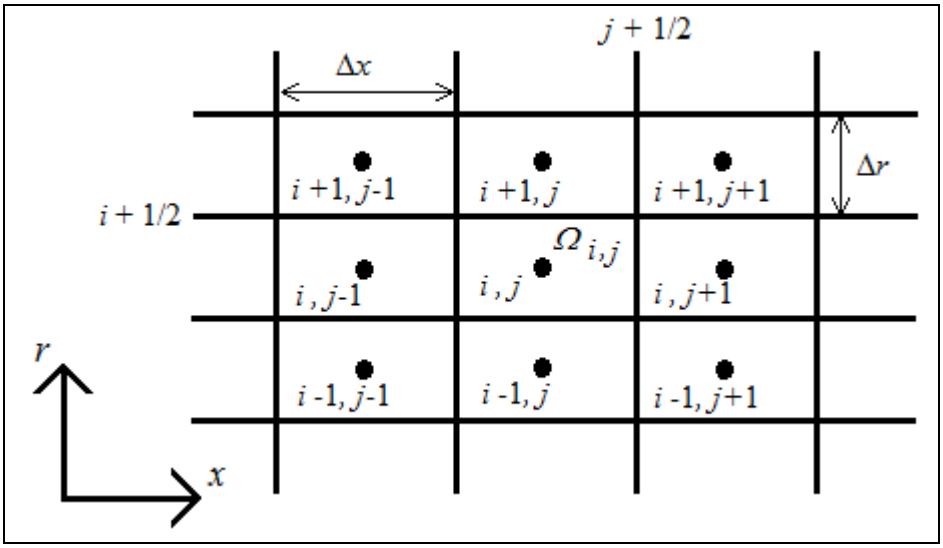

Figure 3.2 Riemann problem at the cell interface

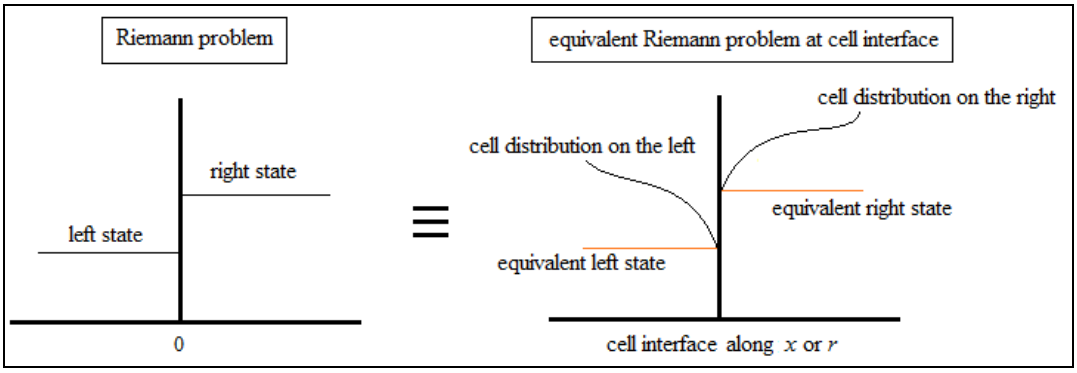

3.2.1. Riemann solution at the cell interface

The Riemann solution is splitted along each direction according to the following procedure

$$\begin{cases} \dfrac{\partial U_r^{1D}}{\partial t} + \dfrac{\partial F^{1D}}{\partial r} = 0 \\ \text{Initial Condition} : \overline{U}_{i,j}^{t} \end{cases} \Rightarrow U_F \qquad \text{along the radial direction} \qquad (3.3)$$

and

$$\begin{cases} \dfrac{\partial U_x^{1D}}{\partial t} + \dfrac{\partial G^{1D}}{\partial x} = 0 \\ \text{Initial Condition} : U_F \end{cases} \Rightarrow \overline{\overline{U}} \qquad \text{along the axial direction} \qquad (3.4)$$

where

$$U_r^{1D} = \begin{bmatrix} \rho \\ \rho V_r \end{bmatrix} ; \; U_x^{1D} = \begin{bmatrix} \rho \\ \rho V_x \end{bmatrix} ; \; F^{1D} = \begin{bmatrix} \rho V_r \\ \rho V_r^2 + P \end{bmatrix} ; \; G^{1D} = \begin{bmatrix} \rho V_r \\ \rho V_x^2 + P \end{bmatrix}. \qquad (3.5)$$

The Jacobian matrix from Eqs. (3.3) and (3.4) are

$$\begin{cases} J_F = \dfrac{\partial F^{1D}}{\partial U_r^{1D}} = \begin{bmatrix} 0 & 1 \\ a^2 - V_r^2 & 2V_r \end{bmatrix} \\ \\ J_G = \dfrac{\partial G^{1D}}{\partial U_x^{1D}} = \begin{bmatrix} 0 & 1 \\ a^2 - V_x^2 & 2V_x \end{bmatrix} \end{cases} \tag{3.6}$$

and their corresponding eigenvalues and right-eigenvectors are

$$\lambda_i^F = \begin{cases} \lambda_1^F = V_r - a \\ \lambda_2^F = V_r + a \end{cases} \quad ; \quad \lambda_i^G = \begin{cases} \lambda_1^G = V_x - a \\ \lambda_2^G = V_x + a \end{cases} \tag{3.7}$$

and

$$\mathrm{K}^F = \begin{bmatrix} \dfrac{1}{V_r - a} & \dfrac{1}{V_r + a} \\ 1 & 1 \end{bmatrix} \quad ; \quad \mathrm{K}^G = \begin{bmatrix} \dfrac{1}{V_x - a} & \dfrac{1}{V_x + a} \\ 1 & 1 \end{bmatrix}. \tag{3.8}$$

Approximate Riemann solution is obtained by assuming frozen Jacobian matrices at each time step where explicit variables are used for the Jacobian matrix entries. Therefore, the system is linearized at each time step. Using the Generalized Riemann Invariant ([127]) across the characteristic lines (see Figure 3.3), gives

$$\begin{cases} \dfrac{d\rho}{\frac{1}{V_r - a}} = \dfrac{d\rho V_r}{1} \ ; \ \text{across} \ \dfrac{dx}{dt} = V_r - a \\ \dfrac{d\rho}{\frac{1}{V_r + a}} = \dfrac{d\rho V_r}{1} \ ; \ \text{across} \ \dfrac{dx}{dt} = V_r + a \end{cases} \quad \text{along the radial direction} \tag{3.9}$$

and

$$\begin{cases} \dfrac{d\rho}{\frac{1}{V_x - a}} = \dfrac{d\rho V_x}{1} \ ; \ \text{across} \ \dfrac{dx}{dt} = V_x - a \\ \dfrac{d\rho}{\frac{1}{V_x + a}} = \dfrac{d\rho V_x}{1} \ ; \ \text{across} \ \dfrac{dx}{dt} = V_x + a \end{cases} \quad \text{along the axial direction ,} \tag{3.10}$$

which leads to the Riemann solution at the radial and axial cell interfaces respectively as follows (see Figure 3.3)

$$\begin{cases} \rho^* = \dfrac{\left(\left(V_r^{\,t} + a\right)\rho^r - \left(\rho V_r\right)^r\right) - \left(\left(V_r^{\,t} - a\right)\rho^l - \left(\rho V_r\right)^l\right)}{2a} \\ \left(\rho V_r\right)^* = \dfrac{\left(\left(V_r^{\,t} + a\right)\rho^r - \left(\rho V_r\right)^r\right)\left(V_r^{\,t} - a\right) - \left(\left(V_r^{\,n} - a\right)\rho^l - \left(\rho V_r\right)^l\right)\left(V_r^{\,t} + a\right)}{2a} \end{cases} \tag{3.11}$$

and

$$\begin{cases} \rho^* = \dfrac{\left(\left(V_x^{\,t} + a\right)\rho^r - \left(\rho V_x\right)^r\right) - \left(\left(V_x^{\,t} - a\right)\rho^l - \left(\rho V_x\right)^l\right)}{2a} \\ \left(\rho V_x\right)^* = \dfrac{\left(\left(V_x^{\,t} + a\right)\rho^r - \left(\rho V_x\right)^r\right)\left(V_x^{\,t} - a\right) - \left(\left(V_x^{\,t} - a\right)\rho^l - \left(\rho V_x\right)^l\right)\left(V_x^{\,t} + a\right)}{2a} \end{cases} \tag{3.12}$$

where the "*" indicates variables at the cell interface and the superscripts "*l*" and "*r*" indicate the variables at the left and right of the cell interface, respectively (see Figure 3.3).

Figure 3.3 Riemann solution

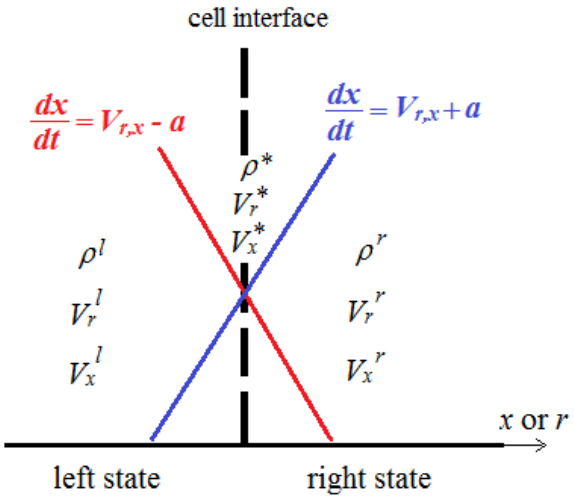

3.2.2. 2nd order of accuracy: MUSCL-Hancock approach

To achieve second (2^{nd}) order accuracy in space, linear reconstruction within each cell is required (Figure 3.4). Since directional splitting operator is used for the Riemann solution (Eqs. 3.3 and 3.4), the sub-cell reconstruction is also splitted along the radial and axial direction. Knowing the cell-averaged data at time level t, the linear reconstruction is realized by considering the following linear cell-distribution

$$\begin{cases} \varpi\left(r, x_j\right) = \overline{U}_{i,j}^{t} + \dfrac{\left(r - r_i\right)}{\Delta r}\Im_i \\ \varpi\left(r_i, x\right) = \overline{U}_{i,j}^{t} + \dfrac{\left(x - x_j\right)}{\Delta x}\Im_j \end{cases} \tag{3.13}$$

where ϖ are the linear reconstructed data. The $\Im_i$ and $\Im_j$ are the slopes along the r and x direction, respectively. A VanLeer slope limiter ([127]) is used to compute those slopes to eliminate spurious oscillations given by

$$\Im_i\left(\Delta^+, \Delta^-\right) = \left[\operatorname{sgn}\left(\Delta^+\right) + \operatorname{sgn}\left(\Delta^-\right)\right]\frac{\left|\Delta^+\right| \cdot \left|\Delta^-\right|}{\left|\Delta^+\right| + \left|\Delta^-\right| + \varepsilon_2} \tag{3.14}$$

where

$$\begin{cases} \Delta^+ = \dfrac{\overline{U}_{i+1,j} - \overline{U}_{i,j}}{\Delta r} \\ \Delta^- = \dfrac{\overline{U}_{i,j} - \overline{U}_{i-1,j}}{\Delta r} \end{cases}; \tag{3.15}$$

ε_2 is a very small number to avoid singularity; and "sgn" is the sign function. $\Im_j$ could be evaluated in a similar way. Notice that $\overline{U}$ in Eq. (3.15) could be any primitive or conservative variable. In this work, the pressure P is chosen to compute the jumps Δ^+ and Δ^-. Other slope limiter such as MINMOD ([127]) is also used and showed almost similar results as VanLeer slope limiter.

Notice from Figures 3.2 and 3.4 that what is important from the reconstruction is to obtain the values at the cell interface which will be considered as left/right states for the Riemann problem. Therefore, assuming a rectangular mesh and evaluating Eq. (3.13) at the cell interfaces i+1/2 and j+1/2, respectively, gives the left and right states for the Riemann problem as follows

along the radial direction:
$$\begin{cases} \varpi^{l}_{i+\frac{1}{2},j} = \overline{U}^{t}_{i,j} + \frac{1}{2}\Im_{i} \\ \varpi^{r}_{i+\frac{1}{2},j} = \overline{U}^{t}_{i+1,j} - \frac{1}{2}\Im_{i+1} \end{cases} \qquad (3.16)$$

along the axial direction
$$\begin{cases} \varpi^{l}_{i,j+\frac{1}{2}} = \overline{U}^{t}_{i,j} + \frac{1}{2}\Im_{j} \\ \varpi^{r}_{i,j+\frac{1}{2}} = \overline{U}^{t}_{i,j+1} - \frac{1}{2}\Im_{j+1} \end{cases} \qquad (3.17)$$

where the superscript '*l*' and '*r*' indicates *left and right states for a Riemann problem at a cell interface (i.e. at* $r_{i+\frac{1}{2}}$ and $x_{j+\frac{1}{2}}$*)*, respectively.

To achieve 2nd order accuracy in space and time, the Hancock approach ([127] is used where the left and right states in Eqs.(3.16) and (3.17) are evolved in time by half time step (at $t+\Delta t/2$), then the Riemann problem is considered using the new updated states. The procedure of Hancock approach is summarized in the following steps:

i. From the linear reconstruction (Eq. (3.13)), the left and right states for a Riemann problem are obtained (Eqs. (3.16) and (3.17)).

ii. Evolution of the left and right states (Eqs. (3.16) and (3.17)) by half time step as follows

along *r*-direction:
$$\begin{cases} \overline{\varpi}^{l}_{i+\frac{1}{2},j} = \varpi^{l}_{i+\frac{1}{2},j} + \frac{1}{2}\frac{\Delta t}{\Delta r}\left[F\left(\varpi^{r}_{i-\frac{1}{2},j}\right) - F\left(\varpi^{l}_{i+\frac{1}{2},j}\right)\right] \\ \overline{\varpi}^{r}_{i+\frac{1}{2},j} = \varpi^{r}_{i+\frac{1}{2},j} + \frac{1}{2}\frac{\Delta t}{\Delta r}\left[F\left(\varpi^{r}_{i+\frac{1}{2},j}\right) - F\left(\varpi^{l}_{i+\frac{3}{2},j}\right)\right] \end{cases} \qquad (3.18)$$

along x-direction:

$$\begin{cases} \overline{\overline{\varpi}}^{l}_{i,j+\frac{1}{2}} = \varpi^{l}_{i,j+\frac{1}{2}} + \frac{1}{2}\frac{\Delta t}{\Delta x}\left[G\left(\varpi^{r}_{i,j-\frac{1}{2}}\right) - G\left(\varpi^{l}_{i,j+\frac{1}{2}}\right)\right] \\ \overline{\overline{\varpi}}^{r}_{i,j+\frac{1}{2}} = \varpi^{r}_{i,j+\frac{1}{2}} + \frac{1}{2}\frac{\Delta t}{\Delta x}\left[G\left(\varpi^{r}_{i,j+\frac{1}{2}}\right) - G\left(\varpi^{l}_{i,j+\frac{3}{2}}\right)\right] \end{cases} \qquad (3.19)$$

iii) The Riemann problem is considered using the new states in Eqs. (3.18) and (3.19) where the Riemann solution (Eqs. (3.11) and (3.12)) is used to compute the fluxes in Eq. (3.1) at the cell interfaces.

Figure 3.4 Linear cell reconstruction along *r*-direction

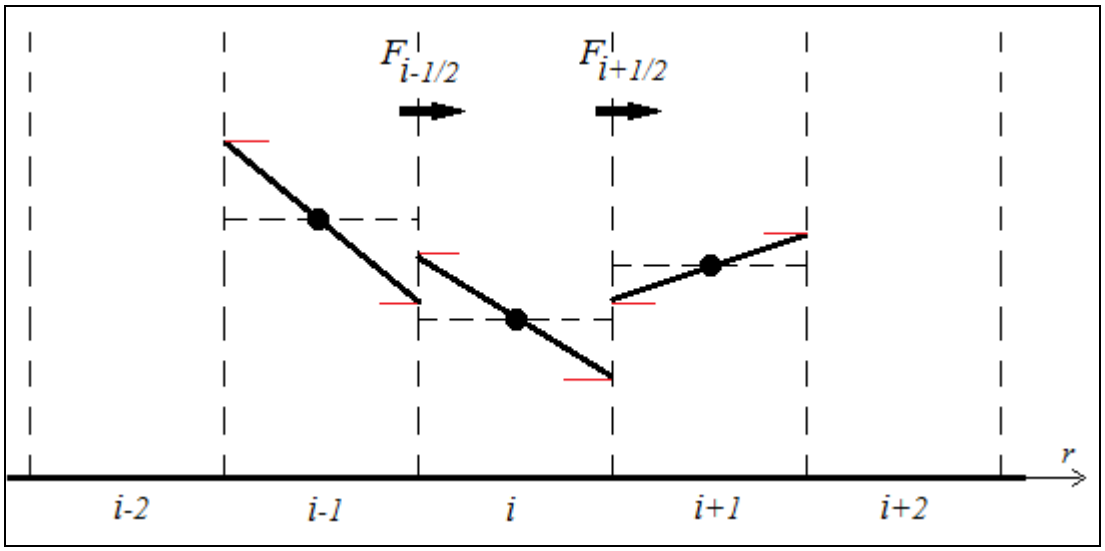

3.2.3. Third order of accuracy: WENO reconstruction

Similarly to the previous linear reconstruction, directional splitting will be used. In this case, to achieve third order of accuracy, one dimensional quadrature reconstruction is required within each control volume as follows

along the x-direction $$\varpi(r_i, x) = U_{i,j} + \overline{\Im}_j\left(x - x_j\right) + \overline{\overline{\Im}}_j\left(x - x_j\right)^2 \qquad (3.20)$$

For consistency and conservation within a finite volume ($\Omega_{i,j}$), the following three conditions must be fulfilled

$$\begin{cases} \overline{U}_{i,j} = \dfrac{1}{\Delta x}\displaystyle\int_{x_{j-1/2}}^{x_{j+1/2}} \varpi\left(r_i, x\right)\, dx \\ U_c\left(r_i, x_{j+1/2}\right) = U_{i,j}^{r} = U_{i,j+\frac{1}{2}}^{l} \\ U\left(r_i, x_{j-1/2}\right) = U_{i,j}^{l} = U_{i,j-\frac{1}{2}}^{r} \end{cases} \qquad (3.21)$$

which result in

$$\begin{cases} U_{i,j} = \dfrac{3}{2}\overline{U}_{i,j} - \dfrac{1}{4}\left(U_{i,j}^{r} + U_{i,j}^{l}\right) \\ \overline{\Im}_j = \dfrac{U_{i,j}^{r} + U_{i,j}^{l}}{\Delta x} \\ \overline{\overline{\Im}}_j = \dfrac{6\left(U_{i,j}^{r} + U_{i,j}^{l} - 2\overline{U}_{i,j}\right)}{\Delta x^2} \end{cases} . \qquad (3.22)$$

Similar solutions could be obtained for the case along the *r*-direction. It is important to notice that in Eq. (3.21) the indexes "*l*" and "*r*" are used to indicate the left and right states of either the control volume or the cell interface based on whether the variable *U* is given at the cell centre (e.g. $U_{i,j}$) or at the a cell interface (e.g. $U_{i,j+1/2}$), respectively.

As stated in the previous section, what is important from a reconstruction is to obtain the values at both sides of the cell interfaces (see Figure 3.2 and Figure 3.4). Essentially, the Weighted Essentially Non-Oscillatory (WENO) reconstruction ([64]) is a Total Variation Diminishing (TVD) technique which determines those left and right states while avoiding spurious oscillation and maintaining the desired order of accuracy of the scheme. Considering the axial direction, the left and right states of the cell centered at *j* from a WENO reconstruction are given as follow ([64])

$$\begin{cases} \varpi_j^r = \sum_{s=0}^{2} \aleph_s^r \ \lambda_s^r \\ \varpi_j^l = \sum_{s=0}^{2} \aleph_s^l \ \lambda_s^l \end{cases} \tag{3.23}$$

where

$$\begin{cases} \lambda_0^r = \frac{1}{3}\overline{U}_j + \frac{5}{6}\overline{U}_{j+1} - \frac{1}{6}\overline{U}_{j+2} \\ \lambda_1^r = -\frac{1}{6}\overline{U}_{j-1} + \frac{5}{6}\overline{U}_j + \frac{1}{3}\overline{U}_{j+1} \\ \lambda_2^r = \frac{1}{3}\overline{U}_{j-2} - \frac{7}{6}\overline{U}_{j-1} + \frac{11}{6}\overline{U}_j \end{cases} ; \tag{3.24}$$

$$\begin{cases} \lambda_0^l = \frac{11}{6}\overline{U}_j - \frac{7}{6}\overline{U}_{j+1} + \frac{1}{3}\overline{U}_{j+2} \\ \lambda_1^l = \frac{1}{3}\overline{U}_{j-1} + \frac{5}{6}\overline{U}_j - \frac{1}{6}\overline{U}_{j+1} \\ \lambda_2^l = -\frac{1}{6}\overline{U}_{j-2} + \frac{5}{6}\overline{U}_{j-1} + \frac{1}{3}\overline{U}_j \end{cases} ; \tag{3.25}$$

$$\begin{cases} \aleph_s^r = \dfrac{\hbar_s^r}{\sum_{m=0}^{2} \hbar_m^r} \quad ; \quad \hbar_s^r = \dfrac{\overline{d}_s^r}{\left(\overline{\beta}_s + \varepsilon\right)^2} \\ \aleph_s^l = \dfrac{\hbar_s^l}{\sum_{m=0}^{2} \hbar_m^l} \quad ; \quad \hbar_s^l = \dfrac{\overline{d}_s^l}{\left(\overline{\beta}_s + \varepsilon\right)^2} \end{cases} ; \tag{3.26}$$

$$\begin{cases} \overline{\beta}_0 = \frac{13}{12}\left(\overline{U}_j - 2\overline{U}_{j+1} + \overline{U}_{j+2}\right)^2 + \frac{1}{4}\left(3\overline{U}_j - 4\overline{U}_{j+1} + \overline{U}_{j+2}\right)^2 \\ \overline{\beta}_1 = \frac{13}{12}\left(\overline{U}_{j-1} - 2\overline{U}_j + \overline{U}_{j+1}\right)^2 + \frac{1}{4}\left(\overline{U}_{j-1} - \overline{U}_{j+1}\right)^2 \\ \overline{\beta}_2 = \frac{13}{12}\left(\overline{U}_{j-2} - 2\overline{U}_{j-1} + \overline{U}_j\right)^2 + \frac{1}{4}\left(\overline{U}_{j-2} - 4\overline{U}_{j-1} + 3\overline{U}_j\right)^2 \end{cases} \text{ and } \tag{3.27}$$

$$\overline{d}_0^r = \overline{d}_2^l = \frac{3}{10} \quad ; \quad \overline{d}_1^r = \overline{d}_1^l = \frac{3}{5} \quad ; \quad \overline{d}_2^r = \overline{d}_0^l = \frac{1}{10} . \tag{3.28}$$

In Eq. (3.26), ε is a "calibration" parameter to avoid singularities. The effect of such parameter on the numerical results is discussed later. Similar procedure (Eqs. (3.23)–(3.28)) is applied for the radial direction.

As seen from the above procedure, the WENO method uses smoothness parameters ($\aleph$ and $\beth$) over five consecutive cells (finite volumes) which, under smooth flow, will achieve 5^{th} order of accuracy ([64], [82]). However, in non-smooth flow, the scheme achieves only 3^{rd} order accuracy. Such scheme is usually referred as third-fifth order scheme. However, since this work considers only smooth flows, this scheme will be referred as fifth (5^{th}) order scheme and its accuracy is tested in later discussion.

3.2.3.1. Second order WENO scheme

The above WENO procedure (Eqs. (3.23) – (3.28)) could be, similarly, applied to obtain a second order WENO scheme ([64]) with linear reconstruction. In this case, the WENO method uses smoothness parameters over three consecutive cells (finite volumes) which, under smooth flow, achieves third order of accuracy. However, in non-smooth flow, the scheme achieves only second order of accuracy. Such scheme is usually referred as second-third order scheme. However since this work considers only smooth flows, it will be referred as third (3^{rd}) order scheme and its accuracy is tested in later discussion.

3.2.4. Evolution stage of the numerical fluxes along the cell interface

This section discusses the evolution stage of the numerical flux *along* the cell interface. As shown from Eq. (3.1), to update the variables to the next time level $t+\Delta t$, two integrals (for an explicit scheme) must be evaluated which describes the distribution of the fluxes *along* the cell interface (Figure 3.5). Two cases are discussed below depending on whether the system (Eq. (2.56)) is linear or not.

Figure 3.5 Sketch example of flux function at cell interface for a three dimensional application showing the need for integration along the cell interface.

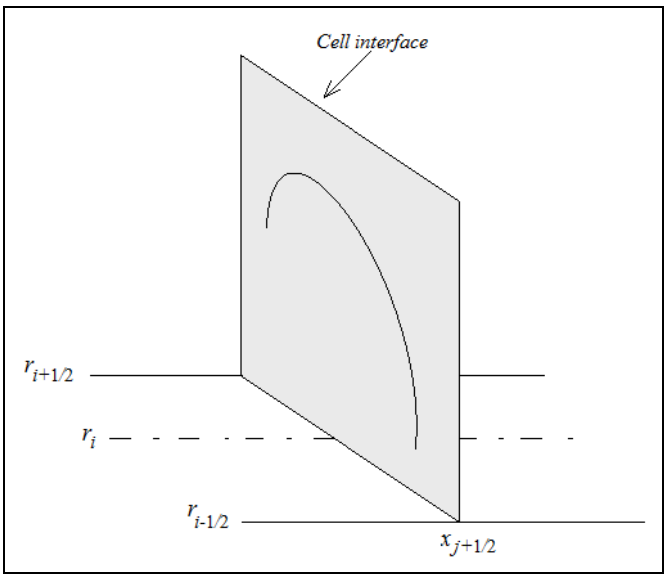

3.2.4.1. Linear scheme for linear flow applications

Water hammer flows are weakly nonlinear. In fact for most WH application, the convective terms, from which most instability rises, are usually neglected. This is because WH flow has very low Mach number ($M_{ch} = V^*/a$) where a is the wave speed and V^* is a characteristic flow velocity (V_x or V_r). The typical wave speed in water- filled conduits is about 1000m/s whilst the flow velocity is usually around 1m/s which results in a Mach number of the order of 10^{-3}. Therefore, this work considers the case of linear system for which the space integrals in Eq. (3.1) are easily evaluated at the central point and Eq. (3.1) becomes

$$\overline{U}_{i,j}^{t+\Delta t} = \overline{U}_{i,j}^{t} + \frac{\Delta t}{\Delta r}\left[F\left(r_{i-1/2}, x_j\right) - F\left(r_{i+1/2}, x_j\right)\right] + \frac{\Delta t}{\Delta x}\left[G\left(r_i, x_{i-1/2}\right) - G\left(r_i, x_{i+1/2}\right)\right] \quad . \qquad (3.29)$$

3.2.4.2. *Nonlinear scheme for nonlinear flow applications*

For nonlinear systems, exact Riemann solution should be used, but since it is computationally very expensive, approximate Riemann solvers ([127]) are used where the Jacobian matrices (Eq. (3.6)) are evaluated explicitly at time *t*. This renders the system quasi-linear. On the other hand, nonlinear flows require special techniques to evaluate the spatial integrals in Eq. (3.1). The widely used technique is the Gaussian quadrature which evaluate the integrals at different Gaussian points ([64]). To achieve third order of accuracy for a two dimensional flow, at least two Gaussian points are required ([64]). The disadvantage of this integrations is the computational (CPU) time added. In fact, the WENO reconstruction procedure would need to be repeated twice along each direction where two fluxes in one cell interface are evaluated (one flux at each Gaussian point). A good discussion about implementation and computational power of ENO and WENO for general system of equations are given in ([11], [12]). Although only weakly nonlinear flows are considered, a nonlinear scheme based on two Gaussian points is developed in this work to check the accuracy of the linear scheme and could be used for future work where nonlinearity becomes important. Through numerical tests, both linear and nonlinear schemes showed similar results for modelling high frequency waves in water hammer flows. However, the CPU time of the nonlinear scheme is twice the CPU time of linear scheme which is due to the double fluxes computation at the Gaussian points.

3.2.5. *Time evolution*

MUSCL-Hancock approach is used for the 2^{nd} order scheme which provides 2^{nd} order accuracy in space and time. However, for 3^{rd} and 5^{th} order schemes, Runge-Kutta (RK) method is used for time evolution. Jiang and Shu ([64]) emphasized that high order scheme should use TVD RK methods to ensure stability of the scheme. However, it is found that the third order TVD RK scheme produces strong spurious oscillations. Although, the second order TVD RK scheme gave stable results, in this work the classical RK is used because it is generally used in the literature and produces stable results at second, third and forth order.

Moreover, for all the numerical test cases studied in this work, comparison between the classical third and second order RK schemes, showed similar results. Since, the third order scheme is computationally more time consuming, the second order scheme is generally used throughout this work. Details of the two and three stages TVD RK method are discussed in Jiang and Shu ([64]), and the details of the classical RK method could be found in Hirsch ([58]).

3.2.6. Viscous terms

When viscous flow is considered, the viscous terms (see Eq. (2.58)) are discretized using a 2^{nd} order central finite difference scheme. Then, operator splitting is used to compute the following equation

$$\frac{d\overline{\overline{U}}}{dt} = S \qquad (3.30)$$

where $\overline{\overline{U}}$ is given by Eq. (3.4). The classical RK method ([58]) is used to solve Eq. (3.30).

3.2.7. Boundary conditions

The boundary conditions are imposed at four different locations namely: at the pipe wall ($r = R$), at the pipe centreline ($r = 0$), at upstream boundary of the pipe ($x = 0$) and at downstream boundary of the pipe ($x = L$), where R and L are the pipe radius and length, respectively. The details of the different boundary conditions used are listed below.

3.2.7.1. Reflective boundary conditions

The reflective boundaries are imposed at the pipe wall and they are given by

$$\left.\begin{array}{l} \left.\dfrac{\partial P}{\partial r}\right|_{r=R} = 0 \\ V_r\big|_{r=R} = 0 \\ \\ \begin{cases} \left.\dfrac{\partial V_x}{\partial r}\right|_{r=R} = 0 \text{ if } n_v = 0 \\ V_x\big|_{r=R} = 0 \text{ if } n_v = 1 \end{cases} \end{array}\right\} \Rightarrow \begin{cases} P\left(r_{\mathrm{NR}-N_{bc}+n_g}, x_j\right) = P\left(r_{\mathrm{NR}-N_{bc}-n_g+1}, x_j\right) \\ V_r\left(r_{\mathrm{NR}-N_{bc}+n_g}, x_j\right) = -V_r\left(r_{\mathrm{NR}-N_{bc}-n_g+1}, x_j\right) \\ V_x\left(r_{\mathrm{NR}-N_{bc}+n_g}, x_j\right) = (-1)^{n_v} V_x\left(r_{\mathrm{NR}-N_{bc}-n_g+1}, x_j\right) \end{cases} \quad (3.31)$$

where N_{bc} is the number of fictitious cells added (which is equal to 2 for linear reconstruction and 3 for quadratic reconstruction); $n_g = \{1, 2 \ldots N_{bc}\}$ is a counter; and n_v=0 or 1 depending on whether the flow is inviscid or viscous, respectively.

3.2.7.2. Symmetric boundary condition

This type of boundary condition is applied at the pipe centreline to satisfy the axi-symmetric behaviour of the flow and they are defined as follows

$$\left.\begin{array}{l} \left.\dfrac{\partial P}{\partial r}\right|_{r=0} = 0 \\ V_r\big|_{r=0} = 0 \\ \left.\dfrac{\partial V_x}{\partial r}\right|_{r=0} = 0 \end{array}\right\} \Rightarrow \begin{cases} P\left(r_{N_{bc}-n_g+1}, x_j\right) = P\left(r_{N_{bc}+n_g}, x_j\right) \\ V_r\left(r_{N_{bc}-n_g+1}, x_j\right) = -V_r\left(r_{N_{bc}+n_g}, x_j\right). \\ V_x\left(r_{N_{bc}-n_g+1}, x_j\right) = V_x\left(r_{N_{bc}+n_g}, x_j\right) \end{cases} \quad (3.32)$$

3.2.7.3. Non-reflective boundary conditions

To study solely the behaviour of high frequency waves in pressurized water-filled pipe, it is required to consider unbounded pipe system. Infinite (long) pipe is computationally very expensive to model, and instead, non-reflective boundary conditions at the upstream and downstream pipe boundaries are considered. Different non-reflective boundary conditions have been developed in the literature such as the characteristic boundary condition (CBC) ([58], [59] [122], and [123]), buffer zone techniques and perfectly matched layer (PML) ([107]). All non-reflective boundary conditions induce numerical reflections, and depending

on the flow application, some methods perform better than the others ([107], [19]). In general, all non-reflective boundaries are affected by the following two major factors

(i) Angle of propagation: waves propagating in the normal direction towards the boundary induce the least numerical reflection. As the propagation angle deviates from the normal direction, numerical reflections increase. This is the most severe factor affecting non-reflecting boundary conditions ([107]).

(ii) Wave frequency: Higher frequencies induce less numerical reflections ([52]).

Although not necessary the most efficient, CBC is the most widely used method in flow dynamic application. This method is based on using the Riemann invariant (or characteristic lines) to eliminate waves propagating from the boundary into the numerical domain, and it is very easy to implement. This work uses the CBC method and this section gives details of its implementation in the developed schemes. The performance of CBC interaction with high frequency waves is studied in later section and the major factors in (i) and (ii) above are discussed.

The CBC method is implemented at the upstream (x=0) and downstream boundaries (x=L) of the pipe, and therefore only the axial direction is considered. The splitted system of equations along the axial direction (Eq. (3.4)) is rewritten using the characteristic variables ($\overline{\psi}_x^{1D}$) as follow ([127])

$$\frac{\partial \overline{\psi}_x^{1D}}{\partial t} + \Lambda^G \frac{\partial \overline{\psi}^{1D}}{\partial x} = 0 \qquad (3.33)$$

where

$$\overline{\psi}_x^{1D} = L_G U_x^{1D} \;\; ; \;\; \Lambda^G = L_G J_G L_G^{-1} = \begin{bmatrix} \lambda_1^G & 0 \\ 0 & \lambda_2^G \end{bmatrix} \qquad (3.34)$$

and L_G is the left eigenvector of J_G which is

$$L_G = \begin{bmatrix} -V_x - a & 1 \\ V_x - a & 1 \end{bmatrix} \tag{3.35}$$

and its inverse is

$$L_G^{-1} = \begin{bmatrix} -\frac{1}{2a} & \frac{1}{2a} \\ -\frac{V_x - a}{2a} & \frac{V_x + a}{2a} \end{bmatrix}. \tag{3.36}$$

The characteristic lines are given by Toro, et al. ([127])

$$\overline{\psi}_x^{1D} = L_G U_x^{1D} = 0 \Rightarrow \begin{cases} d(\rho V_x) - (V_x + a)\, d\rho = 0 \;\; ; \;\; \frac{dx}{dt} = V_x - a \\ d(\rho V_x) - (V_x - a)\, d\rho = 0 \;\; ; \;\; \frac{dx}{dt} = V_x + a \end{cases} \tag{3.37}$$

which after simplification gives

$$\begin{cases} \frac{dV_x}{a} - \frac{d\rho}{\rho} = 0 \;\; ; \;\; \frac{dx}{dt} = V_x - a \\ \frac{dV_x}{a} + \frac{d\rho}{\rho} = 0 \;\; ; \;\; \frac{dx}{dt} = V_x + a \end{cases}. \tag{3.38}$$

Integrating Eq. (3.38), yields

$$\begin{cases} V_x - a\log(\rho) = C^- \;\; ; \;\; \frac{dx}{dt} = V_x - a \\ V_x + a\log(\rho) = C^+ \;\; ; \;\; \frac{dx}{dt} = V_x + a \end{cases} \tag{3.39}$$

where C^- and C^+ are two constants called the Riemann invariants.

Equation (3.39) is applied at the upstream and downstream pipe boundaries (see Figure 3.6) to obtain the unknown variables at the ghost cells as follows

- Non-reflective boundary conditions at the *upstream* boundary

$$\begin{cases} V_r\left(r_i, x_{N_{bc}-n_g+1}\right) = V_r\big|_\infty \\ \rho\left(r_i, x_{N_{bc}-n_g+1}\right) = \exp\left(\dfrac{C^+ - C^-}{2a}\right) \\ V_x\left(r_i, x_{N_{bc}-n_g+1}\right) = C^+ + C^- \end{cases} \tag{3.40}$$

$$\text{with} \quad \begin{cases} C^+ = V_x\big|_\infty + a\log\left(\rho\big|_\infty\right) \\ C^- = V_x\left(r_i, x_{N_{bc}-n_g+2}\right) - a\log\left(\rho\left(r_i, x_{N_{bc}-n_g+2}\right)\right) \end{cases}$$

where the subscript "∞" refers to values at infinity (*i.e.* values at the boundary if the pipe was infinitely long).

- Non-reflective boundary conditions at the *downstream* boundary

$$\begin{cases} V_r\left(r_i, x_{\mathrm{NX}-N_{bc}+n_g}\right) = V_r\big|_\infty \\ \rho\left(r_i, x_{\mathrm{NX}-N_{bc}+n_g}\right) = \exp\left(\dfrac{C^+ - C^-}{2a}\right) \\ V_x\left(r_i, x_{\mathrm{NX}-N_{bc}+n_g}\right) = C^+ + C^- \end{cases} \tag{3.41}$$

$$\text{with} \quad \begin{cases} C^+ = V_x\left(r_i, x_{\mathrm{NX}-N_{bc}+n_g-1}\right) + a\log\left(\rho\left(r_i, x_{\mathrm{NX}-N_{bc}+n_g-1}\right)\right) \\ C^- = V_x\big|_\infty - a\log\left(\rho\big|_\infty\right) \end{cases}$$

Figure 3.6 Characteristic boundary conditions: to the left is the upstream boundary and the right is the downstream boundary.

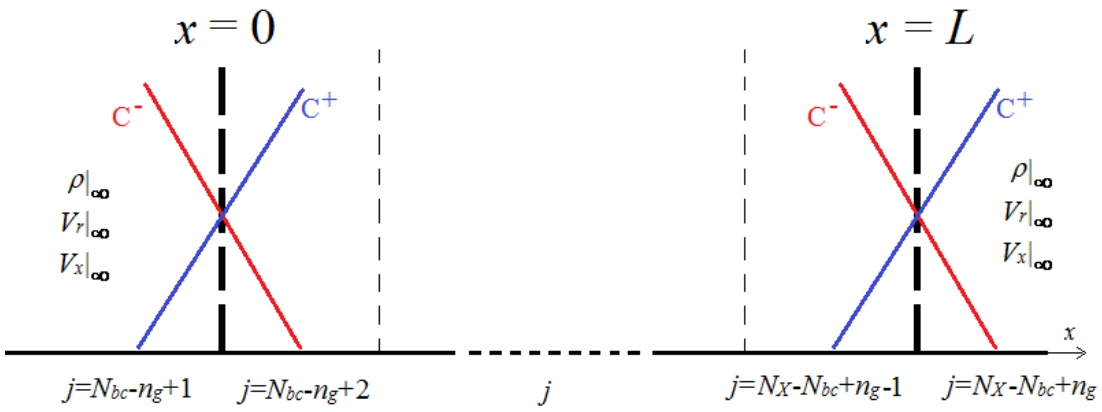

3.2.7.4. *Source boundary condition*

The test rig that will be used in this work is depicted in Figure 3.7, where a wave is generated from a source located at $x=L$ and only the left going waves are considered. The wave form at the source is given in Figure 3.8. This form is chosen because it is smooth and allows the modeller to select the desired frequency bandwidth (FBW). Its mathematical form is

$$\begin{cases} P_F(t) = P_s \exp\left(-4\frac{w_c^{\,2}}{\beta^2}\log(10)\left(t-\frac{\beta}{w_c}\right)^2\right)\sin\left(w_c\left(t-\frac{\beta}{w_c}\right)\right) \\ \text{where } \ 0 < t \le t_{wave} = \frac{\beta}{w_c} \end{cases} \qquad (3.42)$$

where $w_c = 2\pi f_c$ is the angular central frequency (in rad/s) with f_c the central frequency (in Hz); P_F is the pressure at the source; $P_s=0.1P_0$ is the maximum pressure induced by the wave at the source with P_0 the initial pressure in the pipe; t_{wave} is the duration of the wave

generated at the source; and β is a coefficient that controls the FBW and its effect is shown from Figures 3.8 and 3.9 which show the cases for $\beta = 16\pi$ and $\beta = 80\pi$, respectively. The source is considered to be circular in shape with a given diameter D_s and located at the pipe centreline (Figure 3.7). Initially at time t = 0s, the fluid is at rest. The boundary conditions at the source are given by

$$\begin{cases} V_r\left(r_i, x_{\mathrm{NX}-N_{bc}+n_g}\right) = 0 \\ P\left(r_i, x_{\mathrm{NX}-N_{bc}+n_g}\right) = P_0 + P_F \\ \left.\dfrac{\partial V_x}{\partial x}\right|_{x=L} = 0 \end{cases} \quad \text{for} \quad \begin{cases} 0 \le r \le \dfrac{D_s}{2} \\ 0 < t \le t_{wave} \end{cases} \qquad (3.43)$$

Figure 3.7 Sketch of unbounded pipe system

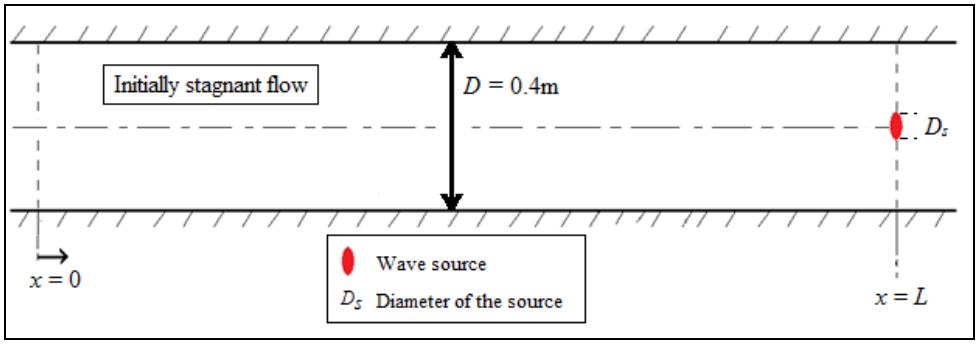

Figure 3.8 Probing wave from ($\beta = 16\pi$).

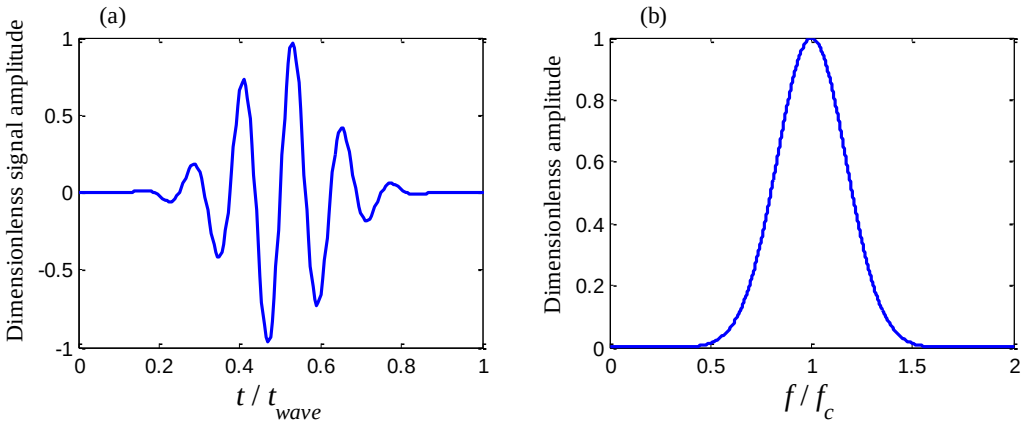

(a) Left Time domain

(b) Right Frequency domain

Figure 3.9 Probing wave from ($\beta = 80\pi$).

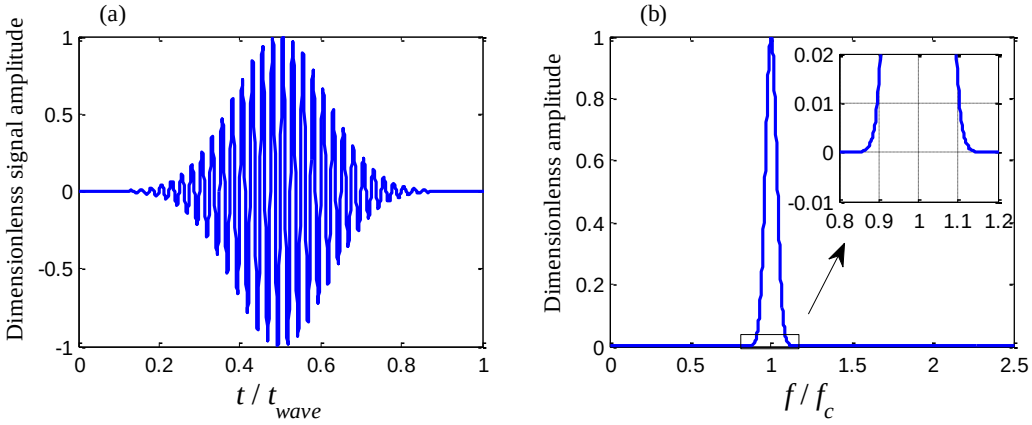

(a) Left Time domain

(b) Right Frequency domain

3.2.7.5. *Boundary conditions for Reservoir-pipe-valve system*

A reservoir-pipe-valve (RPV) system (Figure 3.10) is considered in Chapter 7 to study the generation of radial waves due to an ideal rapid valve closure. The boundary conditions for a reservoir located at the upstream boundary are given by

$$P\big|_{x=0} = P_{res} \;\; ; \;\; \left.\frac{\partial V_r}{\partial x}\right|_{x=0} = 0 \;\; ; \;\; \left.\frac{\partial V_x}{\partial x}\right|_{x=0} = 0 \qquad (3.44)$$

where P_{res} is the fixed pressure at the reservoir. The boundary conditions for a valve located at the downstream boundary are given by

$$\left.\frac{\partial P}{\partial x}\right|_{x=L} = 0 \;\; ; \;\; V_r\big|_{x=L} = 0 \;\; ; \;\; V_x\big|_{x=L} = 0 \qquad (3.45)$$

The RPV system is considered in Chapter 7 to study the special case of ideal suddend valve closure.

Notice that in this case, the third-fifth order WENO scheme (Section 3.2.3) achieves at most 3rd order accuracy. The robusteness and accuracy of this scheme for simulating sharp (non-smooth) waves are discussed in Section 3.3.3.

Figure 3.10 Characteristic boundary conditions

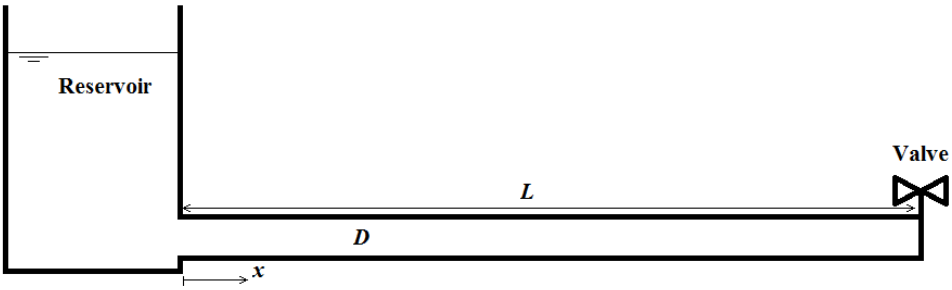

3.3. Study of the schemes features

In this section, the test cases consider the pipe setup in Figure 3.7 where the flow is initially at rest. A smooth transient wave is generated at the source ($x = L$) with waveform as shown in Figure 3.9. Only inviscid flow is considered to study solely the performance of Riemann solver schemes. In all test cases, the radial and axial step sizes are equal ($\Delta r = \Delta x$, where $\Delta r = R/\mathrm{NR}$; $\Delta x = L/\mathrm{NX}$; and $R = D/2$ and L are the pipe radius and length, respectively) to obtain the same dissipation along the different flow directions.

3.3.1. Stability and accuracy order of the scheme

Prior to using the developed schemes to conduct numerical experiments, it is imperative that their accuracy is tested using mesh refinement technique. The schemes showed stability for Courant-Friedrich-Lewy (CFL) number at about 0.1 to 0.3. For consistency in this work, CFL= $a\Delta t/\Delta x$ =0.1 is used for all test cases. The L^2 and L^1 norms (e.g. [14], [110]) are used to compute the accuracy of the scheme. The results are summarized in Tables 3.1, 3.2 and 3.3 for the second, third and fifth order schemes, respectively. Tables 3.1, 3.2 and 3.3 show that the orders of accuracy of these three schemes are about 1.8, 2.9 and 4.5, respectively. The procedure of computing the order of accuracy is as follows

$$\mathrm{Order} = \frac{\log\left(\chi/\chi_{ref}\right)}{\log\left(NR_{ref}/NR\right)} \quad ; \quad \chi = \{\mathrm{L1}, \mathrm{L2}\} \tag{3.46}$$

with

$$\begin{cases} \mathrm{L}^1 = \sum_{N_t} \left| P - P_{exact} \right| \\ \mathrm{L}^2 = \sqrt{\sum_{N_t} \left(P - P_{exact} \right)^2} \end{cases} \tag{3.47}$$

where the subscript "ref" and "exact" refer respectively for reference and exact case which are shown in Tables 3.1, 3.2 and 3.3.

Table 3.1. Mesh refinement convergence tests for the second order scheme (f_c=1000Hz)

#	Order (L^2 norm)	Order (L^1 norm)
N_R =5	- Ref. -	- Ref. -
N_R =10	1.2016	1.1663
N_R =20	1.3529	1.3813
N_R =30	1.5010	1.5307
N_R =40	1.7836	1.8050
N_R =50	exact	exact

Table 3.2. Mesh refinement convergence tests for 3rd order scheme (f_c=500Hz)

#	Order (L^2 norm)	Order (L^1 norm)
N_R =3	1.9438	1.9369
N_R =5	2.0686	2.0395
N_R =10	2.3198	2.2771
N_R =15	2.5913	2.5605
N_R =20	2.9467	2.9284
N_R =30	- Ref -	- Ref -
N_R =40	exact	exact

Table 3.3. Mesh refinement convergence tests for 5th order scheme (f_c=1000Hz)

#	Order (L^2 norm)	Order (L^1 norm)
N_R =25	- Ref. -	- Ref. -
N_R =50	2.9599	3.3352
N_R =100	5.5955	5.8355
N_R =200	4.5717	4.8484
N_R =400	exact	exact

A different approach based on computing the energy flux instead of the L^1 and L^2 norms could be used to determine the order of accuracy of a given scheme. For this purpose, the dissipation rate is defined by the rate of decay of the energy flux (see Eq. (2.137)) measured at 10m away from the source location. The period over which the energy flux is integrated is chosen such that the total injected energy passes through the cross sectional area at 10m away from the source. The dissipation rate is defined as follow

$$\%\text{Dissipation per 10m} = \left[1 - \frac{E_F\left(x = L - 10m\right)}{E_F\left(x = L\right)}\right] \times 100 \qquad (3.48)$$

Using the Dissipation rate defined in Eq. (3.48) as the norm χ in Eq. (3.46), the accuracy of the second, third and fifth order schemes given in Tables 3.4, 3.5 and 3.6 show that the order of these schemes are 1.84, 2.9 and 4.8, respectively, which is consistent with the results from L^1 and L^2 norms.

Table 3.4. Mesh refinement convergence tests for the second order scheme based on energy flux (f_c=1000Hz).

#	Order ($\chi \equiv E_F$)
N_R =5	- Ref. -
N_R =10	1.0126
N_R =20	1.5730
N_R =30	1.7741
N_R =40	1.8284
N_R =50	1.8484

Table 3.5. Mesh refinement convergence tests for 3rd order scheme based on energy flux (f_c=1000Hz).

#	Order ($\chi \equiv E_F$)
N_R =5	- Ref. -
N_R =10	2.4007
N_R =15	2.8725
N_R =20	2.9305

Table 3.6. Mesh refinement convergence tests for 5th order scheme based on energy flux (f_c=4000Hz).

#	Order ($\chi \equiv E_F$)
N_R =10	- Ref. -
N_R =20	4.4993
N_R =30	4.8227

3.3.2. Dissipation and computational time

In this section the dissipation rate is defined as given in Eq. (3.48). It is observed that for energy dissipation below 2%, the measured pressure decay at a given location becomes very low. Therefore, 2% energy dissipation is set as a minimum convergence target for the different schemes.

The computational (CPU) time is computed based on a non-parallel and non-optimized algorithm. For consistency, all test cases are run under the same algorithm structure. Therefore the CPU time computed here is for worse scenario and could be improved using optimized/parallelized algorithm structures. In this study, the CPU time unit is chosen to be in minutes (min).

Figure 3.11 compares the dissipation rate and the CPU time variation with N_R between the second and third order schemes for the case of f_c=500Hz. Figure 3.11a shows that the rate of dissipation is almost similar for these two schemes at frequencies within 500Hz. For N_R=10 and N_R =15, the dissipation rate of the third order scheme is slightly less than the second order, but both are less than 2%. However, Figure 3.11b shows that the CPU time is twice higher for the third order scheme than for the second order scheme. This makes the second order scheme more efficient for simulating very low frequency (f < 500Hz) waves.

Figure 3.11 Comparison of the dissipation rate and the CPU time between the second and third order schemes for the case of f_c=500Hz

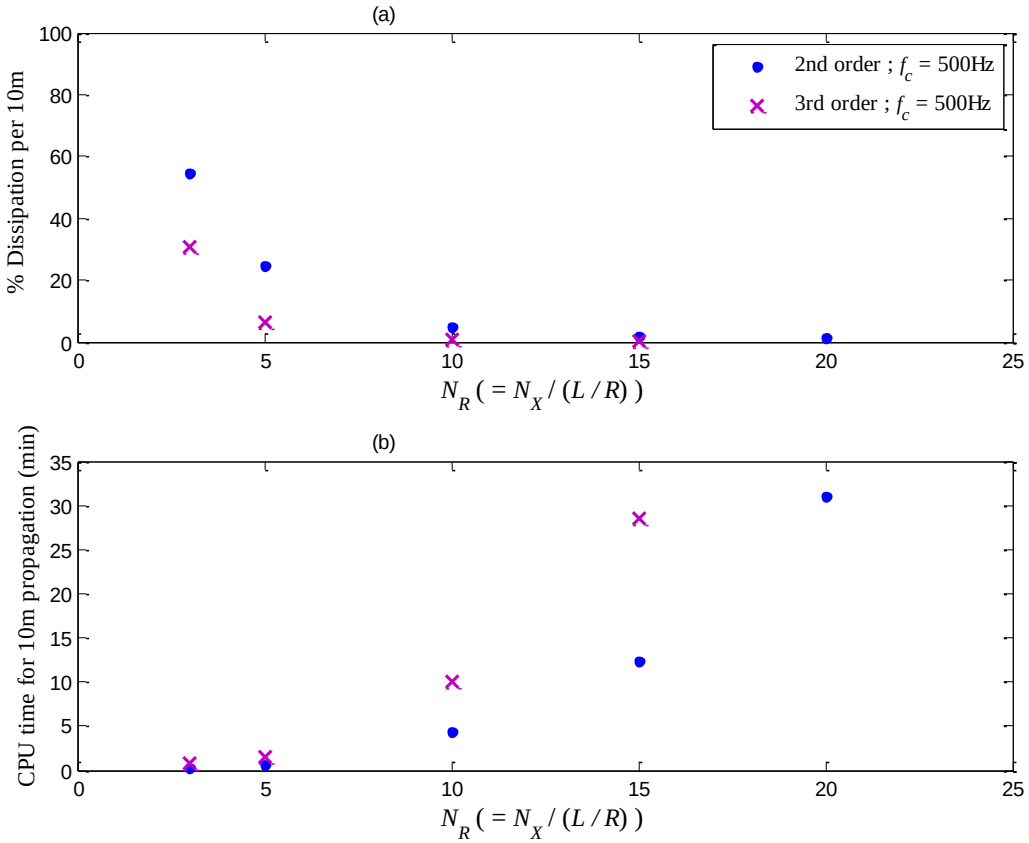

(a) Top Dissipation rate

(b) Bottom CPU time

Figure 3.12 compares the dissipation rate and the CPU time variation with N_R between the second, third and fifth order schemes for the case of f_c=1000Hz. Figure 3.12a shows that the second, third and fifth order schemes achieve dissipation rate less than 2% for $N_R = 40$, $N_R = 20$ and $N_R = 5$, respectively. In comparison with f_c=500Hz case (Figure 3.11), Figure 3.12b shows that the third order scheme becomes much more efficient than the second order scheme for simulating waves at frequencies within 1kHz. Figure 3.12 shows that, for f_c=1000Hz, the fifth order scheme gives slightly better efficiency in comparison to the third order scheme. On the other hand, Figure 3.13 gives the case for higher frequency where f_c=4000Hz and shows that the efficiency of fifth order scheme increases whereas the second and third order schemes become computationally no longer practical. In fact, Figure 3.13 shows that the fifth order scheme converges to 2% dissipation for NR=20, while the third order scheme converges to 50% for five times higher CPU time (Figure 3.13b) at $N_R = 40$; and the second order scheme has even much lower efficiency than the third order. This shows that the second and third order schemes becomes computationally very expensive and unsuitable for simulating wave propagation at frequencies higher than 1 kHz.

Figures 3.11, 3.12 and 3.13 illustrate the need for higher order schemes as the wave frequency increases. It is therefore very important to know which most efficient order of accuracy required for simulating wave propagation at a given frequency. The rest of this section determines an empirical equation that gives an "approximate" most efficient order of accuracy for a given frequency and desired CPU time based on the current RS (Riemann solver) schemes.

Figure 3.12 Comparison of the dissipation rate and the CPU time between the second, third and fifth order schemes for the case of f_c=1000Hz

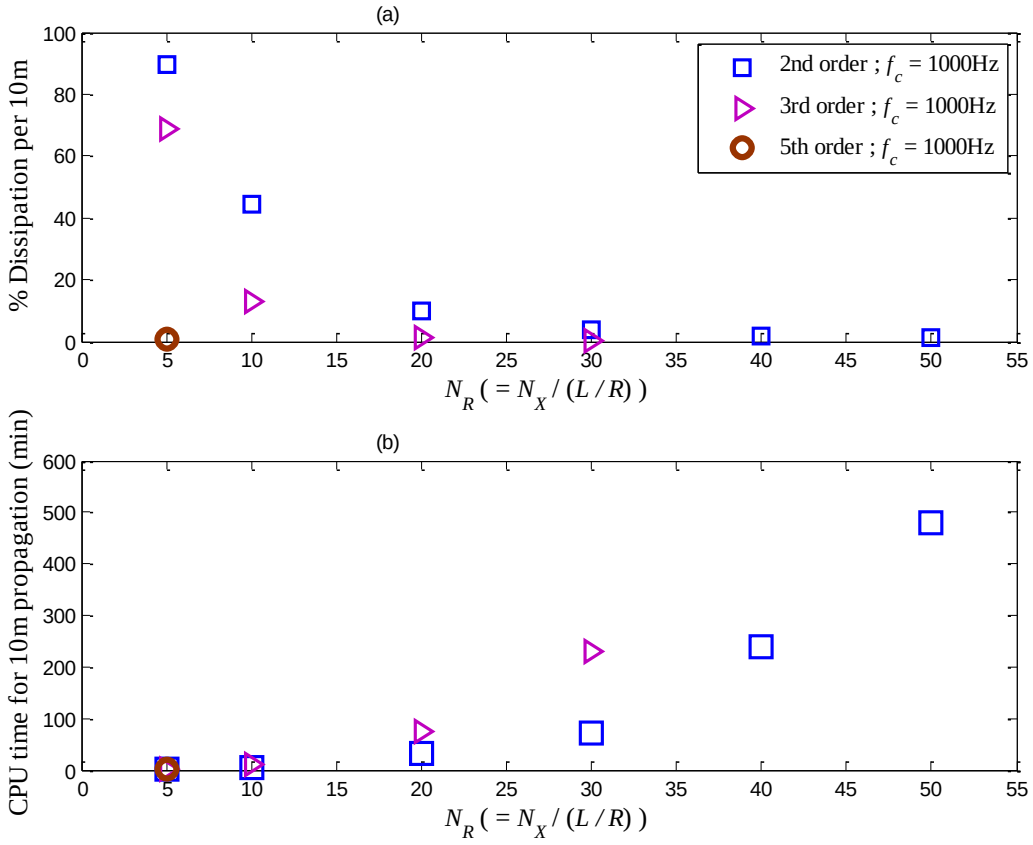

(a) Top **Dissipation rate**

(b) Bottom **CPU time**

Figure 3.13 Comparison of the dissipation rate and the CPU time between the second, third and fifth order schemes for the case of f_c=4000Hz

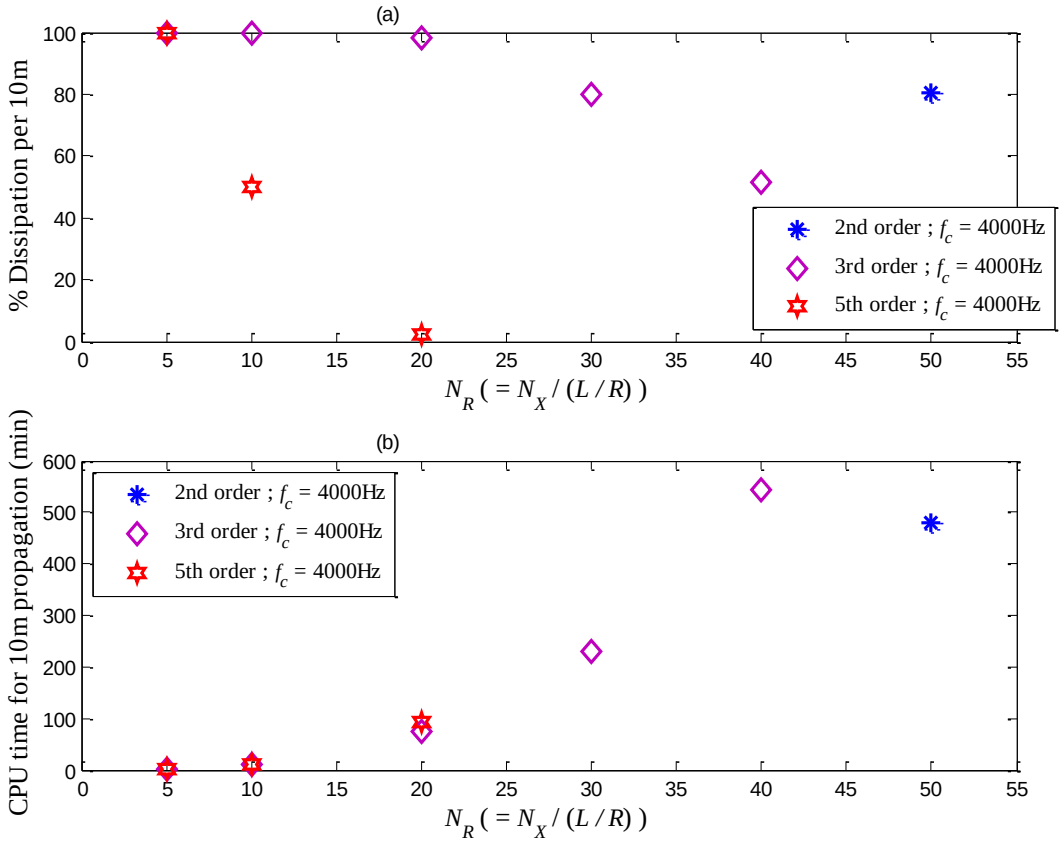

(a) Top Dissipation rate

(b) Bottom CPU time

3.3.2.1. "Approximate" most efficient order of accuracy

Denoting by N_S the number of discretized FV per central wavelength (a/f_c) which is given as follows

$$N_S = \frac{a}{f_c \Delta r} = \frac{a}{f_c}\frac{N_R}{R} = \frac{a}{f_c}\frac{N_X}{L} \qquad (3.49)$$

Figure 3.14 Comparison of the dissipation rate with change of number of discretized FV per wavelength between the second, third and fifth order schemes.

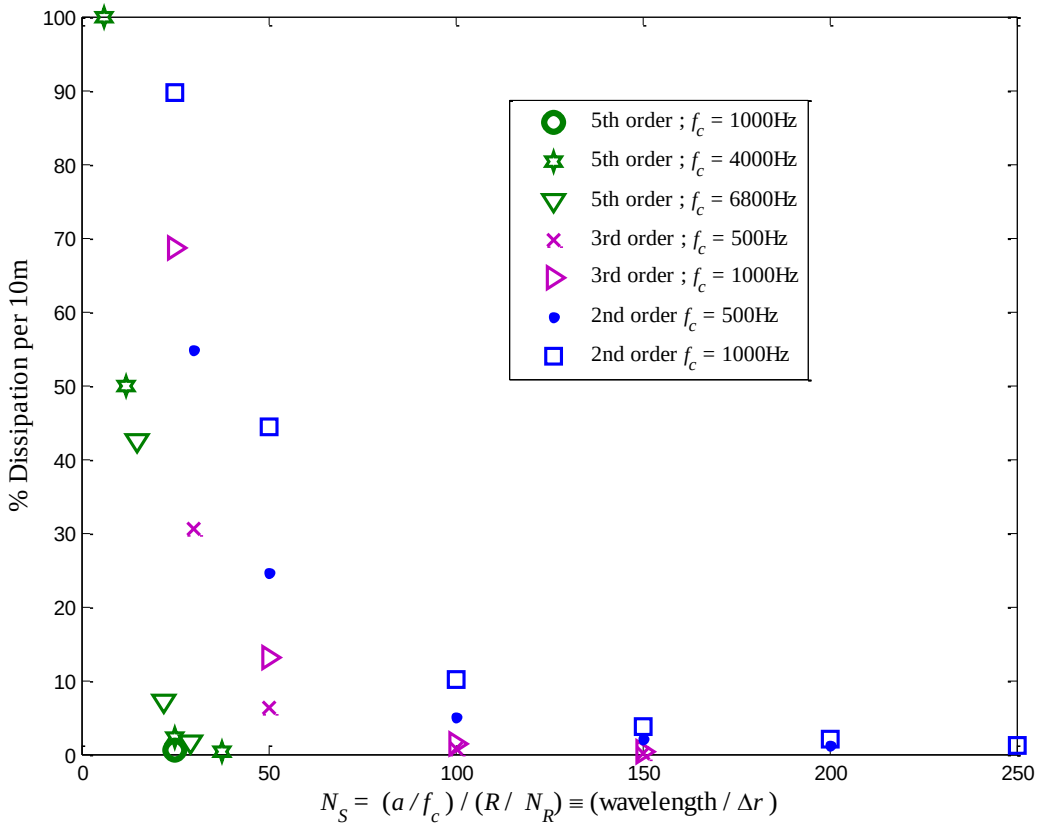

Figure 3.14 compares the dissipation rate with respect to NS between the second, third and fifth order schemes for different central frequencies (f_c). Figure 3.14 shows that each scheme converges for specific N_S value for different frequencies. For example, the second, third and fifth order schemes converges respectively for an averaged N_S^b close to $N_S^2 = 250$, $N_S^3 = 130$ and $N_S^5 = 25$ where the superscript "b" denotes the scheme order. Throughout different numerical tests and fitting, it is found that the following empirical equation holds

$$\frac{N_S^{b_0}}{N_S^b} = \left(\frac{b}{b_0}\right)^{\left(\frac{b}{b_0}\right)} \qquad (3.50)$$

where b_0 is a reference scheme order of accuracy. For example, if $b_0 = 2$ and $b = 5$, Eq. (3.49) gives $N_S^2 / N_S^5 \approx 10$ which is close to the N_S ratio (~250/25) between the fifth and second order schemes observed in Figure 3.14.

Moreover at convergence (Dissipation rate <2%), Eq. (3.49) gives

$$N_R^b = N_S^b \frac{R}{a} f_c \tag{3.51}$$

where N_R^b is the N_R used for the scheme of order b at convergence. On the other hand, the CPU time variation with N_R for different schemes is fitted exponentilally as follows

$$\mathrm{T}_b^{\mathrm{CPU}} = \Gamma_b \exp\left(\bar{\tau}_b \, N_R\right) \tag{3.52}$$

where $\mathrm{T}_b^{\mathrm{CPU}}$ is the fitted CPU time function for a given scheme of order b; Γ_b is a constant defining the CPU time at very low N_R; and $\bar{\tau}_b$ is the rate at which the CPU time increases. At convergence, Eq. (3.52) gives

$$N_R^b = \frac{1}{\bar{\tau}_b} \log\left(\frac{\mathrm{T}_b^{CPU}}{\Gamma_b}\right). \tag{3.53}$$

Combining Eq. (3.51) and Eq. (3.53), yields

$$N_S^b = \frac{a}{R} \frac{1}{\bar{\tau}_b f_c} \log\left(\frac{\mathrm{T}_b^{CPU}}{\Gamma_b}\right). \tag{3.54}$$

Inserting Eq. (3.54) into Eq. (3.50), yields

$$\left(\frac{b}{b_0}\right)^{\left(\frac{b}{b_0}\right)} = \frac{N_S^{b_0}}{\log\left(\frac{\mathrm{T}_b^{CPU}}{\Gamma_b}\right)} \frac{R}{a} \bar{\tau}_b f_c. \tag{3.55}$$

It is found that the rate τ_b is relatively similar for the three different schemes which is about 0.084, 0.089 and 0.092 for the second, third and fifth order schemes, respectively. For the purpose of approximation, τ_b is assumed to be fixed at 0.1. Moreover, for simplicity, Γ_b is also fixed to an average value of 1 min per 10m wave propagation for all schemes when using very small N_R, and that Γ_b increases linearly with the propagation length. For example, for 20m propagation, Γ_b becomes 2min, etc. Choosing the second order as reference scheme order ($b_0 = 2$) and assuming that N_S^2 is known, Eq. (3.55) for 10m wave propagation becomes

$$\left(\frac{b}{2}\right)^{\left(\frac{b}{2}\right)} - \frac{N_S^2}{\log\left(\mathrm{T}_b^{\mathrm{CPU}}\right)} \frac{R}{a} \tau_b f_c = 0 \qquad (3.56)$$

Applying Eq. (3.56) for the case of R = 0.2m, a = 1000m/s, N_S^2 = 250 and desiring $\mathrm{T}_b^{\mathrm{CPU}}$ to be 15 min, the variation of the scheme order with f_c could be obtained as shown in Figure 3.15. Figure 3.15 shows that for frequency ranging from 5kHz to 100kHz, the required order of accuracy increases from 5 to 8.

Figure 3.15 Approximated most efficient order of accuracy (Eq. (3.56)) variation with the central frequency (f_c).

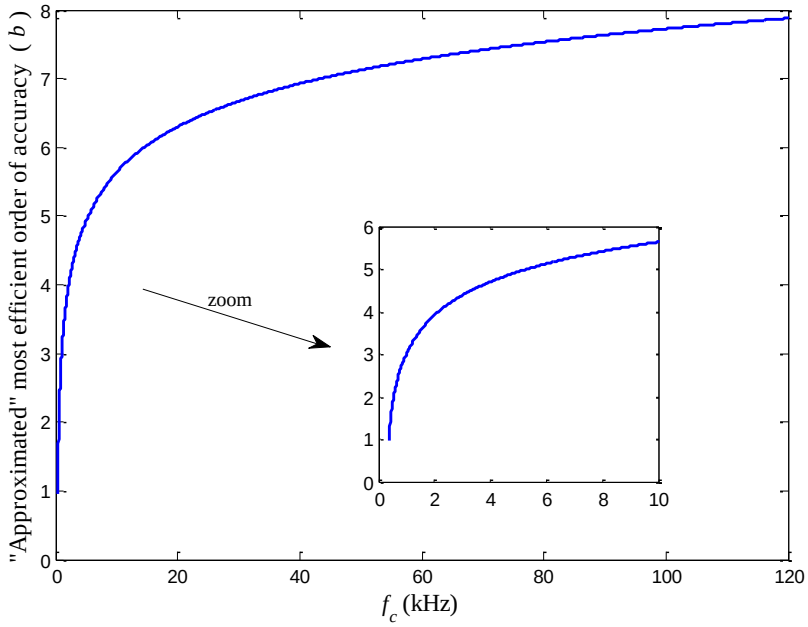

3.3.3. Numerical dispersion (classical WH test case)

The schemes developed in this work are used in Chapter 7 to study the behaviour of high frequency (dispersive) waves in water-filled pipe system. Throughout different test cases and results in Chapter 7, it is shown that the proposed schemes have little numerical dispersion when modelling smooth HFW (see Eq. (3.42)) since they were able to capture the physical dispersive characteristics of HFW (see Chapter 7). This section investigates the robustness of the proposed scheme in simulating sharp (non-smooth) waves.

The test case for non-smooth wave consists of a rapid valve closure in a RPV system (see Section 3.2.7.5) with initial flow. This is a typical test case for water-hammer application ([137]). Inviscid and viscous-laminar flows are considered. The initial conditions for the inviscid flow case are uniform radial velocity distribution and constant initial pressure along the pipe given as follows

$$\begin{cases} V_x(r) = V_x^0 = \dfrac{\nu \mathrm{R_e}}{D} & 0 \le r \le R \\ P(x) = P_0 = \rho_0 g H_0 & 0 \le x \le L \end{cases} \qquad (3.57)$$

where ν = kinematic viscosity in water ($\nu \approx 10^{-6}$ m^2/s); $\mathrm{R_e}$ = Reynolds number (fixed at $\mathrm{R_e} = 500$); D = pipe diameter ($D = 0.4$ m); V_x^0 = constant initial velocity; ρ_0 = initial density ($\rho_0 = 1000$ kg/m^3); H_0 = initial pressure head ($H_0 = 10$ m); P_0 = constant initial gauge pressure in the pipe. The viscous-laminar flow case is a Poiseuille flow with details as follows

$$\begin{cases} V_x(r) = 2V_x^0\left(1 - \dfrac{r^2}{R^2}\right) & 0 \le r \le R \\ P(x) = P_0 - \dfrac{8\rho_0 V_x^0 \nu}{R^2} x & 0 \le x \le L \end{cases} \qquad (3.58)$$

For both cases, the length of the pipe is chosen to be L = 10m. For the case of inviscid flow, the method of characteristics (MOC) gives an exact solution for a sudden valve closure in a RPV system. Figure 3.16 gives the dimensionless pressure variation with time measured at the valve where the pressure magnitude is normalized by the Joukowsky pressure ($P_{\mathrm{Jou}} = \rho_0 V_x^0 a$). The exact solution is compared with the results from the 2$^{\mathrm{nd}}$ order MUSCL-Hancock and the 5$^{\mathrm{th}}$ order WENO schemes in Figures 3.16a and 3.16b, respectively. The results show that both schemes give accurate results except that the 5$^{\mathrm{th}}$ order WENO scheme induces localized spurious oscillations near severe pressure jumps (Figures 3.16b).

Figure 3.16 Dimensionless pressure variation with time for the case of inviscid flow. A comparison between 2nd and 5th order schemes.

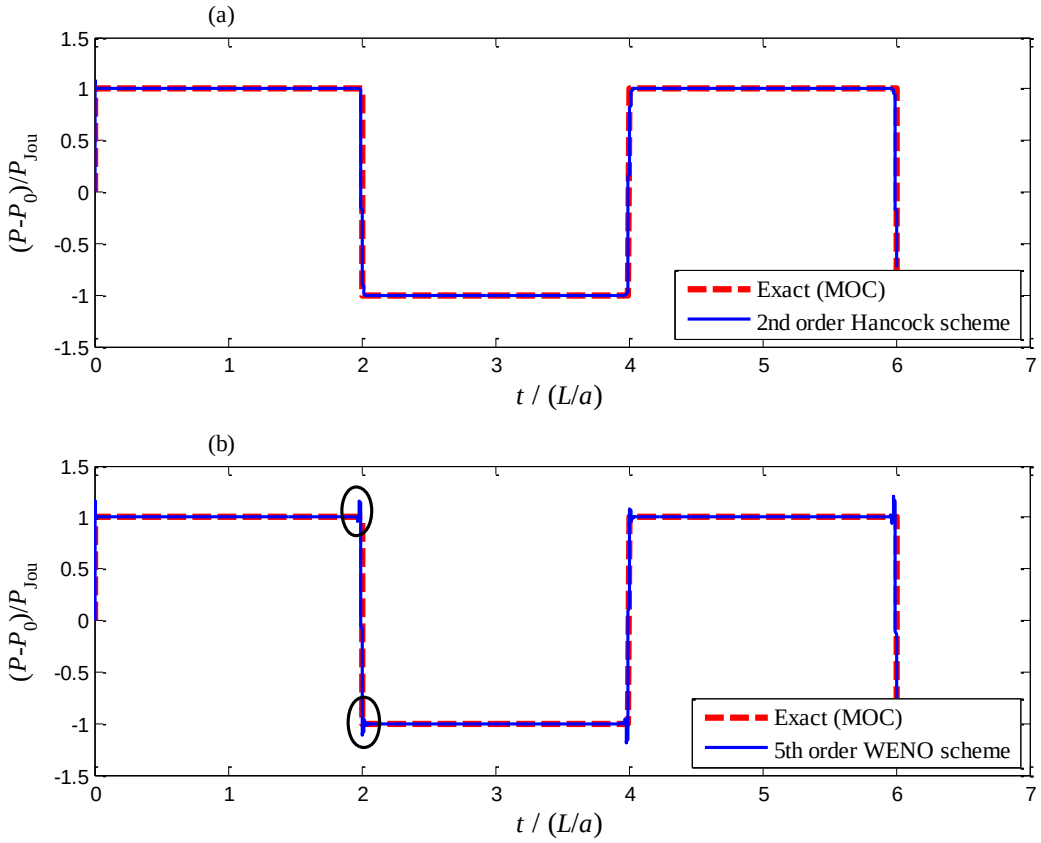

(a) Top **2nd order MUSCL-Hancock scheme**

(b) Bottom **5th order WENO scheme**

Figures 3.17a and 3.17b gives the dimensionless pressure variation with time for the case of viscous-Poiseuille flow using the 2nd order MUSCL-Hancock and the 5th order WENO schemes, respectively. In this case, radial waves are excited at the valve and therefore the oscillations observed in Figures 3.17 should not be thought of as spurious oscillations. The fact that the increase in pressure at the valve is twice as large as the Joukowsky pressure is because the maximum velocity at the centerline is twice the average velocity for a steady state pipe Poiseuille flow (Eq. (3.58)). These radial waves will be discussed later in

Chapter 7. The 2nd order MUSCL-Hancock and the 5th order WENO schemes are compared in Figures 3.18 and the results show that both schemes agree well except at the sudden jump where local pre/post-jump spurious oscillations are generated by the 5th order WENO scheme. These spurious oscillations are small and they are eliminated if the jump (i.e. valve closure) is slightly less severe. In fact, Figure 3.19 gives the case of linear valve closure with time closure $t_{closure} = 1/a = 10^{-3}$ (s) and shows that the spurious oscillations are no longer generated although the time closure is vary small.

Figure 3.17 Dimensionless pressure variation with time for the case of viscous. A comparison between 2nd and 5th order schemes.

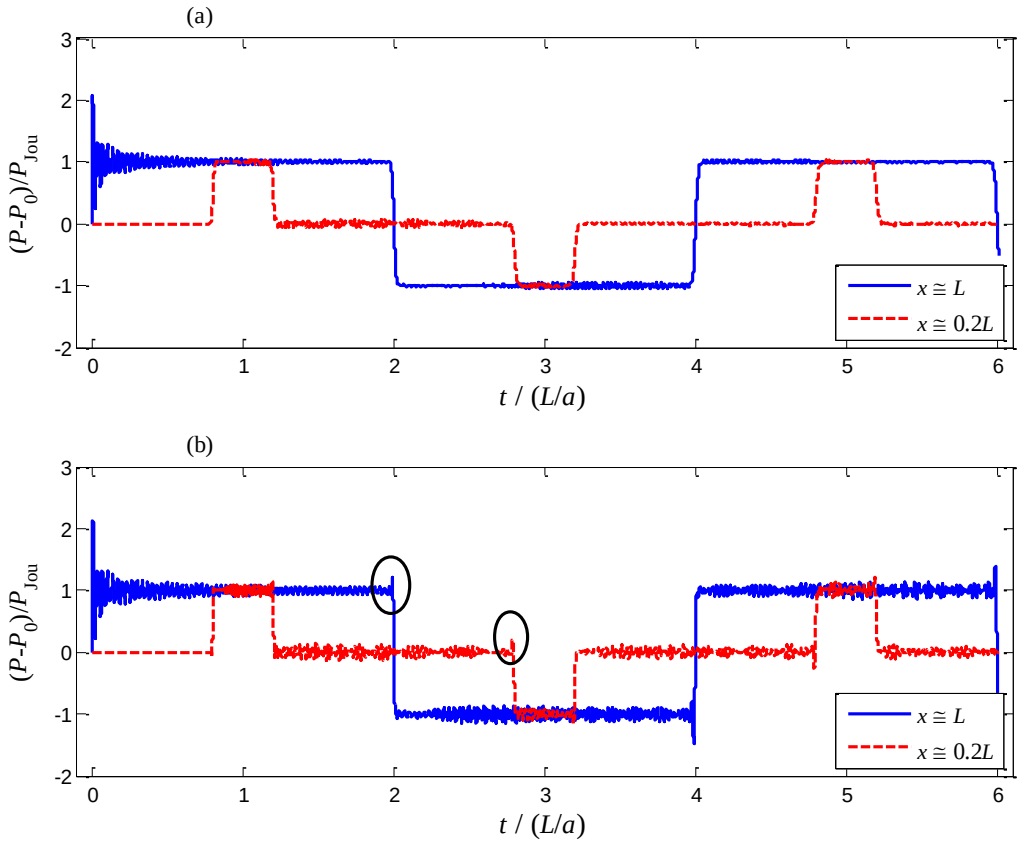

(a) Top **2nd order MUSCL-Hancock scheme**

(b) Bottom **5th order WENO scheme**

In conclusion, the WENO scheme is quite robust for modelling both smooth and non-smooth flows. It is more efficient than the 2nd order MUSCL-Hancock scheme because it requires much less computational time. Indeed for this test case, the 5th order WENO scheme uses a mesh with N_R =10 and N_X=500 while the 2nd order MUSCL-Hancock scheme uses N_R=50 and N_X=2500, and yet the 2nd order scheme has much more dissipation as shown in Figures 3.17a where the radial waves after $t = 4L/a$ become undetectable.

Figure 3.18 Enlarged figure of dimensionless pressure variation with time for the case of *viscous* flow. A comparison between 2nd and 5th order schemes. (at the pipe centreline)

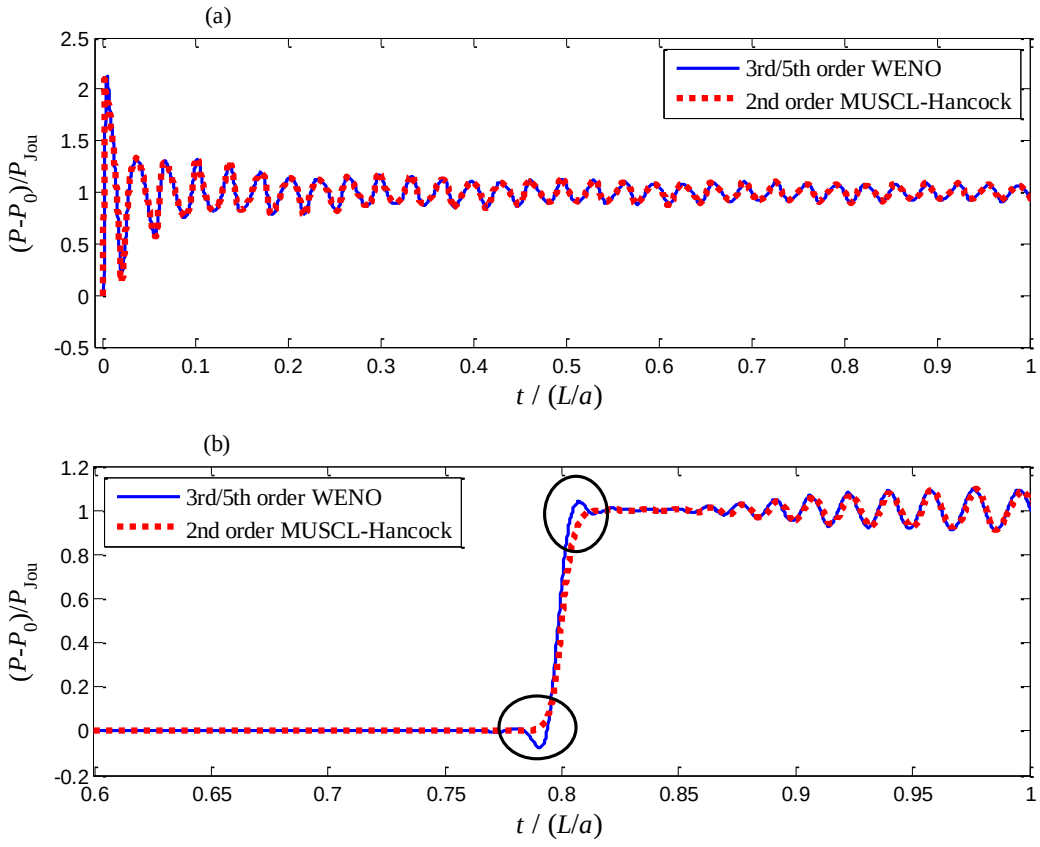

(a) Top **At $x = L$ (at the valve)**

(b) Bottom **At $r = 0.2L$**

Figure 3.19 Dimensionless pressure variation with time for the case of linear valve closure using the 5th order WENO schemes.

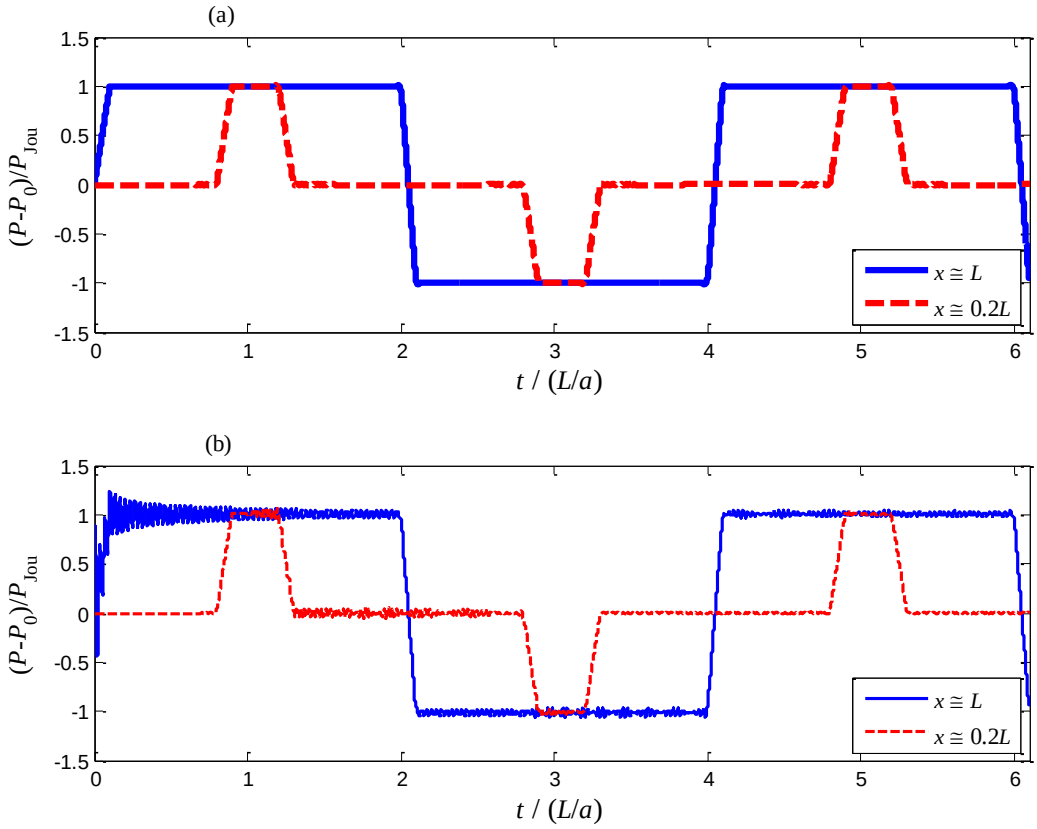

(a) Top **Inviscid flow**

(b) Bottom **Viscous flow**

3.3.4. Numerical reflections at the boundaries

In Chapter 7, the behaviour of high frequency waves is investigated where non-reflective boundary are used to model infinite pipe length. The characteristic boundary condition (CBC) ([19], [107], and [58]) is used to model the non-reflective boundary condition. Numerical reflections are difficult to eliminate and they depend severely on the propagation angle of the wave ([52]). As discussed in Chapter 2 (Section 2.6.4), waves at high modes propagate at

different angles and these angles vary with frequency (see Figure 2.13). This section studies the performance of CBC for high frequency wave's simulation. The numerical reflections are studied in terms of energy using the fifth order scheme. Denote by E_T the total injected wave, E_n the energy content in a given mode *n* and E_n^r the reflected energy from a given mode *n*. The energy quantities are computed using the numerical data and the energy equation derived in Chapter 2 section 2.5. The plane mode reflections are studied by considering a source diameter (see Figure 3.7) $D_s = D$ such that no radial modes are generated. This case is referred as case 0. When studying the high mode cases, the source diameter is $D_s = 0.2D$. The frequency ranges used are [0.9 f_c to 1.1 f_c] where f_c=3720Hz and f_c=6800Hz cases are used. The f_c=3720Hz case excites only the plane mode M0 and the first high mode M1. This case is referred as case 1. The f_c=6800Hz case excites M0, M1 and the second high mode M2. This case is referred as case 2. The numerical reflections in different cases are shown in Figures 3.20 and 3.21.

Figure 3.20 Pressure measurement with time at the pipe centreline showing the M0 and M1 numerical reflection from CBC for the case of f_c = 3715Hz.

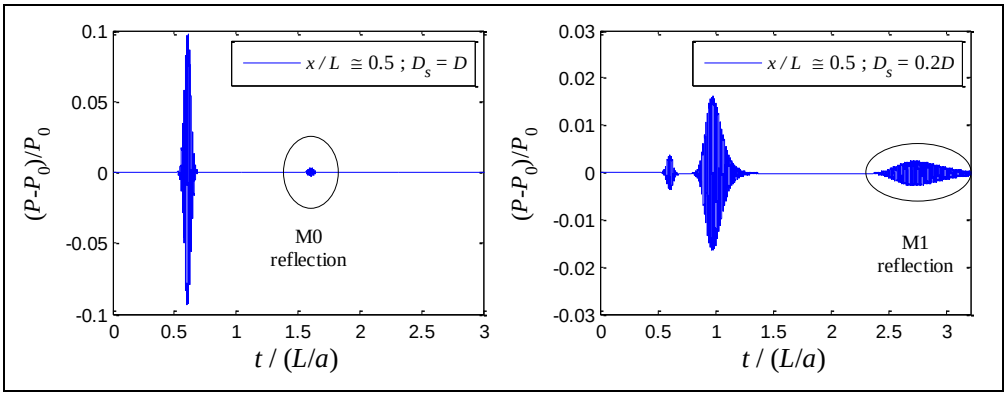

(a) Left $D_s = D$

(b) Right $D_s = 0.2D$

Figure 3.21 Pressure measurement with time at the pipe centreline showing the M0, M1 and M2 numerical reflection from CBC for the case of f_c = 6800Hz.

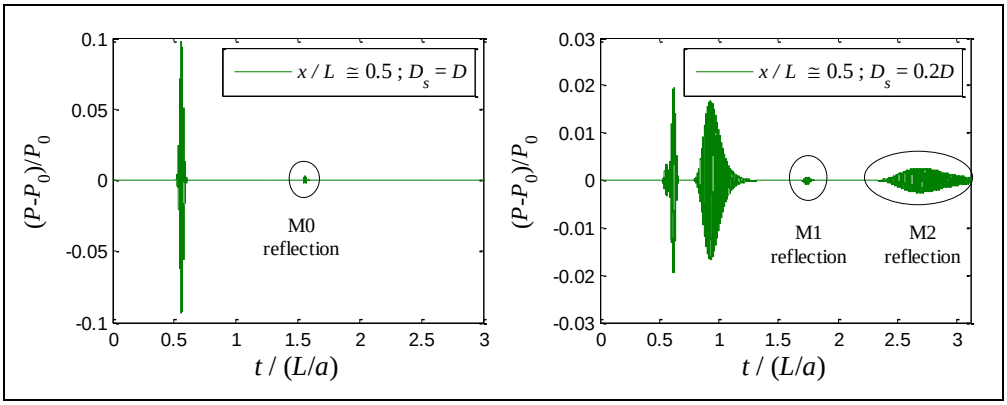

(a) Left $D_s = D$

(b) Right $D_s = 0.2D$

Table 3.7 gives the energy reflection for case 0 for the two different central frequencies (f_c=3720Hz and f_c=6800Hz). For case 0, the propagation angle is zero, and therefore, the difference in the reflected energy is only due to the change in frequency. Table 3.7 shows that numerical refection decreases as the frequency increases. Such feature is usually observed in other acoustic applications ([107], [52]). For case 0, the ratio between the energy reflections for f_c=3720Hz and f_c=6800Hz is about 1.56. Such ratio is set as reference of change in energy reflection due solely to change in frequency.

Table 3.8 gives the energy reflection for case 1 and case 2. Table 3.8 shows that the M1 energy reflection is much higher for case 1 (f_c=3720Hz) than for case 2 (f_c=6800Hz). The ratio between the M1 energy reflections in case 1 and 2 is about 26. Although the frequency is higher for case 2, the reflection ratio is too large (26 >> 1.56) to be only due to frequency change. Such huge difference is, in fact, due to the change in propagation angle. As seen from Table 3.8, the M1 propagation angle for case 1 is twice higher than for the case 2. This illustrates that variation in the propagation angle affect severely the numerical reflection. Such effect is also observed in other acoustic application using CBC and other non-reflective boundary condition methods ([107], [52]).

From Table 3.8, the range of propagation angle is the same for M2 in case 2 and M1 in case 1. Therefore, their energy reflection could be compared based on the change in frequency and mode number only. Table 3.8 shows that the ratio of energy reflection between M1 and M2 is about 1.4 (< 1.56) which is only slightly lower than the energy reflection ratio due solely to change in frequency. This shows that high modes have almost similar reflection rates at the same propagation angle. The slight difference in reflection ratio between M1 and M2 could be due to the radial wave form of high modes (see Chapter 7).

In all the test cases investigating the behaviour of high frequency waves in unbounded pipe system, the pipe length is chosen such that the numerical reflections do not affect the domain of study.

Table 3.7. Case 0: Plane mode wave reflection ($D_s = D$)

Mode	Frequency range	Angle range (in degrees)	$\frac{E_0^r}{E_T}$
M0	[3350 4100] f_c=3720Hz	0	0.089%
M0	[6120 7480] f_c=6800Hz	0	0.057%

Table 3.8. M1 and M2 wave reflection (D_s = 0.2D)

Case #	Mode	Frequency range (in Hz)	Angle range (in degrees)	$\frac{E_n^r}{E_n}$
1	M1	[3350 to 4100] f_c = 3715	[48 to 65] $\theta_{k1}(f_c)$ = 55	10.57%
2	M1	[6120 to 7480] f_c = 6800	[24 to 30] $\theta_{k1}(f_c)$ = 26.6	0.3%
2	M2	[6120 to 7480] f_c = 6800	[48 to 65] $\theta_{k2}(f_c)$ = 55	7.54%

3.3.5. WENO "calibration" parameter

In the WENO reconstruction procedure (see Section 3.2.3), a calibration parameter (ε) (Eq. (3.26)) is introduced in the weighting functions to avoid singularities. This section studies the effect of ε on the numerical results. Figure 3.22 gives the pressure variation with time for different ε values. Figure 3.22a shows that for $\varepsilon = 10^{-10}$ the signal has spurious oscillations. However, for $\varepsilon = 10^{-6}$ (Figure 3.22b), the spurious oscillations are eliminated. When ε is further decreased to 10^{-5} (Figure 3.22c), the numerical reflection is reduced and gets almost eliminated at $\varepsilon = 10^{-4}$ (Figure 3.22d). However, when comparing the case of $\varepsilon = 10^{-4}$ (Figure 3.22d) and $\varepsilon = 10^{-6}$ (Figure 3.22b), it is found that the pressure amplitude is slightly reduced for $\varepsilon = 10^{-4}$ case. It is therefore assumed that the nearly elimination of the M0 reflection is probably due to slightly extra numerical dissipation as ε get reduced. In this work, $\varepsilon = 10^{-6}$ is used.

Figure 3.22 Pressure variation with time at the pipe centreline for different ε values (fifth order scheme; f_c = 1000Hz; D_s=D).

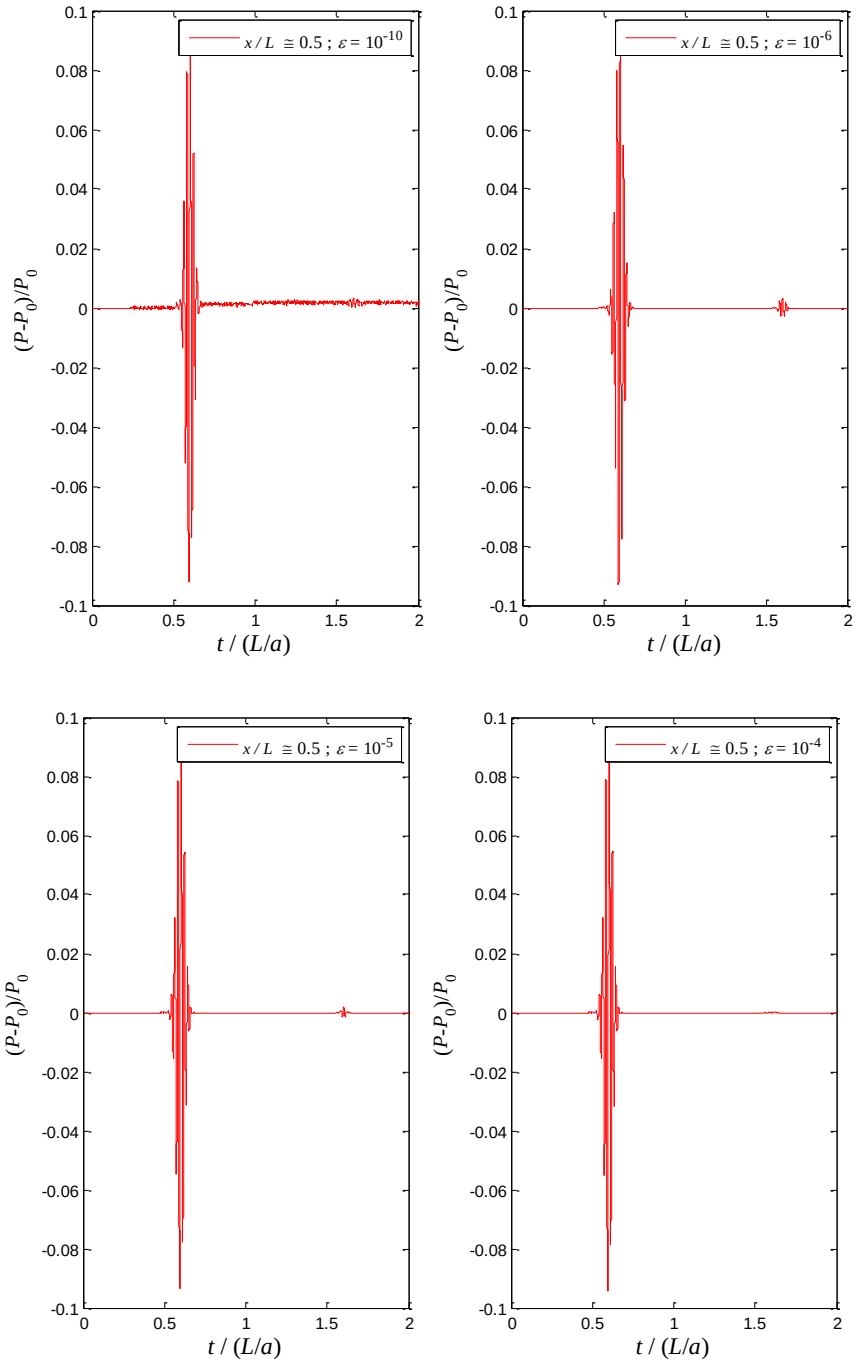

(a) Top Left $\varepsilon = 10^{-10}$

(b) Top Right $\varepsilon = 10^{-6}$

(c) Bottom Left $\varepsilon = 10^{-5}$

(d) Bottom Right $\varepsilon = 10^{-4}$

3.4. Summary

This chapter gives details of the 2D RS-based FV numerical scheme developed and used in this work. Its robustness and accuracy are tested for modelling dispersive high frequency waves in pipe flows. This chapter also gives details of the boundary conditions and test cases setups used. The 5^{th} order scheme for smooth waves is used in Chapter 7 to study the behaviour of HFW.

CHAPTER 4

WAVE SCATTERING IN UNBOUNDED PIPE SYSTEM

4.1. Introduction

Previous research showed that variation in the cross sectional area of a pipe induces a shift in the eigenfrequencies (natural resonant frequencies) with respect to the intact pipe case (e.g., [32], [106], [28], [27], [41], [117], [56], [89], and [112]). Such eigenfrequency shift is used as key input information for TBDDM ([32], [35], [106], [89], and [112]). These methods are still limited in terms of accuracy, convergence rate and pipe system complexity. One way to improve these methods is to understand the wave-blockage interaction mechanism causing the shift in eigenfrequencies. In this chapter, analytical and numerical methods are used to study the processes of transmission and reflection of a pressure wave in a one dimensional unbounded pipe system with non-uniformities in the cross sectional area. This choice allows (i) the examination of the direct interaction between waves and blockage without interference from other effects and (ii) to establish the existence of frequency bands where the signal reflection is enhanced (*i.e.*, Bragg-type reflection or resonance) and others bands where total transmission is possible. Knowledge of which waves transmit and which do not, provides information on the coupling mechanism between the upstream and downstream regions of the blockage as well as the design of probing signals in TBDDM.

4.2. Bragg-type resonance effect in unbounded pipe system

Prior to embarking on the analytical and numerical details, it is instructive to gain an appreciation of the complex interaction between waves and conduit non-uniformities. Consider a wave train generated by a sensor, a hydraulic device, or a transmitter of an acoustic communication system which propagates toward the conduit non-uniformity. Suppose that this incident wave train has a wave-number, *k*, and an angular frequency, *w*, and of the form exp(*ikx*-*iwt*) with $i=\sqrt{-1}$. When this wave arrives to the non-uniformity in conduit's area, it is reflected and transmitted so that the wave field within the non-uniform region of the conduit is $p^{ref}\exp(ikx\text{-}iwt) + p^{tr}\exp(\text{-}ikx\text{-}iwt)$, where p^{ref} and p^{tr} are the amplitude of the reflected and transmitted pressure wave (*P*), respectively. For the purpose of elucidation, the classical water-hammer equation in a frictionless pipe that results from the coupling of continuity and momentum ([13], [137], and [50]) and realizing that water supply systems are low Mach number flows is considered and has the following form ([50]):

$$\begin{aligned} & A\frac{\partial^2 P}{\partial t^2} = a^2\frac{\partial}{\partial x}\left(A\frac{\partial P}{\partial x}\right) \\ & \Rightarrow \frac{\partial^2 P}{\partial t^2} - a^2\frac{\partial^2 P}{\partial x^2} = a^2\frac{\partial \log A}{\partial x}\frac{\partial P}{\partial x} \\ & \Rightarrow \frac{\partial^2 P}{\partial t^2} - a^2\frac{\partial^2 P}{\partial x^2} = a^2\frac{\partial\left(\log\left(A/A_0\right)\right)}{\partial x}\frac{\partial P}{\partial x} \end{aligned} \qquad (4.1)$$

where *a* is the acoustic wave speed; and $A(x)$ and A_0 are the area of the conduit in the non-uniform region and the uniform region, respectively. Using a Fourier series expansion, one can write $\log\left(A(x)/A_0\right)=\sum_m C_m e^{ik_m x}$ where k_m and C_m are the wave-number and amplitude of the m^{th} mode. Therefore,

$$\begin{aligned} & \frac{\partial^2 P}{\partial t^2} - a^2\frac{\partial^2 P}{\partial x^2} = a^2\frac{\partial\left(\log\left(A/A_0\right)\right)}{\partial x}\frac{\partial P}{\partial x} \\ & = ka^2\left[\, p^{ref}e^{ikx-iwt} - p^{tr}e^{-ikx-iwt}\,\right]\sum_m k_m C_m e^{ik_m x} \end{aligned} \qquad (4.2)$$

which clearly shows that the right hand side resonates with the reflected wave when $k_m - k = k$ and with the transmitted wave when $k_m + k = -k$. That is, resonance occurs when

$$k_m = \pm\, 2k \qquad (4.3)$$

which is the classical Bragg resonance condition ([84]). Therefore, a wave propagating towards conduit's non-uniformities in crossectional area that involve a mode whose wavelength is half of the wavelength of the incident wave, cannot easily penetrate (transmit) through these non-uniformities (due to resonance). The implications of such result to defect detection are profound. Indeed, large reflection towards the source of the wave gives great potential for detecting the defect provided that the pressure sensor is situated between the generator and the defect ([36]).

4.3. Analytical Investigation

Consider the pipe system depicted in Figure 4.1. An incident wave train is initiated at infinity and propagates to the left towards the non-uniformity in the cross sectional area (blockage). The objective is to study the scattering effect imposed on the incident wave by the variation in the cross sectional area (non-uniformities). The variation in the cross sectional area is idealized as step function, and therefore, the whole system is equivalent to the junction of multiple pipes with different diameter.

Introducing harmonic excitation at the source (see Figure 4.1) and using the method of separation of variables, one can assume that Eq. (4.1) has a solution of the form $p(x,w)\exp(-iwt)$, where w and $p(x,w)$ are the radian frequency and the amplitude of the propagating wave in the pipe, respectively. Noting that the cross section A varies from pipe to pipe but is constant for each pipe section, Eq. (4.1) for each pipe "j" (=1, 2, 3) becomes as follows:

$$\frac{d^2 p_j}{dx} + k_j^2 p_j = 0 \qquad (4.4)$$

where $k_j = w/a$ is the wave-number of the j^{th} pipe segment. For simplicity but without loss of generality, the wave speed a is assumed to be the same for all segments. The solution of Eq. (4.4) is

$$p_j = p_j^{ref} \exp\left(ik_j x\right) + p_j^{tr} \exp\left(-ik_j x\right) \qquad (4.5)$$

where p_j^{tr} and p_j^{ref} are the transmitted and reflected wave amplitude in pipe j, respectively. The conditions of pressure and flow continuity at the junction of segments j and j+1 are:

$$\begin{cases} p_j = p_{j+1} \\ A_j \dfrac{dp_j}{dx} = A_{j+1} \dfrac{dp_{j+1}}{dx} \end{cases} \quad \text{at } x = -l_{j+1} + \sum_1^j l_{j+1} \;\; ; \text{ where } j = 1, 2, 3... \qquad (4.6)$$

where A_j and l_j are the area and length of the j^{th} pipe. Equations (4.5) and (4.6) together with the fact that the pipe is unbounded (*i.e.*, p_1^{ref} = 0) can be solved for any number of blockages. For simplicity, only the solution for one and two blockages are given and discussed in this chapter. The extension to more than two-blockages is algebraically involved, but can be performed using software packages such as MATLAB.

Figure 4.1 sketch of a pipe system with three blockages (non-uniformities)

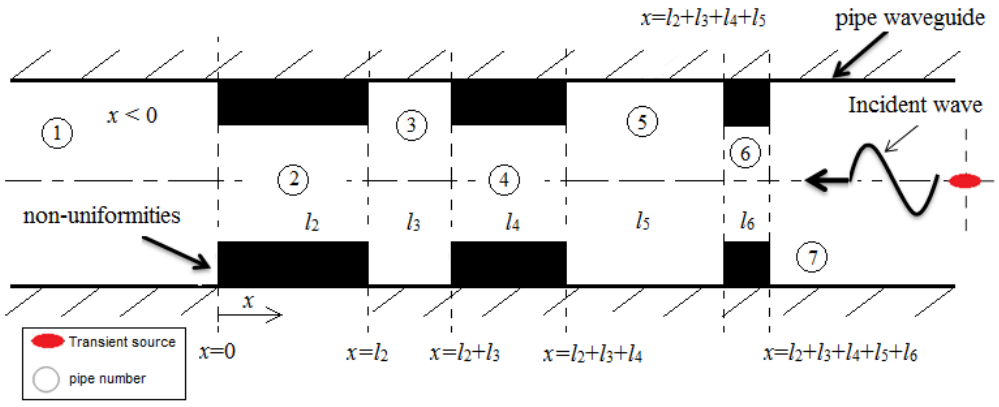

4.4. One blockage case

Considering one blockage case as shown in Figure 4.2 and solving for the boundary condition of pressure and flow continuity at each junction (Eq. (4.6)) by assuming no reflections from the upstream and downstream boundaries ($p_1^{ref} = 0$ and $p_3^{tr} = p_0$ with p_0 the amplitude of the incident wave), lead to the final results

$$\begin{cases} \dfrac{p_3^{ref}}{p_0} = \dfrac{2\left(1-\alpha^2\right)\left[\left(1+\alpha^2\right)\sin^2\left(kl_2\right)+2i\alpha\cos\left(kl_2\right)\sin\left(kl_2\right)\right]}{2\left(1+\alpha^4\right)\sin^2\left(kl_2\right)+4\alpha\left(\cos^2\left(kl_2\right)+1\right)} \\ \dfrac{p_1^{tr}}{p_0} = \dfrac{1}{\cos\left(kl_2\right)+i\dfrac{1+\alpha^2}{2\alpha}\sin\left(kl_2\right)} \end{cases} \quad (4.7)$$

where

$$\alpha = A_2 / A_0 \quad (4.8)$$

Reflection from the blockage (p_3^{ref}) and transmission through the blockage (p_1^{tr}) have reciprocal relationship and therefore studying either of them leads to the same conclusions. Since the expression of the transmitted amplitude is easier, it will be considered for the analytical investigation. The norm squared of p_1^{tr} normalized by p_0 is:

$$\left|\frac{p_1^{tr}}{p_0}\right|^2 = \frac{1}{\cos^2\left(kl_2\right)+\left[\dfrac{1+\alpha^2}{2\alpha}\right]^2\sin^2\left(kl_2\right)} \quad (4.9)$$

The traditional approach used for the case of a bounded pipe (e.g., a reservoir in one end and a valve in the other ([32]), which will be discussed in Chapter 5 and Chapter 6, is to solve for the resonant frequencies by setting the denominator of the wave amplitude to zero. Such approach provides a quantitative measure of the impact of a blockage on the resonant frequencies of a pipe system and has been used to develop algorithms for blockage detection in pipes. However, the denominator of Eq. (4.9) is strictly positive. The absence of resonance in this case is due to the fact that the pipe considered is unbounded so that waves

transmitted from the blockage propagate towards infinity without reflection. That is, the unbounded pipe allows (i) the examination of the direct interaction between waves and blockage without interference from other effects and (ii) the investigation of which waves transmit least and by implication which waves reflect most towards the source. Knowledge of which waves transmit and which do not provides information on the coupling mechanism between the upstream and downstream regions of the blockage as well as the design of probing signals in TBDDM. For example Duan, et al. ([36]) used a blockage detection technique that relies on measuring the reflection coefficient. In their experimental work, they varied the central frequency of the generated wave to determine which waves reflect most, and consequently, led them to best accurate results.

To find the frequencies for which p_1^{tr} is minimum and maximum, the first and second derivatives of Eq. (4.9) with respect to the frequency are performed and the results are:

The frequencies at which maximum reflection occur are given by

$$\cos\left(kl_2\right)=0 \;\Rightarrow\; w_{\bar{m}}^{R}\left(l_2\right)=2\pi\left[\left(2\bar{m}-1\right)\frac{a}{4l_2}\right] \;;\; \bar{m}=1,2,3... \qquad (4.10)$$

and the frequencies at which maximum transmission occur are given by

$$\sin\left(kl_2\right)=0 \;\Rightarrow\; w_{\bar{m}}^{T}\left(l_2\right)=2\pi\left[2\left(\bar{m}-1\right)\frac{a}{4l_2}\right] \;;\; \bar{m}=1,2,3... \qquad (4.11)$$

Equation (4.10) indicates that if the blockage length is an odd multiple of the quarter wavelength, then maximum wave reflection from the blockage occurs. On the other hand, Eq. (4.11) indicates that if the blockage length is a multiple of the half wavelength, then the injected wave is totally transmitted through the blockage. Indeed, Duan, et al. ([36]) have noticed the condition of maximum reflection in their experiment.

Figures 4.3 and 4.4 show the variation of transmitted and reflected amplitude with respect to the frequency (w) for two different blockage length l_2, respectively. In order to investigate the effect of the radial extent, α =0.64, α =0.36 and α =0.16 are considered in Figures 4.3 and 4.4. The existence of Bragg-type resonance, where there are frequency bands

for which there is full transmission and others for which there is near complete reflection is clear in Figures 4.3 and 4.4 and occur for all parameters ranges. The frequencies at which maximum reflection and maximum transmission occur correspond to Eq. (4.10) and Eq. (4.11), respectively. The near complete reflection is due to multiple wave reflections from the junction boundaries of the blockage. For instance, consider the wave impinging on the blockage in region 2 (see Figure 4.2), upon reaching the right junction boundary, part of the incident wave gets reflected and part gets transmitted. The transmitted part of the wave propagates to the left and gets split into a reflected and transmitted once it reaches the left junction boundary. The reflected part gets split into a reflected and transmitted once it reaches the right junction boundary. The transmitted part, having the same phase as the impinging wave, resonates with the incident wave in region 3.

From Eq. (4.10), the smallest frequency at which an incident wave suffers maximum reflection towards the source (*i.e.*, minimum transmission through the blockage) is:

$$w = 2\pi f = w_1^R = 2\pi f_1^R = 2\pi \frac{a}{4l_2} \qquad (4.12)$$

That is, an incident wave whose wavelength is $4l_2$ interacts with the blockage in such a way that maximum reflection towards the wave source occurs. An analogous result is found for shallow water waves propagating in a channel that contains a shelf ([84]). The physical interpretation of Eq. (4.10) and Eq. (4.11) is as follows. Consider a train of waves generated at the source (Figure 4.2). Any wave in this train that arrives at the blockage ($x=l_2$) experiences scattering whereby a part is reflected back towards the source and a part is transmitted towards the other end of the blockage($x=0$). Once the transmitted part of the wave arrives at $x=0$, it gets scattered where a part is reflected towards $x=l_2$. The result is that each wave in the train experiences multiple scattering at the two ends of the blockage $x=l_2$ and $x=0$ and interacts with the waves that are both ahead and after it in the train. Waves with frequencies given by Eq. (4.11) exhibit destructive interference at $x=l_2$, while waves with frequencies given by Eq. (4.10) exhibit constructive interference at $x=l_2$. It is precisely this type of interaction that TBDDM exploits to identify defects. For example, measuring the frequency spectrum of p_1^{tr} (Figure 4.3) allows the identification of the blockage properties.

The blockage length is determined by reading the lowest frequency at which the amplitude of the spectrum is minimum and plugging this value into the left hand side of Eq. (4.12). In addition, the radial extent of the blockage is inferred by reading the height of the first minimum of the frequency spectrum of p_1^{tr}, plugging it into Eq. (4.9) and keeping the physically meaningful solution for which α <1. The result is:

$$\alpha = \left|\frac{p_0}{p_1^{tr}\left(w_1^R\right)}\right| - \sqrt{\left(\left|\frac{p_0}{p_1^{tr}\left(w_1^R\right)}\right| - 1\right)} \qquad (4.13)$$

Figure 4.2 Pipe system with one blockage

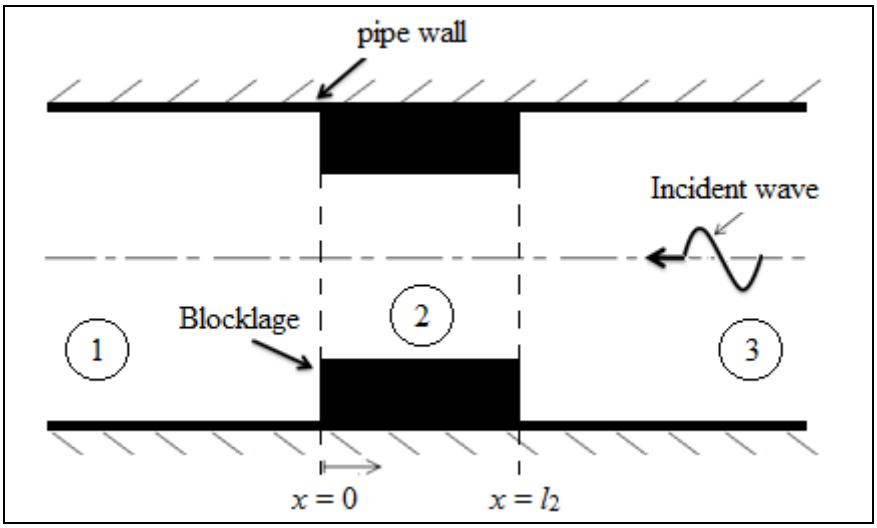

Figures 4.3 and 4.4 show that wider blockage (extended blockage) leads to narrower frequency bands of the Bragg-type resonance. Moreover, Figures 4.3 and 4.4 show that the maximum reflection and the maximum transmission amplitudes are merely depending on the radial extent α and that these amplitudes increase for more severe blockages (as α decreases). Figures 4.3 and 4.4a show that for severe short blockages, the frequency bands of maximum reflection becomes wider that the frequency bands of maximum transmission. This means that severe-short blockage (e.g. malfunctioning valve that is slightly opened)

reflects most of the waves an allows only narrow frequency bands to transmit through. Such features will help later analysis on eigenfrequency shift mechanism due to change in the cross sectional area in bounded pipe system (Chapter 5 and Chapter 6).

Figure 4.3 Transmission amplitude variation with frequency

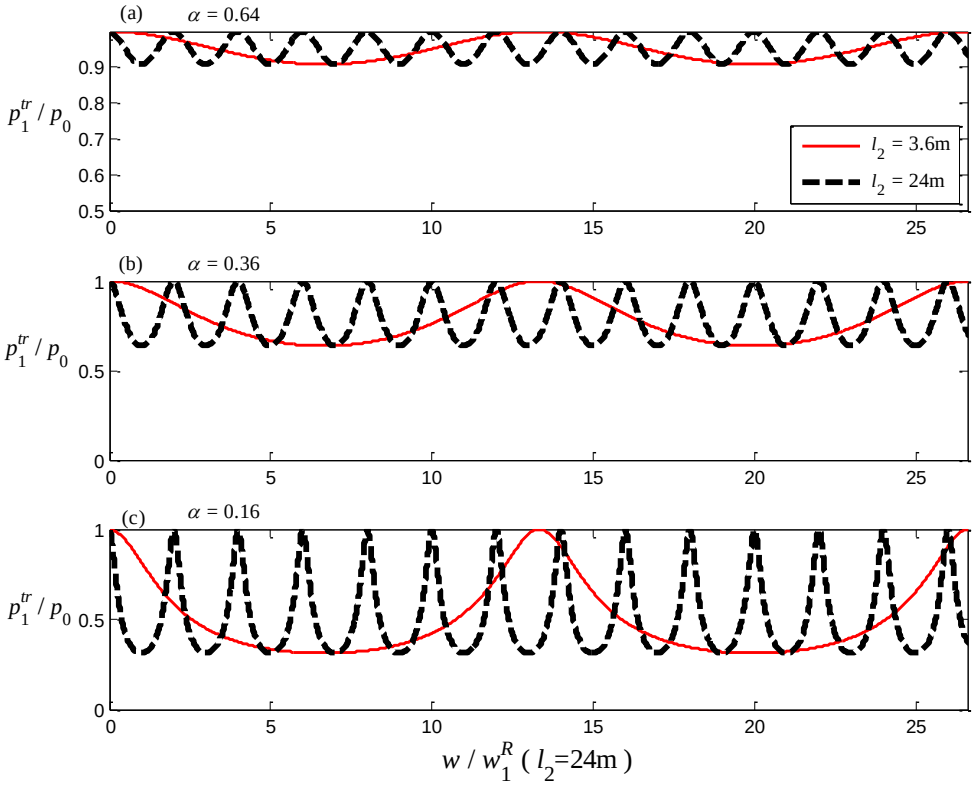

(a) Top α **= 0.64**

(b) Middle α **= 0.36**

(c) Bottom α **= 0.16**

Figure 4.4 Reflection amplitude variation with frequency

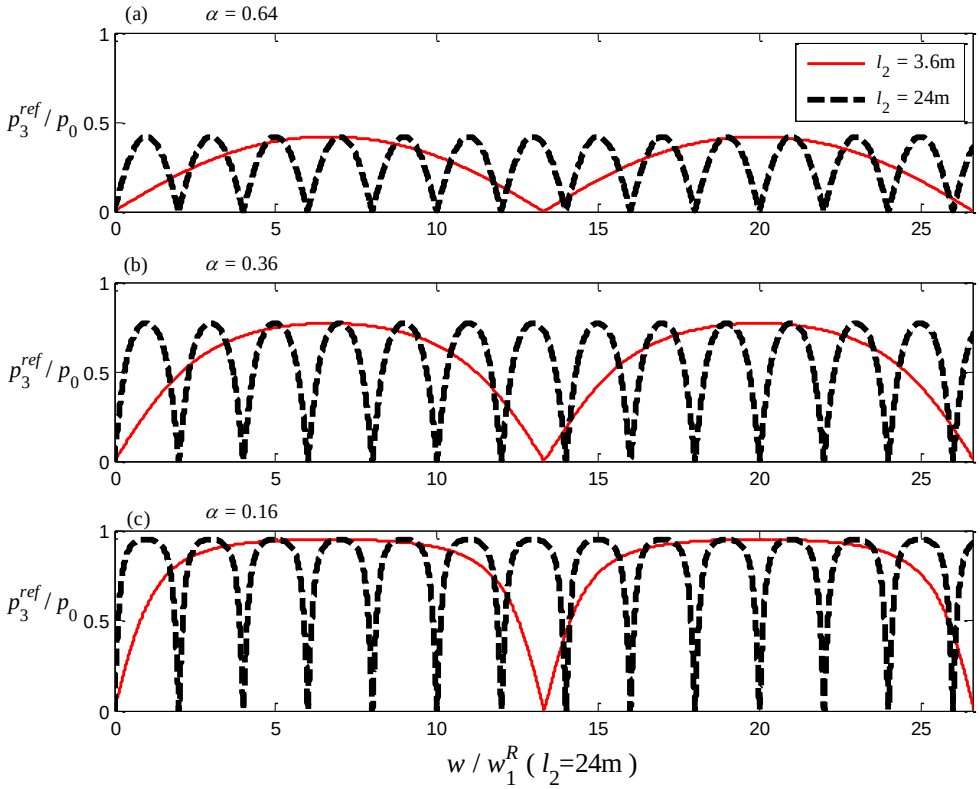

(a) Top α **= 0.64**

(b) Middle α **= 0.36**

(c) Bottom α **= 0.16**

4.4.1. Numerical Investigation

Numerical tests are conducted using the method of characteristic (MOC) to study the wave reflection and transmission in an unbounded pipe system. The tests consider a blockage with length l_2=3.6 and α = 0.16. The waveform of the incident wave in region 3 (see Figure 4.2) is given by

$$\begin{cases} P_3^I(t) = p_0 \exp\left(-4\frac{w_c^{\,2}}{\beta^2}\log(10)\left(t-\frac{\beta}{w_c}\right)^2\right)\sin\left(w_c\left(t-\frac{\beta}{w_c}\right)\right) \\ \text{where } \; 0 < t \le t_{wave} = \frac{\beta}{w_c} \text{ with } \beta = 100\pi \end{cases} \qquad (4.14)$$

where w_c is the central frequency and β is a coefficient that controls the frequency bandwidth (FBW). Figure 4.5 shows the time domain and the frequency domain of the wave form generated. Such wave form is chosen because it gives control on the FBW and the central frequency generated. As shown in Figure 4.5, very narrow FBW will be considered. The flow in the pipe is assumed initially stagnant. P_3^I and P_3^R denote the incident and reflected pressure wave in region 3, respectively; and P_1 is the pressure wave in region 1.

Figure 4.5 Input signal as transient source for numerical investigation

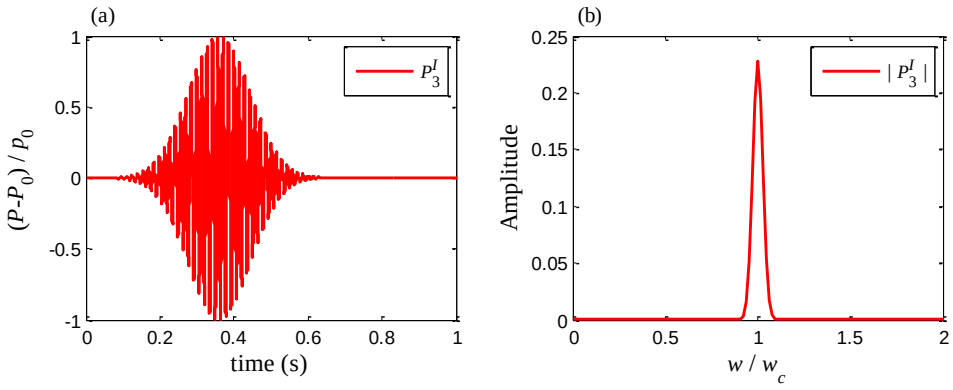

(a) Left **Time domain**

(b) Right **Frequency domain**

Figure 4.6 gives the time and frequency domain of the pressure signal at regions 1 and 3 where the central frequency of the generated wave is $w_c = w_1^R$ (Eq. (4.10)). According to the discussion in the previous section, maximum reflection occurs at $w = w_1^R$. Indeed,

Figure 4.6a shows that most of the wave is reflected comparing the transmitted wave shown in Figure 4.6c. Moreover, Figure 4.6b shows that the amplitude of the reflected wave has the same order of magnitude as the generated wave; whereas Figure 4.6c shows that the amplitude of the incident wave is much smaller.

On the other hand, Figure 4.7 shows the case where the central frequency is $w_c = w_2^T = 2w_1^R$ (Eq. (4.11)). In this case, maximum transmission is predicted to occur. Comparing Figures 4.7a-b to Figures 4.7c-d shows that the amplitude of the reflected wave (P_3^R) is much smaller than the transmitted wave (P_1). Figure 4.7b shows that the wave propagating at exactly w_2^T is completely transmitted as expected from Figure 4.3.

Figure 4.6 Pressure measurement in region 1 (upstream) and region 3 (downstream) of the blocked pipe system (Figure 4.2) when $w_c = w_1^R$ (Eq. (4.10))

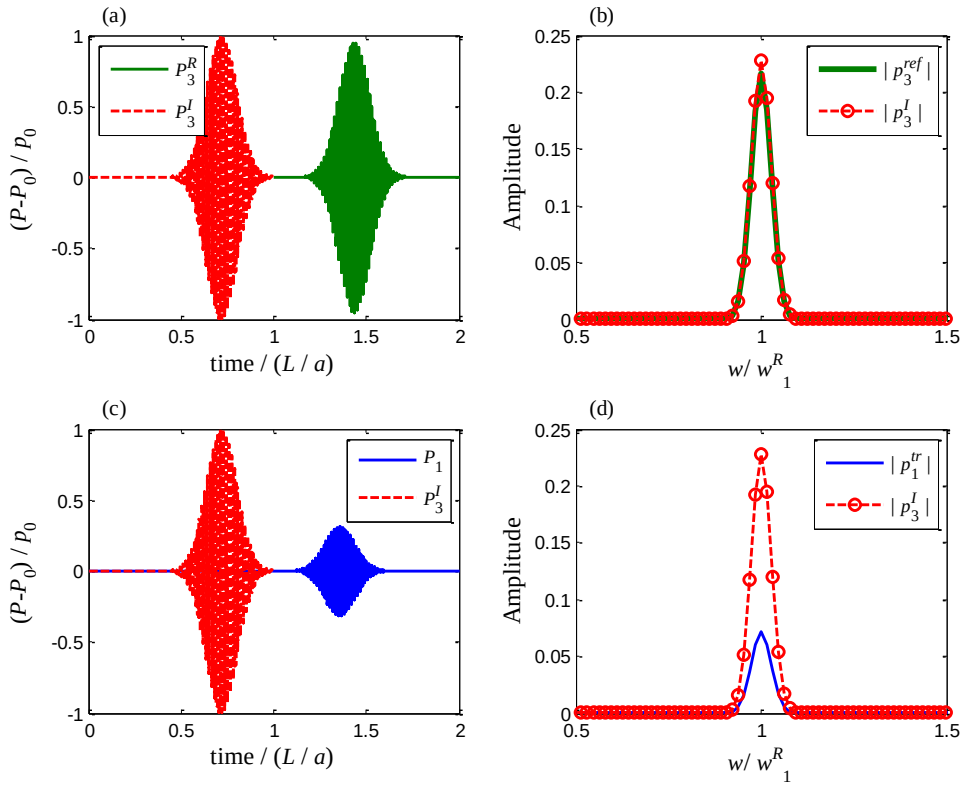

(a) Top left **Time domain of the reflected pressure measurement in region 3 compared to the transmitted pressure in region 3.**

(b) Top right **Frequency domain of the reflected pressure amplitude in region 3 compared to the transmitted pressure amplitude in region 3.**

(c) Bottom left **Time domain of the reflected pressure measurement in region 1 compared to the transmitted pressure in region 3.**

(d) Bottom right **Frequency domain of the reflected pressure amplitude in region 1 compared to the transmitted pressure amplitude in region 3.**

Figure 4.7 Pressure measurement in region 1 (upstream) and region 3 (downstream) of the blocked pipe system (Figure 4.2) when $w_c = w_2^T$ (Eq. (4.11))

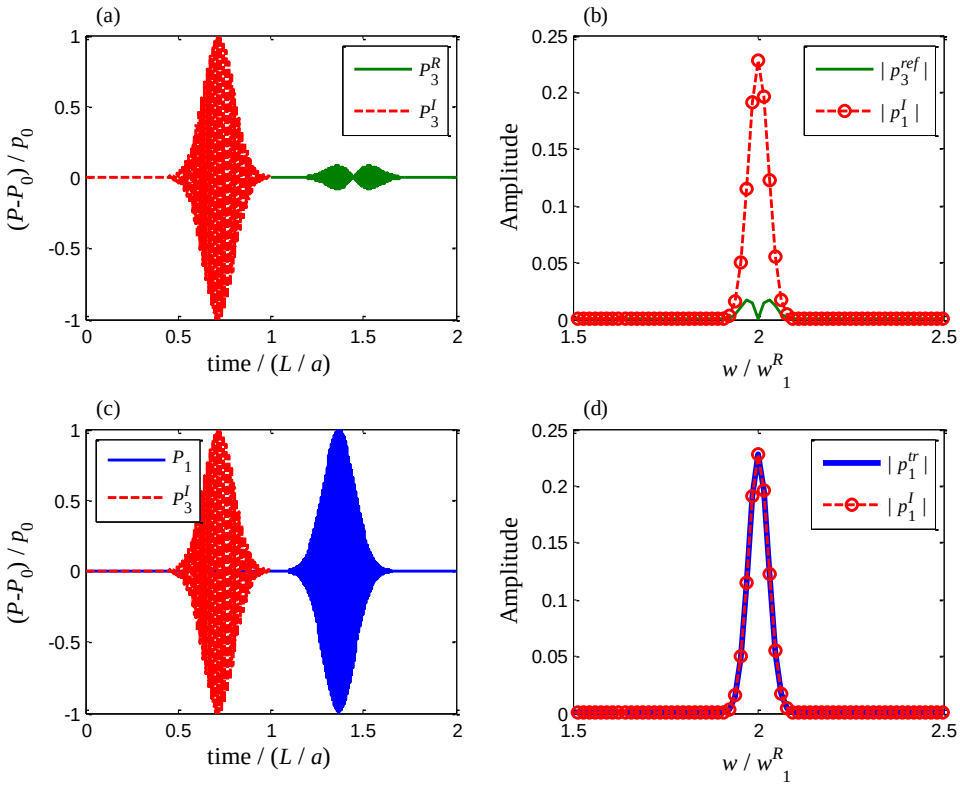

(a) Top left **Time domain of the reflected pressure measurement in region 3 compared to the transmitted pressure in region 3.**

(b) Top right **Frequency domain of the reflected pressure amplitude in region 3 compared to the transmitted pressure amplitude in region 3.**

(c) Bottom left **Time domain of the reflected pressure measurement in region 1 compared to the transmitted pressure in region 3.**

(d) Bottom right **Frequency domain of the reflected pressure amplitude in region 1 compared to the transmitted pressure amplitude in region 3.**

4.5. Two blockages case

Considering the two blockages case (regions 2 and 4) shown in Figure 4.8, and applying Eq. (4.5) and Eq. (4.6) to solve for p_1^{tr} yields

$$\frac{p_0}{p_1^{tr}} = \begin{bmatrix} \cos(kl_2)\sin(kl_3)\cos(kl_4) \\ -\left(\frac{1+(\alpha\alpha_4)^2}{2\alpha\alpha_4}\right)\sin(kl_2)\sin(kl_3)\sin(kl_4) \\ +\left(\frac{1+\alpha_4^{\,2}}{2\alpha_4}\right)\cos(kl_2)\cos(kl_3)\sin(kl_4) \\ +\left(\frac{1+\alpha^2}{2\alpha}\right)\sin(kl_2)\cos(kl_3)\cos(kl_4) \end{bmatrix} \times i + \begin{bmatrix} \cos(kl_2)\cos(kl_3)\cos(kl_4) \\ -\left(\frac{1+(\alpha_4/\alpha)^2}{2\,\alpha_4/\alpha}\right)\sin(kl_2)\cos(kl_3)\sin(kl_4) \\ -\left(\frac{1+\alpha_4^{\,2}}{2\alpha_4}\right)\cos(kl_2)\sin(kl_3)\sin(kl_4) \\ -\left(\frac{1+\alpha^2}{2\alpha}\right)\sin(kl_2)\sin(kl_3)\cos(kl_4) \end{bmatrix} \quad (4.15)$$

where $\alpha_4 = A_4/A_0$. It is instructive to note that all terms in Eq. (4.15) that contain information about the radial extent of blockage 2 (*i.e.*, α) and blockage 4 (*i.e.*, α_4) involves $\sin(kl_2)$ and $\sin(kl_4)$ in their coefficients, respectively. Therefore, information about blockage 2 is reduced if the probing length is such that $\sin(kl_2)$ is small, where "small" refers to the sine function being of order 0.15 or less (*i.e.*, an angle of $\pi/20$ or smaller). Similarly, information about blockage 4 is reduced if the probing length is such that $\sin(kl_4)$ is small. Therefore, to ensure identifiability of both blockages, it is important that the spectrum of the probing wave is wide enough such that the minimum (kl_2 , kl_4) is significantly larger than $\pi/20$. In terms of wavelength, this requirement is that minimum (l_2/λ , l_4/λ) is significantly larger than 1/40. The generalization of this result to *N* blockages

is that the minimum (l_j/λ) >>1/40 for j=1,2,…N. This theoretical result is corroborated with the numerical results of next section.

In fact, taking the limit when the length of one of the blockages (say blockage 2 in region 2 (Figure 4.8)) is small in comparison to the probing length scale λ such as l_2/λ <<1 results in

$$\frac{p_0}{p_1^{tr}} = \underbrace{\left[\cos(kl_4)+\left(\frac{1+\alpha_4^{\,2}}{2\alpha_4}\right)\sin(kl_4)\times i\right]\exp(ikl_3)}_{\text{1 blockage equation}} + \left(\frac{kl_2}{2\alpha}\right)\left[\cos(kl_4)\times i\exp(ikl_3)-\frac{\sin(kl_4)}{\alpha_4}\left(\sin(kl_3)\times i+\alpha_4^{\,2}\cos(kl_3)\right)\right] \quad (4.16)$$

Now, if also l_2/λ << α, then Eq. (4.16) becomes

$$\frac{p_1^{tr}}{p_0} = \frac{1}{\left[\cos(kl_4)+\left(\frac{1+\alpha_4^{\,2}}{2\alpha_4}\right)\sin(kl_4)\times i\right]\exp(ikl_3)} \quad (4.17)$$

which is equivalent to the one blockage equation given by Eq. (4.7). Notice that Eq. (4.17) is reduced to a one blockages case when the blockage is assumed not very deep. This will be discussed further in the next section.

Figure 4.8 Pipe system with one blockage

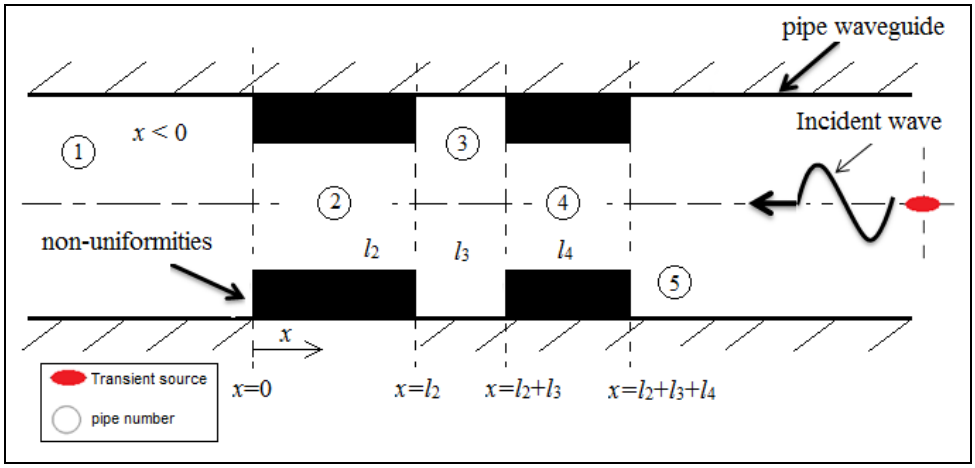

4.5.1. Frequency content versus resolution

As seen from last section (Eq. (4.17)), the effect of a blockage may get neglected when its length scale is small. This section studies the effect of the probing frequency range (*i.e.* probing frequency bandwidth) on resolving multi-scale blockage in a pipe. For this purpose, a set of test cases, as described in Table 4.1, are conducted and analyzed. The method of characteristics (MOC) ([137], [13]) is used for the numerical tests cases (Test 1a and Test 1b) and the results are compared with the analytical solution of the previous section.

Table 4.1 Test cases with 2 blockages in unbounded pipe system

	Test 1a	Test 1b	Test 2a	Test 2b	Test 2c	Test 3a	Test 3b	Test 3c
l_2 (m)	1.2	0.12	0.12	0	0.12	0.12	0	0.12
A_2/A_0	0.5	0.5	0.5	1	0.5	0.16	1	0.16
l_3 (m)	2.1	0.21	21.1	21.1	21.1	21.1	21.1	21.1
A_3/A_0	1	1	1	1	1	1	1	1
l_4 (m)	3.5	0.35	35.1	35.1	0	35.1	35.1	0
A_4/A_0	0.25	0.25	0.25	0.25	1	0.25	0.25	1

The following Gaussian-type impulse is used as injected wave at the source for the numerical tests.

$$\begin{cases} P(t) = P_0 + 0.1P_0 \exp\left(-2\frac{{w_c}^2}{\beta^2}\log(10)\left(t - \frac{\beta}{w_c} \right)^2 \right) \\ \text{where } \ 0 < t \le t_{wave} = \frac{\beta}{w_c} \ \text{ with } \beta = 4\pi \end{cases} \qquad (4.18)$$

where P_0 is the initial pressure in the pipe. The Gaussian impulse is chosen because it allows the modeler to introduce and tests the system response to the desired bandwidth.

Results of Test 1a and Test 1b are shown in Figure 4.9a and Figure 4.9b, respectively. Both tests include two blockages but the length scales of the blockages and the distance between the blockages are 10 times bigger for Test 1a. Comparing the results for Test 1a and 1b, it is first noticed that for the same accuracy of the frequency spectrum, the wave frequency bandwidth (FBW) needed for Test1b is 10 times larger than the FBW used in Test 1a. Therefore, the smaller the length scale of the blockages are, the wider must be the generated FBW. This result is in good agreement with the analytical solution (see Eq. (4.15)) of the previous section which shows that the natural scaling parameter for a blockage with length l and a probing wave with length λ is l/λ. Therefore, the wave-blockage interaction for a blockage with length l and a probing wave with length λ is the same as that of a blockage of length $l/10$ and $\lambda/10$. Second, it is clear that when wider FBWs are used, more information on the frequency spectrum are given and by consequences more accurate TBDDM analysis can be conducted ([71]).

Figure 4.9 Comparison of the transmitted wave amplitude for at different central frequencies with the exact 1D analytical solution

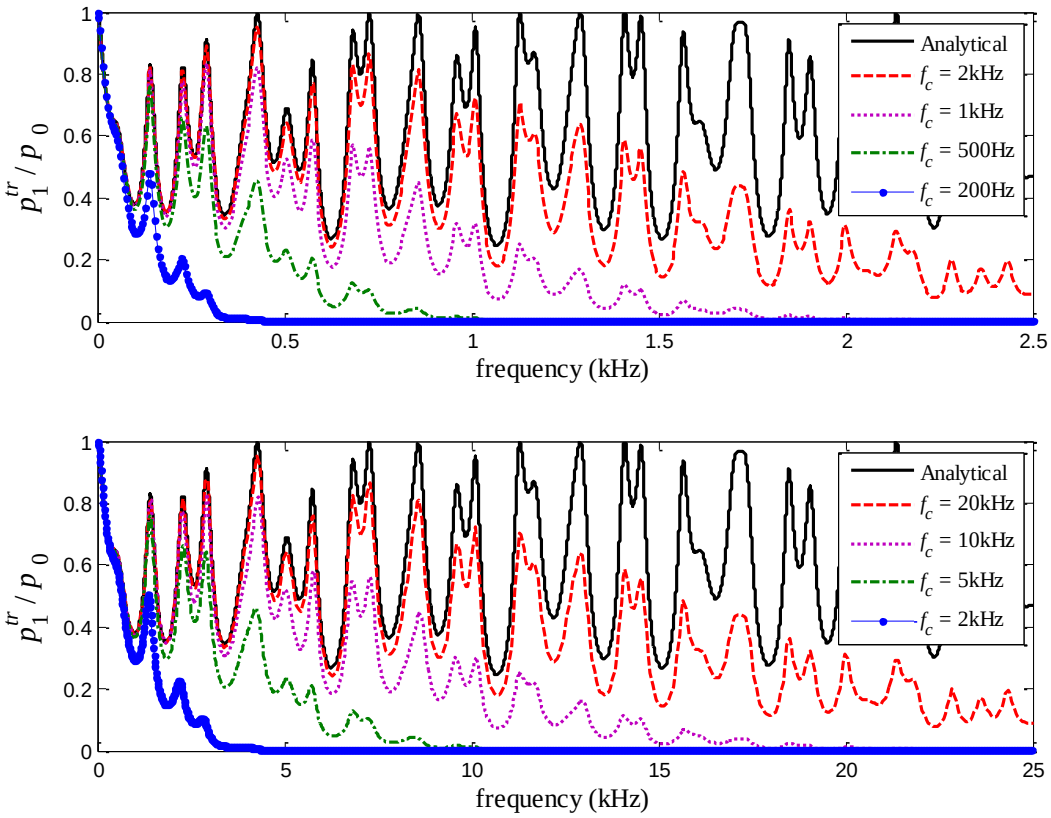

(a) Top Test 1a

(b) Bottom Test 1b

Test 2a includes two blockages with one blockage being much smaller than the other (see Table 4.1) so as to show the effect of mixed blockage length scales. In Figure 4.10, this test is compared with test 2b and test 2c where only one blockage (either the large or the small one) is considered (see Table 4.1). The analytical solution shows that the detectability of both blockages requires a probing wave such that minimum (l_2/λ , l_4/λ)>>1/40. Using the data of Test 2a, this requirement leads to λ <<0.12×40m ≈ 5m and l_2/λ = (0.12/35.1) l_4/λ >>1/40 (*i.e.*, l_4/λ >>7). Indeed, Figure 4.10a shows that the small blockage has no influence on the results when l_4/λ is about 2 or less. In fact, the influence of the small length blockage

first becomes perceptible only when l_4/λ is about 5 or larger (Figure 4.10b). The effect of the small blockage is prominent once l_4/λ exceeds 10 (Figure 4.10c) or equivalently when and l_2/λ exceeds about 1/30. Figure 4.10d shows wide bandwidth plot of the transmitted wave amplitude for tests 2a-c. The green curve is for the case of a small blockage only. The minimum transmission for test 2c occurs when $4l_4/\lambda$ is around 290. Since this is a single blockage, then Eq. (4.10) applies and predicts that the minimum transmission (maximum reflection) occurs at minimum $kl_2=\pi/2$. (*i.e.*, $l_2/\lambda = 1/4$). Since $l_2/ l_4= 0.12/35.1$, then $l_2/\lambda = 1/4$ is equivalent to $4l_4/\lambda = 292.5$ which is very close to the 290 read from the Figure 4.10d. In fact, envelope of the minimum values of the blue curve is approximately the superposition of the red and green curves. That is, the interaction between the wave and the two blockages, one small and one large, is the superposition of the results for the case of wave-large blockage interaction and the case of wave-small blockage interaction.

Figure 4.10 Comparison of transmitted amplitude for tests 2a, 2b and 2c

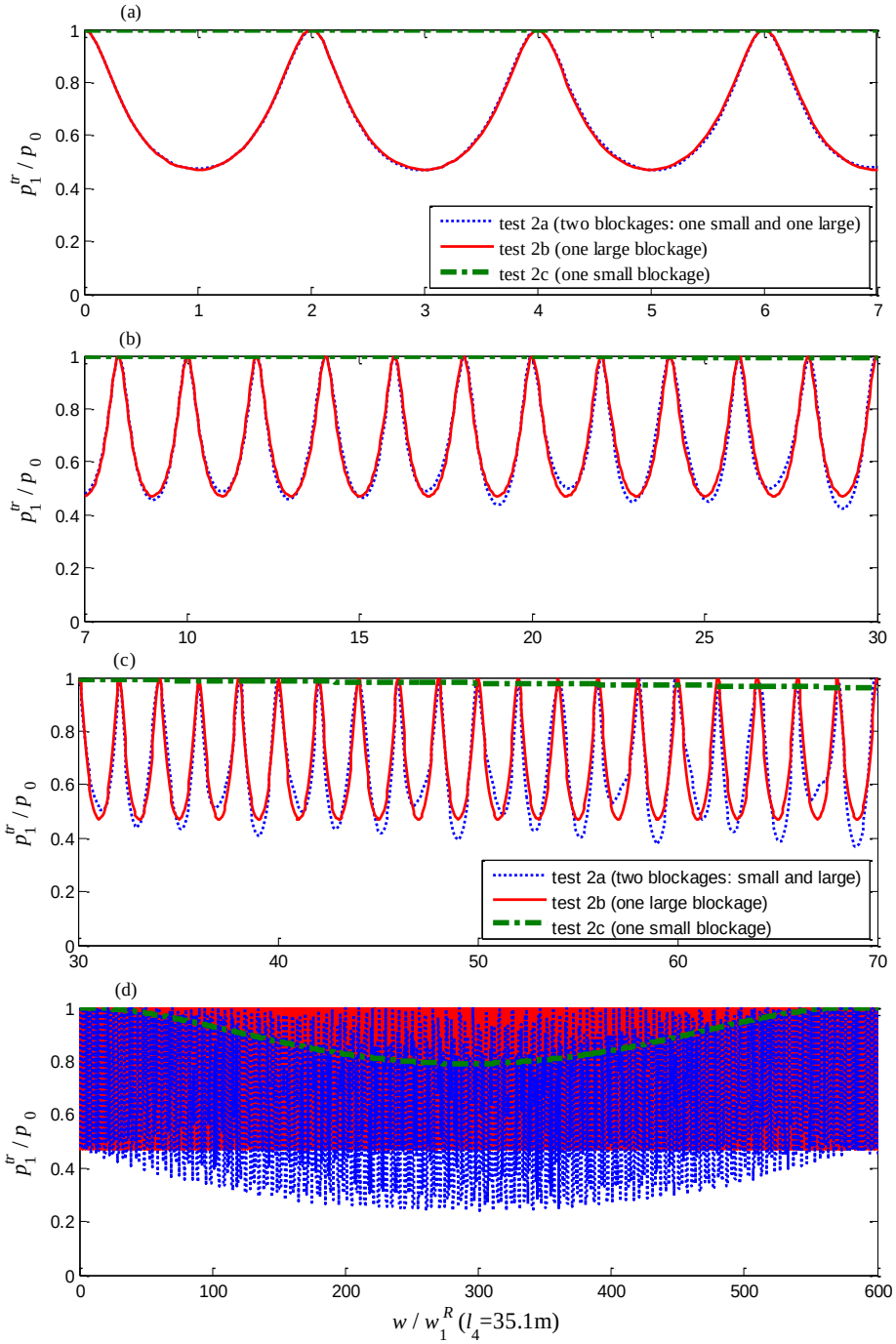

(a) Top **Frequency axis :[0 to 7]** $\times w/w_1^R\left(l_4=35.1\text{m}\right)$

(b) Second to Top **Frequency axis :[7 to 30]** $\times w/w_1^R\left(l_4=35.1\text{m}\right)$

(c) Second to Bottom **Frequency axis :[30 to 70]** $\times w/w_1^R\left(l_4=35.1\text{m}\right)$

(d) Bottom **Frequency axis :[0 to 600]** $\times w/w_1^R\left(l_4=35.1\text{m}\right)$

As seen from Eq. (4.16), if the area of the blockage is very small (*i.e.* severe blockage), then the influence of the blockage would be distinct even at a low frequency. Test 3a-c are designed to verify this behavior where the area of region 2 (see Figure 4.8) being too small (see Table 4.1). The results of these tests are shown in Figure 4.11. Both the analytical solution and the numerical results show that for blockages with $A_j/A<<1$, strong interaction between the injected wave and all blockages occurs provided that minimum $(l_j/\lambda)\times(A/A_j)$ is of order 1.

Figure 4.11 Transmitted amplitude at different bandwidth for tests 3a, 3b and 3c

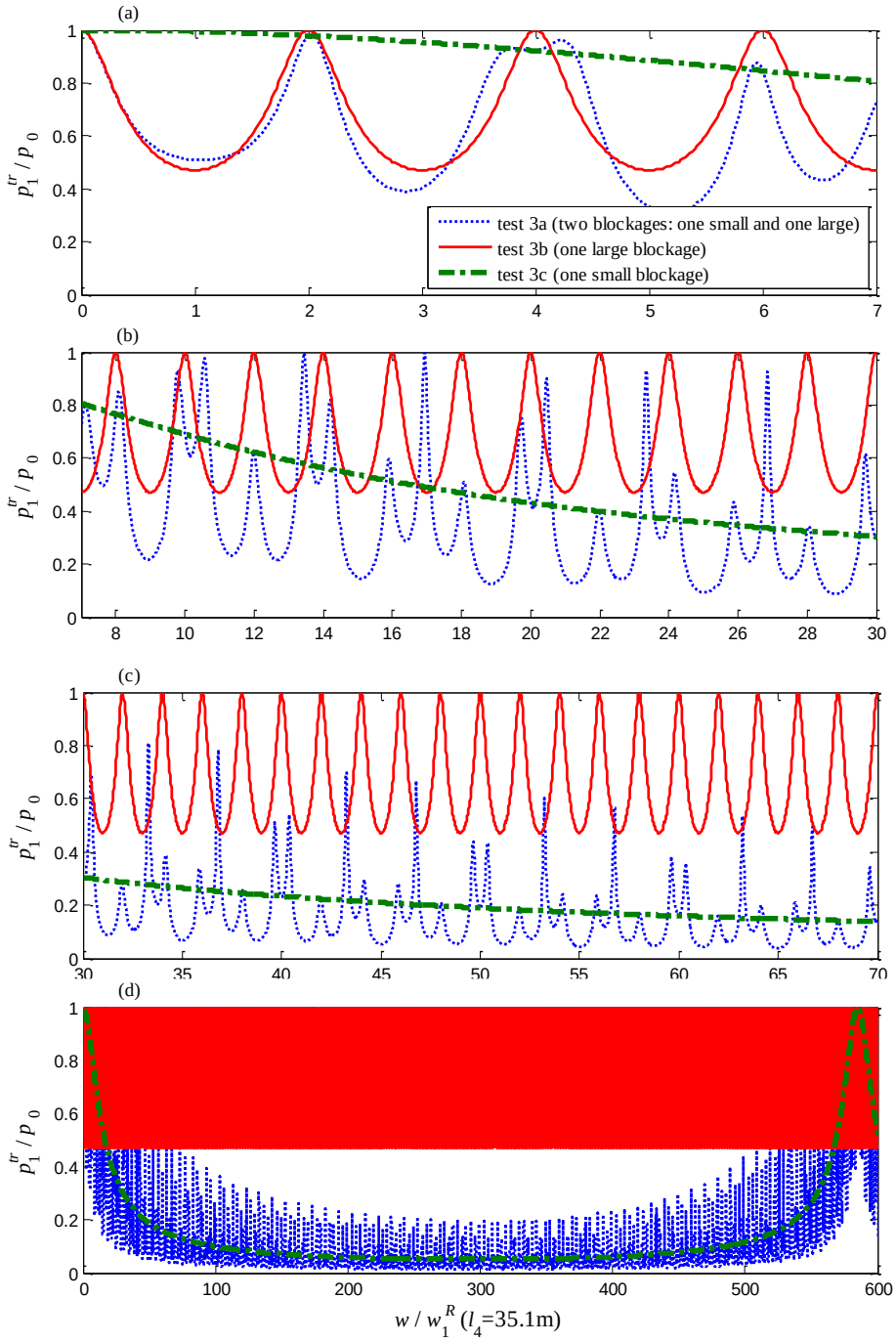

(a) Top **Frequency axis :[0 to 7]** $\times w/w_1^R(l_4 = 35.1\text{m})$

(b) Second to Top **Frequency axis :[7 to 30]** $\times w/w_1^R(l_4 = 35.1\text{m})$

(c) Second to Bottom **Frequency axis :[30 to 70]** $\times w/w_1^R(l_4 = 35.1\text{m})$

(d) Bottom **Frequency axis :[0 to 600]** $\times w/w_1^R(l_4 = 35.1\text{m})$

4.5.2. Periodic blockages

Taking the special case where the lengths of the two blockages and the spacing between them is the same (*i.e.* $l_2 = l_3 = l_4 = l_b$ with l_b is the length of the blockage), and where $A_2 = A_4$. In this case, Eq. (4.15) becomes

$$\left|\frac{p_1^{tr}}{p_0}\right| = \frac{1}{\sqrt{\begin{array}{l}\cos^6(kl_b) + \dfrac{\left(1+\alpha^2+\alpha^4\right)}{\alpha^2}\cos^4(kl_b)\sin^2(kl_b) \\ -\dfrac{\left(1-\alpha^2-3\alpha^3-\alpha^4+\alpha^6\right)}{\alpha^3}\cos^2(kl_b)\sin^4(kl_b) \\ +\dfrac{\left(1+\alpha^4\right)^2}{4\alpha^4}\sin^6(kl_b)\end{array}}} \qquad (4.19)$$

where $\alpha = A_4/A_0 = A_2/A_0$.

Figure 4.12 gives a comparison between the variation of transmitted amplitude with dimensionless frequency for the case of a single blockage and two periodic blockages, respectively. Figure 4.12a gives the case for $\alpha = 0.16$ and Figure 4.12b gives the case for $\alpha = 0.64$. Figure 4.12 shows that, for the case of two periodic blockages, total transmission and local minimum transmission occur at frequencies that are different from the Bragg resonance frequencies (Eq. (4.10) and Eq. (4.11)). The conditions of maximum and minimum transmission are obtained by equating to zero the derivative of $\left|p_1^{tr}\right|$ (Eq. (4.19)) with respect to *k* which gives

$$\begin{cases} \cos(kl_b) = 0 \\ \sin(kl_b) = 0 \\ \sin^2(kl_b) = \dfrac{2\alpha}{(1+\alpha)^2} \Leftrightarrow \cos^2(kl_b) = \dfrac{(1+\alpha^2)}{(1+\alpha)^2} \\ \sin^2(kl_b) = \dfrac{2\alpha}{3(1+\alpha)^2} \Leftrightarrow \cos^2(kl_b) = \dfrac{3+4\alpha+3\alpha^2}{3(1+\alpha)^2} \end{cases} \qquad (4.20)$$

The first and second conditions in Eq. (4.19) give the Bragg resonace frequencies of maximum reflection (Eq. (4.10)) and total transmission (Eq. (4.11)) found for the one blockage case, respectively. The two additional conditions in Eq. (4.19) are due to the effect of the added blockage. Inserting the four conditions in Eq. (4.19) gives respectively

$$\begin{cases} \left|p_1^{tr}/p_0\right| = \dfrac{2\alpha^2}{1+\alpha^4} \\ \left|p_1^{tr}/p_0\right| = 1 \\ \left|p_1^{tr}/p_0\right| = 1 \\ \left|p_1^{tr}/p_0\right| = \sqrt{\dfrac{3^3\alpha}{8+11\alpha+8\alpha^2}} \end{cases} \qquad (4.21)$$

Equation (4.21) shows that the second and third condions in Eq. (4.19) give total transmission, whereas the two others give minumum transmission whith the least transmission given by the first condition. Therefore, the third condition in Eq. (4.19) gives the extra frequencies of total transmission as follows

$$\sin^2\left(kl_b\right) = \frac{2\alpha}{\left(1+\alpha\right)^2} \Rightarrow \frac{w_{\bar{m}}(\alpha)}{w_1^R} = 2\left(\bar{m}-2\right)+1+\frac{2}{\pi}\arccos\left(\left(-1\right)^{\bar{m}}\frac{\sqrt{2\alpha}}{\left(1+\alpha\right)}\right) \qquad (4.22)$$

For example, for $\bar{m}$ = 1, Eq. (4.22) gives $w_1\left(0.16\right)/w_1^R = 0.3243$ which is as shown in Figure 4.12a. On the other hand, the fourth condition in Eq. (4.19) gives the extra frequencies of minimum transmission as follows

$$\sin^2\left(kl_b\right) = \frac{2\alpha}{3\left(1+\alpha\right)^2} \Rightarrow \frac{w_{\bar{m}}}{w_1^R} = 2\left(\bar{m}-2\right)+1+\frac{2}{\pi}\arccos\left(\left(-1\right)^{\bar{m}}\frac{\sqrt{2\alpha}}{\sqrt{3}\left(1+\alpha\right)}\right) \qquad (4.23)$$

For example, for $\bar{m}$ = 1, Eq. (4.23) gives $w_1\left(0.16\right)/w_1^R = 0.1817$ which is as shown in Figure 4.12a. As shown by compairing Figure 4.12a and 4.12b, those extrat frequencies of total and minimum transmission varies with α . For example, Eq. (4.22) gives $w_1\left(0.64\right)/w_1^R = 0.4847$ which is as shown in Figure 4.12b.

Moreover, both one single blockage and two periodic blockages give minimuum transmission (*i.e.* maximum reflection) at the Bragg resonance of maximum reflection (Eq. (4.10)). However, for the case of one blockage, the minimum transmission is given by inserting Eq. (4.10) into Eq. (4.9) which leads to

$$\left|\frac{p_1^{tr}}{p_0}\right| = \frac{2\alpha}{1+\alpha} \qquad (4.24)$$

Comparing Eq. (4.24) and the first equation in Eq. (4.19) shows that, at the Bragg resonance of maximum reflection (Eq. (4.10)), the two periodic blockages behaves as a single blockage but with more severe blocked area (i.e $A_2/A_0 = \alpha_{1b}^2$ with α_{1b} is the area ratio for single blockage case) as shown in Figure 4.12. Although not presented in this work, but similar effect of additional total and local minimum transmission as well as inhanced maximum reflection occur for larger number of periodic blockages ([80]).

Figure 4.12 Transmission amplitude variation with frequency: comparison between one blockage and two periodic blockages cases.

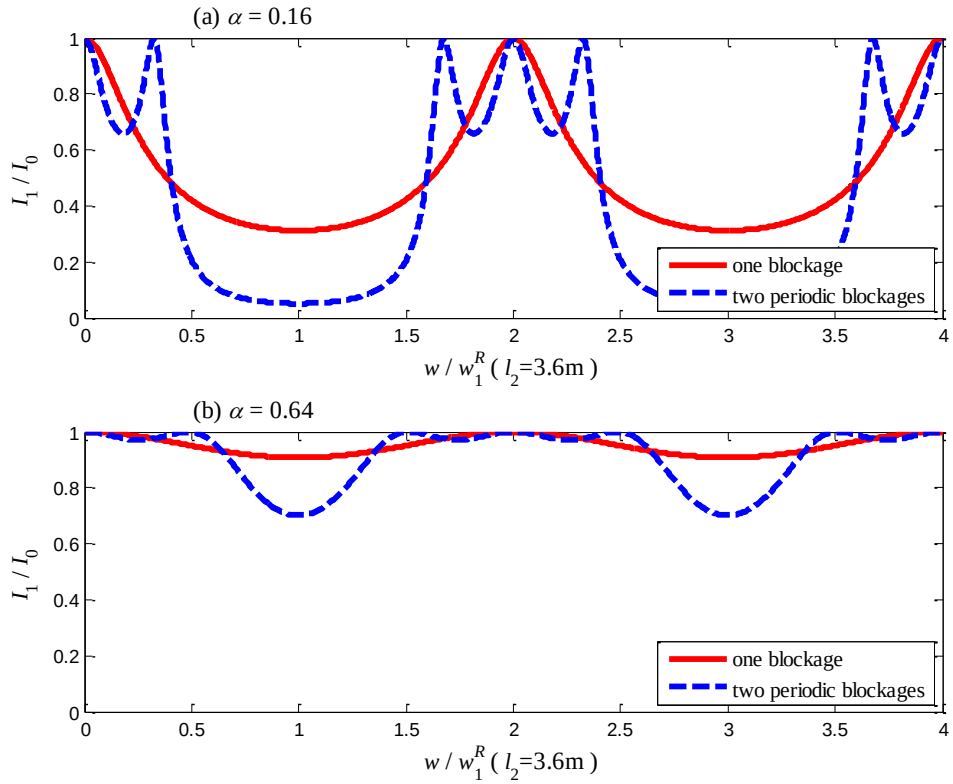

(a) Top α **= 0.16**

(b) Bottom α **= 0.64**

4.6. Summary

This chapter used analytical and numerical means to investigate how waves interact with non-uniformities with varying length scales and establishes the existence of Bragg-type resonance in water pipe systems. This understanding is pre-requisite for developing inverse techniques where measured wave signals are used to infer the size and location of blockages. This is accomplished by introducing a harmonic wave with wavelength λ into an unbounded

pipe of area (A) containing N blockages. Each blockage is modelled as a pipe segment of length l_j and area A_j, where j=1, 2,…N. The key conclusions are:

(i) Waves experience enormous reflections (Bragg-type resonance) due to the non-uniformities for a particular frequency range and maximum transmission otherwise. The ranges of large reflection and maximum transmission convey much information about the non-uniformities and are fundamental to defect detection in pipes.

(ii) As expected, the wave length λ and the intact pipe diameter are found to be the natural length scales in the longitudinal and radial direction, respectively.

(iii) For blockages with small radial extent (*i.e.*, α ~1), strong interaction between the injected wave and all blockages only occurs if the probing wavelength is such that the minimum $l_j/\lambda >> 1/40$. Any probing wave and blockage whose length scales do not satisfy this criteria do not interact (*i.e.* a wave passes through without interaction with any blockage whose length is significantly smaller than λ)

(iv) For severe blockages (*i.e.* $\alpha << 1$), strong interaction between the injected wave and all blockages occurs provided that minimum $(l_j/\lambda)\times(A/A_j)$ is of order 1.

(v) Wider blockage (extended blockage) leads to narrower frequency bands of the Bragg-type resonance.

(vi) The maximum reflection and the maximum transmission amplitudes are merely depending on the radial extent α and that these amplitudes increase for more severe blockages (as α decreases).

(vii) For severe-short blockages, the frequency bands of maximum reflection become wider that the frequency bands of maximum transmission. This means that severe-short blockage (e.g. malfunctioning valve that is slightly opened) reflects most of the waves and allows only narrow frequency bands to transmit through.

(viii) The addition of more blockages showed that the equations and analysis became involved and require further attentions. Initial results show that Bragg resonance effects occur for the case of multi-blockages. These preliminary results show that there exists regularity (periodicity) in the distribution of the Bragg resonances frequency bands.

(ix) The special case of of periodic blockages is stidied. Results show that two periodic blockages behave as a one single blockage but with more severe blocked area (i.e $A_2/A_0 \equiv \alpha_{1b}^2$ with α_{1b} is the area ratio for single blockage case). Therefore, under transient events, periodic irregularites in the pipe crossectional area could induce very large pressure which might lead to weakening of the pipe wall condition and therefore increasing the potential for leaks!

Next chapter studies the mechanism of eigenfrequency shift due to blockage-wave interaction in bounded pipe system, and shows the effect of Bragg-type resonance on the eigenfrequency shift. Moreover, the conclusions on wave-blockage interaction in unbounded pipe system, such as the blockage length effect, will be shown to have direct implication on the eigenfrequency shift mechanism in bounded pipe system.

CHAPTER 5

WAVE SCATTERING IN BOUNDED PIPE SYSTEM: STUDY OF THE EIGENFREQUENCY SHIFT DUE TO A BLOCKAGE AT THE BOUNDARY

5.1. Introduction

The problem of using a measured pressure trace to infer the internal shape of a conduct is of interest to water supply researchers. In particular, it is found that the eigenfrequencies of a measured pressure signal vary with the cross sectional area of the conduit (e.g. [112], [89], [28], [27], [106], and [32]). So far, most of the focus in the literature is on employing inverse problem techniques that use the eigenfrequency shift information for the reconstruction of the cross sectional area function of a pipe system (e.g. [32], [35], [25], [120], [113], [106], [105], [92], [91], [118], [28], [27], [41], [117], [56], [89], and [112]). This chapter, on the other hand, focuses on studying the forward approaches to understand the mechanism causing such eigenfrequency shift and how it behaves under both shallow blockage (with small radial protrusion) and severe blockage (with large radial protrusion) cases. Such understanding is essential to improve the accuracy and the convergence rate of inverse techniques for TBDDM and cross-sectional pipe assessment. This chapter considers a blocked pipe system with a blockage located at the boundary. Such system consists of the junction of two pipes with different diameter which is the simplest configuration of blocked pipe system. A more involved blocked pipe system with an interior blockage will be considered in the next chapter.

5.2. Problem statement

Duan, et al. ([32]) formulated the following dispersion relationship for the case of an arbitrary number of unknown blockages, N:

$$\sum_{j=0}^{\overline{\overline{N}}-1}\left[\underline{C}_j \cos\left(\sigma_j\right)\right]=0 \qquad (5.1)$$

where $\underline{C}_j=(-1)^{\sum_{\bar{\nu}=1}^{\bar{N}}\bar{J}_{\bar{\nu}}}\left[\frac{a}{gA_1}+(-1)^{\bar{J}_1}\frac{a}{gA_2}\right]\prod_{\bar{\xi}=2}^{\bar{N}}\left[(-1)^{\bar{J}_{\bar{\xi}-1}}\frac{a}{gA_{\bar{\xi}}}+(-1)^{\bar{J}_{\bar{\xi}}}\frac{a}{gA_{\bar{\xi}+1}}\right]$ and

$\bar{\sigma}_j=\left[k_m l_1+\sum_{\bar{\xi}=2}^{N}(-1)^{\bar{J}_{\bar{\xi}}}\left(k_m l_{\bar{\xi}}\right)\right]$; $k_m=w_m/a$ and w_m are the wavenumber and the resonant frequency (eigenfrequency) of the m^{th} fundamental (resonant) mode, respectively; a is the acoustic wave speed, which is assumed to be unaffected by the blockages; g is the standard gravitational acceleration; S = total number of junctions between blockages and the unblocked section (*i.e.* $\bar{N}=N-1$); $\overline{\overline{N}}=2^{N-1}$; j, $\bar{\xi}$ and $\bar{\nu}$ are counting numbers; $\bar{J}_n$ = 0 or 1 and represents the number at n^{th} binary position of j. Applying Eq. (5.1) to the blocked pipe system in Figure 5.1 gives:

$$\cos\left(k_m l_2\right)\cos\left(k_m l_1\right)-\alpha\sin\left(k_m l_2\right)\sin\left(k_m l_1\right)=0 \qquad (5.2)$$

where $\alpha=A_2/A_0$, A_0 is the cross sectional area of the intact pipe section whose length is l_1, A_2 ($A_2<A_0$) is the cross sectional area of the blocked pipe section whose length is l_2, $L=l_1+l_2$ is total pipe length, and $k_m=w_m/a$ is the wavenumber of the m^{th} fundamental (resonant) mode. Trigonometric manipulation of Eq. (5.2) gives

$$\cos\left(k_m L\right)+(1-\alpha)\sin\left(k_m l_2\right)\sin\left(k_m l_1\right)=0 \qquad (5.3)$$

Note that the second term in Eq. (5.3) represents the effect of the blockage on the dispersion relation. In fact, for $\alpha=1$, this second term vanishes and Eq. (5.3) becomes identical to the dispersion relation of an intact reservoir-pipe-valve (RPV) system (Eq. (2.54)).

Figure 5.2 plots the eigenfrequency variation with dimensionless length $\eta_2=l_2/L$ for the first four modes (m = 1, 2, 3 and 4) and for different values of α. Since $\alpha=1$ represent the eigenfrequencies of the intact pipe case, these eigenfrequencies are independent of η_2 and are shown as horizontal lines in Figure 5.2. When $\alpha\neq1$, the second term on the left hand side of Eq. (5.3) is not zero. Therefore, the eigenfrequency at a given mode m (w_m) deviates

from its intact case (w_m^0) (see Figure 5.2). In fact, Figure 5.2 shows that the eigenfrequencies for $\alpha \neq 1$ are oscillating with respect to the eigenfrequencies of the intact case (w_m^0). The eigenfrequency shift $\Delta w_m = \left(w_m - w_m^0 \right)$ takes positive values for some range of blockage length η_2 , negative values for some range of blockage length η_2 , and equal zero for particular values of blockage length η_2 . In addition, Figure 5.2 shows that the eigenfrequency shift (Δw_m) becomes pronounced with the severity of the blockage (*i.e.*, as α gets smaller), except for some special values of η_2 where the eigenfrequency shift is zero regardless of the severity of the blockages. Furthermore, Figure 5.2 shows that for $\eta_2 \neq 1/2$, the maximum eigenfrequency shift occurs at different blockage lengths as the blockage severity increases (*i.e.* the value of η_2 which Δw_m is an extremum varies with α). On the other hand, Δw_m reaches its extremum at $\eta_2 = 1/2$ regardless of the value of α .

The primary objective in this section is to provide physical and mathematical insights that can explain the above observations that emerged from Figure 5.2. Such understanding is presently lacking; yet, this insight is essential if the dispersion relation (Eq. (5.1)) is to become a viable approach for identifying blockages in fluid lines.

Figure 5.1 Reservoir-pipe-valve system with change in cross-sectional area.

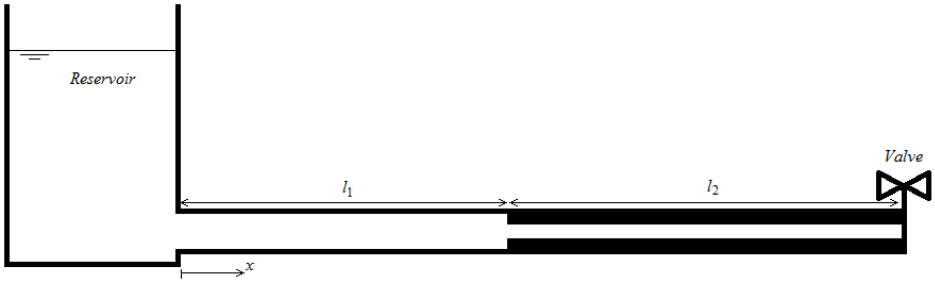

Figure 5.2 Dimensionless eigenfrequency variation with dimensionless length η_2 for the first four modes with different α values.

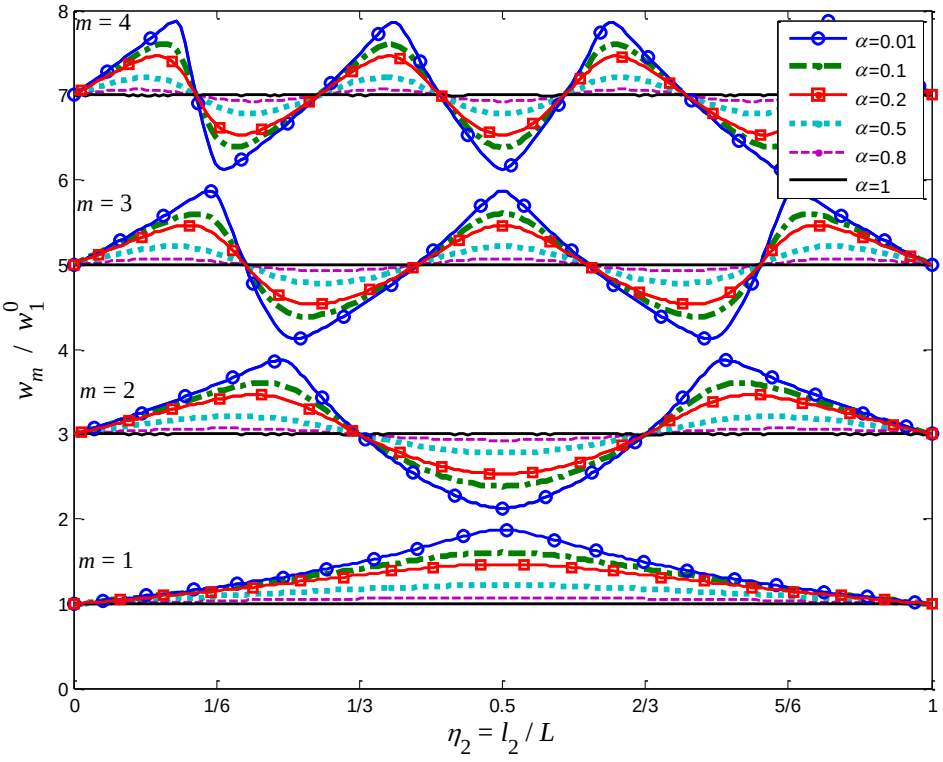

5.3. Harmonic solution for the case of blockage at the boundary

The transfer matrix method ([13]) can be used to determine q and h at any location $x \geq l_1$ in the junction pipe system (Figure 5.1) as follow

$$\begin{pmatrix} q(x,k_m) \\ h(x,k_m) \end{pmatrix} = \begin{bmatrix} \cos\left(k_m\left(x-l_1\right)\right) & -i\dfrac{gA_2}{a}\sin\left(k_m\left(x-l_1\right)\right) \\ -i\dfrac{a}{gA_2}\sin\left(k_m l_x\right) & \cos\left(k_m\left(x-l_1\right)\right) \end{bmatrix} \times \begin{bmatrix} 1 & 0 \\ 0 & 1 \end{bmatrix}$$
$$\times \begin{bmatrix} \cos\left(k_m l_1\right) & -i\dfrac{gA_0}{a}\sin\left(k_m l_1\right) \\ -i\dfrac{a}{gA_0}\sin\left(k_m l_1\right) & \cos\left(k_m l_1\right) \end{bmatrix} \times \begin{pmatrix} q(0,k_m) \\ h(0,k_m) \end{pmatrix} \;;\; \text{if } x \geq l_1 \tag{5.4}$$

where m represents the m^{th} natural harmonic mode and k_m is the m^{th} wavenumber. Equation (5.4) can be written as

$$\begin{pmatrix} q(x,k_m) \\ h(x,k_m) \end{pmatrix} = \begin{bmatrix} \underline{U}_{11} & \underline{U}_{12} \\ \underline{U}_{21} & \underline{U}_{22} \end{bmatrix} \begin{pmatrix} q(0,k_m) \\ h(0,k_m) \end{pmatrix} \tag{5.5}$$

where $\underline{U}_{11}$, $\underline{U}_{12}$, $\underline{U}_{21}$ and $\underline{U}_{22}$ can be determined from the matrix multiplication in Eq. (5.4). The pressure head and discharge at the reservoir are given by (see Section 2.3)

$$\begin{cases} h(0,k_m) = 0 \\ q(0,k_m) = -2\dfrac{g}{a}A_0 C = q_m^{amp} = i\dfrac{g}{a}A_0 h_m^{amp} \end{cases} \tag{5.6}$$

where q_m^{amp} and h_m^{amp} are the maximum flow and pressure head amplitudes which are complex constants, respectively; C is a complex constant of integration. Using Eq. (5.6), Eq. (5.5) yields

$$\begin{cases} q(x,k_m) = U_{11} q_m^{amp} \\ h(x,k_m) = U_{21} q_m^{amp} \end{cases} \tag{5.7}$$

Obtaining $\underline{U}_{11}$ and $\underline{U}_{21}$ from Eq. (5.4) leads to

$$\Rightarrow \begin{cases} \overline{q_m}(x,k_m) = \dfrac{q_m(x,k)}{q_m^{\text{amp}}} = \begin{bmatrix} \cos\left(k_m\left(x-l_1\right)\right)\cos\left(k_m l_1\right) \\ -\alpha\sin\left(k_m\left(x-l_1\right)\right)\sin\left(k_m l_1\right) \end{bmatrix} \\ \overline{h_m}(x,k_m) = \dfrac{h_m(x,k)}{h_m^{\text{amp}}} = \dfrac{1}{\alpha}\begin{bmatrix} \sin\left(k_m\left(x-l_1\right)\right)\cos\left(k_m l_1\right) \\ +\alpha\cos\left(k_m\left(x-l_1\right)\right)\sin\left(k_m l_1\right) \end{bmatrix} \end{cases} \quad (5.8)$$

where $\alpha = A_2/A_0$; $\bar{q}$ and $\bar{h}$ are the dimensionless discharge and pressure head, respectively.

The normalized kinetic energy ($\overline{T}_m$) and potential energy ($\overline{U}_m$) at a given location $x \geq l_1$ can be obtained from Eq. (5.8) as follows

$$\begin{cases} \overline{T}_m = \dfrac{T_m}{\frac{\rho}{2A_0}\left(q_m^{\text{amp}}\right)^2} = \dfrac{\frac{\rho}{2A_2}q_m^2}{\frac{\rho}{2A_0}\left(q_m^{\text{amp}}\right)^2} = \dfrac{1}{\alpha}\begin{bmatrix} \cos\left(k_m\left(x-l_1\right)\right)\cos\left(k_m l_1\right) \\ -\alpha\sin\left(k_m\left(x-l_1\right)\right)\sin\left(k_m l_1\right) \end{bmatrix}^2 \\ \overline{U}_m = \dfrac{U_m}{\frac{\rho}{2A_0}\left(q_m^{\text{amp}}\right)^2} = \dfrac{\frac{\rho}{2}A_2\left(\frac{g}{a}\right)^2 h_m^2}{\frac{\rho}{2A_0}\left(q_m^{\text{amp}}\right)^2} = \dfrac{1}{\alpha}\begin{bmatrix} \sin\left(k_m\left(x-l_1\right)\right)\cos\left(k_m l_1\right) \\ +\alpha\cos\left(k_m\left(x-l_1\right)\right)\sin\left(k_m l_1\right) \end{bmatrix}^2 \end{cases} \quad (5.9)$$

where $k_m = w_m/a$ is the m^{th} wavenumber, w_m is the m^{th} eigenfrequency (natural resonant frequency of the system) with the subscript "m" refers to the m^{th} resonant mode. Applying the boundary condition at the valve ($x = L$) where the flow and the kinetic energy are zero, Eq. (5.9) leads to Eq. (5.2).

5.4. Analysis and discussion of frequency-blockage interaction for blockage with small radial protrusion (*i.e.* α near 1)

5.4.1. Relationship between eigenfrequency shift and change in energy

The principle of action invariance, which states that the action is invariant for processes whose time scale is significantly larger than the period of oscillations, was successfully used by [112] to show that the shift in frequency due to change in area in a vocal tract is related to the change in total energy brought about by the work done on air by the contraction and

expansion of the vocal tract. In this section, the principle of action invariance is applied to the blockage shown in Figure 5.1. The derivation that follows is along the lines of that proposed by Fant ([41]).

The potential energy (U_m) and kinetic energy (T_m) per unit length for the m^{th} mode are ([65])

$$U_m = \frac{\rho A_0}{2}\left(\frac{g}{a}\right)^2 h_m^2 \;;\; T_m = \frac{\rho_0}{2} A_0 V_m^2 = \frac{\rho}{2A_0} q_m^2 \;;\; E_m = U_m + T_m = \frac{\rho A_0}{2}\left[\left(\frac{g}{a}\right)^2 h_m^2 + \frac{q_m^2}{A_0^2}\right] \quad (5.10)$$

where h_m, q_m and V_m are the unsteady pressure head, flow discharge and flow velocity of the m^{th} mode, respectively; ρ_0 is the fluid density; U_m, T_m and E_m are potential energy, kinetic energy and total energy for the m^{th} mode, respectively; a is the acoustic wave speed; g is the standard gravitational acceleration constant; A_0 is the intact cross sectional area of the pipe.

5.4.1.1. Short (discrete) blockage

Consider a short section of the blockage with length Δx and with radial extent small enough so that the associated changes in head and flow are small and can be neglected. As a result, the changes in kinetic, potential and total energies of mode m are:

$$\Delta U_m = \frac{\rho}{2}\Delta A\left(\frac{g}{a}\right)^2 h_m^2 \Delta x \;;\; \Delta T_m = -\frac{\rho \Delta A}{2A_0^2} q_m^2 \Delta x \;;\; \Delta E_m = \frac{\rho}{2}\Delta A\left[\left(\frac{g}{a}\right)^2 h_m^2 - \frac{q_m^2}{A_0^2}\right]\Delta x \quad (5.11)$$

where $\Delta A = A_2 - A_0 \le 0 = (\alpha - 1)A_0$ such that $\alpha = A_2/A_0$ is the dimensionless change in pipe cross sectional area due to the blockage. Equation (5.11) shows that a small localized blockage increases the kinetic energy and, conversely, reduces the potential energy. To explain, the blockage occupies some space that was occupied by the fluid prior to the formation of the blockage. Therefore, the mass of the fluid in the blockage region is smaller by a factor of $(1-\alpha)$ than the mass that was there before the blockage was formed. Since the change in head due to the small blockage is negligible (see Figure 5.3), the reduction of mass by a factor of $(1-\alpha)$ results in reduction in potential energy by the same factor. Since the change in flow rate due to the small blockage is negligible (see Figure 5.3), the flow velocity at the blockage is $1/\alpha$ times the flow velocity without the blockage. The reduction

in mass and increase in velocity due to the blockage result in an increase in kinetic energy by a factor of $1/(1-\alpha)$.

The explicit dependence of energy on frequency is brought about by considering the momentum and continuity equations (Eq. (2.48)) :

$$iwq_m^0 = -gA_0 \frac{dh_m^0}{dx} \tag{5.12}$$

$$iwh_m^0 = -\frac{a^2}{gA_0} \frac{dq_m^0}{dx} \tag{5.13}$$

where $i = \sqrt{-1}$ and the superscript "0" denotes intact pipe case. Therefore, the kinetic energy for the case with and without blockage are

$$T_m^0\left(w_m^0\right) = \frac{\rho}{2A_0}\left(q_m^0\right)^2 = -\frac{1}{\left(w_m^0\right)^2}\frac{\rho A_0 g^2}{2}\left(\frac{dh_m^0}{dx}\right)^2 \tag{5.14}$$

$$T_m^I\left(w_m^I\right) = T_m^0\left(w_m^0\right) + \Delta T_m = -\left[1+\frac{\Delta A}{A_0}\right]\frac{1}{\left(w_m^I\right)^2}\frac{\rho A_0 g^2}{2}\left(\frac{dh_m^0}{dx}\right)^2 \tag{5.15}$$

where w_m^0 is the m^{th} eigenfrequency for the case without blockage, and w_m^I is the m^{th} eigenfrequency for the case with blockage that would result from the change in kinetic energy only.

Dividing Eq. (5.14) by Eq. (5.15) yields

$$\frac{\left(w_m^I\right)^2}{\left(w_m^0\right)^2} = \left(1+\frac{\Delta A}{A_0}\right)\frac{T_m^0}{T_m^0 + \Delta T_m} \tag{5.16}$$

While the change in kinetic energy shifts the frequency of mode m from w_m^0 to w_m^I, the change in potential energy shifts the frequency of the same mode from w_m^I to w_m^{II}. Therefore,

$$U_m^I = \frac{\rho A_0}{2}\left(\frac{g}{a}\right)^2 \left(h_m^0\right)^2 = -\frac{1}{\left(w_m^I\right)^2}\frac{\rho a^2}{2A_0}\left(\frac{dq_m^0}{dx}\right)^2 \tag{5.17}$$

$$U_m^{II} = U_m^I\left(w_m^I\right) + \Delta U_m = -\left[1-\frac{\Delta A}{A_0}\right]\frac{1}{\left(w_m^{II}\right)^2}\frac{\rho a^2}{2A_0}\left(\frac{dq_m^0}{dx}\right)^2 \tag{5.18}$$

Dividing Eq. (5.17) by Eq. (5.18), yields

$$\frac{\left(w_m^{II}\right)^2}{\left(w_m^I\right)^2} = \left(1-\frac{\Delta A}{A_0}\right)\frac{U_m^I}{\left(U_m^I + \Delta U_m\right)} \tag{5.19}$$

Multiplying Eq. (5.16) with Eq. (5.19) yields

$$\frac{\left(w_m^{II}\right)^2}{\left(w_m^0\right)^2} = \frac{\left[1-\left(\Delta A/A_0\right)^2\right]}{\left(1+\frac{\Delta U_m}{U_m^I}\right)\left(1+\frac{\Delta T_m}{T_m^0}\right)} \approx \frac{1}{\left(1+\frac{\Delta U_m}{U_m^I}\right)}\frac{1}{\left(1+\frac{\Delta T_m}{T_m^0}\right)} \tag{5.20}$$

Since a small blockage results in small change in energy, Eq. (5.20) can be rewritten as:

$$\frac{\left(w_m^{II}\right)^2}{\left(w_m^0\right)^2} = \left(1-\frac{\Delta U_m}{U_m^I}\right)\left(1-\frac{\Delta T_m}{T_m^0}\right) \Rightarrow \frac{w_m^{II}}{w_m^0} = \left(1-\frac{\Delta U_m}{U_m^I}\right)^{\frac{1}{2}}\left(1-\frac{\Delta T_m}{T_m^0}\right)^{\frac{1}{2}} \tag{5.21}$$

Using Taylor expansion and neglecting second order terms, Eq. (5.21) becomes

$$\frac{w_m^{II}}{w_m^0} = 1-\frac{1}{2}\left(\frac{\Delta U_m}{U_m^I}+\frac{\Delta T_m}{T_m^0}\right) \tag{5.22}$$

The equipartition theorem for linear wave problems states that ([84]):

$$U_m^I\left(w_m^I\right) = T_m^0\left(w_m^0\right) = \frac{E_m^0}{2} \tag{5.23}$$

where E_m^0 is the total energy of the mode *m* for the case without blockage. Inserting Eq. (5.23) into Eq. (5.22), yields

$$\frac{w_m^{II}}{w_m^0}=1-\left(\frac{\Delta U_m}{E_m^0}+\frac{\Delta T_m}{E_m^0}\right)\Rightarrow\frac{w_m^{II}-w_m^0}{w_m^0}=-\frac{\left(\Delta U_m+\Delta T_m\right)}{E_m^0}\Leftrightarrow\frac{\Delta w_m}{w_m^0}=-\frac{\Delta E_m}{E_m^0} \qquad (5.24)$$

where Δw_m and ΔE_m are the eigenfrequency shift and the change in energy due to the blockage of the m^{th} mode, respectively. The same relation arises in many areas such as quantum mechanics, where it is referred to as the Ehrenfest theorem ([37]), and classical mechanics (e.g., oscillations of pendulums and acoustic waves in vocal tracts ([112]). Using Eq. (5.11), Eq. (5.24) becomes

$$\frac{\Delta w_m}{w_m^0}=-\frac{\Delta E_m}{E_m^0}=-\frac{\rho\Delta A}{2E_m^0}\Delta x\left[\left(\frac{g}{a}\right)^2\left(h_m^0\right)^2-\left(\frac{q_m^0}{A_0}\right)^2\right]=\left(\frac{\left|\Delta U_m\right|}{E_m^0}-\frac{\left|\Delta T_m\right|}{E_m^0}\right) \qquad (5.25)$$

It is clear from Eq. (5.25) that Δw_m is proportional to w_m^0. Thus, the eigenfrequency shift Δw_m will only become visible for very large frequencies w_m^0. Such high frequencies cannot be generated by mechanical devices such as valves and are susceptible to viscous dissipation even if they could be generated. It is for this reason that the focus in the literature is to develop detection methods for discrete blockages on the basis of local damping that such blockages generate (e.g., [99], [134]) rather than on the basis of the small shift that they produce.

5.4.1.2. Extended blockage

The eigenfrequency shift due to extended blockage such as the one shown in Figure 5.1 is determined by integrating Eq. (5.25) along the pipe as follows:

$$\frac{\overline{\Delta w_m}}{w_m^0}=\frac{\int_0^L\Delta w_m dx}{w_m^0}=-\int_0^L\frac{\Delta E_m}{E_m^0}dx=-\frac{\rho}{2E_m^0}\Delta A\int_{l_1}^L\left[\left(\frac{g}{a}\right)^2\left(h_m^0\right)^2-\frac{\left(q_m^0\right)^2}{A_0^2}\right]dx \qquad (5.26)$$

where $\overline{\Delta w_m}$ and $\Delta\overline{E_m}$ are the shift in eigenfrequency and the change in energy due to the extended blockage, respectively. Note that ΔA came out from under the integral because it is a constant for the example being considered (Figure 5.1). The pressure head and discharge solution for an intact Reservoir-Pipe-Valve system are (Eq. (2.52)):

$$\begin{cases} h_m\left(x,k_m^0\right)=2iC\sin\left(k_m^0x\right)=h_m^{\text{amp}}\sin\left(k_m^0x\right) \\ q_m\left(x,k_m^0\right)=-2C\dfrac{g}{a}A_0\cos\left(k_m^0x\right)=q_m^{\text{amp}}\cos\left(k_m^0x\right) \end{cases} \tag{5.27}$$

where C is a complex constant of integration ; h_m^{amp} and q_m^{amp} are the m^{th} maximum complex amplitudes of pressure head and flow discharge, respectively. Inserting Eq. (5.27) into Eq. (5.10) gives

$$E_m^0=\frac{\rho LA_0}{2}\left(4\left|C\right|^2\left(\frac{g}{a}\right)^2\right)=\frac{\rho LA_0}{2}\left(\frac{g}{a}\right)^2h_m^{amp}\overline{h_m^{amp}}=\frac{\rho LA_0}{2}\left(\frac{1}{A_0}\right)^2q_m^{amp}\overline{q_m^{amp}} \tag{5.28}$$

and inserting Eq. (5.28) into Eq. (5.25) yields

$$\frac{\overline{\Delta w_m}}{w_m^0}=-\frac{\overline{\Delta E_m}}{E_m^0}=-\frac{\Delta A}{A_0}\int_{l_1}^{L}\left[\left(\frac{h_m^0}{h_m^{\text{amp}}}\right)^2-\left(\frac{q_m^0}{q_m^{\text{amp}}}\right)^2\right]\frac{dx}{L}=\int_{l_1}^{L}\left(\frac{\left|\Delta U_m\right|}{E_m^0}-\frac{\left|\Delta T_m\right|}{E_m^0}\right)dx \tag{5.29}$$

Equation (5.29) shows that the eigenfrequency shift is related directly to the change in energy for blockages whose radial extent is small enough that the head and flow of each mode for the blocked pipe are approximately equal to the blockage-free case (*i.e.*, h_m and q_m with and without blockage are the same (see Figure 5.3)).

Inserting Eq. (5.27) into Eq. (5.29) and carrying out the integration gives

$$\begin{aligned} \frac{\overline{\Delta w_m}}{w_m^0}&=-\frac{\overline{\Delta E_m}}{E_m^0}=-\frac{\Delta A}{A_0}\int_{L-l_2}^{L}\left[\sin^2\left(k_m^0x\right)-\cos^2\left(k_m^0x\right)\right]\frac{dx}{L} \\ &=\frac{\Delta A}{2Lk_m^0A_0}\left[\sin\left(2Lk_m^0\right)-\sin\left(2Lk_m^0-2k_m^0l_2\right)\right]. \end{aligned} \tag{5.30}$$

Using Eq. (2.54) yields

$$\begin{aligned} \frac{\overline{\Delta w_m}}{w_m^0}&=-\frac{\overline{\Delta E_m}}{E_m^0}=\frac{\Delta A}{2L\left(2m-1\right)\dfrac{\pi}{2L}A_0}\begin{bmatrix}\sin\left(\left(2m-1\right)\pi\right) \\ -\sin\left(\left(2m-1\right)\pi-\left(2m-1\right)\pi\eta_2\right)\end{bmatrix} \\ &=\frac{-\Delta A}{\left(2m-1\right)\pi A_0}\sin\left(\left(2m-1\right)\pi\eta_2\right) \end{aligned} \tag{5.31}$$

which gives

$$\frac{\overline{\Delta w_m}}{w_1^0} = -\left(2m-1\right)\frac{\overline{\Delta E_m}}{E_m^0} = \frac{\left(1-\alpha\right)}{\pi}\sin\left(2\pi\left(2m-1\right)\frac{\eta_2}{2}\right) \qquad (5.32)$$

Equation (5.32) is consistent with the form in Qunli and Fricke ([105]) and Duan, et al. ([35]), and shows the explicit relationship between eigenfrequency shift and change in energy resulting from the extended blockage. It is clear from Eq. (5.32) that when α tends to 1 (*i.e.*, blockage-free case), both the eigenfrequency shift and the change in energy approach zero for all η_2. In addition, Figure 5.4 plots the eigenfrequency variation given by Eq. (5.32) as well as that given by the full dispersion relation (Eq. (5.3)) for the case of mode m = 2. Good quantitative agreement between Eq. (5.3) and its approximate form (Eq. (5.32)) is found for $\alpha \geq 0.7$. There is overall qualitative agreement between these two equations for all α. Although not plotted here, a similar conclusion is found for other m modes. Such agreement supports the application of the principle of action invariance to analyse the eigenfrequency shift induced by a blockage in terms of the change in energy in a pipe due to the presence of blockage.

It could be shown that Eq. (5.32) is symmetric around η_2 =0.5 which agrees with the symmetry feature observed in Figure 5.2. This symmetry feature is a special instance of the junction case under consideration, and therefore is not general to all random variation of blockages in a pipe system. More involved and complex blockage in a pipe will be considered in future work.

Figure 5.3 Pressure head and flow harmonics variations for shallow blockage ($\alpha = 0.8$)

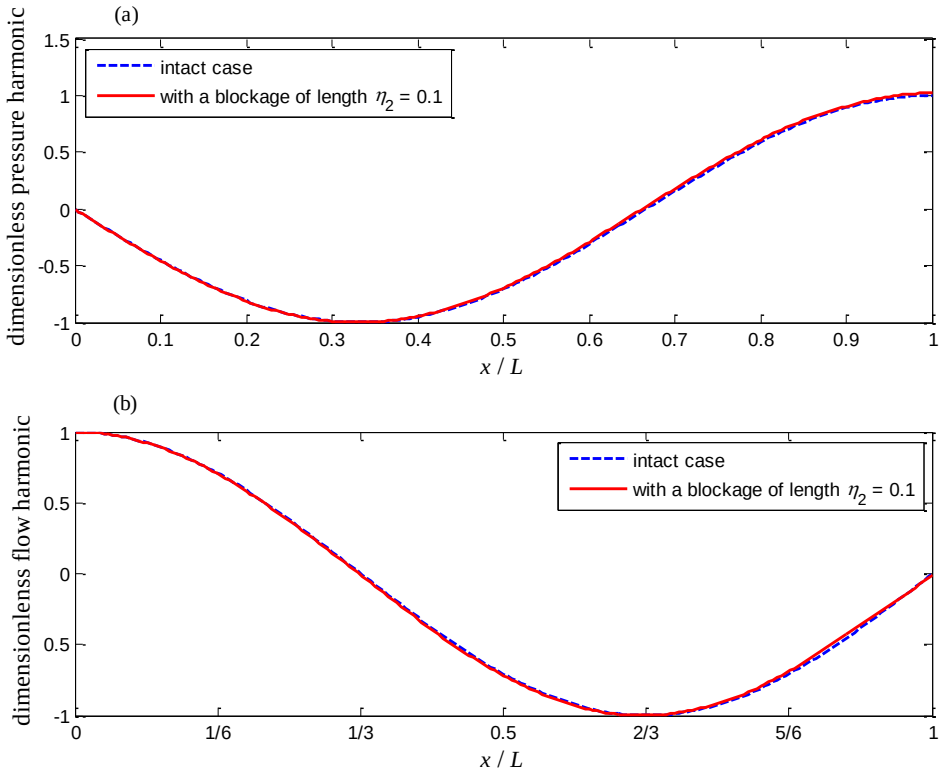

(a) Top **Pressure head harmonic at *m* = 2**

(b) Bottom **Flow harmonic at *m* = 2**

Figure 5.4 Normalized eigenfrequency variation with length η_2 for *m* = 2: comparison between exact solution (Eq. (5.3)) and approximate solution (Eq. (5.32)) (Energy approach).

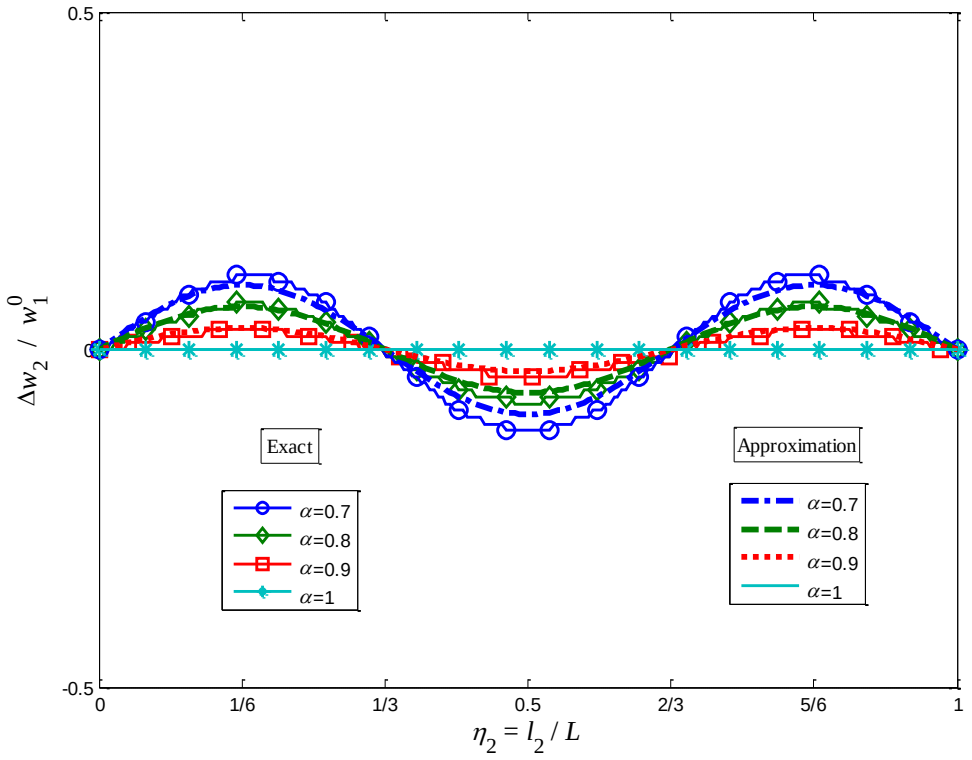

5.4.2. Work of the radiation pressure

The change in energy of the m^{th} mode, given by Eq. (5.32), is due to the work done to form the blockage ([112]). This work is performed against the radiation pressure and it is derived below. To relate the change in energy to the work of the radiation pressure ([7], [6]), multiply Eq. (5.13) by the complex conjugate of head ($\overline{h_m^0}$) and Eq. (5.12) by the complex conjugate of the velocity ($\overline{V_m^0}$). Taking the difference gives

$$\overline{V_m^0}\frac{dh_m^0}{dx} - \overline{h_m^0}\frac{dV_m^0}{dx} = iw_m^0\left(\frac{g\overline{h_m^0}h_m^0}{a^2} - \frac{\overline{V_m^0}V_m^0}{g}\right). \qquad (5.33)$$

Adding $h_m^0 \frac{d\overline{V_m^0}}{dx} - h_m^0 \frac{d\overline{V_m^0}}{dx}$ to the left hand side of Eq. (5.33) gives

$$\frac{d\left(h_m^0 \overline{V_m^0}\right)}{dx} - \left(\overline{h_m^0} \frac{dV_m^0}{dx} + h_m^0 \frac{d\overline{V_m^0}}{dx} \right) = iw_m^0 \left(\frac{g\overline{h_m^0} h_m^0}{a^2} - \frac{\overline{V_m^0} V_m^0}{g} \right). \qquad (5.34)$$

Note that

$$\overline{h_m^0} \frac{dV_m^0}{dx} + h_m^0 \frac{d\overline{V_m^0}}{dx} = \overline{h_m^0} \frac{dV_m^0}{dx} + \overline{\overline{h_m^0} \frac{dV_m^0}{dx}} \qquad (5.35)$$

where according to Eq. (5.13),

$$-\frac{igw_m^0 h_m^0 \overline{h_m^0}}{a^2} = \overline{h_m^0} \frac{dV_m^0}{dx}. \qquad (5.36)$$

Thus

$$\overline{h_m^0} \frac{dV_m^0}{dx} + \overline{\overline{h_m^0} \frac{dV_m^0}{dx}} = -\frac{igw_m^0 h_m^0 \overline{h_m^0}}{a^2} + \frac{igw_m^0 h_m^0 \overline{h_m^0}}{a^2} = 0 \qquad (5.37)$$

and therefore,

$$\frac{d\left(h_m^0 \overline{V_m^0}\right)}{dx} = i \frac{w_m^0}{g} \underbrace{\left(\frac{g^2}{a^2} \overline{h_m^0} h_m^0 - \overline{V_m^0} V_m^0 \right)}_{\text{radiation pressure}}. \qquad (5.38)$$

The work of the radiation pressure to form the blockage is:

$$\int_{l_1}^{L} \Delta A \frac{\rho}{2} \left(\frac{g^2}{a^2} \overline{h_m^0} h_m^0 - \overline{V_m^0} V_m^0 \right) dx = -\frac{ig}{w_m^0} \frac{\rho}{2} \int_{l_1}^{L} \Delta A \frac{d\left(h_m^0 \overline{V_m^0}\right)}{dx} dx \qquad (5.39)$$

Equation (5.39) shows that

$$\int_{l_1}^{L} \Delta A \frac{\rho}{2}\left(\frac{g^2}{a^2}\overline{h_m^0}h_m^0 - \overline{V_m^0}V_m^0\right)dx = -\frac{ig}{w_m^0}\frac{\rho}{2}\int_{l_1}^{L}\Delta A\frac{d\left(h_m^0\overline{V_m^0}\right)}{dx}dx$$
$$= -\frac{ig}{w_m^0}\frac{\rho}{2}\Delta A\left[\left(h_m^0\overline{V_m^0}\right)_L - \left(h_m^0\overline{V_m^0}\right)_{l_1}\right] \qquad (5.40)$$

Using Equation (5.29) gives

$$\frac{\overline{\Delta w_m}}{w_m^0} = \mathrm{Re}\left[\frac{ig}{E_m^0 w_m^0}\frac{\rho}{2}\frac{\Delta A}{A}\int_{l_1}^{L}\frac{d\left(h_m^0\overline{q_m^0}\right)}{dx}dx\right] = \xi_m\left[\left(\frac{h_m^0\overline{q_m^0}}{h_m^{amp}\overline{q_m^{amp}}}\right)_{l_1} - \left(\frac{h_m^0\overline{q_m^0}}{h_m^{amp}\overline{q_m^{amp}}}\right)_L\right] \qquad (5.41)$$

with

$$\xi_m = -i\frac{\rho g}{2w_m^0 E_m^0}\frac{\Delta A}{A}h_m^{amp}\overline{q_m^{amp}} = \frac{a}{w_m^0 L}(1-\alpha) \qquad (5.42)$$

and "Re" denotes real part. Equation (5.41) shows that the eigenfrequency shift depends on the difference between the works done at the blockage boundaries. For the current case of a blockage at the downstream boundary, the work at the valve is always zero, and therefore, Eq. (5.41) becomes

$$\frac{\overline{\Delta w_m}}{w_m^0} = \xi_m\left(\frac{h_m^0\overline{q_m^0}}{h_m^{amp}\overline{q_m^{amp}}}\right)_{l_1} \qquad (5.43)$$

Inserting Eq. (5.27) into Eq. (5.43) leads to Eq. (5.32).

5.4.3. Analysis and discussion of the zero eigenfrequency shift

Figure 5.2 shows there is zero shift for m = 1 at η_2 = 0, 1; m = 2 at η_2 = 0, 1/3, 2/3 1; m = 3 at η_2 = 0, 1/5, 2/5, 3/5, 4/5, 1, and m = 4 at η_2 = 0, 1/7, 2/7, 3/7, 4/7, 5/7, 6//7, 1. This result can be generalized for all m by setting Eq. (5.32) to zero:

$$\sin\left(2\pi\left(2m-1\right)\frac{\eta_2}{2}\right)=0\Rightarrow\pi\left(2m-1\right)\eta_2=\left(\tau-1\right)\pi\ \ ;\ \ \tau=1,2,3...$$
$$\Rightarrow\eta_2=\eta_2\left(m,\tau\right)=\frac{\tau-1}{\left(2m-1\right)}\ \le 1\ ;\ \ \tau\le 2m \qquad (5.44)$$

Equation (5.44) gives the length of the blockage for which the m^{th} mode experiences no shift. Note that the condition that $\tau \le 2m$ is due to the fact that the blockage cannot be longer than the pipe (*i.e.*, $\eta_2 \le 1$). The values of η_2 where zero frequency is obtained from Figure 5.2 can be derived by evaluating Eq. (5.44) for m = 1, 2, 3 and 4. For example, evaluating Eq. (5.44) for m=2 gives $\eta_2\left(2,1\right)=0$, $\eta_2\left(2,2\right)=1/3$, $\eta_2\left(2,3\right)=2/3$ and $\eta_2\left(2,4\right)=1$. These values correspond to the zero shift locations shown in Figure 5.2.

From an energy perspective, Eq. (5.29) shows that the zero shift of the m^{th} mode occurs when the blockage produces either (i) zero change in the potential energy and the kinetic energy or (ii) non-zero but equal change in potential and kinetic energy. This is illustrated in Figure 5.5 for m=2. It is evident that the change in potential and kinetic energy are non-zero, but equal at η_2 = 1/3, while the change in both potential and kinetic energy are zero at η_2 = 0, 2/3, 1 (see Figure 5.5).

The zero eigenfrequency shift of mode m due to a blockage means that the work done by the radiation pressure to form the blockage is zero ([112]). According to Eq. (5.43) this work is zero when either the pressure or velocity at the edge of the blockage is zero. When the blockage extends from the valve to x = 2L/3, the pressure of mode m = 2 is zero at x = 2L/3 (see Figure 5.6). Therefore, the work of the radiation pressure is zero implying the change in energy of mode m = 2 is zero and, thus, the eigenfrequency shift is zero. When the blockage extends from the valve to x = L/3, the velocity of mode m = 2 is zero at x = L/3 (see Figure 5.6). Therefore, the work of the radiation pressure is zero implying the change in energy of mode m = 2 is zero and, thus, the eigenfrequency shift is zero. In general, the eigenfrequency shift of mode m is zero when the values of ($h_m^0 V_m^0$) of this mode at either end of the blockage are equal.

Physically, when the blockage extends from the downstream end to the pressure node (η_2 = 2/3, case (a) in Figure 5.7), the pipe system for this mode m = 2 is effectively divided into

two pipe subsystems. Subsystem I is a reservoir-pipe-valve with a pipe length equal to the blockage length $l_2 = L/3$. Subsystem II is a reservoir-pipe-reservoir with a pipe length equal to $l_1 = L\text{-}l_2 = 2L/3$. The wavelengths of the natural modes of subsystem I are $\lambda_n = 4l_2/(2\bar{n}-1) = 4L/3(2\bar{n}-1)$ for $\bar{n} = 1, 2\ldots$. Therefore, the wavelength of the fundamental (n=1) mode is $\lambda_1 = 4l_2$ which explains the quarter wave in subsystem I (see Figure 5.7, case (a)). The wavelengths of the natural modes of subsystem II are $\lambda_n = 2l_2/\bar{n} = 4L/3\bar{n}$ for $\bar{n} = 1, 2\ldots$. Therefore, the wavelength of the fundamental ($\bar{n}$=1) mode is $\lambda_1 = 2l_2$, which explains the half wave in subsystem II (see Figure 5.7, case (a)). That is, mode m = 2 of the whole pipe system is made up of the two fundamental modes of subsystem I and II. The same reasoning can be used to explain the subsystems in Figure 5.7, case (b), as well as the zero shifts that occur for other modes m.

Figure 5.5 Variation with η_2 of total change in potential and kinetic energy in the pipe with blockage along with the eigenfrequency shift at mode m = 2 and $\alpha = 0.8$.

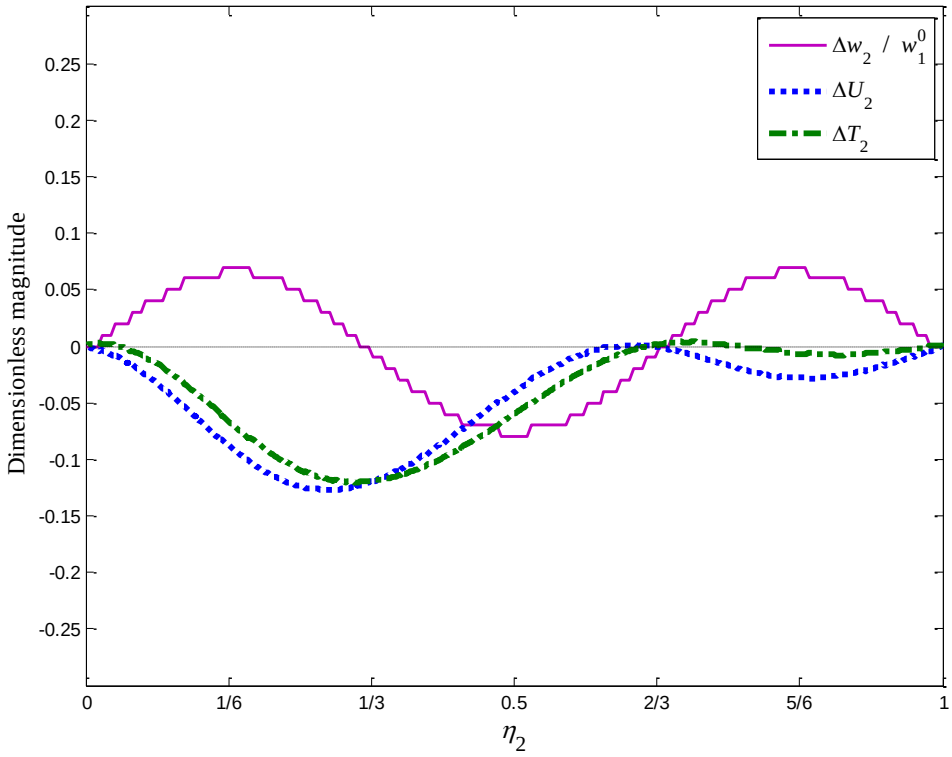

Figure 5.6 Eigenfrequency shift variation at mode *m* = 2 for different α values along with the intact pressure harmonic.

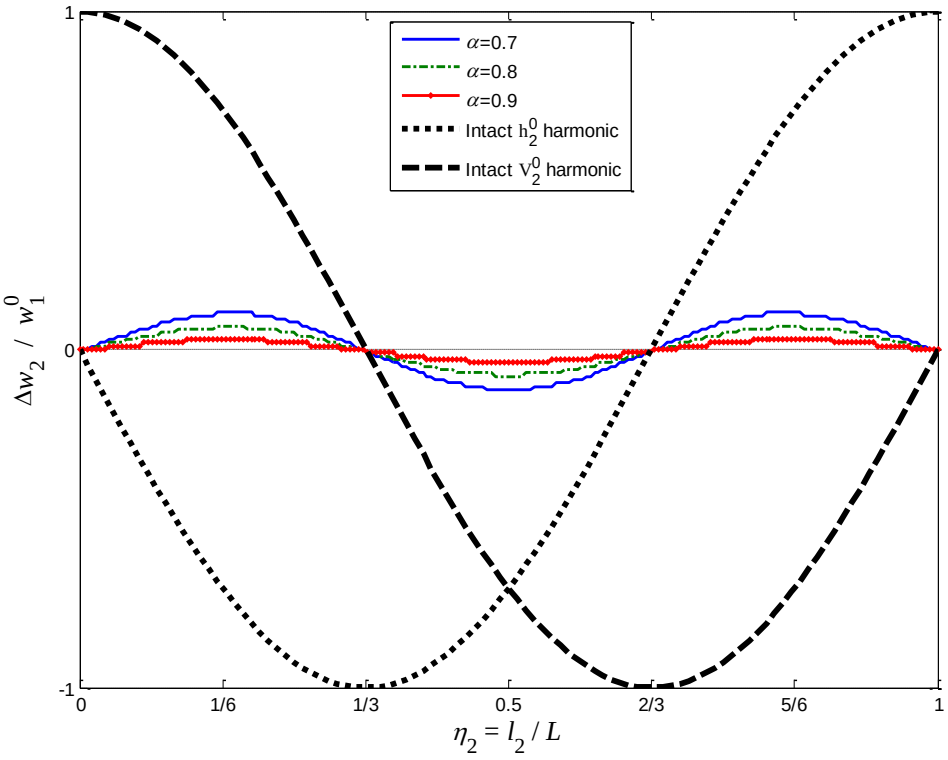

Figure 5.7 Sketch depicting how the harmonic at mode *m* = 2 is subdivided into single subharmonics. Case (a) and case (b) correspond to the zero shift cases where $\eta_2 = 1/3$ and $\eta_2 = 2/3$, respectively.

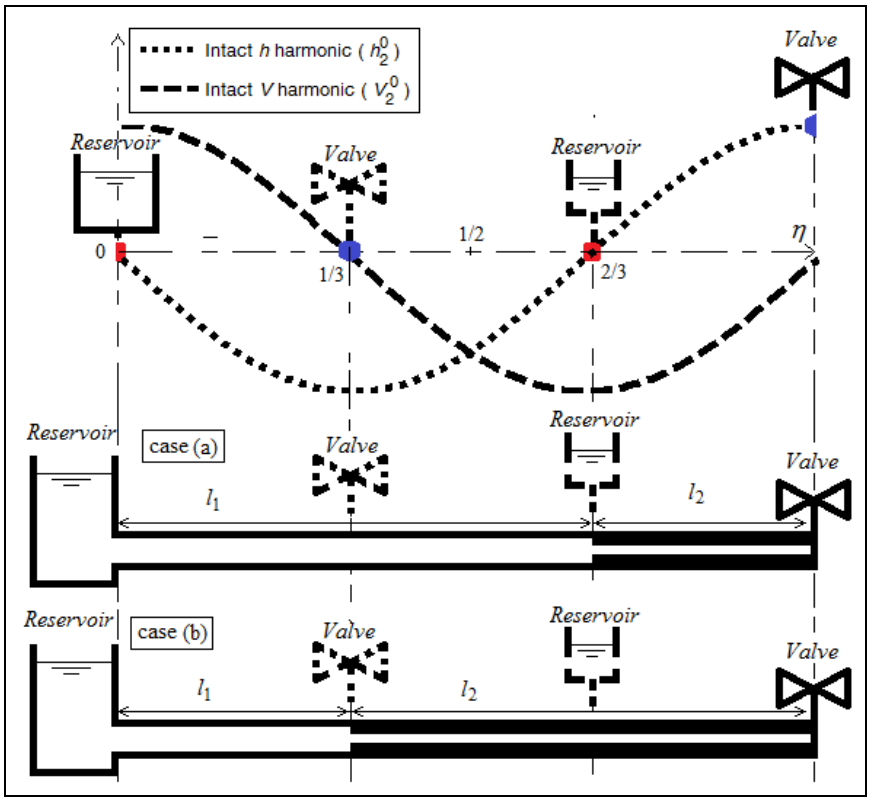

5.4.4. Analysis and discussion of the positive and negative eigenfrequency shift

Figure 5.2 shows that mode *m* = 1 experiences positive shift for all η_2 (*i.e.*, for all blockage lengths); mode *m* = 2 experiences positive for η_2 in]0,*L*/3[∪]2*L*/3, *L*[and negative elsewhere; mode *m* = 3 experiences positive for η_2 in]0,*L*/5[∪]2*L*/5, 3*L*/5[∪]4*L*/5, *L*[and negative elsewhere; and mode *m* = 4 experiences positive for η_2 in]0, *L*/7[∪]2*L*/7, 3*L*/7[∪]4*L*/7, 5*L*/7[∪]6*L*/7, *L*[and negative elsewhere. These observations are corroborated by Eq. (5.32).

Equation (5.29) shows that a positive eigenfrequency shift in mode *m* occurs when the presence of the blockage results in a net negative change in the total energy of this mode.

This, in turn, occurs when the change in potential energy is larger than the change in kinetic energy (see right hand side of Eq. (5.29)). Conversely, Eq. (5.29) shows that a negative eigenfrequency shift in mode *m* occurs when the presence of the blockage results in a net positive change in the total energy of this mode. This in turn occurs when the change in potential energy is less than the change in kinetic energy (see right hand side of Eq. (5.29)). This is illustrated in Figure 5.5 for the case of *m* = 2. In particular, Figure 5.5 shows that the change in potential energy is larger than the change in kinetic energy of mode *m* = 2 for η_2 in]0, *L*/3[$\cup$]2*L*/3, *L*[which is the region where there is a positive eigenfrequency shift of mode *m* =2 (see Figure 5.2). In addition, Figure 5.5 shows that change in potential energy is less than the change in kinetic energy of mode *m* = 2 for η_2 in]*L*/3, 2*L*/3[which is the region where there is negative eigenfrequency shift of mode *m* =2 (see Figure 5.2).

To further investigate the eigenfrequency shift in mode *m* = 2, Figure 5.8 shows two cases for which the shift is positive (case (c)) and negative (case (d)). The pressure head and velocity harmonics corresponding to case (c) and case (d) are given in Figure 5.9a and 5.9b, respectively. It is clear from Figure 5.9a that mode *m* = 2 has a positive *h* and a negative *V* at *x* = 5*L*/6. Therefore, $hV\Delta A$ of this mode is negative at *x* = 5*L*/6 implying that the work of the radiation pressure (Eq. (5.39)) and the change in energy for a blockage that extends from the valve to *x* = 2*L*/3 are negative. This explains why mode *m* = 2 experiences a negative shift in this case (Figure 5.2). Figure 5.9b shows that mode *m* = 2 has negative *h* and *V* at *x* = 7*L*/12. Therefore, $hV\Delta A$ of this mode is positive at *x* = 7*L*/12 implying that the work of the radiation pressure (Eq. (5.39)) and the change in energy for a blockage that extends from the valve to *x* = 7*L*/12 are positive. This explains why mode *m* = 2 experiences a positive shift in this case (Figure 5.2). In fact, $hV\Delta A$ of the m^{th} mode varies as $\sin\left(\left(2m-1\right)\pi\eta_2\right)$; thus, there is (i) a positive shift when the argument of the sine function varies is in the range $]2\mu\,\pi$, $(2\mu+1)\pi[$ where μ is an integer counting number and (ii) a negative shift otherwise. In general, a given mode *m* experiences negative eigenfrequency shift when the work of the radiation pressure due to the formation of the blockage is positive and experiences a positive eigenfrequency shift when the work of the radiation pressure due to the formation of the blockage is negative. It is noted that a positive eigenfrequency shift is sometimes referred to as *length shortening* and a negative eigenfrequency shift as *length extending* (e.g., [105]).

The maximum eigenfrequency shift position corresponds to the length of the blockage at which the change in energy is an extremum. Mathematically, this occurs when the derivative of Eq. (5.32) is zero; that is,

$$\cos\left(2\pi(2m-1)\frac{\eta_2}{2}\right)=0\Rightarrow 2\pi(2m-1)\frac{\eta_2}{2}=(2\overline{m}'-1)\frac{\pi}{2}\quad;\quad \overline{m}'=1,2,3$$
$$\Rightarrow \eta_2=\eta_2\left(m,\overline{m}'\right)=\frac{(2\overline{m}'-1)}{2(2m-1)}\le 1\quad;\quad \overline{m}'\le 2m-1 \qquad (5.45)$$

For example, consider the case of m = 2. The condition, $n \le 2m$-1 = 3 gives $\overline{m}'$ = 1, 2 and 3. Therefore, there are three maxima at 1/6, 1/2 and 5/6 (see Figure 5.4). These maxima correspond to $h_m V_m\ \Delta A$, which varies as $\sin\left((2m-1)\pi\eta_2\right)$, having the largest magnitude (*i.e.*, where the work of the radiation pressure is extremum).

Figure 5.8 Sketches of the junction system for two shift cases: Case (a) gives leads to positive shift ($\eta_2 = 1/6$) and case (d) leads to negative shift ($\eta_2 = 5/12$).

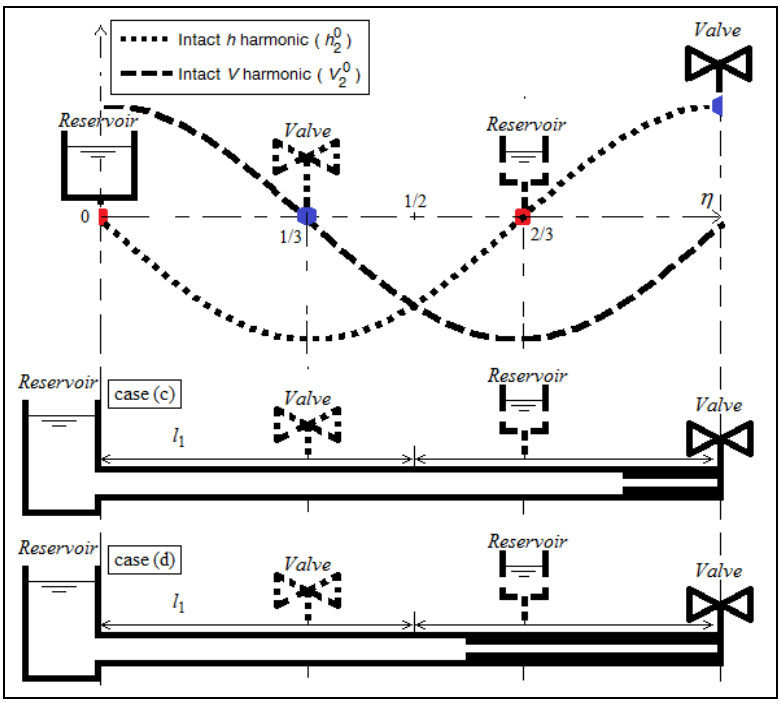

Figure 5.9 Dimensionless pressure and velocity harmonics when *m* = 2 and $\alpha = 0.4$. The black squared boxes are sketchs of the blockage.

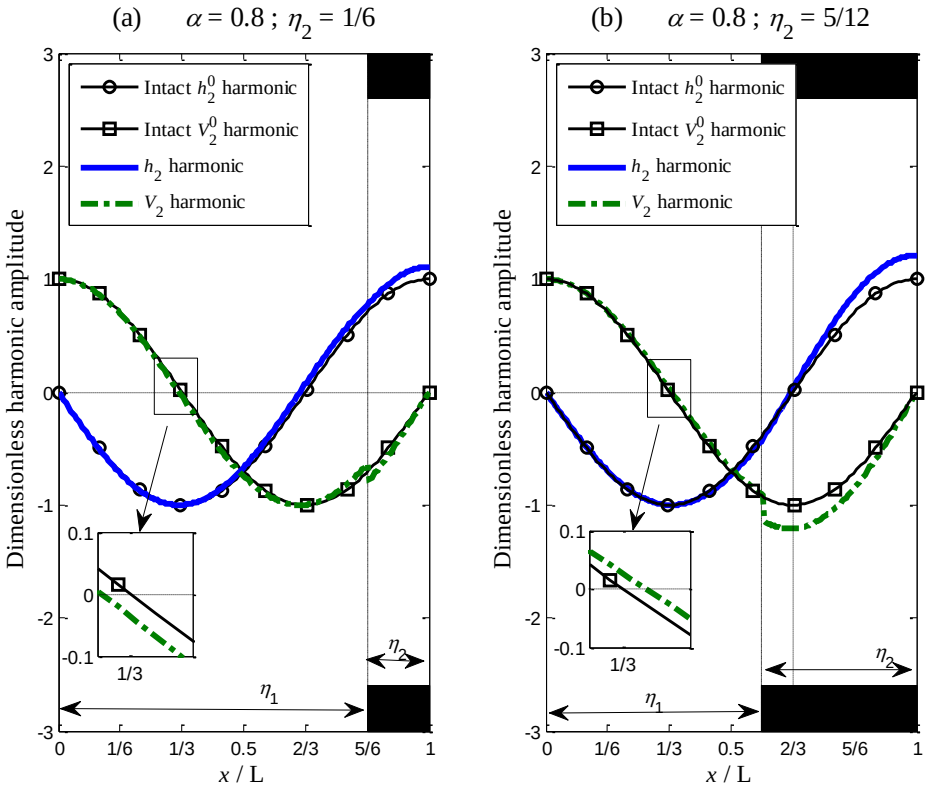

(a) Left $\eta_2 = 1/6$ **leads to positive shift**

(b) Right $\eta_2 = 5/12$ **leads to negative shift**

5.5. Analysis and discussion of frequency-blockage interaction for blockage with large radial protrusion (*i.e.*, α near 0)

The previous section is devoted to blockage with small radial protrusion. In this section, a blockage with large radial protrusion (referred to as severe blockage in this work) is investigated.

For a severe blockage (*i.e.*, α tends to 0), Eq. (5.2) reduces to

$$\cos(kl_1)\cos(kl_2) = 0 \tag{5.46}$$

which implies

$$\cos(kl_1) = 0 \Rightarrow \frac{w_m^{s_1}}{w_1^0} = \frac{(2m-1)}{\eta_1} \quad ; \quad m = 1, 2, 3... \tag{5.47}$$

or

$$\cos(kl_2) = 0 \Rightarrow \frac{w_m^{s_2}}{w_1^0} = \frac{(2m-1)}{\eta_2} \quad ; \quad m = 1, 2, 3... \tag{5.48}$$

where w_1^0 is the first eigenfrequency of the intact pipe case and $w_m^{s_1}$ and $w_m^{s_2}$ are the m^{th} eigenfrequency for the case of severe blockage. Effectively, the severe blockage decouples the pipe system responses into two independent subsystems. Subsystem 1 consists of the pipe with length l_1 bounded by the upstream reservoir and the blockage. The blockage, being severe, would act in a manner similar to a valve. That is, a severe blockage imposes large impedance on the flow as a valve would. Therefore, subsystem 1's response is equivalent to a reservoir-pipe-valve system. In fact, the resonant frequencies given by Eq. (5.47) are for a RPV system, where the pipe has a length l_1. It is for this reason that a superscript "s_1" is used in Eq. (5.47). Subsystem 2 consists of another reservoir-pipe-valve system in which the narrow blockage opening functions as a small diameter pipe of length l_2, while the much larger pipe diameter of lengths l_1 acts as a reservoir. Indeed, the resonant frequencies given by Eq. (5.48) are for a RPV system, where the pipe has a length l_2. A sketch showing the decoupling into two RPV subsystems is given in Figure 5.10.

The decoupling of the pipe system into two subsystems can be understood from an energy perspective. The ratio of reflected to incident energy at the interface between the blocked and unblocked pipe sections is $(Z_1-Z_2)^2/(Z_1+Z_2)^2 = (\alpha-1)^2/(\alpha+1)^2$, where $Z_1 = \rho a/A_0$ is the impedance of the unblocked pipe section and $Z_2 = \rho a/A_2$ is the impedance of the pipe section that has the severe blockage. The ratio of the transmitted to incident energy at the interface between the blocked and unblocked pipe sections is $4Z_1Z_2/(Z_1+Z_2)^2 = 4\alpha/(\alpha+1)^2$. Clearly, as α tends to 0, the reflection coefficient approaches 1 and the transmission coefficient approaches zero. Therefore, a wave that is generated in subsystem 1 is largely trapped in this

subsystem. Conversely, a wave that is generated in subsystem 2 is largely trapped in this subsystem. It is in this sense that the decoupling should be understood.

Figure 5.10 Schematic figure of the decoupling of the junction system into two intact uncoupled RPV subsystems when α tends to 0

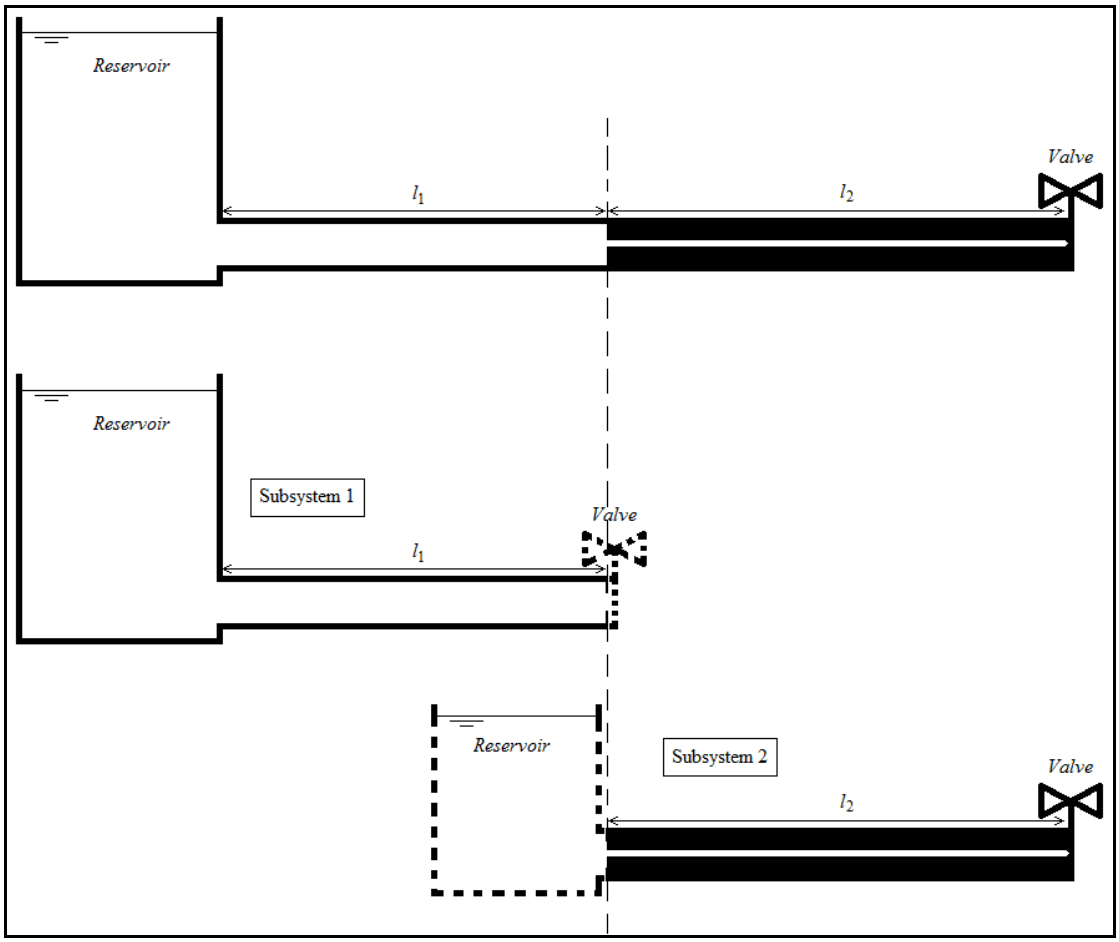

The eigenfrequencies of the whole system are the union of the eigenfrequencies of subsystems 1 and 2. That is, $w_m = \{(2m\text{-}1)a\pi/(2l_1)\} \cup \{(2m\text{-}1)a\pi/(2l_2)\}$, where $\cup$ is the union operator. It is clear that if the blockage length l_2 is much smaller than l_1, then the low frequencies are governed by subsystem 1 and vice-versa. To see this, consider Figure 5.11. The fundamental frequencies of subsystem 1 ($\cos(kl_1) = 0$) and subsystem 2 ($\cos(kl_2) = 0$) are plotted for m = 1, 2, 3 and 4. It can be seen that w_1, w_2, w_3 and w_4 are governed by subsystem

2 for a short (*i.e.*, η_2 close to 0) blockage and by subsystem 1 for a long (*i.e.*, η_2 close to 1) blockage. For example, using Eq. (5.47), the first four dimensionless eigenfrequencies for subsystem 1 for η_2 = 1/3 are 3/2, 9/2, 15/2 and 21/2. In addition, using Eq. (5.48), the first four dimensionless eigenfrequencies for subsystem 2 for η_2 = 1/3 are 3, 9, 15 and 21. The union of these eigenfrequencies is {3/2, 9/2, 15/2, 21/2}$\bigcup${3, 9, 15, 21} = {3/2, 3, 9/2, 15/2, 9, 21/2, 15, 21}. Therefore, the first four dimensionless resonant frequencies for the overall system are {3/2, 3, 9/2, 15/2} which agree with values that can be read from Figure 5.11 when η_2 = 1/3. Note that the first, third and fourth of these frequencies are the first three resonant frequencies of subsystem 1 and the second is the eigenfrequency of subsystem 2. In the preceding eigenfrequency sets, the four fundamental frequencies of the overall system are determined manually by calculating the four fundamental frequencies of each subsystem and then sorting them from lowest to largest value. In order to automate this sorting process, the following condition is specified on Eq. (5.3):

$$-1 \;\le\; \underbrace{\cos(kL) = -\sin(kl_1)\sin(kl_2)}_{(\alpha \approx 0)} \;\le\; 1 \qquad (5.49)$$

which gives

$$2(m-1) \le \frac{w_m^s}{w_1^0} \le 2m \;;\; m = 1,2,3... \qquad (5.50)$$

where w_m^s is the m^{th} eigenfrequency of the whole junction system for the case of severe cross sectional area variation (α tends to 0). Imposing the condition in Eq. (5.50) on Eqs. (5.47) and (5.48), gives

$$\frac{w_m}{w_1^0} = \begin{cases} \dfrac{w_{m_1}^{s_1}}{w_1^0} = \dfrac{(2m_1 - 1)}{1-\eta_2} \;\; ; \;\; \text{when: } 2m \le \dfrac{w_{m_1}^d}{w_1^0} \le 2m+2 \\ \\ \dfrac{w_{m_2}^{s_2}}{w_1^0} = \dfrac{(2m_2 - 1)}{\eta_2} \;\; ; \;\; \text{when: } 2m \le \dfrac{w_{m_2}^d}{w_1^0} \le 2m+2 \end{cases} \qquad (5.51)$$

where, just for clarity, m_1 and m_2 are introduced as mode numbers for the uncoupled subsystem 1 and subsystem 2, respectively.

changing the conditions in Eq. (5.51) in terms of η_2 yields

$$\frac{w_m^d}{w_1^0}=\begin{cases}\dfrac{w_{m_1}^{(1)}}{w_1^0}=\dfrac{(2m_1+1)}{1-\eta_2} \;\; ; \;\; \text{when: } 0\le 1-\dfrac{(2m_1+1)}{2m}\le\eta_2\le 1-\dfrac{(2m_1+1)}{(2m+2)}\le 1 \\ \dfrac{w_{m_2}^{(2)}}{w_1^0}=\dfrac{(2m_2+1)}{\eta_2} \;\; ; \;\; \text{when: } 0\le\dfrac{(2m_2+1)}{(2m+2)}\le\eta_2\le\dfrac{(2m_2+1)}{2m}\le 1\end{cases} \qquad (5.52)$$

Equation (5.52) gives the different asymptotic branches at a given mode m as η_2 varies, and as observed from Figure 5.11, these branches define the solution domain of the eigenfrequency shift variations for $0\le\alpha\le 1$.

Figure 5.11 Dimensionless eigenfrequency variation with length η_2 of the first four modes for different α along with the asymptotic solution from Eqs. (5.47) and (5.48).

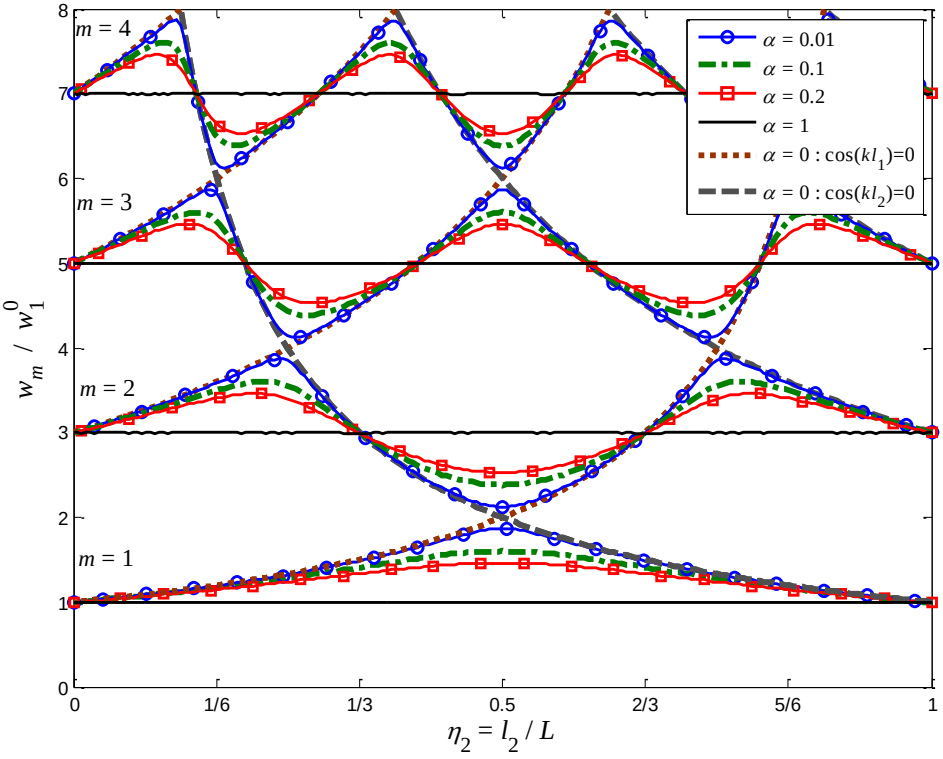

5.6. Analysis and discussion of frequency-blockage interaction for blockage with moderate radial protrusion

The last two sections focused on blockages with small radial protrusion (α near 1) and blockages with large radial protrusion (α near 0). It is found that the small blockage assumption is accurate for $\alpha \geq 0.7$ (see Figure 5.4). In addition, the large blockage assumption is valid for $\alpha < 0.7$ provided that the values of the frequencies of subsystem 1 (Eq. (5.47)) and subsystem 2 (Eq. (5.48)) are not equal or close to each other (see Figure 5.11). This section focuses on the case $\alpha < 0.7$ for systems where the frequencies of subsystem 1 (Eq. (5.47)) and subsystem 2 (Eq. (5.48)) are equal or near each other. In this case, the waves in subsystem 1 act as forcing functions to subsystem 2, where the forcing frequency is equal or close to the eigenfrequency of subsystem 2. Similarly, the waves in subsystem 2 act as a forcing function to subsystem 1, where the forcing frequency is equal or close to the eigenfrequency of subsystem 1. That is, both subsystems are driven at or near resonance. Therefore, although the ratio of transmitted to incident energy on the interface between the blocked and unblocked pipe sections of each incoming wave is of the order of $4\alpha/(\alpha+1)^2$ (*i.e.*, small), the fact that each of the two subsystems is driven near its resonance frequency means that the transmitted energy accumulates with time and forces the overall system to behave more as a coupled rather than an uncoupled system.

To first order, the wavenumbers and eigenfrequencies of the coupled system are those of the uncoupled system plus a perturbation (*i.e.*, $k_m = k_m^s + \delta k_m$ and $w_m = w_m^s + \delta w_m$). Therefore, Eq. (5.2) gives: $\delta k_m = \pm\sqrt{\alpha/(l_1 l_2)}$ which gives $\delta w_m = \pm a\sqrt{\alpha/(l_1 l_2)}$. To illustrate this, consider the case α = 0.2, m = 1, l_1 = $L/2$ = l_2. Then, $\delta w_1/w_1^0 = \pm(\alpha/l_1 l_2)^{1/2}/(\pi/2L) = \pm(\alpha/L/2L/2)^{1/2}/(\pi/2L) = \pm(4/\pi)(\alpha)^{1/2} = \pm 0.569$, which is in good agreement with the deviations that can be read from Figure 5.11. Note that $\delta w_m = \pm a\sqrt{\alpha/(l_1 l_2)}$ is independent of *m* which agrees with Figure 5.2.

It is noted from Figure 5.11 that the zero shift locations are independent of α. This result can be explained from Eq. (5.2). In particular, for any $\alpha \neq 1$, Eq. (5.2) gives the intact pipe frequencies whenever the blockage length is such that either $\sin(kl_1) = 0$ or $\sin(kl_2) = 0$.

Figure 5.2 shows that the position of the maximum shift changes as a function of α except when the blockage length is half of the pipe length (*i.e.*, $\eta_2 = 0.5$). An expression for the maximum eigenfrequency shift and the location η_2 at which it occurs can be obtained from Eq. (5.3) as follows

$$\cos(kL) + \frac{1-\alpha}{1+\alpha}\cos(kL - 2kl_2) = 0 \tag{5.53}$$

where the second term on the left hand side of Eq. (5.53) is what causes the shift in frequency. The maximum shift occurs when that term is maximum which gives

$$\begin{aligned} &\sin(kL - 2kl_2) = 0 \;\Rightarrow\; k_m^{\max} L - 2k_m^{\max} l_2 = (\overline{m'} - 1)\pi \;\;;\;\; \overline{m'} = 1, 2, 3... \\ &\Rightarrow \cos\left(k_m^{\max} L - 2k_m^{\max} l_2\right) = (-1)^{(\overline{m'}-1)} \end{aligned} \tag{5.54}$$

where $k_m^{\max} = w_m^{\max}/a$ is the wavenumber corresponding to the maximum m^{th} eigenfrequency ($w_m^{\max}$) magnitude at a given α. Inserting Eq. (5.54) into Eq. (5.53), yields

$$\Rightarrow k_m^{\max} L = \operatorname{acos}\left[(-1)^{\overline{m'}-1+m}\left(\frac{1-\alpha}{1+\alpha}\right)\right] + (m-1)\pi \;\;;\;\; m = 1, 2, 3... \tag{5.55}$$

which gives

$$\begin{cases} \dfrac{\Delta w_m^{\max}(m, \alpha, \overline{m'})}{w_1^0} = \dfrac{w_m^{\max} - w_m^0}{w_1^0} = \dfrac{2}{\pi}\operatorname{acos}\left[(-1)^{2m-\overline{m'}}\left(\dfrac{1-\alpha}{1+\alpha}\right)\right] - 1 \\ \text{where} \quad \overline{m'} - 1 \equiv (m-n);\;\; \overline{m'} = 1, 2, 3... \end{cases} \tag{5.56}$$

where $\Delta w_m^{\max}(m, \alpha, \overline{m'})$ is the maximum shift at a given mode *m*, a given α and a given positive or negative shift region $\overline{m'}$ (between two successive zero shift locations (see Figure 5.2 and Eq. (5.44)). For example, the first shift region ($\overline{m'} = 1$) as η_2 increases in Figure 5.2 is located at $\eta_2(2,1) = 0 \le \eta_2 \le \eta_2(2,2) = 1/3$ (see Figure 5.2 and Eq. (5.44)). Thus, at mode *m* = 2, α = 0.2 and $\overline{m'} = 1$, Eq. (5.56) shows that the magnitude of the eigenfrequency shift is $\Delta w_m^{\max}(2, 0.2, 1)/w_1^0$ = 0.4646 which agrees with Figure 5.11.

The location corresponding to each maximum shift is obtained by inserting Eq. (5.55) into Eq. (5.54) which leads to

$$\Rightarrow \begin{cases} \eta_2 = \eta_2\left(m, \alpha, \overline{m'}\right) = \dfrac{1}{2}\left[1 - \dfrac{\left(m - \overline{m'}\right)\pi}{\operatorname{acos}\left(\left(-1\right)^{2m-\overline{m'}}\dfrac{1-\alpha}{1+\alpha}\right) + m\pi}\right]; \\ \text{where} \quad 0 \le \eta_2 \le 1 \Rightarrow \overline{m'} \le 2m-1 \end{cases} \qquad (5.57)$$

For example, at mode m = 2, α = 0.2 and $\overline{m'}=1$, Eq. (5.57) shows that the position of the maximum shift is $\eta_2\left(2, 0.2, 1\right)$ = 0.2114 which agrees with Figure 5.11.

5.7. Symmetric pipe system with blockage at the boundary

The above discussions and findings could be similarly applied for the case of symmetric pipe system such as reservoir-pipe-reservoir (RPR) system (see Figure 5.12a) or valve-pipe-valve (VPV) system (see Figure 5.12b). This section gives briefly the main eigenfrequency shift features for the case of symmetric pipe system with blockage at the boundary.

Figure 5.12 Symmetric pipe systems with change in cross-sectional area.

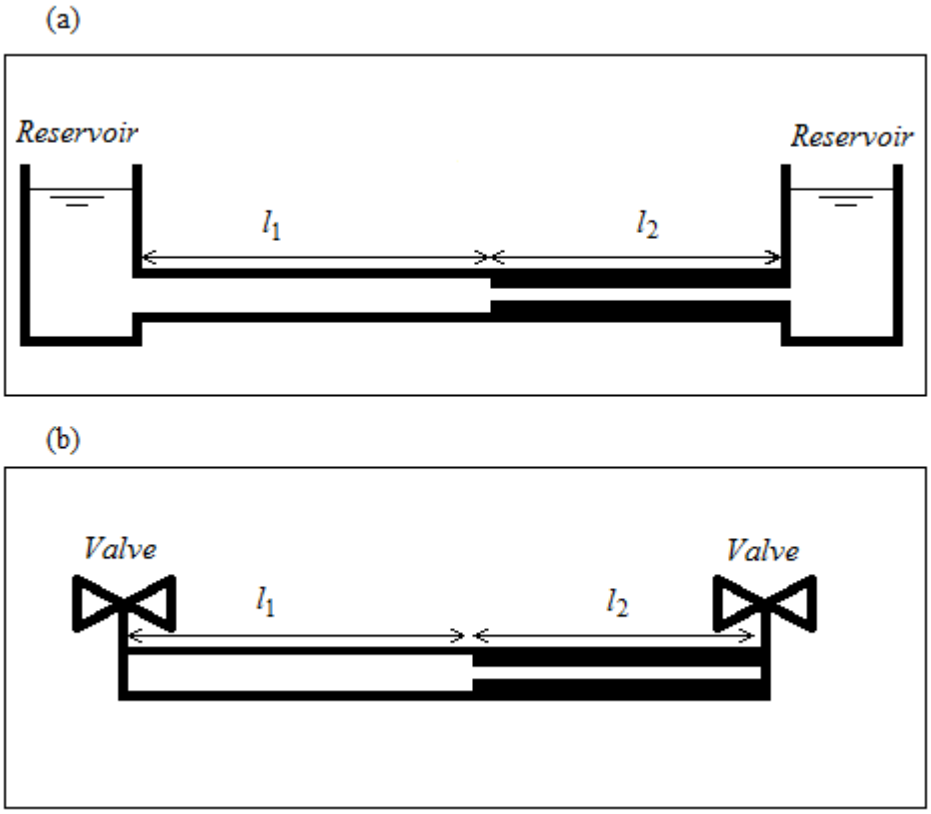

(a) Left RPR system

(b) Right VPV system

Applying Eq. (5.1) to the blocked RPR system in Figure 5.12a gives:

$$\cos(k_m l_1)\sin(k_m l_2)+\alpha\sin(k_m l_1)\cos(k_m l_2)=0 \qquad (5.58)$$

Notice that Eq. (5.58) could is also the dispersion relation for the VPV system in Figure 5.12b but with the blockage at the upstream boundary. Using trigonometric manipulation of Eq. (5.58) gives

$$\sin(k_m L)+(\alpha-1)\sin(k_m l_1)\cos(k_m l_2)=0 \qquad (5.59)$$

or

$$\sin\left(k_m L\right)-\frac{1-\alpha}{1+\alpha}\sin\left(k_m\left(L-2l_2\right)\right)=0 \qquad (5.60)$$

Note that the second term in Eq. (5.59) and Eq. (5.60) represents the effect of the blockage on the dispersion relation. In fact, for $\alpha=1$, this second term vanishes and Eqs. (5.59) and (5.60) become identical to the dispersion relation of an intact RPR system.

Figure 5.13 gives the dimensionless eigenfrequency variation with dimensionless length $\eta_2=l_2/L$ for the case of RPR system. The first four modes (*m* = 1, 2, 3 and 4) are plotted for different values of α. As seen for the case of RPV system, the eigenfrequency shift takes positive values for some range of blockage length η_2, negative values for some other range of blockage length η_2, and equal zero for particular values of blockage length η_2. Again, the zero shift locations are independent on α whereas the maximum shift location changes with α.

For of blockage with small radial protrusion in RPR system, Eq. (5.29) or Eq. (5.41) gives the following RPR shift equation

$$\frac{\overline{\Delta w_m}}{w_1^0}=\frac{\left(1-\alpha\right)}{\pi}\sin\left(2\pi\left(2m\right)\frac{\eta_2}{2}\right) \qquad (5.61)$$

from which the zero shift locations could be obtain as follows

$$\begin{aligned}&\sin\left(2\pi\left(2m\right)\frac{\eta_2}{2}\right)=0\Rightarrow 2\pi m\eta_2=\left(\tau-1\right)\pi \;\;;\;\; \tau=1,2,3...\\&\Rightarrow \eta_2=\eta_2\left(m,\tau\right)=\frac{\tau-1}{2m}\;\le 1\;\;;\;\; \tau\le 2m+1\end{aligned} \qquad (5.62)$$

Equation (5.62) gives the length of the blockage for which the m^{th} mode experiences no shift. The values of η_2 where zero frequency is obtained from Figure 5.13 can be derived by evaluating Eq. (5.62) for *m* = 1, 2, 3 and 4. For example, evaluating Eq. (5.62) for *m*=2 gives $\eta_2\left(2,1\right)=0$, $\eta_2\left(2,2\right)=1/4$, $\eta_2\left(2,3\right)=1/2$, $\eta_2\left(2,4\right)=3/4$ and $\eta_2\left(2,5\right)=1$. These values correspond to the zero shift locations shown in Figure 5.13.

The maximum shift occurs when the second term in Eq. (5.60) is maximum which gives

$$\begin{aligned} &\cos\left(kL-2kl_2\right)=0 \;\Rightarrow\; k_m^{\max}L-2k_m^{\max}l_2=\left(2n-1\right)\frac{\pi}{2} \;\;;\; n=0,\pm1,\pm2... \\ &\Rightarrow \sin\left(k_m^{\max}L-2k_m^{\max}l_2\right)=\left(-1\right)^{(n-1)} \end{aligned} \qquad (5.63)$$

Inserting Eq. (5.63) into Eq. (5.60), yields

$$k_m^{\max}L+\frac{\pi}{2}=\arccos\left[\left(-1\right)^{n+m}\left(\frac{1-\alpha}{1+\alpha}\right)\right]+m\pi \qquad (5.64)$$

which leads to

$$\begin{cases} \dfrac{\Delta w_m^{\max}\left(m,\alpha,n\right)}{\left(\dfrac{\pi a}{2L}\right)}=\dfrac{2}{\pi}\arccos\left[\left(-1\right)^{2m-n+1}\left(\dfrac{1-\alpha}{1+\alpha}\right)\right]-1 \\ \text{where}\quad n-1\equiv\left(m-n\right)\;\;;\; n\equiv1,2.. \end{cases} \qquad (5.65)$$

where $\Delta w_m^{\max}\left(m,\alpha,n\right)$ is the maximum shift at a given mode *m*, a given α and a given positive or negative shift region *n* (between two successive zero shift locations (see Figure 5.13 and Eq. (5.62)). For example, at mode *m* = 1, α = 0.2 and $n=1$, Eq. (5.65) gives the magnitude of the eigenfrequency shift $\Delta w_m^{\max}\left(1,0.2,1\right)/w_1^0$ = –0.4646 which agrees with Figure 5.13.

The location corresponding to each maximum shift is obtained by inserting Eq. (5.64) into Eq. (5.63) which gives

$$\begin{cases} \eta_2\left(m,\alpha,n\right)=\dfrac{1}{2}\left[1-\dfrac{2\left(m-n+1\right)-1}{\dfrac{2}{\pi}\arccos\left[\dfrac{1-\alpha}{1+\alpha}\left(-1\right)^{2m-n+1}\right]+\left(2m-1\right)}\right] \\ \text{where}\quad 0\le\eta_2\le1\Rightarrow n\le2m \end{cases} \qquad (5.66)$$

For example, at mode *m* = 1, α = 0.2 and $n=1$, Eq. (5.66) gives the position of the maximum shift $\eta_2\left(1,0.2,1\right)$ = 0.1744 which agrees with Figure 5.13.

Figure 5.13 Dimensionless eigenfrequency variation with η_2 for the case of RPR system: first four modes with different α values.

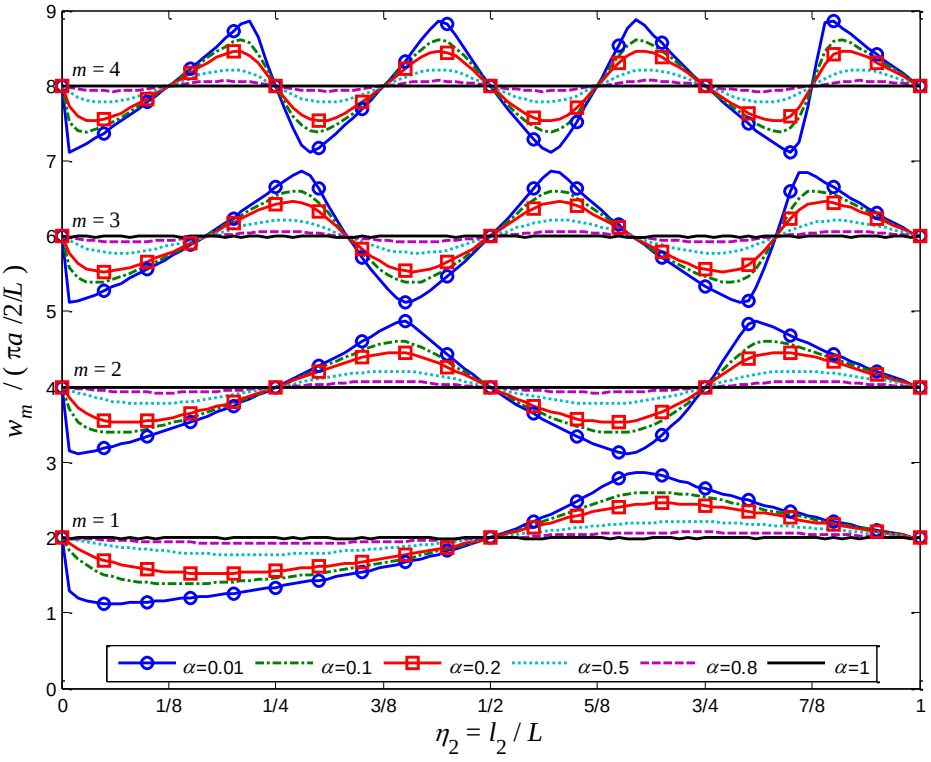

For a severe blockage (*i.e.*, α tends to 0), Eq. (5.58) reduces to

$$\cos\left(k_m l_1\right)\sin\left(k_m l_2\right)=0 \tag{5.67}$$

which implies

$$\cos\left(kl_1\right)=0 \Rightarrow \frac{w_m^{s_1}}{w_1^0}=\frac{\left(2m-1\right)}{\eta_1} \quad ; \quad m=1,2,3... \tag{5.68}$$

or

$$\sin\left(kl_2\right)=0 \Rightarrow \frac{w_m^{s_2}}{w_1^0}=\frac{2m}{\eta_2} \quad ; \quad m=1,2,3... \tag{5.69}$$

Similarly to the blocked RPV system, the severe blockage decouples the pipe system responses into two independent subsystems. In this case of RPR system, subsystem 1 consists of an intact RPV system with length l_1; and subsystem 2 is an intact RPR system with length l_2. A sketch showing the decoupling into two RPV subsystems is given in Figure 5.14. Figure 5.15 gives the fundamental frequencies of subsystem 1 ($\cos(kl_1) = 0$) and subsystem 2 ($\sin(kl_2) = 0$) are plotted for m = 1, 2, 3 and 4 along with the eigenfrequency variations. Figure 5.15 shows that the asymptotic solutions (Eq. (5.68) and Eq. (5.69)) fits very well the eigenfrequency variation except where the frequencies of subsystem 1 (Eq. (5.68)) and subsystem 2 (Eq. (5.69)) are equal or near each other. That is, both subsystems are driven at or near resonance where the transmitted energy accumulates with time and forces the overall system to behave more as a coupled rather than an uncoupled system.

Figure 5.14 Schematic figure of the decoupling of the junction system into two intact uncoupled RPV subsystems when α tends to 0

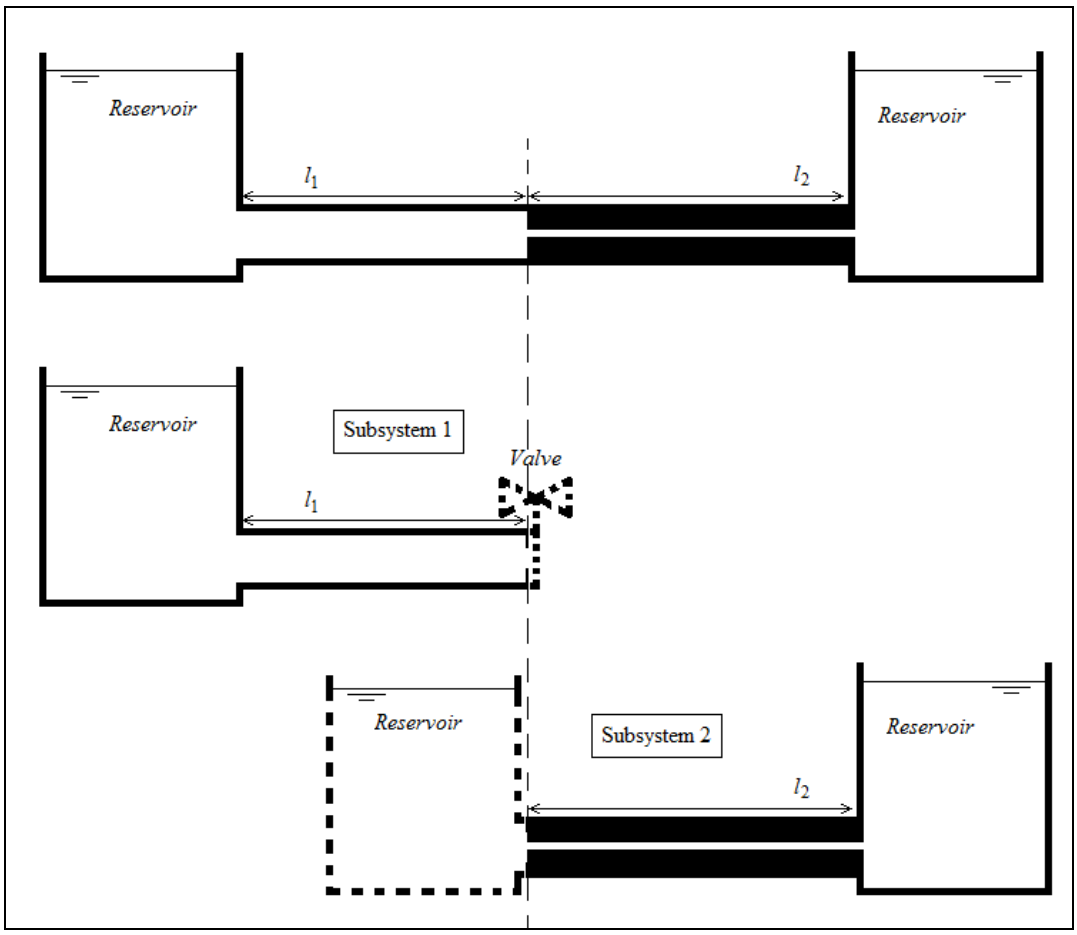

Figure 5.15 Dimensionless eigenfrequency variation with η_2 for the case of RPR system along with the asymptotic solutions: first four modes with different α values.

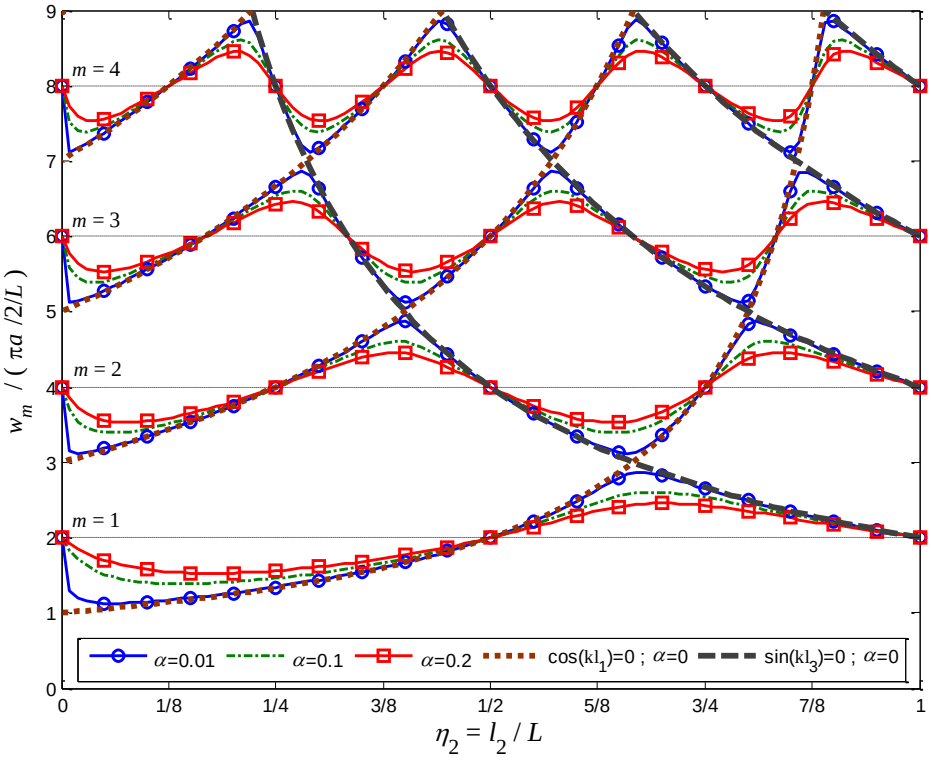

5.8. Summary

The eigenfrequency shift due to variation in the cross sectional area of a conduit is investigated with the primary goal being to understand and describe the mechanisms that cause such eigenfrequency shift. The cross sectional area variation in this chapter consists of a blockage located at the pipe boundary. The key findings are summarized below:

(i) For shallow blockage case, $w_m E_m$ is conversed implying $\Delta w_m/w_m = -\Delta E_m/E_m$ for all modes m. Moreover, the change in energy is found to equal the work of the radiation pressure during the formation of the blockage. For an energy prospective, the test cases confirm that (a) a blockage that causes an increase in total energy of a mode m would produce a negative shift of the eigenfrequency of this mode; (b) a

blockage that causes a decrease in total energy of a mode *m* would produce a positive shift of the frequency of this mode; and (c) blockage that causes a zero change in total energy of a mode *m* would produce no shift of the frequency of this mode.

(ii) Moreover, it is found that the eigenfrequency shift variation caused by a shallow blockage in a conduit could be analyzed by studying the variation of the work of radiation pressure at the blockage boundaries.

(iii) A severe blockage decouples the pipe system into independent intact subsystems with different lengths. The eigenfrequencies of these subsystems defines the asymptotic solutions of the eigenfrequency variations at the limit of most severe blockage cases $\alpha \to 0$. In this case, the system is described as uncoupled pipe system. This decoupling effect is weakened when the eigenfrequencies of the two subsystems are close or equal to each other. When this happens, waves in the blockage act as forcing functions that drive the rest of the pipe system at or near resonance. Similarly, waves outside the blockage are forcing functions that drive the waves within the blockage at or near resonance. The fact that both subsystems are driving one another at or near resonance is what brings about the coupling even for a very severe blockage. In this case, perturbation theory is found to provide a simple and explicit relationship between the eigenfrequency shift and the properties of the blockage.

(iv) The assumption of shallow blockage (with small radial protrusion) is applicable when the blockage occupies 35% of the pipe's area or less. The assumption of severe blockage is applicable when the blockage occupies 35% of the pipe's area or more provided that the eigenfrequencies of the asymptotic subsystems are not equal or close to each others.

This chapter gave some primary knowledge and understanding of the eigenfrequency shift mechanism for a simple blocked pipe system consisting of blockage at the boundary. A more involved and common blocked pipe system with interior blockage is considered in the next chapter.

CHAPTER 6

WAVE SCATTERING IN BOUNDED PIPE SYSTEM: STUDY OF THE EIGENFREQUENCY SHIFT DUE TO AN INTERIOR BLOCKAGE

6.1. Introduction

Similarly to the previous chapter, this current chapter focuses on studying the forward approaches which consists in understanding the eigenfrequency shift mechanism. While the previous chapter considered a simple blocked pipe system with a blockage at the boundary, this chapter considers the case of interior blockage. The differences between both cases are highlighted and investigated. In particular, the effect of the Bragg-type resonance (see Chapter 4) on the eigenfrequency shift is studied through analytical and experimental means.

6.2. Problem statement

This section studies the eigenfrequency shift mechanism due to an interior single blockage in a bounded pipe system. For this purpose, a reservoir-pipe-valve system is considered as shown in Figure 6.1. The blocked pipe system is modelled as the junction of three pipes in series with different diameters (see Figure 6.1). The three pipes are defined as pipe 1 with length l_1 and cross sectional area $A_1=A_0$, pipe 2 with length l_2 and cross sectional area $A_2<A_0$ and pipe 3 with length l_3 and cross sectional area $A_3=A_0$ where A_0 is the intact cross sectional area. The blocked pipe system (Figure 6.1) is linked to a reservoir at the upstream boundary and to a valve at the downstream boundary. The ratio between the cross sectional areas is $\alpha = A_2 / A_0$ and the dimensionless lengths are defined by x/L , $\eta_1 = l_1/L$, $\eta_2 = l_2/L$ and

$\eta_3 = l_3/L$ where $L=l_1+l_2+l_3$ is the total length of the blocked pipe system and x is the distance along the pipe length from the reservoir (Figure 6.1). The pipe flow is assumed one dimensional with frictionless fluid. In what follow, the case without blockage (*i.e.* $\alpha = 1$) is referred to as intact pipe case.

The dispersion relation that governs the eigenfrequencies of the blocked pipe system (Figure 6.1) could be obtained by extending the transfer matrix solution (e.g. Eq. (5.4) to three pipes system) and the result is ([39],[32])

$$\begin{aligned} &\alpha \cos(k_m l_1)\cos(k_m l_2)\cos(k_m l_3) \\ &-\cos(k_m l_1)\sin(k_m l_2)\sin(k_m l_3) \\ &-\alpha^2 \sin(k_m l_1)\sin(k_m l_2)\cos(k_m l_3) \\ &-\alpha \sin(k_m l_1)\cos(k_m l_2)\sin(k_m l_3) = 0 \end{aligned} \qquad (6.1)$$

which could also be written as

$$\begin{aligned} &\cos(k_m L) \\ &+\frac{(1-\alpha)}{(1+\alpha)}\cos\left(k_m\left(l_1-l_2-l_3\right)\right) \\ &-\frac{(1-\alpha)}{(1+\alpha)}\cos\left(k_m\left(l_1+l_2-l_3\right)\right) \\ &-\frac{(1-\alpha)^2}{(1+\alpha)^2}\cos\left(k_m\left(l_1-l_2+l_3\right)\right) = 0 \end{aligned} \qquad (6.2)$$

where the subscript "m" refers to the m^{th} natural resonant mode and $k_m = w_m/a$ is the m^{th} wavenumber with w_m is the m^{th} eigenfrequency and a is the acoustic wave speed. When $\alpha = 1$, Eq. (6.2) becomes

$$\cos\left(k_m^0 L\right) = 0 \;\Rightarrow\; w_m^0 = a k_m^0 = 2\pi\left[\left(2m-1\right)\frac{a}{4L}\right] \;;\; m = 1,2,3... \qquad (6.3)$$

which is the dispersion relation of an intact pipe system (Eq. (2.54)) with $k_m^0 = w_m^0/a$ is the m^{th} wavenumber and w_m^0 is the m^{th} eigenfrequency of the intact pipe system.

Figure 6.1 A single blockage in a reservoir-pipe-valve (RPV) system

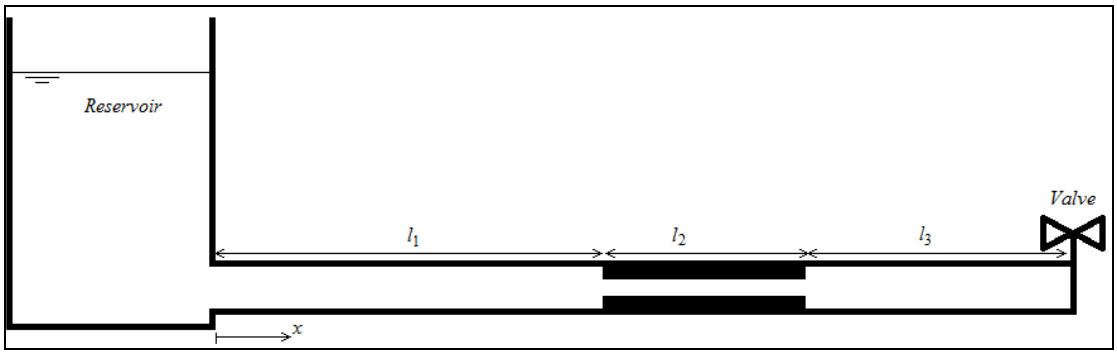

The eigenfrequencies of the blocked pipe system are obtained by solving Eq. (6.1) graphically. Figure 6.2 and Figure 6.3 show the eigenfrequency (w_m) variation with length $\eta_b = \eta_3 + 0.5\eta_2$ for the first five modes and different α values when $\eta_2 = 0.15$ and $\eta_2 = 0.027$, respectively. The cases where $\alpha = 1$ in Figure 6.2 and Figure 6.3 represent the eigenfrequencies of the intact pipe case which are constant and vary as straight horizontal lines with $\eta_b = \eta_3 + \eta_2/2$. When $\alpha \neq 1$, the effect of the blockage is introduced, and as a result, the eigenfrequency at a given mode *m* (w_m) deviates from the intact case (w_m^0) as observed in Figure 6.2 and Figure 6.3. The eigenfrequency shift is defined as $\Delta w_m = \left(w_m - w_m^0 \right)$ which could take positive, negative or zero values (see Figure 6.2 and Figure 6.3).

Figure 6.2 and Figure 6.3 show that the magnitudes of maximum positive and negative shift vary for a given α at different modes *m*. Moreover, comparing Figure 6.2 and Figure 6.3 shows that the variation of blockage length induces a change in the maximum shift magnitude at given mode *m* and dimensionless area α. Furthermore, at a given mode *m*, the zero shift locations varies as α changes. These features were not observed in the case of blockage at the boundary (Figure 5.2).

The main objective of this section is to provide physical and mathematical insights that can explain the above observations that emerged from Figure 6.2 and Figure 6.3 some of which differ from the case of blockage at the boundary discussed in Chapter 5. Such understanding

is presently lacking; yet, this insight is essential if the dispersion relation (Eq. (5.1)) is to become a viable approach for identifying blockages in fluid lines.

Figure 6.2 Normalized eigenfrequency variation with length $\eta_b = \eta_3 + 0.5\eta_2$ of the first 5 modes for different α values when $\eta_2 = 0.15$

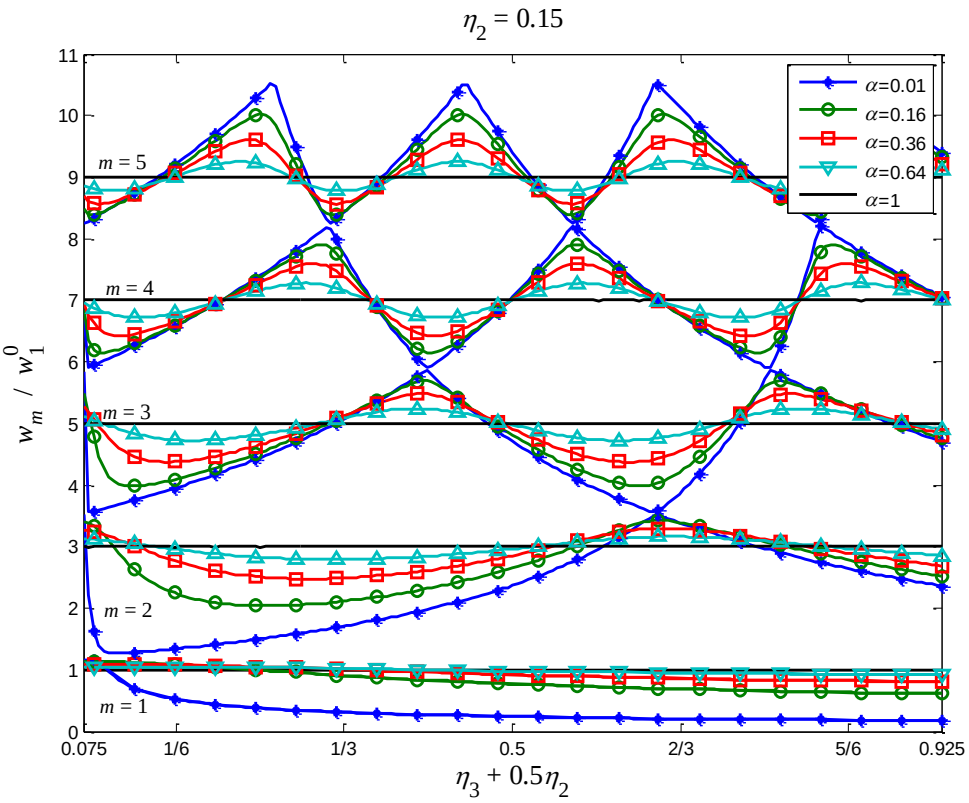

Figure 6.3 Normalized eigenfrequency variation with length $\eta_b = \eta_3 + 0.5\eta_2$ of the first 5 modes for different α values when $\eta_2 = 0.027$

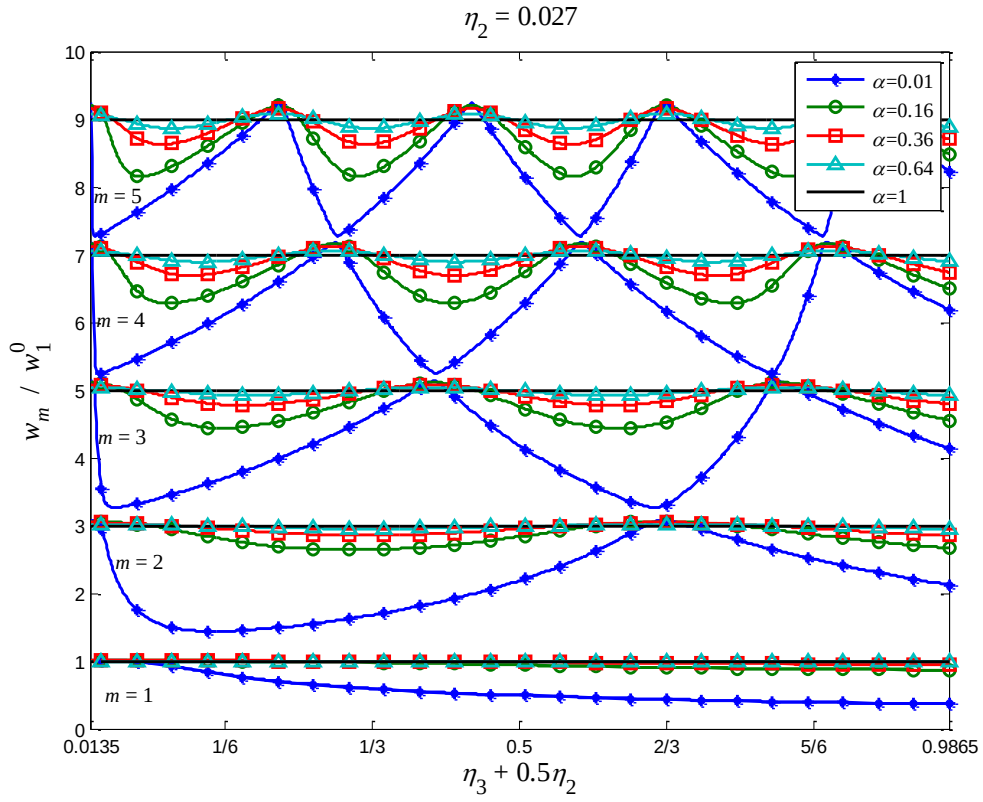

6.3. Harmonic solution for the case of interior blockage

Using the transfer matrix ([13]) method, it can be shown that the pressure head and flow harmonics are given by

$$\begin{cases} \dfrac{h(x)}{h_m^{amp}} = \dfrac{M_{u-x}^{12}}{M_{u-d}^{22}} \\ \dfrac{q(x)}{q_m^{amp}} = \dfrac{M_{u-x}^{22}}{M_{u-d}^{22}} \end{cases} \qquad (6.4)$$

where

$$M_{u-x}^{12}=\begin{cases}\text{if } x\le l_1:\\ -\sin\left(k_m x\right)\\ \text{if } l_1\le x\le l_1+l_2:\\ -\begin{bmatrix}\cos\left(k_m\left(x-l_1\right)\right)\sin\left(k_m l_1\right)\\ +\left(1/\alpha\right)\sin\left(k_m\left(x-l_1\right)\right)\cos\left(k_m l_1\right)\end{bmatrix}\\ \text{if } x\ge l_1+l_2:\\ -\begin{bmatrix}\cos\left(k_m\left(x-l_1-l_2\right)\right)\begin{pmatrix}\cos\left(k_m l_2\right)\sin\left(k_m l_1\right)\\ +\left(1/\alpha\right)\sin\left(k_m l_2\right)\cos\left(k_m l_1\right)\end{pmatrix}\\ +\sin\left(k_m\left(x-l_1-l_2\right)\right)\begin{pmatrix}\cos\left(k_m l_1\right)\cos\left(k_m l_2\right)\\ -\alpha\sin\left(k_m l_2\right)\sin\left(k_m l_1\right)\end{pmatrix}\end{bmatrix}\end{cases}, \qquad (6.5)$$

$$M_{u-x}^{22}=\begin{cases}\text{if } x\le l_1:\\ \cos\left(k_m x\right)\\ \text{if } l_1\le x\le l_1+l_2:\\ \begin{bmatrix}\cos\left(k_m\left(x-l_1\right)\right)\cos\left(k_m l_1\right)\\ -\left(1/\alpha\right)\sin\left(k_m\left(x-l_1\right)\right)\sin\left(k_m l_1\right)\end{bmatrix}\\ \text{if } x\ge l_1+l_2:\\ \begin{bmatrix}\cos\left(k_m\left(x-l_1-l_2\right)\right)\begin{pmatrix}\cos\left(k_m l_1\right)\cos\left(k_m l_2\right)\\ -\left(1/\alpha\right)\sin\left(k_m l_1\right)\sin\left(k_m l_2\right)\end{pmatrix}\\ -\sin\left(k_m\left(x-l_1-l_2\right)\right)\begin{pmatrix}\cos\left(k_m l_2\right)\sin\left(k_m l_1\right)\\ +\alpha\cos\left(k_m l_1\right)\sin\left(k_m l_2\right)\end{pmatrix}\end{bmatrix}\end{cases} \qquad (6.6)$$

and

$$M_{u-d}^{22}=\begin{bmatrix}\cos\left(k_m l_3\right)\begin{pmatrix}\cos\left(k_m l_1\right)\cos\left(k_m l_2\right)\\ -\left(1/\alpha\right)\sin\left(k_m l_1\right)\sin\left(k_m l_2\right)\end{pmatrix}\\ -\sin\left(k_m l_3\right)\begin{pmatrix}\cos\left(k_m l_2\right)\sin\left(k_m l_1\right)\\ +\alpha\cos\left(k_m l_1\right)\sin\left(k_m l_2\right)\end{pmatrix}\end{bmatrix} \qquad (6.7)$$

Applying the boundary condition at the valve ($x = L$) where the flow is zero, Eq. (6.4) leads to Eq. (6.1).

6.4. Analysis and discussion of eigenfrequency shift variation for interior blockage with small radial protrusion (*i.e.,* α near 1)

At a given mode *m,* Figures 6.2 and 6.3 show that the eigenfrequency shift sign varies if the blockage location and /or size change. Considering a blockage with small radial protrusion, the shift equation (Eq. (5.41)) could be applied for the case of interior blockage and gives

$$\frac{\overline{\Delta w_m}}{w_m^0} = \mathrm{Re}\left[\frac{ig}{E_m^0 w_m^0}\frac{\rho}{2}\frac{\Delta A}{A}\int_{l_1}^{l_1+l_2}\frac{d\left(h_m^0\overline{q_m^0}\right)}{dx}dx\right] = \xi_m\left[\left(\frac{h_m^0\overline{q_m^0}}{h_m^{amp}\overline{q_m^{amp}}}\right)_{l_1} - \left(\frac{h_m^0\overline{q_m^0}}{h_m^{amp}\overline{q_m^{amp}}}\right)_{l_1+l_2}\right] \qquad (6.8)$$

Inserting Eq. (5.27) into Eq. (6.8) gives

$$\frac{\overline{\Delta w_m}}{w_1^0} = \frac{2}{\pi}(1-\alpha)\left[\sin\left(k_m^0 l_1\right)\cos\left(k_m^0 l_1\right) - \sin\left(k_m^0\left(l_1+l_2\right)\right)\cos\left(k_m^0\left(l_1+l_2\right)\right)\right] \qquad (6.9)$$

$$\begin{aligned}
\Rightarrow \frac{\overline{\Delta w_m}}{w_1^0} &= \frac{(1-\alpha)}{\pi}\left[\sin\left((2m-1)\pi\eta_1\right) - \sin\left((2m-1)\pi\left(\eta_1+\eta_2\right)\right)\right] \\
&= \frac{(1-\alpha)}{\pi}\left[\sin\left((2m-1)\pi\left(\eta_3+\eta_2\right)\right) - \sin\left((2m-1)\pi\eta_3\right)\right] \qquad (6.10) \\
&= \frac{(1-\alpha)}{\pi}\left[2\sin\left((2m-1)\frac{\pi}{2}\eta_2\right)\cos\left((2m-1)\pi\left(\eta_3+\frac{\eta_2}{2}\right)\right)\right]
\end{aligned}$$

Equation (6.10) is the simplified shift equation obtained in Duan, et al. ([35]) by assuming small shift and using Taylor expansion on the dispersion relation (Eq. (6.2)). Equation (6.8) is a much simpler approach to obtain the simplified shift equation (Eq. (6.10)). Equation (6.10) could also be obtained by carrying integration in Eq. (5.29) between the blockage boundaries. Figure 6.4 give the comparison between the approximated eigenfrequency shift from Eq. (6.10) and the exact eigenfrequency from the dispersion relation (Eq. (6.1)) for different α values. Figure 6.4 shows good quantitative agreement between the exact shift solution from Eq. (6.1) and its approximate form (Eq. (6.10)) for $\alpha > 0.6$. There is overall qualitative agreement between these two equations for all α. Similar conclusion is found for other *m* modes as shown in Figure 6.5 which gives the comparison between the exact and approximated eigenfrequency variation for the first eight

modes with $\alpha = 0.64$. Such agreement supports the use of Eq. (6.10) to analyse the eigenfrequency shift signs and maximum shift locations.

Figure 6.4 Normalized eigenfrequency shift variation with length $\eta_3 + \eta_2/2$ for *m* = 2 and $\eta_2 = 0.15$: comparison between exact solution (Eq. (6.1)) and approximate solution (Eq. (6.10)).

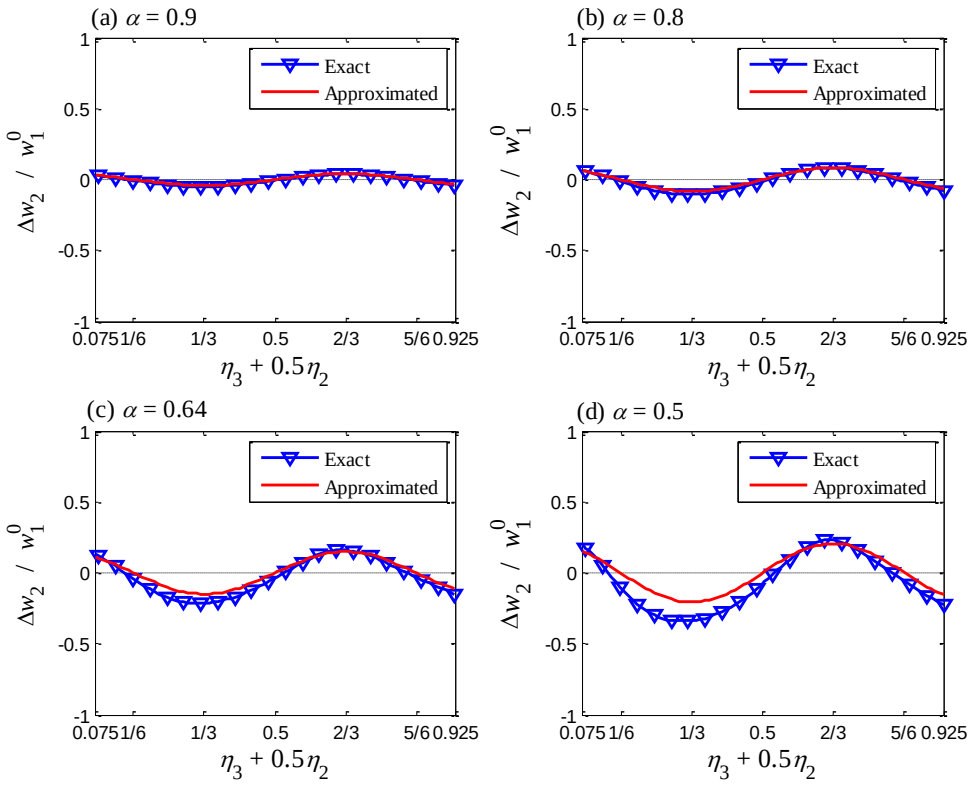

(a) Top left **α = 0.9**

(b) Top right **α = 0.8**

(c) Bottom left **α = 0.64**

(d) Bottom right **α = 0.5**

Figure 6.5 Normalized eigenfrequency variation with length $\eta_3+\eta_2/2$ for the first eight modes with α=0.64 and $\eta_2=0.15$: comparison between exact solution (Eq. (6.1)) and approximate solution (Eq. (6.10)).

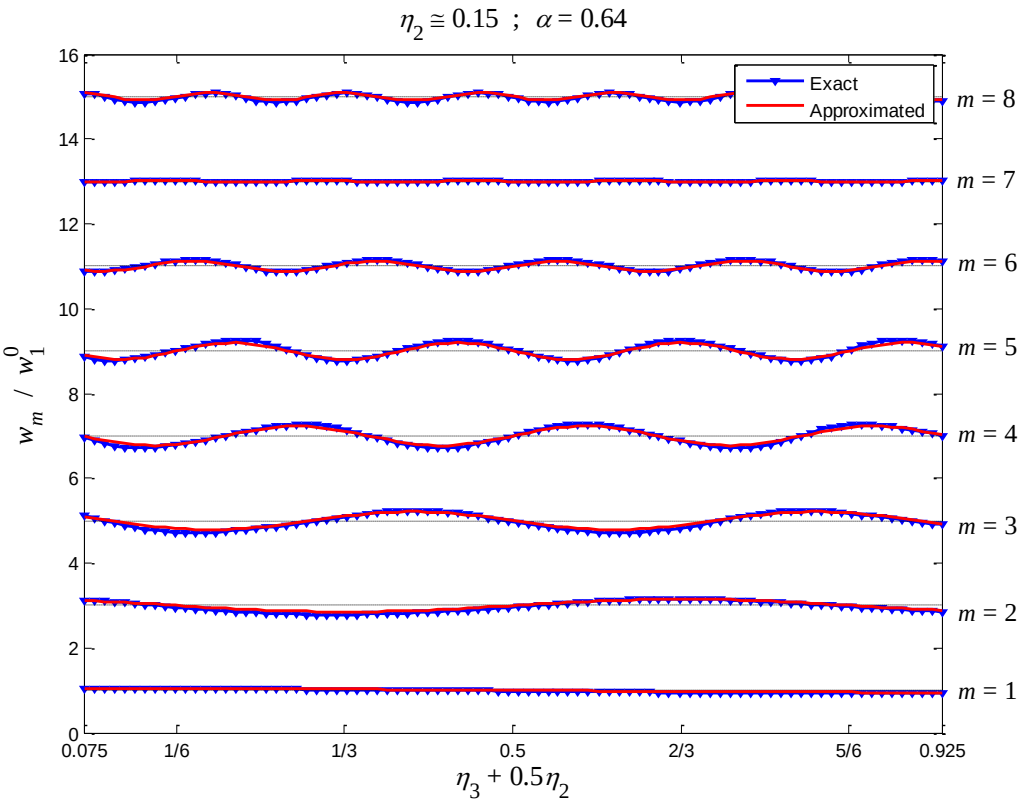

6.4.1. Analysis and discussion of the zero eigenfrequency shift

Setting Eq. (6.10) to zero gives the conditions for which the eigenfrequency shift is zero at a given mode *m* as follows

$$\begin{cases} \sin\left(\left(2m-1\right)\dfrac{\pi}{2}\eta_2\right)=0 \\ \text{or} \\ \cos\left(\left(2m-1\right)\pi\left(\eta_3+\dfrac{\eta_2}{2}\right)\right)=0 \end{cases} \qquad (6.11)$$

which leads to

$$\begin{cases} \eta_2 = \dfrac{2\left(\overline{m}-1\right)}{\left(2m-1\right)} \\ \text{or} \qquad\qquad\qquad ; \quad \overline{m} = 1, 2... \\ \eta_3 + \dfrac{\eta_2}{2} = \dfrac{2\overline{m}-1}{2\left(2m-1\right)} \end{cases} \tag{6.12}$$

The first equation in Eq. (6.12) corresponds to the Bragg resonance condition of total transmission (Eq. (4.11)) as follows

$$\eta_2 = \frac{2\left(\overline{m}-1\right)}{\left(2m-1\right)} \quad \Leftrightarrow \quad \frac{w_m^0}{w_{\overline{m}}^T\left(l_2\right)} = 1 \quad \Leftrightarrow \quad l_2 = \frac{\left(\overline{m}-1\right)}{2}\left[\frac{4L}{\left(2m-1\right)}\right] \tag{6.13}$$

which states that the shift is zero if the blockage length is a multiple of half wavelength of the m^{th} mode harmonic. The second equation in Eq. (6.12) corresponds to the location of the blockage mid-length from the downstream boundary where

$$\sin\left(k_m^0 L\left(\eta_3 + \frac{\eta_2}{2}\right)\right) = \pm\cos\left(k_m^0 L\left(\eta_3 + \frac{\eta_2}{2}\right)\right) \Rightarrow \frac{h_m^0}{h_m^{amp}} = \pm\frac{q_m^0}{q_m^{amp}} \tag{6.14}$$

which states that the shift is zero if the blockage mid-length is located at a position where the pressure head and the flow harmonics are equal in magnitude. At a given blockage length η_2, the first equation in Eq. (6.12) is independent on the blockage location whereas the second equation depends on the blockage location. Figures 6.6a and 6.6b give the dimensionless pressure and flow harmonics variations along the pipe at modes m = 7 and m = 2, respectively. In this case, the blockage length is equal to half wavelength of the 7th mode harmonic which is η_2 = 2/(2×7-1) = 0.1538 ≈ 0.15. Three different locations are considered in Figures 6.6a and 6.6b. Figure 6.6a shows that at any blockage location along the pipe, the products of the pressure head and flow at the blockage boundaries are equal in magnitudes and signs. Therefore from Eq. (6.8), the shift is zero at any location along the pipe at mode 7 as observed in Figure 6.5. Notice that in Figure 6.6b, the first equation in Eq. (6.12) is not satisfied where the blockage length is smaller than half wavelength of the 2nd mode harmonic. The blockage location cases shown in Figure 6.6b satisfy the second equation in Eq. (6.12) where the blockage mid-length is situated at the position of equal

pressure head and flow magnitudes. At these specific blockage locations, the products of the pressure head and flow at the blockage boundaries are also equal which leads to zero shift. Consequently, the second equation in Eq. (6.12) gives the zero shift location at any given mode *m* as observed in Figures 6.2 and 6.5 except when the blockage length is a multiple of half wavelength of the m^{th} mode harmonic where the shift becomes zero at any blockage location along the pipe.

Figure 6.6 Dimensionless pressure head and flow harmonics variation along the pipe where different blockage location cases are shown to discuss the zero shift equations (Eq. (6.12))

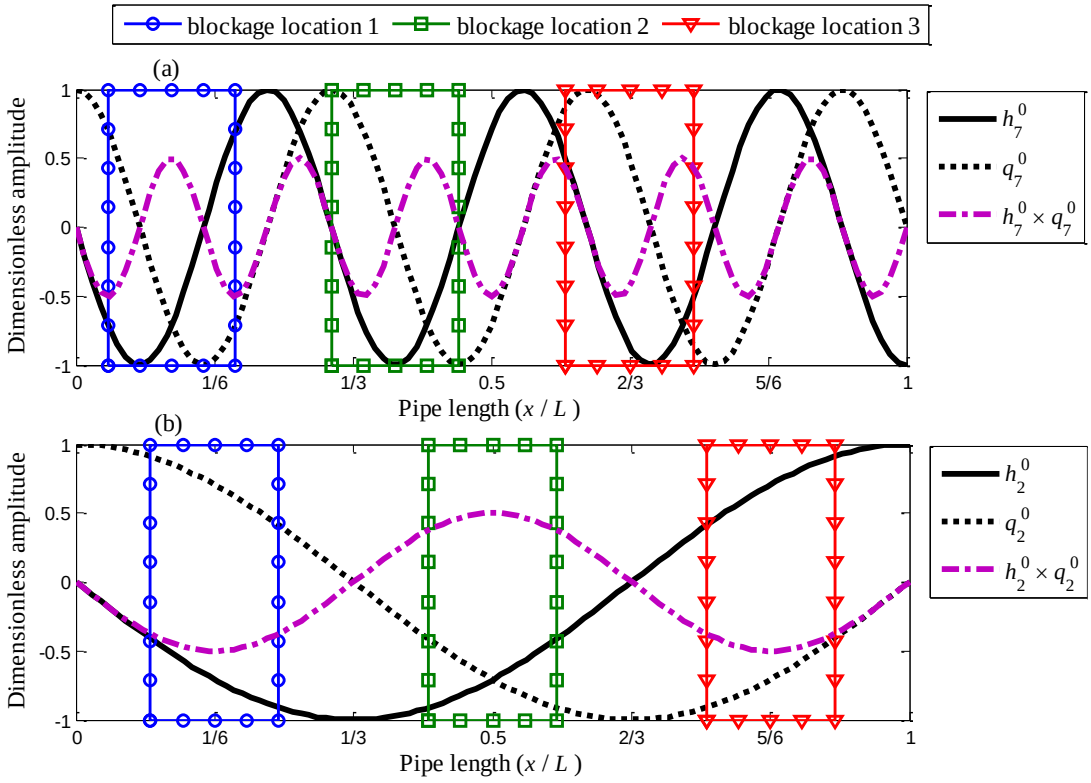

(a) Top **7^{th} mode of pressure and flow harmonics**

(b) Bottom **2^{nd} mode of pressure and flow harmonics**

6.4.2. Analysis and discussion of the positive and negative eigenfrequency shift

As observed from Figures 6.2 and 6.5, the shift sign alternates between consecutive zero shift locations. Moreover within two zero shift locations, the shift reaches either a positive or negative maximum shift. This section studies the mechanism causing such variation of shift sign and magnitude for shallow blockage case. Conditions for maximum shift are obtained by equating the gradient of Eq. (6.10) to zero which gives

$$\begin{cases} \cos\left(\left(2m-1\right)\dfrac{\pi}{2}\eta_2\right)=0 \\ \text{and} \\ \sin\left(\left(2m-1\right)\pi\left(\eta_3+\dfrac{\eta_2}{2}\right)\right)=0 \end{cases} \qquad (6.15)$$

yields

$$\begin{cases} \eta_2=\dfrac{2\overline{m}-1}{\left(2m-1\right)} \quad ; \quad \overline{m}=1,2,... \\ \text{and} \\ \eta_3+\dfrac{\eta_2}{2}=\dfrac{\overline{m'}}{2m-1} \quad ; \quad \overline{m'}=1,2,... \end{cases} \qquad (6.16)$$

The first equation in Eq. (6.16) corresponds to the Bragg resonance condition of maximum reflection (Eq. (4.10)) as follows

$$\eta_2=\frac{2\overline{m}-1}{2m-1} \quad \Leftrightarrow \quad \frac{w_m^0}{w_m^R\left(l_2\right)}=1 \quad \Leftrightarrow \quad l_2=\frac{\left(2\overline{m}-1\right)}{4}\left[\frac{4L}{2m-1}\right] \qquad (6.17)$$

which states that the shift is maximum if the blockage length is an odd multiple of quarter wavelength of the m^{th} mode harmonic. The second equation in Eq. (6.16) corresponds to the location of the blockage mid-length from the downstream boundary where

$$\begin{cases} \eta_3 + \dfrac{\eta_2}{2} = \dfrac{2\overline{m'}}{2m-1} \\ \text{or} \\ \eta_3 + \dfrac{\eta_2}{2} = \dfrac{2\overline{m'}-1}{2m-1} \end{cases} \Rightarrow \begin{cases} \sin\left(k_m^0 L\left(\eta_3 + \dfrac{\eta_2}{2}\right)\right) = 0 \\ \text{or} \\ \cos\left(k_m^0 L\left(\eta_3 + \dfrac{\eta_2}{2}\right)\right) = 0 \end{cases} \Rightarrow \begin{cases} \dfrac{h_m^0}{h_m^{amp}} = 0 \\ \text{or} \\ \dfrac{q_m^0}{q_m^{amp}} = 0 \end{cases} \quad (6.18)$$

which states that the shift is maximum if the blockage mid-length is located at a position of either a pressure node or stagnation point. Conversely to the zero shift case where either satisfied condition in Eq. (6.12) leads to zero shift, the maximum shift requires both equations in Eq. (6.16) to be fulfilled. That is the maximum shift is given when the blockage length is an odd multiple of quarter wavelength of the m^{th} mode harmonic and its mid-length is located at a position of either a pressure node or stagnation point. Figure 6.7 gives the dimensionless pressure and flow harmonics variations along the pipe at modes m=4. In this case, the blockage length is equal to quarter wavelength of the 4^{th} mode harmonic which is $\eta_2 = 1/(2\times4-1) \approx 0.15$. Three different locations are considered in Figure 6.7 to discuss the properties of Eq. (6.16). The blockage locations 1 and 3 are as such the blockage mid-length is placed respectively at a stagnation point and pressure node where both equations in Eq. (6.16) are satisfied. In these cases, Figure 6.7 shows that the products of the pressure head and flow at the blockage boundaries are equal in magnitudes but with different signs. Therefore the works at the boundaries in Eq. (6.8) are added up and since the product of sine and cosine is maximum when these two functions are equal, Eq. (6.8) gives maximum shift magnitude. At the blockage locations 1 and 3, Figure 6.5 shows that the shift magnitude is maximum.

The blockage location 2 in Figure 6.7 is as such the blockage mid-length is placed at a location of equal pressure head and flow which satisfies the second condition of zero shift (Eq. (6.12)) but not the second equation in Eq. (6.16). In this case, the product of the pressure head and flow at the blockage boundaries becomes of equal magnitudes and signs. Therefore from Eq. (6.8), the shift is zero as observed from Figure 6.5. This shows the necessity of both satisfied equations in Eq. (6.16) to produce maximum shift.

Figure 6.7 Dimensionless pressure head and flow harmonics of the 4th mode where different blockage location cases are shown to discuss the maximum shift equations (Eq. (6.16))

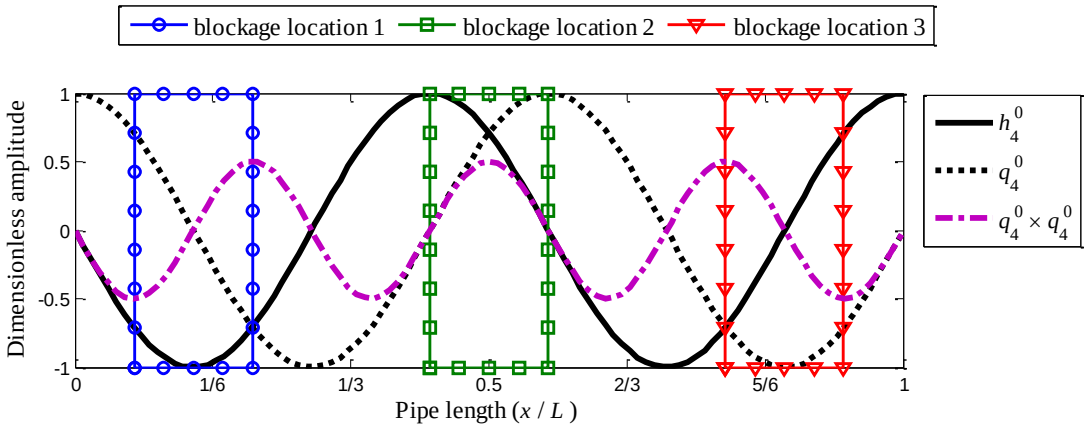

In order to distinguish between positive and negative maximum shifts, the determinant of the Hessian matrix is computed and analyzed as follows

$$D_H = \frac{\partial^2\left(\frac{\overline{\Delta w_m}}{w_1^0}\right)}{\partial\left(\eta_3+\frac{\eta_2}{2}\right)^2}\frac{\partial^2\left(\frac{\overline{\Delta w_m}}{w_1^0}\right)}{\partial(\eta_3)^2} - \frac{\partial^2\left(\frac{\overline{\Delta w_m}}{w_1^0}\right)}{\partial\left(\eta_3+\frac{\eta_2}{2}\right)\partial(\eta_3)} \qquad (6.19)$$

with

$$\begin{cases} \dfrac{\partial^2\left(\dfrac{\overline{\Delta w_m}}{w_1^0}\right)}{\partial\left(\eta_3+\dfrac{\eta_2}{2}\right)^2} = -\dfrac{(1-\alpha)}{\pi}\left[(2m-1)\pi\right]^2\left[\begin{array}{l} 2\sin\left((2m-1)\dfrac{\pi}{2}\eta_2\right) \\ \cos\left((2m-1)\pi\left(\eta_3+\dfrac{\eta_2}{2}\right)\right)\end{array}\right] \\ \dfrac{\partial^2\left(\dfrac{\overline{\Delta w_m}}{w_1^0}\right)}{\partial(\eta_2)^2} = -\dfrac{(1-\alpha)}{\pi}\left[(2m-1)\dfrac{\pi}{2}\right]^2\left[\begin{array}{l} 2\sin\left((2m-1)\dfrac{\pi}{2}\eta_2\right) \\ \cos\left((2m-1)\pi\left(\eta_3+\dfrac{\eta_2}{2}\right)\right)\end{array}\right] \\ \dfrac{\partial^2\left(\dfrac{\overline{\Delta w_m}}{w_1^0}\right)}{\partial\left(\eta_3+\dfrac{\eta_2}{2}\right)\partial(\eta_3)} = -\dfrac{(1-\alpha)}{2\pi}\left[(2m-1)\pi\right]^2\left[\begin{array}{l} 2\cos\left((2m-1)\dfrac{\pi}{2}\eta_2\right) \\ \sin\left((2m-1)\pi\left(\eta_3+\dfrac{\eta_2}{2}\right)\right)\end{array}\right] \end{cases} \quad (6.20)$$

which at the critical points conditions (Eq. (6.15)) gives

$$D_H = \left[\frac{(1-\alpha)}{\pi}\right]^2\left[(2m-1)\pi\right]^4(-1)^{2\left(\overline{m}+\overline{m}'+1\right)} > 0 \quad (6.21)$$

with

$$\begin{cases} \dfrac{\partial^2\left(\overline{\dfrac{\Delta w_m}{w_1^0}}\right)}{\partial\left(\eta_3+\dfrac{\eta_2}{2}\right)^2} = -2\dfrac{(1-\alpha)}{\pi}\left[(2m-1)\pi\right]^2(-1)^{\bar{m}+\bar{m}'+1} \\ \dfrac{\partial^2\left(\overline{\dfrac{\Delta w_m}{w_1^0}}\right)}{\partial(\eta_2)^2} = -2\dfrac{(1-\alpha)}{\pi}\left[(2m-1)\dfrac{\pi}{2}\right]^2(-1)^{\bar{m}+\bar{m}'+1} \\ \dfrac{\partial^2\left(\overline{\dfrac{\Delta w_m}{w_1^0}}\right)}{\partial\left(\eta_3+\dfrac{\eta_2}{2}\right)\partial(\eta_3)} = 0 \end{cases} \quad (6.22)$$

Therefore, if $\bar{m}$ and $\bar{m}'$ have the same parity, then the maximum shift is negative. However, if $\bar{m}$ and $\bar{m}'$ have different parity, then the maximum shift is positive. This means that at given $\bar{m}$ for which the Bragg resonance condition of maximum reflection in Eq. (6.16) is satisfied, if $\bar{m}$ is even, then the maximum shift is positive or negative when the blockage mid-length is located respectively at a pressure node or stagnation point (see Eq. (6.18)); and vice versa if $\bar{m}$ is odd. For example, Figure 6.7 shows the pressure and flow harmonics at mode $m = 4$ which corresponds to the first Bragg resonance frequency of maximum reflection ($\bar{m}$=1). The mid-length of the blockage location 1 in Figure 6.7 is at a stagnation point which from Figure 6.5 gives positive maximum shift as expected. On the other hand, the mid-length of the blockage location 3 in Figure 6.7 is at a pressure node which from Figure 6.5 gives, also as expected, a negative maximum shift.

Equation (6.16) gives the conditions for "absolute" maximum shift which is given at specific modes that satisfy the Bragg resonance condition of maximum reflection. However, at any given mode *m*, the eigenfrequency variation undergoes "local" maximum shift although the Bragg resonance condition of maximum reflection is not satisfied. The location of those "local" maximum shift at any given mode *m* are determined by considering a fixed blockage

length η_2. Therefore, assuming a fixed blockage length η_2 and equating to zero the first derivative of the shift equation (Eq. (6.10)) with respect to the mid-length blockage location $(\eta_3+\eta_2/2)$, give

$$\sin\left(\left(2m-1\right)\pi\left(\eta_3+\frac{\eta_2}{2}\right)\right)=0 \;\Rightarrow\; \eta_3+\frac{\eta_2}{2}=\frac{\overline{m}}{2m-1} \tag{6.23}$$

which gives the second condition in Eq. (6.16). The maximum shift sign is obtained by computing the second derivative at the maximum shift locations as follows

$$\frac{\partial^2\left(\overline{\Delta w_m}/w_1^0\right)}{\partial\left(\eta_3+\eta_2/2\right)^2}=2\frac{\left(1-\alpha\right)}{\pi}\left[\left(2m-1\right)\pi\right]^2\sin\left(\left(2m-1\right)\frac{\pi}{2}\eta_2\right)\left(-1\right)^{\overline{m}+1} \tag{6.24}$$

Knowing that $\sin\left(\left(2m-1\right)\pi\eta_2/2\right)$ changes sign between two consecutive Bragg resonance frequencies of total transmission (Eq. (4.11)), Eq. (6.24) gives

$$\operatorname{sgn}\left[\frac{\partial^2\left(\overline{\Delta w_m}/w_1^0\right)}{\partial\left(\eta_3+\eta_2/2\right)^2}\right]=\left(-1\right)^{n_T+\overline{m}}\begin{cases}\text{if } >0 \;\Rightarrow\; \text{maximum shift is negative}\\ \text{if } <0 \;\Rightarrow\; \text{maximum shift is positive}\end{cases} \tag{6.25}$$

where "sgn" is the sign function; and n_T is an integer that gives the number of modes region between two consecutive Bragg resonance frequencies of total transmission defined as

$$n_T=\operatorname{Floor}\left(\left(2m-1\right)\frac{\eta_2}{2}\right)+1 \tag{6.26}$$

where "Floor" is a function that gives the largest previous integer. The second derivative in Eq. (6.25) is positive when n_T and $\overline{m}$ have the same parity which leads to negative maximum shift; and positive when n_T and $\overline{m}$ have different parity which leads to positive maximum shift. This means that at given m such that n_T is even, then the maximum shift is positive or negative when the blockage mid-length is located respectively at a pressure node or stagnation point (see Eq. (6.18)); and vice versa if n_T is odd. For example, Figure 6.8 gives the dimensionless pressure and flow harmonics at mode $m = 2$ where the blockage

length is $\eta_2 \approx 0.15$ which gives $n_T = 1$ (Eq. (6.26)). Two blockage location cases are shown in Figure 6.8. The mid-length of blockage locations 1 and 2 are placed respectively at a stagnation point and a pressure node. Figure 6.5 shows that at these blockage locations the maximum shift is respectively positive and negative which is as expected from Eq. (6.25).

Figure 6.8 Dimensionless pressure head and flow harmonics of the 2nd mode where different blockage location cases are shown to discuss the maximum shift equations at given mode *m* (Eqs. (6.23) and (6.25))

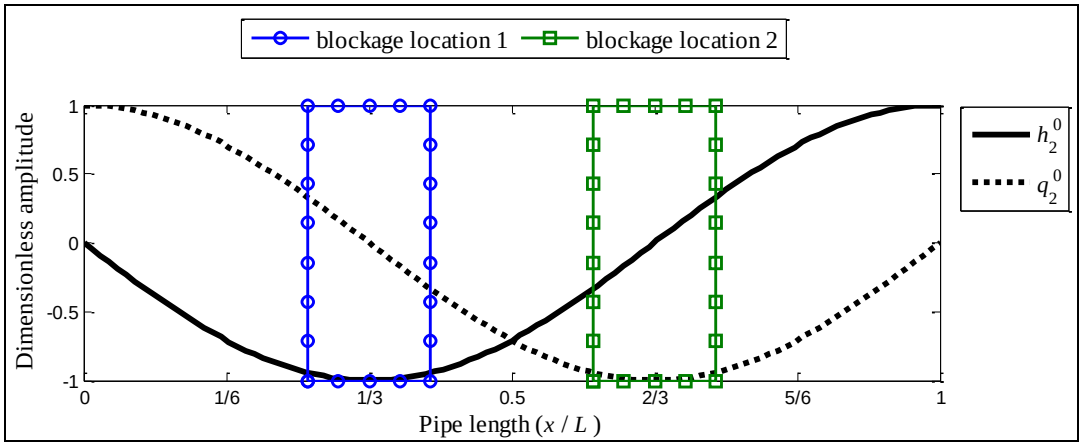

6.5. Analysis and discussion of eigenfrequency shift variation for interior blockage with large and moderate radial protrusion

6.5.1. Asymptotic solutions

For the case of a blockage at the boundary (Chapter 5 Section 5.5), it is shown that the solution for extremely blocked pipe (asymptotic solution) is very informative about the mechanism of coupling and decoupling (interaction) between the blocked and intact pipe sections. In this section, the asymptotic solutions for the case of interior blockage are discussed to aid demonstrating the relationship between eigenfrequency shift variations and Bragg-type resonance discussed in Chapter 4.

For severely blocked pipe such as $\alpha = A_2/A_0 \to 0$, the dispersion relationship in Eq. (6.1) becomes

$$\cos\left(k_m^s l_1\right)\sin\left(k_m^s l_2\right)\sin\left(k_m^s l_3\right) = 0 \qquad (6.27)$$

where the superscript "s" refers to severe blockage case. Equation (6.27) is equivalent to

$$\cos\left(k_{m_1}^s l_1\right) = 0 \quad \Leftrightarrow \quad w_{m_1}^s = a k_{m_1}^s = 2\pi\left(\left(2m_1 - 1\right)\frac{a}{4l_1}\right) \;\; ; \;\; m_1 = 1, 2, 3... \qquad (6.28)$$

or

$$\sin\left(k_{m_2}^s l_2\right) = 0 \quad \Leftrightarrow \quad w_{m_2}^s = a k_{m_2}^s = 2\pi\left(2m_2\frac{a}{4l_2}\right) \;\; ; \;\; m_2 = 1, 2, 3... \qquad (6.29)$$

or

$$\sin\left(k_{m_3}^s l_3\right) = 0 \quad \Leftrightarrow \quad w_{m_3}^s = a k_{m_3}^s = 2\pi\left(2m_3\frac{a}{4l_3}\right) \;\; ; \;\; m_3 = 1, 2, 3... \qquad (6.30)$$

Equation (6.28) is equivalent to a dispersion relation of an intact RPV system with length l_1. Equation (6.29) is equivalent to a dispersion relationship of either an intact Reservoir-pipe-Reservoir (RPR) system or Valve-pipe-Valve (VPV) system with length l_2. Similarly, Eq. (6.30) is equivalent to a dispersion relationship of an intact VPV system with length l_3. Therefore, Eqs. (6.28)-(6.30) show that, for severe blockage case, the blocked pipe system shown in Figure 6.1 is equivalent to three intact pipe subsystems with different upstream and downstream boundaries as sketched in Figure 6.9. In this case (Figure 6.9), subsystem 2 is an RPR intact system with length l_2 where pipe 1 and pipe 3 are considered as the upstream and downstream reservoirs, respectively. On the other hand, pipe 2 plays a role of a valve at the downstream and upstream boundaries of subsystem 1 and subsystem 3, respectively. In this way, the blocked pipe system is referred as *uncoupled* pipe system and its eigenfrequencies solutions in Eqs. (6.28)-(6.30) are referred as asymptotic solutions.

In Figure 6.10 and Figure 6.11, the asymptotic solutions from Eqs. (6.28) and (6.30) are plotted along with the eigenfrequency variation obtained from Eq. (6.1) for $\eta_2 = 0.15$ and

$\eta_2 = 0.027$, respectively. The case of highly severe blockage ($\alpha = 0.01$) in Figure 6.10 and Figure 6.11, although unrealistic, shows that the eigenfrequency solutions converge to the asymptotic solutions. However, the less severe blockage case ($\alpha = 0.16$) shows that the eigenfrequency variations approaches the asymptotic solutions at specific resonant modes only. For example, at mode $m = 4$, the eigenfrequency variation for $\alpha = 0.16$ is better approximated by the asymptotic solutions than the case for mode m = 1, 2 or 3.

Since the maximum shift magnitudes are varying at different modes, the eigenfrequency variation with $\eta_b = \eta_3 + 0.5\eta_2$ at high modes are shown in Figure 6.12 where the first 15 modes for the case $\alpha = 0.16$ and $\eta_2 = 0.15$ are given along with the asymptotic solutions. Figure 6.12 shows that the shift takes maximum values at given modes (e.g. $m \approx 4$, 11) where the eigenfrequency variation fits very well with the asymptotic solutions. On the other hand, the shift becomes zero at any position η_b for other given modes (e.g. $m \approx 7$ and 14). Similar features were observed in Section 6.4 for the case of interior blockage with small radial protrusion.

The case of short blockage length $\eta_2 = 0.027$ is given in Figure 6.13 and shows that modes exhibiting maximum shifts or nearly zero shifts occur but at much higher frequency comparing to the case $\eta_2 = 0.15$. Moreover, Figure 6.13 shows that many modes undergo maximum shift with excellent fitting between the eigenfrequency variation and the asymptotic solutions (e.g. m=8 to m=29), however, fewer modes experience nearly zero shift (e.g. m=35 to m=38). Although not shown here, but similar features are observed for different α values in both $\eta_2 = 0.15$ and $\eta_2 = 0.027$ cases.

Figure 6.9 Schematic figures of uncoupled subsystems for severe blockage case.

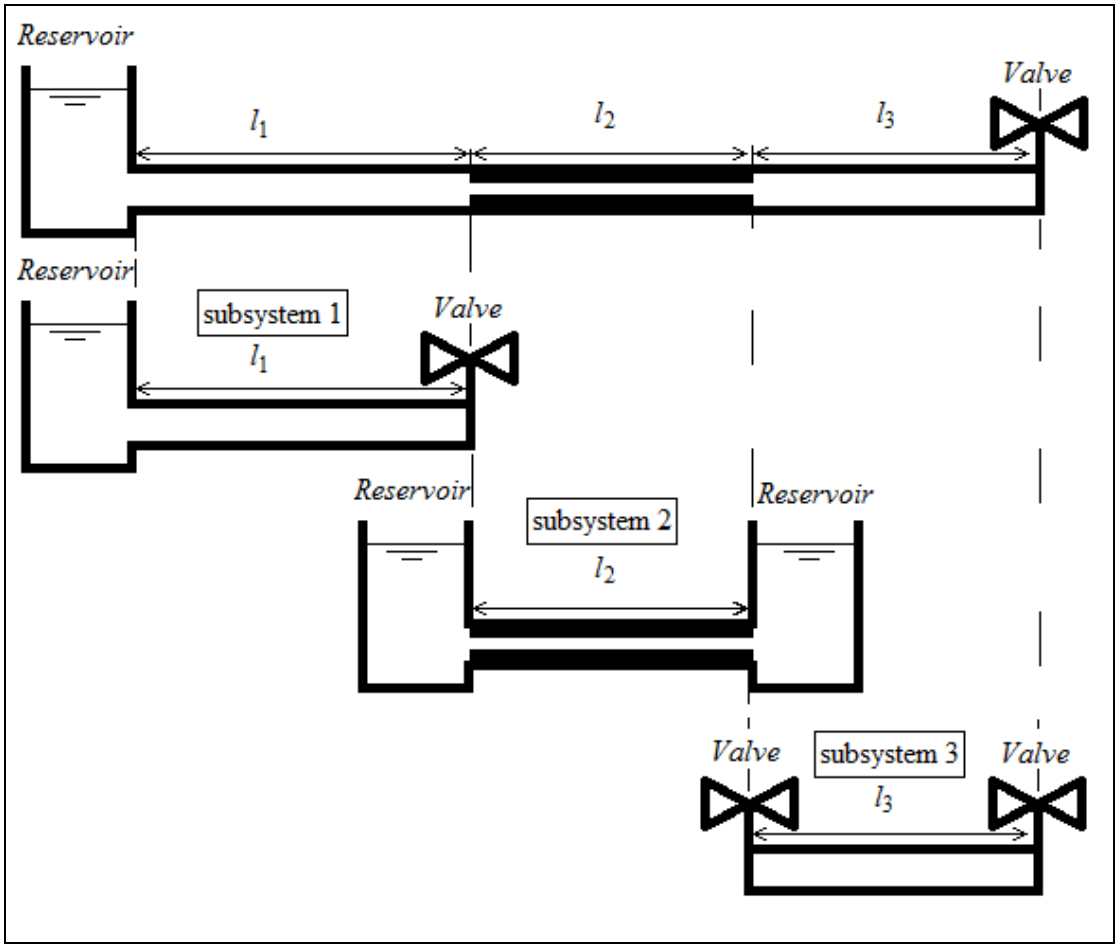

Figure 6.10 Normalized eigenfrequency variation with length $\eta_b = \eta_3 + 0.5\eta_2$ of the first 5 modes for different α values when $\eta_2 = 0.15$ along with the eigenfrequencies of the uncoupled subsystems

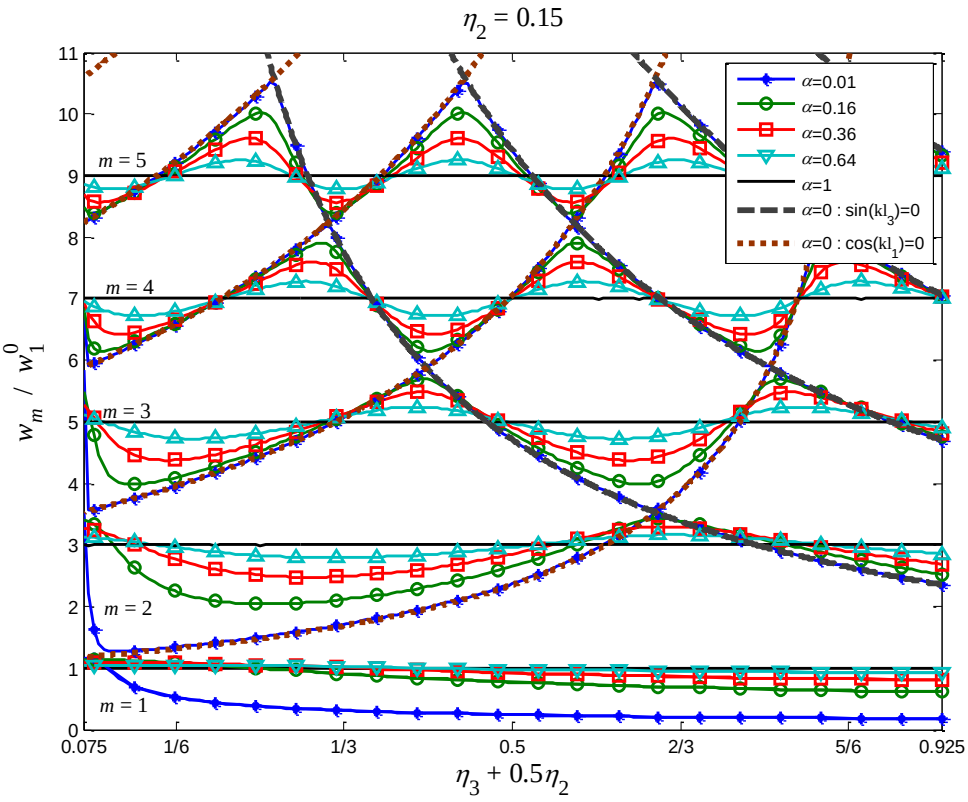

Figure 6.11 Normalized eigenfrequency variation with length $\eta_b = \eta_3 + 0.5\eta_2$ of the first 5 modes for different α values when $\eta_2 = 0.027$ along with the eigenfrequencies of the uncoupled subsystems

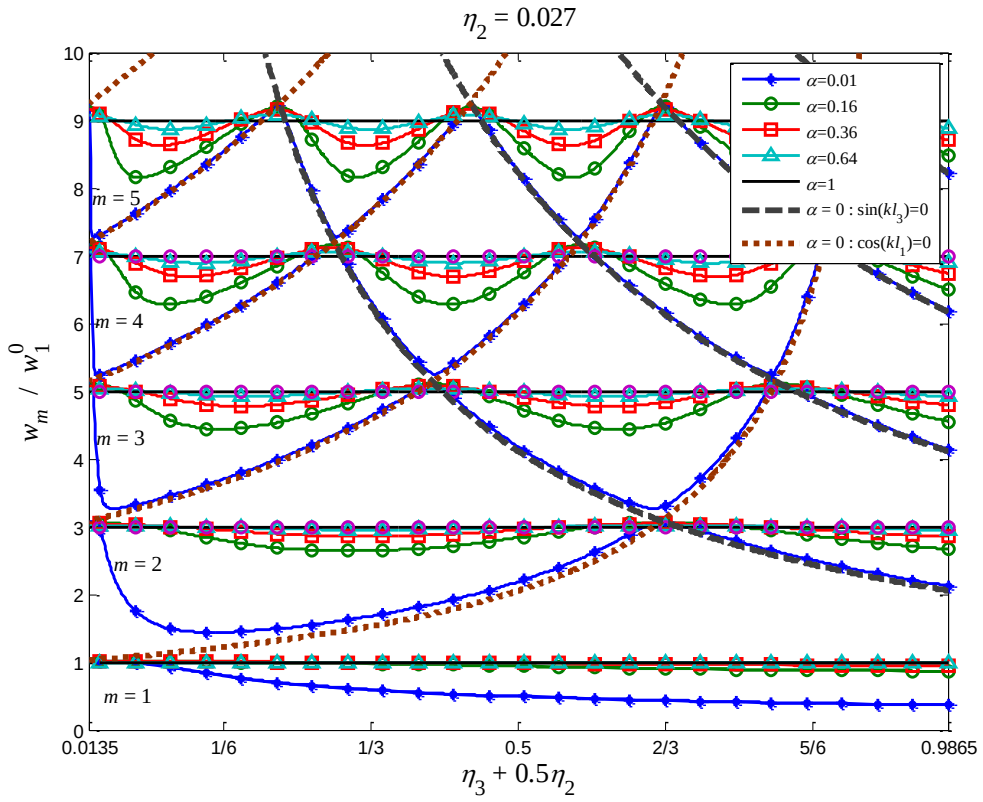

Figure 6.12 Normalized eigenfrequency variation with length $\eta_b = \eta_3 + 0.5\eta_2$ of the first 15 modes when $\alpha = 0.16$ and $\eta_2 = 0.15$ along with the asymptotic solutions

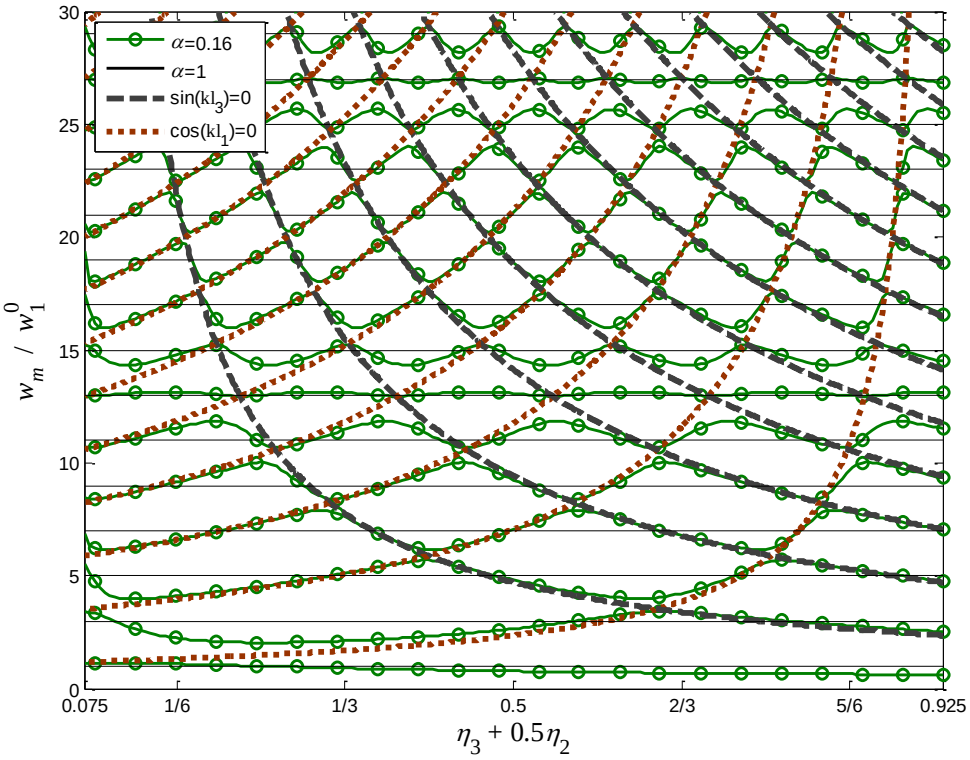

Figure 6.13 Normalized eigenfrequency variation with length $\eta_b = \eta_3 + 0.5\eta_2$ when $\alpha = 0.16$ and $\eta_2 = 0.027$ along with the asymptotic solutions

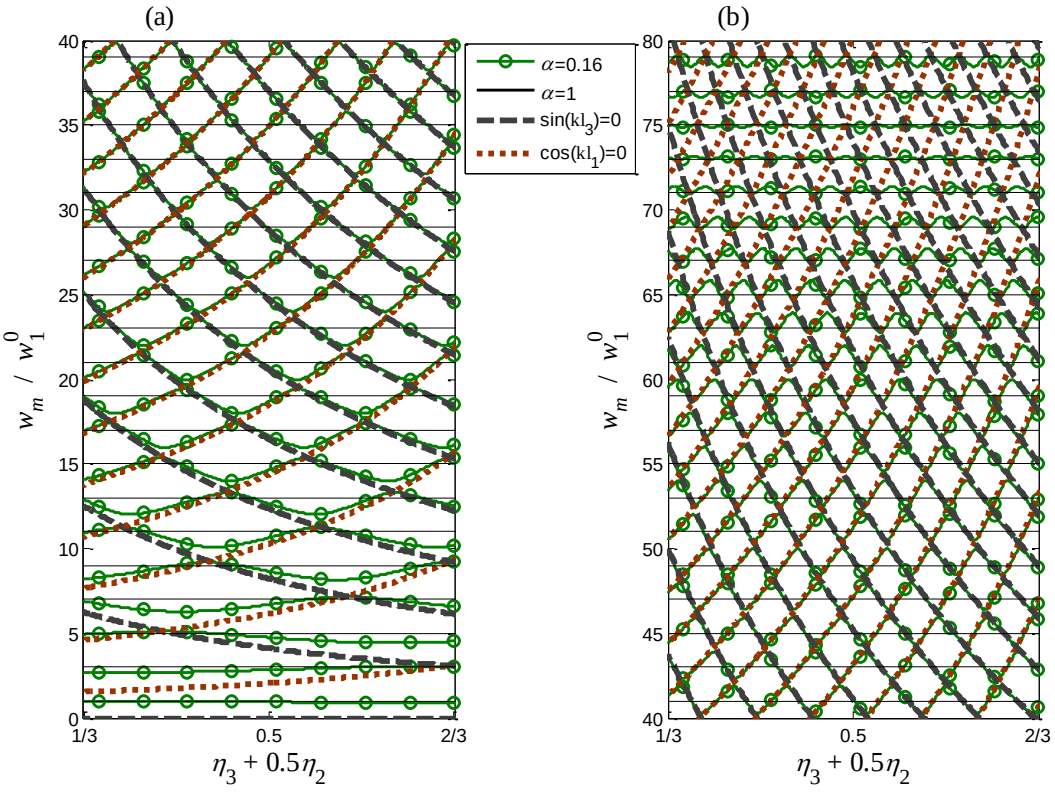

(a) Left **The first 20 modes**

(b) Right **Modes *m*=21 to *m*=40.**

6.5.2. Relation between eigenfrequency variation and Bragg-type resonance

In Chapter 4, the wave-blockage interaction in unbounded pipe system is studied where it was shown that such interaction induces Bragg-type resonance that informs which waves transmit least through a blockage and, by implication, which waves reflect most towards the source. This section shows how Bragg resonance is related to the eigenfrequency variation in bounded pipe system. For this purpose, the reflection amplitude variation in unbounded pipe system (Figure 4.4c) is compared to the eigenfrequency variation in bounded pipe system (Figures 6.12 and 6.13). However, since the frequency axis in Figure 4.4c is different from

the frequency axis in Figures 6.12 and 6.13, a change of variable is required so that comparison at the same axis could be made. Thus, the following change of variable is used

$$\frac{w}{w_1^R(l_2)} = \frac{w}{2\pi\dfrac{a}{4l_2}} = \frac{w}{2\pi\dfrac{a}{4L}\dfrac{L}{l_2}} = \eta_2\frac{w}{w_1^0} \quad \Rightarrow \quad \frac{w}{w_1^0} = \frac{1}{\eta_2}\frac{w}{w_1^R(l_2)} \tag{6.31}$$

which makes Figures 4.4c and Figures 6.12 and 6.13 having the same dimensionless frequency axis. Using the change of variable in Eq. (6.31), Figures 4.4c and Figure 6.12 are compared in Figure 6.14 for the case $\alpha = 0.16$ and $\eta_2 = 0.15$ where Figure 6.14a shows the eigenfrequency variation with $\eta_3 + \eta_2/2$ for the first 15 modes (where only $1/3 \le \eta_3 + \eta_2/2 \le 2/3$ is considered for the clarity of the Figure); and Figure 6.14b gives the reflection amplitude (horizontal axis) variation with the dimensionless frequency (vertical axis). Figure 6.14 shows that the maximum shift regions, which also correspond to the regions where the eigenfrequencies are best approximated by the asymptotic solutions, occur at modes with eigenfrequencies close to the Bragg resonance frequency of maximum reflection ($w_m \approx w_m^R$). On the other hand, zero or nearly zero shift regions occur at modes with frequencies close to the Bragg resonance frequency of total transmission ($w_m \approx w_m^T$). The mechanism behind this is as follows. When *maximum wave reflection* occurs ($w_m \approx w_m^R$), the blockage increases the uncoupling effect between pipe 1 and pipe 3 by preventing the transmission of the waves from pipe 1 to pipe 3 and vice versa (Figure 4.6). Therefore, in this case, the eigenfrequency variation approaches the asymptotic solution. However, when *total wave transmission* occurs ($w_m \approx w_m^T$), the blockage allows all the waves from pipe 1 to transmit to pipe 3 and vice versa with no reflections (Figure 4.7) as if the blockage did not exist. In this case, the eigenfrequency variation approaches the intact pipe solution and therefore the shift approaches zero.

Similarly, using the change of variable in Eq. (6.31), Figures 4.4c is compared to Figure 6.13 for the case $\alpha = 0.16$ and $\eta_2 = 0.027$, and the results are shown in Figures 6.15 and 6.16 where Figure 6.15 shows the comparison for the first 20 modes and Figure 6.16 shows the comparison for modes m = 21 to m = 40. Again, the maximum and minimum shift regions occur at modes with eigenfrequency close to the Bragg resonance

frequencies of maximum reflection ($w_m \approx w_{\overline{m}}^R$) and total transmission ($w_m \approx w_{\overline{m}}^T$), respectively.

As discussed in the unbounded pipe case (Chapter 4), Bragg resonance frequencies (Eq. (4.10) and Eq. (4.11)) are much higher for short blockage case than for extended blockage case (Figures 4.4). For example, the first Bragg resonance frequency of maximum reflection for the case $\eta_2 = 0.027$ occurs at $m = 18$, whereas it occurs at $m \approx 4$ for the case $\eta_2 = 0.15$. By consequences, the shorter the blockage is, the smaller the shift induced at low modes. This supports the results from Lee, et al. ([71]) where they concluded that the generation of high frequency waves are needed for small scale defect-detection with TBDDM. On the other hand, if a short blockage has large radial protrusion (severe-short blockage), the Bragg resonance effect of maximum reflection affects large frequency bandwidth as shown in Figure 4.3 and 4.4; and therefore, the shift induced by a severe-short blockage could becomes large at much lower modes than the mode at which the eigenfrequency is close to the Brag resonance frequency of maximum reflection. This is why Figure 6.15 shows that at the first five low modes, the shift is small and the eigenfrequencies do not fit with the asymptotic solutions, whereas from the 6th mode, the shift magnitude increases and the eigenfrequencies approach the asymptotic solutions.

The effect of Bragg resonance on the eigenfrequency shift could be observed by inserting the Bragg resonant frequencies (Eq. (4.10) and Eq. (4.11)) into the dispersion relation Eq. (6.1). First, inserting Eq. (4.11) into Eq. (6.1) gives

$$\alpha \cos\left(w_{\overline{m}}^T l_2 / a\right)\begin{bmatrix}\cos\left(w_{\overline{m}}^T l_1 / a\right)\cos\left(w_{\overline{m}}^T l_3 / a\right) \\ -\sin\left(w_{\overline{m}}^T l_1 / a\right)\sin\left(w_{\overline{m}}^T l_3 / a\right)\end{bmatrix} = 0 \qquad (6.32)$$

which leads to

$$\cos\left(w_{\overline{m}}^T \left(l_1 + l_3\right) / a\right)\cos\left(w_{\overline{m}}^T l_2 / a\right) = 0\,. \qquad (6.33)$$

Considering the following manipulation

$$\cos\left(w_{\overline{m}}^T \left(l_1 + l_3\right) / a\right)\cos\left(w_{\overline{m}}^T l_2 / a\right) - \underbrace{\sin\left(w_{\overline{m}}^T l_2 / a\right)\cos\left(w_{\overline{m}}^T \left(l_1 + l_3\right) / a\right)}_{=0} = 0 \qquad (6.34)$$

yields

$$\cos\left(w_m^T L / a\right) = 0 \qquad (6.35)$$

which is the dispersion relation for intact pipe case (Eq. (6.3)) at $w_m = w_m^T$ (total transmission) and that is why the shift is zero at those frequencies for any blockage length η_2 and radial protrusion α.

Similarly, inserting Eq. (4.10) into Eq. (6.1) gives

$$\sin\left(w_m^R l_2 / a\right)\left[\alpha^2 \sin\left(w_m^R l_1 / a\right)\cos\left(w_m^R l_3 / a\right) + \cos\left(w_m^R l_1 / a\right)\sin\left(w_m^R l_3 / a\right)\right] = 0 \qquad (6.36)$$

which leads to

$$\alpha^2 \sin\left(w_m^R l_1 / a\right)\cos\left(w_m^R l_3 / a\right) + \cos\left(w_m^R l_1 / a\right)\sin\left(w_m^R l_3 / a\right) = 0 \qquad (6.37)$$

Equation (6.37) corresponds to the dispersion relation of either a RPR system with length (l_1+l_3) having a blockage at the downstream boundary with a blockage length l_3 and an area ratio α^2 as shown in Figure 6.17a; or a VPV system with length (l_1+l_3) having a blockage at the upstream boundary with a blockage length l_1 and an area ratio α^2 as shown in Figure 6.17b. This means that at maximum reflection region ($w_m = w_m^R$), the eigenfrequency shift behaves similarly to the shift in a blocked pipe system with a blockage at the boundary where the dimensionless length and area of the blockage are the blockage location (η_1 or η_3) and α^2, respectively. The eigenfrequency shift mechanism for this simple blocked pipe system with a blockage at the boundary is well studied and understood in Chapter 5.

Figure 6.14 Relation between Bragg-type resonance and eigenfrequency variation by comparison between the eigenfrequency shift in bounded system and the reflected amplitude variation with frequency in unbounded system (frequency bands of Bragg-type resonance) when $\eta_2 = 0.15$ and $\alpha = 0.16$

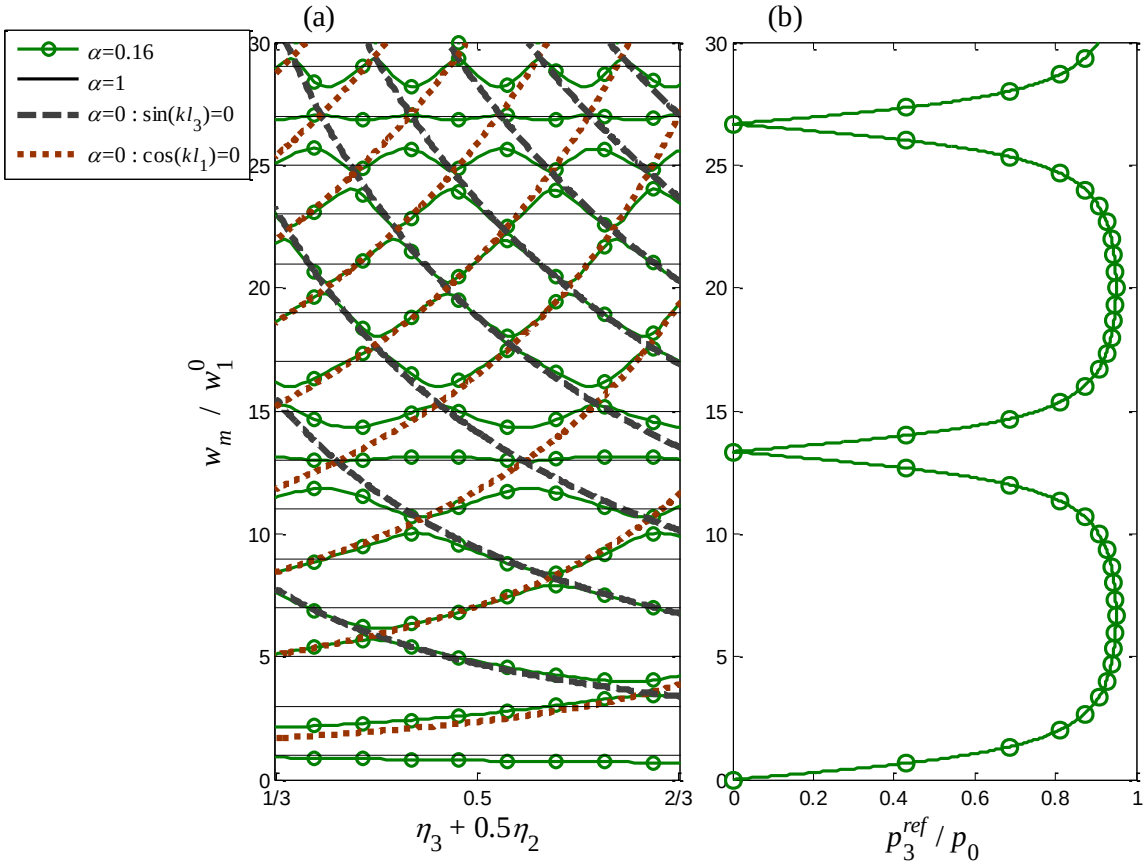

(a) Left **Eigenfrequency shift variation: $\eta_3 + 0.5\eta_2$ axis limited to [1/3 to 2/3]**

(b) Right **Reflected amplitude variation (see 4.4c) with modified frequency (see Eq. (6.31)) in unbounded system**

Figure 6.15 Relation between Bragg-type resonance and eigenfrequency variation by comparison between the eigenfrequency shift in bounded system and the reflected

amplitude variation with frequency in unbounded system (frequency bands of Bragg-type resonance) when $\eta_2 = 0.027$ and $\alpha = 0.16$ (up to mode 20)

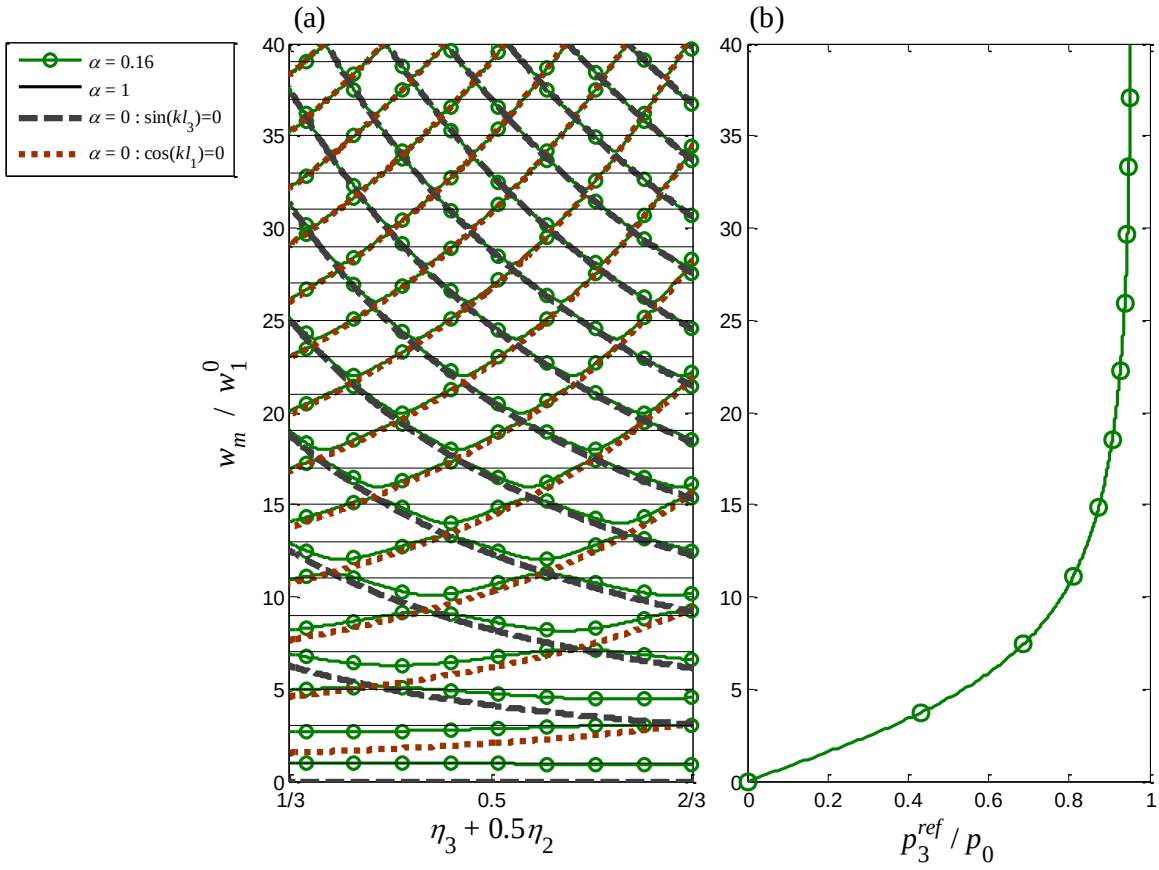

(a) Left **Eigenfrequency shift variation: $\eta_3 + 0.5\eta_2$ axis limited to [1/3 to 2/3]**

(b) Right **Reflected amplitude variation (see 4.4c) with modified frequency (see Eq. (6.31)) in unbounded system**

Figure 6.16 Relation between Bragg-type resonance and eigenfrequency variation by comparison between the eigenfrequency shift in bounded system and the reflected amplitude variation with frequency in unbounded system (frequency bands of Bragg-type resonance) when $\eta_2 = 0.027$ and $\alpha = 0.16$ (from mode 20 to 40)

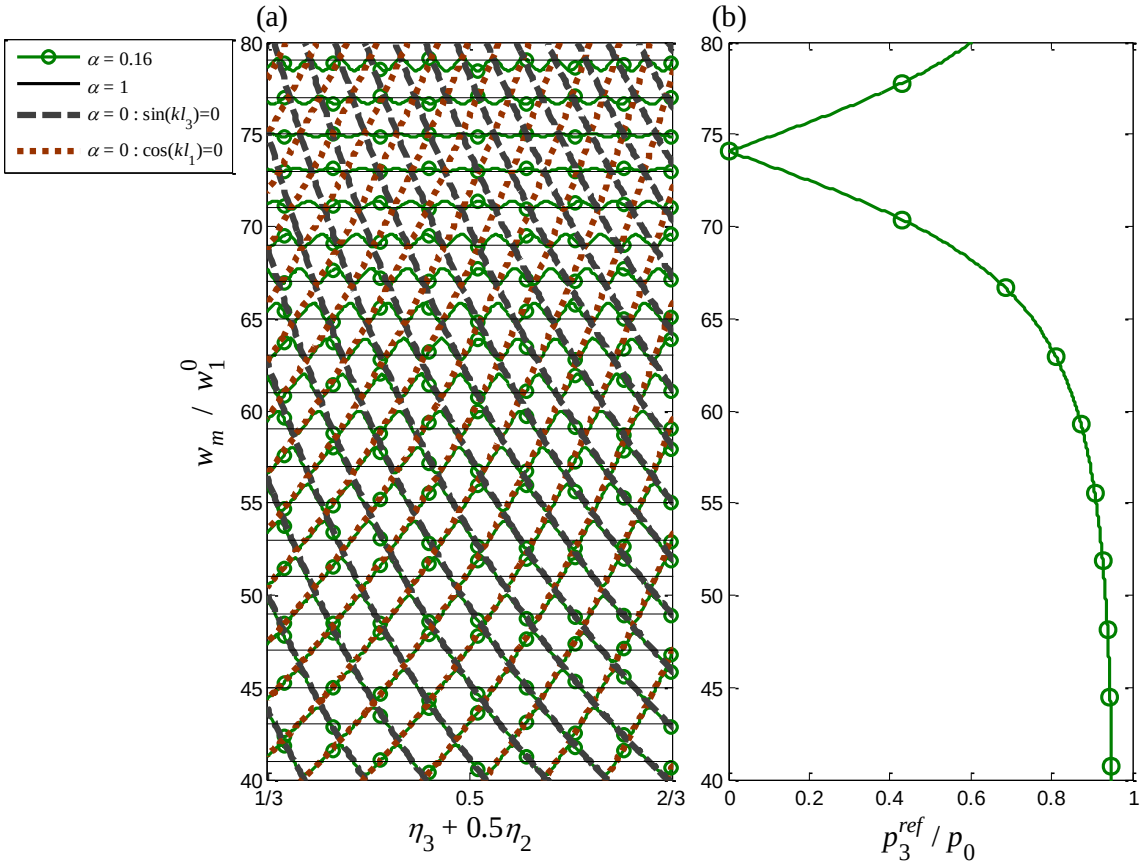

(a) Left **Eigenfrequency shift variation: $\eta_3 + 0.5\eta_2$ axis limited to [1/3 to 2/3]**

(b) Right **Reflected amplitude variation (see 4.4c) with modified frequency (see Eq. (6.31)) in unbounded system**

Figure 6.17 Equivalent pipe system with length (l_1+l_3) containing a blockage at the boundary with dimensionless blocked area α^2 corresponding to the dispersion relation in Eq. (6.37)

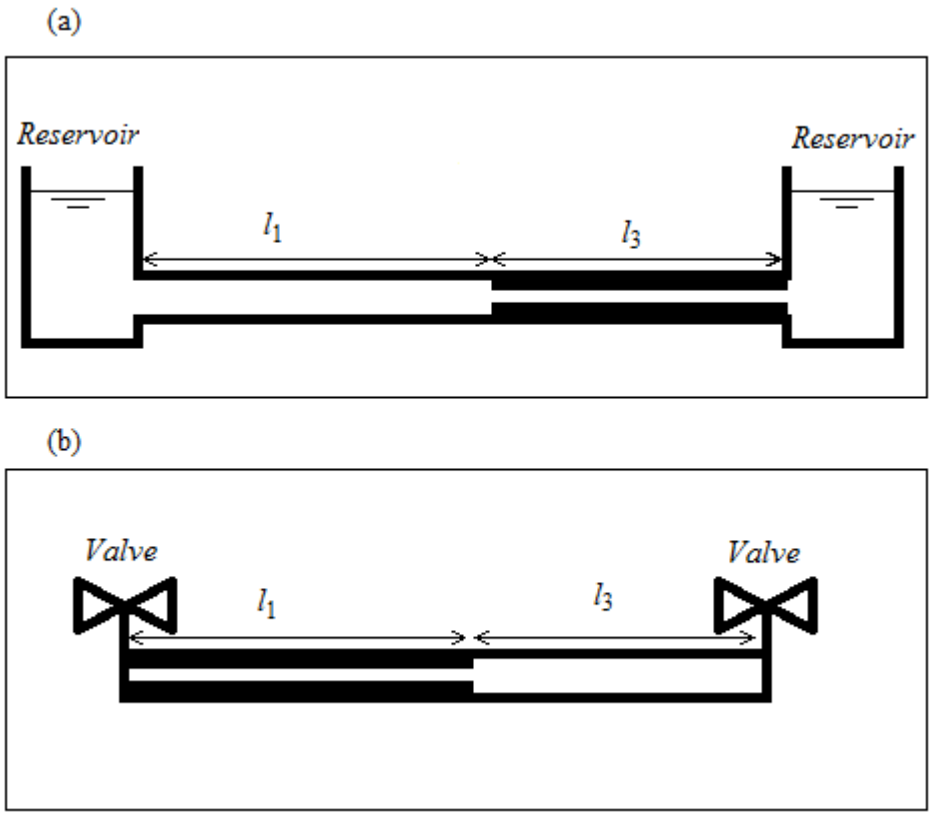

(a) Top **RPR system with a blockage of length l_3 at the downstream boundary**

(b) Bottom **VPV system with a blockage of length l_1 at the upstream boundary**

6.5.3. Variation of zero shift locations with the radial protrusion of the blockage

For the case of blocked pipe system with blockage at the boundary (see Figure 5.2), the zero shift locations are independent on α. However for interior blockage case, Figure 6.2 and Figure 6.3 show that the zero shift locations at a given mode vary with α except at the modes corresponding to the Bragg resonance frequency of maximum reflections (for

example see 4th mode in Figure 6.2). In fact, at these exception modes, the pipe system with interior blockage behaves as a blocked pipe system with blockage at the boundary; and that is why the zero shift location becomes independent on α. In order to determine the variation of the zero shift locations, the dispersion relation for blocked RPV system with interior blockage (Eq. (6.2)) is rewritten as follows

$$\begin{aligned}&\cos\left(k_m L\right)\\&+\frac{\left(1-\alpha\right)}{\left(1+\alpha\right)}\cos\left(k_m L\left(1-\left(2\eta_3+\eta_2\right)-\eta_2\right)\right)\\&-\frac{\left(1-\alpha\right)}{\left(1+\alpha\right)}\cos\left(k_m L\left(1-\left(2\eta_3+\eta_2\right)+\eta_2\right)\right)\\&-\frac{\left(1-\alpha\right)^2}{\left(1+\alpha\right)^2}\cos\left(k_m L\left(1-2\eta_2\right)\right)=0\end{aligned} \qquad (6.38)$$

Using the fact that at zero shift, $k_m = k_m^0 = \left(2m-1\right)\frac{\pi}{2L}$ leads to

$$\begin{aligned}&\sin\left(\left(2m-1\right)\frac{\pi}{2}\left(2\eta_3+\eta_2\right)+\left(2m-1\right)\frac{\pi}{2}\eta_2\right)\\&-\sin\left(\left(2m-1\right)\frac{\pi}{2}\left(2\eta_3+\eta_2\right)-\left(2m-1\right)\frac{\pi}{2}\eta_2\right).\\&-\frac{\left(1-\alpha\right)}{\left(1+\alpha\right)}\sin\left(\left(2m-1\right)\frac{\pi}{2}2\eta_2\right)=0\end{aligned} \qquad (6.39)$$

Using trigonometric manipulation on Eq. (6.39) , yields

$$\begin{aligned}&2\sin\left(\left(2m-1\right)\frac{\pi}{2}\eta_2\right)\cos\left(\left(2m-1\right)\frac{\pi}{2}\left(2\eta_3+\eta_2\right)\right)\\&-2\frac{\left(1-\alpha\right)}{\left(1+\alpha\right)}\sin\left(\left(2m-1\right)\frac{\pi}{2}\eta_2\right)\cos\left(\left(2m-1\right)\frac{\pi}{2}\eta_2\right)=0\end{aligned} \qquad (6.40)$$

which gives

$$\begin{bmatrix} \cos\left((2m-1)\dfrac{\pi}{2}(2\eta_3+\eta_2)\right) \\ -\dfrac{(1-\alpha)}{(1+\alpha)}\cos\left((2m-1)\dfrac{\pi}{2}\eta_2\right) \end{bmatrix} \sin\left((2m-1)\frac{\pi}{2}\eta_2\right)=0 \qquad (6.41)$$

There are two possible solutions for Eq. (6.41). First is

$$\sin\left((2m-1)\pi\eta_2/2\right)=0 \qquad (6.42)$$

which gives the Bragg resonance frequencies of total transmission; and corresponds to the first equation in Eq. (6.12) for small radial protrusion case. The second is given by

$$\cos\left((2m-1)\frac{\pi}{2}(2\eta_3+\eta_2)\right)-\frac{(1-\alpha)}{(1+\alpha)}\cos\left((2m-1)\frac{\pi}{2}\eta_2\right)=0 \qquad (6.43)$$

which has the following solution (see Appendix B)

$$(2m-1)\frac{\pi}{2}(2\eta_3+\eta_2)=-\arccos\left[(-1)^{\bar{m}}\frac{(1-\alpha)}{(1+\alpha)}\cos\left((2m-1)\frac{\pi}{2}\eta_2\right)\right]+\bar{m}\pi \qquad (6.44)$$

leading to

$$\eta_3+\frac{\eta_2}{2}=\frac{2\bar{m}-\dfrac{2}{\pi}\arccos\left[(-1)^{\bar{m}}\dfrac{(1-\alpha)}{(1+\alpha)}\cos\left((2m-1)\dfrac{\pi}{2}\eta_2\right)\right]}{2(2m-1)} \qquad (6.45)$$

Equation (6.45) gives the zero shift locations ($\bar{m}$) at a given mode *m* and for a given dimensionless area α. For example, the zero shift locations from Eq. (6.45) at the second mode (*m* = 2) and for α = 0.16 and η_2 = 0.15 are

$$\eta_3+\frac{\eta_2}{2}=0.1048 \quad ; \quad \eta_3+\frac{\eta_2}{2}=0.5619 \quad ; \quad \eta_3+\frac{\eta_2}{2}=0.7715 \qquad (6.46)$$

which agree with the zero shift locations observed in Figure 6.12.

Notice that when

$$\cos\left(\left(2m-1\right)\pi\,\eta_2/2\right)=0\,, \tag{6.47}$$

which gives the Bragg resonance frequencies of maximum reflection, Eq. (6.45) becomes

$$\eta_3+\frac{\eta_2}{2}=\frac{2\overline{m}-1}{2\left(2m-1\right)} \tag{6.48}$$

which is independent on α and corresponds to the second zero shift equation in Eq. (6.12) for small radial protrusion case. Moreover, Eq. (6.47) gives

$$\eta_2=\frac{2\overline{m'}-1}{\left(2m-1\right)}\quad;\quad \overline{m'}=1,2,3...<m \tag{6.49}$$

and when inserted into Eq. (6.48) yields

$$\eta_3=\frac{\overline{m''}}{\left(2m-1\right)}\quad;\quad \overline{m''}\equiv\overline{m}-\overline{m'}-1=1,2,3... \tag{6.50}$$

which could be written as

$$\frac{l_3}{\left(l_1+l_3\right)}\left(1-\eta_2\right)=\frac{\overline{m''}}{\left(2m-1\right)}\quad\Rightarrow\quad\frac{l_3}{\left(l_1+l_3\right)}=\frac{\overline{m''}}{2\left(m-\overline{m'}\right)} \tag{6.51}$$

Equation (6.51) corresponds to the zero shift locations for the case of blocked RPR system with blockage at the boundary (Eq. (5.62) This is because at Bragg resonance frequencies of maximum reflections, the blocked RPV system with interior blockage behaves as blocked RPR system with total length l_1+l_3 and having a blockage at the downstream boundary with length l_3 (see Eq. (6.37) and Eq. (5.58)).

Equation (6.45) could be written as follows

$$\eta_3+\frac{\eta_2}{2}=\frac{2\overline{m}-1}{2\left(2m-1\right)}+\frac{1-\frac{2}{\pi}\arccos\left[\left(-1\right)^{\overline{m}}\frac{1-\alpha}{1+\alpha}\cos\left(\left(2m-1\right)\frac{\pi}{2}\eta_2\right)\right]}{2\left(2m-1\right)} \tag{6.52}$$

The first term on the right hand side of Eq. (6.52) is the zero shift locations for the case of blockage with small radial protrusion (shallow blockage). The second term on the right hand side represents the deviation from the zero shift locations of shallow blockage case. The variation range of the deviation is

$$\left[\frac{-1}{2(2m-1)} \text{ to } \frac{1}{2(2m-1)}\right], \tag{6.53}$$

Notice that these deviations become very small at high modes. For example, at modes m=2 and m=3, the deviation range becomes

$$\left[\frac{-1}{6} \text{ to } \frac{1}{6}\right] \text{ and } \left[\frac{-1}{10} \text{ to } \frac{1}{10}\right], \tag{6.54}$$

respectively. Therefore Eq. (6.52) could be approximated by the equation of zero shift locations for shallow blockages (Eq. (6.48)) at relatively high modes.

6.5.4. Variation of the maximum shift locations and magnitudes

In both, interior blockage and blockage at the boundary cases, the maximum shift locations change as the radial protrusion of the blockage (α) varies (see Figure 6.2 and Figure 5.2). For the case of blockage at the boundary, the maximum shift locations can be determined from Eq. (5.57). To obtain the maximum shift locations for the case of interior blockage, the dispersion relation (Eq. (6.2)) is rewritten as follow

$$\begin{aligned}&\cos(k_m L)\\&+\frac{1-\alpha}{1+\alpha}\left[\cos\left(k_m L\left(1-(2\eta_3+\eta_2)-\eta_2\right)\right)-\cos\left(k_m L\left(1-(2\eta_3+\eta_2)+\eta_2\right)\right)\right]\\&-\left(\frac{1-\alpha}{1+\alpha}\right)^2\cos\left(k_m L(1-2\eta_2)\right)=0\end{aligned} \tag{6.55}$$

which gives

$$\cos\left(k_m L\right)+\frac{1-\alpha}{1+\alpha}\left\{\begin{array}{l}2\sin\left(k_m L\left(1-\left(2\eta_3+\eta_2\right)\right)\right)\sin\left(k_m L\eta_2\right)\\ -\dfrac{1-\alpha}{1+\alpha}\cos\left(k_m L\left(1-2\eta_2\right)\right)\end{array}\right\}=0 \qquad (6.56)$$

Note that the second term in Eq. (6.56) represents the effect of the blockage on the dispersion relation. In fact, for $\alpha=1$, this second term vanishes and Eq. (6.56) becomes identical to the dispersion relation of an intact RPV system (Eq. (2.54)). Therefore, the shift is maximum when the term inside the curly brackets is maximum. Denoting this term by

$$\Theta=2\sin\left(k_m L\left(1-\left(2\eta_3+\eta_2\right)\right)\right)\sin\left(k_m L\eta_2\right)-\frac{1-\alpha}{1+\alpha}\cos\left(k_m L\left(1-2\eta_2\right)\right) \qquad (6.57)$$

and equating its gradient to zero, give

$$\left\{\begin{array}{l}\dfrac{\partial\Theta}{\partial\left(k_m L\right)}=\left\{\begin{array}{l}2\left[\begin{array}{l}\left(1-\left(2\eta_3+\eta_2\right)\right)\cos\left(k_m^{\max}L\left(1-\left(2\eta_3+\eta_2\right)\right)\right)\sin\left(k_m^{\max}L\eta_2\right)\\ +\eta_2\sin\left(k_m^{\max}L\left(1-\left(2\eta_3+\eta_2\right)\right)\right)\cos\left(k_m^{\max}L\eta_2\right)\end{array}\right]\\ +\dfrac{1-\alpha}{1+\alpha}\left(1-2\eta_2\right)\sin\left(k_m^{\max}L\left(1-2\eta_2\right)\right)\end{array}\right\}=0\\ \text{and}\\ \dfrac{\partial\Theta}{\partial\left(2\eta_3+\eta_2\right)}=-2k_m^{\max}L\cos\left(k_m^{\max}L\left(1-\left(2\eta_3+\eta_2\right)\right)\right)\sin\left(k_m^{\max}L\eta_2\right)=0\end{array}\right. \qquad (6.58)$$

which yields

$$\left\{\begin{array}{l}2\left(-1\right)^{\overline{m}+1}\eta_2\cos\left(k_m^{\max}L\eta_2\right)+\dfrac{1-\alpha}{1+\alpha}\left(1-2\eta_2\right)\sin\left(k_m^{\max}L\left(1-2\eta_2\right)\right)=0\\ \text{and}\\ \cos\left(k_m^{\max}L\left(1-\left(2\eta_3+\eta_2\right)\right)\right)=0\ \Rightarrow\ k_m^{\max}L\left(1-\left(2\eta_3+\eta_2\right)\right)=\left(2\overline{m}-1\right)\dfrac{\pi}{2}\end{array}\right. \qquad (6.59)$$

Solving for the second equation in Eq. (6.59) gives the blockage locations at maximum eigenfrequencies as follows

$$\eta_3 + \frac{\eta_2}{2} = \frac{1}{2}\left[1 - \frac{2\left(m - \overline{m}\right) - 1}{w_m^{\max} / w_1^0}\right]; \text{ with } \begin{cases} \frac{\eta_2}{2} < \eta_3 + \frac{\eta_2}{2} < 1 - \frac{\eta_2}{2} \\ \overline{m} = 1, 2, 3... \end{cases} \quad (6.60)$$

By studying the sign of the Hessian matrix determinant, it can be shown that the distinction between maximum and minimum eigenfrequency magnitudes is governed by Eq. (6.25). To verify Eq. (6.60), considering the case of $\eta_2 = 0.15$ in Figure 6.2 where the maximum and minimum eigenfrequency magnitudes at mode $m = 3$ and $\alpha = 0.16$ are $w_3^{\max} / w_1^0 = 5.69$ and $w_3^{\min} / w_1^0 = 4$, respectively. Inserting the maximum eigenfrequency magnitude into Eq. (6.60) and taking into account Eq. (6.25), give

$$\eta_3 + \frac{\eta_2}{2} = 0.4121 \quad \text{or} \quad \eta_3 + \frac{\eta_2}{2} = 0.7636 \quad (6.61)$$

which agree with the maximum positive shift locations observed in Figure 6.2. Inserting the maximum eigenfrequency magnitude into Eq. (6.60) and taking into account Eq. (6.25), give

$$\eta_3 + \frac{\eta_2}{2} = 0.125 \quad \text{or} \quad \eta_3 + \frac{\eta_2}{2} = 0.625 \quad (6.62)$$

which also agree with the maximum negative shift locations observed in Figure 6.2.

For the cases of blockage with small radial protrusion, the positive and negative shift magnitudes are about the same at a given mode (see Figure 6.5 and Eq. (6.10)). However, Figures 6.10 and 6.12 and Figures 6.11 and 6.13 show that the magnitudes of the positive and negative maximum shifts oscillate as the mode number increases. For example Figure 6.12 shows that at the 2nd and 3rd modes, the magnitude of the positive maximum shift is lower than the negative maximum shift. However at the 4th mode, which is near the Bragg resonance condition of maximum reflection, both negative and positive maximum shift magnitudes are the same. But at the 5th and 6th modes, the magnitude of the positive maximum shift becomes larger than the negative shift. Overall, Figure 6.12 and 6.13 show that, between two modes where total transmission occur, the magnitude of the positive maximum shift is low at low modes and increases as the frequency increases, and conversely, the negative maximum shift is high at low modes and decreases as the frequency

increases. Both negative and positive shift magnitudes become the same at the Brag resonance frequency of maximum reflection.

Solution of the first equation in Eq. (6.59) gives the maximum eigenfrequency magnitudes at a given mode *m*. However, attempts to solve for the first equation in Eq. (6.59) and find a close form for the maximum eingenfrequency at a given mode *m* have failed. Fortunately, the features observed for the maximum shift variation could be explained qualitatively.

Equations (6.52) and (6.53) show that the variation range of zero shift location is

$$\eta_3 + \frac{\eta_2}{2} = \left[\frac{\bar{m} - 1}{(2m-1)} \quad \text{to} \quad \frac{\bar{m}}{(2m-1)} \right] \tag{6.63}$$

The boundaries in Eq. (6.63) are the locations of a positive and negative shift for shallow blockages. This implies that the zero shift locations could coincide with a maximum shift location preventing the maximum shift to occur. To further illustrate this effect, consider the case of a blockage with large radial protrusion such that $\alpha \approx 0$. In this case, the zero shift equation in Eq. (6.45) gives

$$\eta_3 + \frac{\eta_2}{2} = \frac{2\bar{m} - \frac{2}{\pi} \arccos\left[(-1)^{\bar{m}} \cos\left((2m-1)\frac{\pi}{2}\eta_2 \right) \right]}{2(2m-1)} \tag{6.64}$$

which leads to two cases depending on whether the zero shift location $\bar{m}$ is even or odd as follows

$$\begin{cases} \eta_3 + \frac{\eta_2}{2} = \frac{\bar{m} - 1}{(2m-1)} + \frac{\eta_2}{2} & \text{if } \bar{m} \text{ is odd} \\ \eta_3 + \frac{\eta_2}{2} = \frac{\bar{m}}{(2m-1)} - \frac{\eta_2}{2} & \text{if } \bar{m} \text{ is even} \end{cases} \tag{6.65}$$

In general and in simpler form, Eq. (6.65) becomes

$$\eta_3 + \frac{\eta_2}{2} = \frac{2\bar{m}}{(2m-1)} \pm \frac{\eta_2}{2} \tag{6.66}$$

This shows that the zero shift location for severe blockages could approach the maximum shift at even locations for certain modes. Knowing that the maximum shift sign at even locations changes at different modes, therefore the zero shift locations approach positive maximum shift locations at certain modes, and approch the negative maximum shift locations at other modes. For example, Figures 6.10 and 6.12 show that for the case of η_2 = 0.15, the 2nd maximum shift (as $\eta_3+\eta_2/2$ increases) is positive at modes m = 2 and m = 3. Figures 6.10 and 6.12 show that at those modes, the zero shift locations are close to the maximum positive shift location, and therefore, the magnitude of the positive shift is reduced.

Moreover, for very short blockages, Eq. (6.65) shows that two consecutive zero shifts take almost the same location at low modes. Since a shift occurs between two zero shift locations, this would prevent the shift at even locations to take place. For example, the case of η_2 = 0.027 in Figures 6.11 and 6.13 shows that, at low modes such as m = 2, almost only negative shifts occur and that the zero shift locations coincides at almost $\eta_3+\eta_2/2$ = 2/3.

Equation (6.66) approaches the zero shift locations for small radial protrusion when

$$\begin{aligned} &\eta_3+\frac{\eta_2}{2}=\frac{2m''}{(2m-1)}\pm\frac{\eta_2}{2}\approx\frac{2m'-1}{2(2m-1)} \\ &\Rightarrow \mp\eta_2\approx\frac{2(2m''-m')+1}{(2m-1)} \end{aligned} \qquad (6.67)$$

which is the condition for Bragg resonance frequency of maximum reflections (see Eq. (6.17) and Eq. (4.11)). This is as shown above in Eq. (6.48), and as expected from Figures 6.14, 6.15 and 6.16. On the other hand, Eq. (6.66) approaches the odd maximum shift locations when

$$\begin{aligned} &\eta_3+\frac{\eta_2}{2}=\frac{2\overline{m}}{(2m-1)}\pm\frac{\eta_2}{2}\approx\frac{2\overline{m}'-1}{(2m-1)} \\ &\Rightarrow \mp\eta_2\approx\frac{2(2\overline{m}-2\overline{m}'+1)}{(2m-1)} \end{aligned} \qquad (6.68)$$

which is the condition for Bragg resonance frequency of total transmission (see Eq. (6.13) and Eq. (4.11)). In addition, Eqs. (6.25) and (6.26) show that the maximum negative shifts occur at odd locations for modes below the first Bragg resonance frequency of total transmission. This is why Figures 6.12 and 6.13 show that as the mode number approaches the Bragg resonance frequency of total transmission, the magnitude of negative shifts decreases, and the zero shift locations move towards the negative shift locations. Notice that once the mode number exceeds the Bragg resonance frequency of total transmission, the zero shift locations switch from being close to the negative shift locations to being near the positive shift locations. This is because, from Eqs. (6.25) and (6.26), the positive shift switches from being at even locations to odd locations when the mode number crosses a Bragg resonance frequency of total transmission.

6.5.5. Low frequency approximation

For severe blockage case, Figure 6.10 shows that the lowest mode takes mostly negative shift. In this case, if the first eigenfrequency is assumed very small ($w_1/w_1^0 << 1$), then a first order Taylor expansion could be applied on sine and cosine functions in the dispersion relation (Eq. (6.1)) which gives

$$\begin{aligned} &\alpha - (k_1 L)^2 \eta_2 \eta_3 - \alpha^2 (k_1 L)^2 \eta_1 \eta_2 - \alpha (k_1 L)^2 \eta_1 \eta_3 \approx 0 \\ &\Rightarrow \frac{w_1}{w_1^0} \approx \frac{2}{\pi} \sqrt{\frac{\alpha}{\alpha^2 \eta_1 \eta_2 + \alpha \eta_1 \eta_3 + \eta_2 \eta_3}} \end{aligned} \qquad (6.69)$$

Taking into account that $\alpha << 1$, Eq. (6.69) becomes

$$\frac{w_1}{w_1^0} \approx \frac{2}{\pi} \sqrt{\frac{\alpha}{\eta_2 \eta_3}} \qquad (6.70)$$

To understand the physical meaning of the natural frequency in Eq. (6.70), consider the RPV blocked system in Figure 6.18 and assuming that the pipe with length l_2, representing the blockage, has very small area ($\alpha = A_2/A << 1$) such that the pipe with length l_1 becomes as part of the reservoir with respect to pipe 2. At very low frequency, the system composed

of pipe 2 and pipe 3 behaves as a Helmholtz resonator ([120]) where pipe 2 is equivalent to an acoustic mass (most of the energy is in pipe 2 is kinetic energy) and pipe 3 is equivalent to an acoustic compliance (most of the energy in pipe 3 is potential energy). Applying the one dimensional momentum equation (Eq. (2.41)) in pipe 2 and assuming ideal flow, give

$$\frac{dV_2}{dt} = -\frac{1}{\rho}\frac{\partial P}{\partial x} \Rightarrow \frac{dV_2}{dt} \approx -\frac{1}{\rho}\frac{P_c}{l_2} \tag{6.71}$$

where V_2 is the velocity in pipe 2; P is the pressure; P_c is a characteristic pressure difference and ρ is the density. Applying the continuity equation (Eq. (2.41)) in pipe 3 gives

$$\frac{dP_c}{dt} = -\rho a^2 \frac{\partial V_3}{\partial x} \Rightarrow \frac{dP_c}{dt} \approx -\rho a^2 \frac{dV_3}{l_3} \tag{6.72}$$

where V_3 is the velocity in pipe 3 and l_3 is the length of pipe 3. Using the continuity of flow at the junction between pipe 2 and pipe 3, yields

$$\frac{dP_c}{dt} \approx -\rho a^2 \alpha \frac{dV_2}{l_3} \Rightarrow \frac{d^2P_c}{dt^2} \approx -\rho a^2 \frac{\alpha}{l_3}\frac{dV_2}{dt} \tag{6.73}$$

Inserting Eq. (6.71) into Eq. (6.73), gives

$$\frac{d^2P_c}{dt^2} - \frac{a^2}{L^2}\frac{\alpha}{\eta_3\eta_2}P_c = 0 \tag{6.74}$$

which is the ordinary differential equation of a Helmholtz resonator system ([120]) with natural frequency

$$w_H = \frac{a}{L}\sqrt{\frac{\alpha}{\eta_3\eta_2}} \Rightarrow \frac{w_H}{w_1^0} = \frac{2}{\pi}\sqrt{\frac{\alpha}{\eta_3\eta_2}} \tag{6.75}$$

This is identical to Eq. (6.70). Notice that for short blockage case (see Figure 6.11), the shift is almost always nearly zero at the lowest mode (m = 1). Therefore, a significant shift of the lowest eigenfrequency is a good indication of severe blockage case where Eq. (6.70) could become an accurate approximation.

Figure 6.18 Severely blocked RPV system.

6.6. Symmetric pipe system with interior blockage

The above discussions and findings could be similarly applied for the case of symmetric pipe system such as reservoir-pipe-reservoir (RPR) system (see Figure 6.19a) or valve-pipe-valve (VPV) system (see Figure 6.19b). This section gives briefly the main eigenfrequency shift features for the case of symmetric pipe systems with interior blockage at the boundary.

Figure 6.19 Symmetric pipe systems with interior blockage.

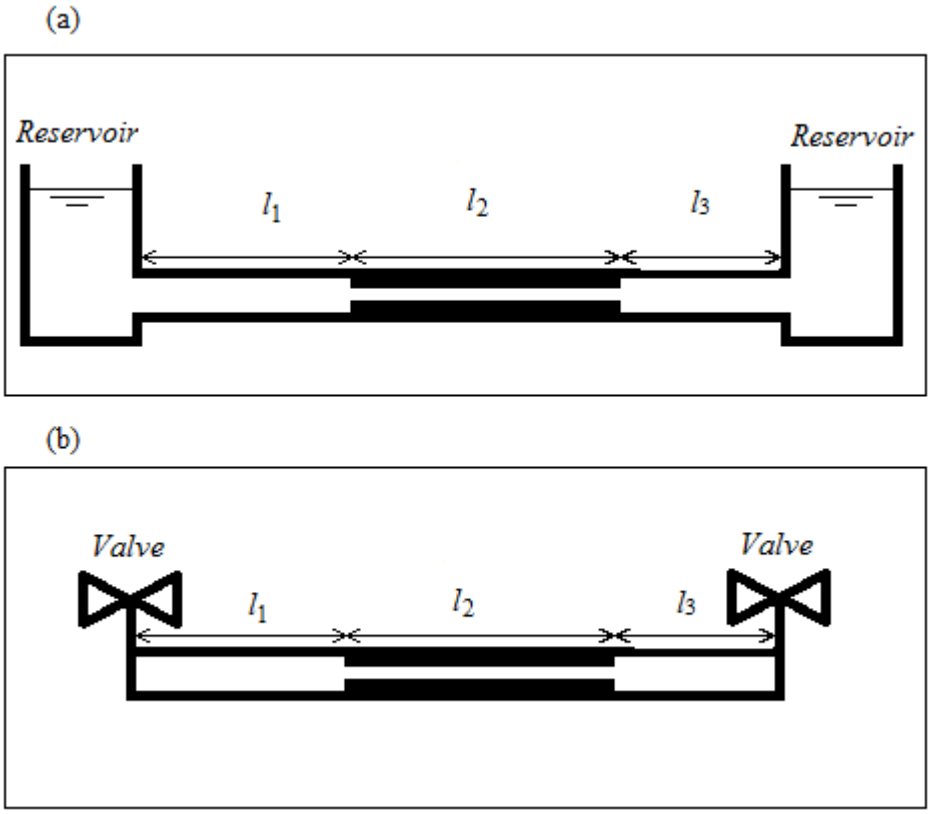

(a) Left **RPR system**

(b) Right **VPV system**

Applying Eq. (5.1) to the blocked RPR and VPV systems in Figure 5.12 gives respectively:

RPR:

$$\begin{aligned}&\alpha^2 \sin(k_m l_1)\sin(k_m l_2)\sin(k_m l_3)\\ &-\alpha\cos(k_m l_1)\cos(k_m l_2)\sin(k_m l_3)\\ &-\alpha\sin(k_m l_1)\cos(k_m l_2)\cos(k_m l_3)\\ &-\cos(k_m l_1)\sin(k_m l_2)\cos(k_m l_3)=0\end{aligned} \qquad (6.76)$$

and

VPV:
$$\begin{aligned}&\sin\left(k_m l_1\right)\sin\left(k_m l_2\right)\sin\left(k_m l_3\right)\\&-\alpha\cos\left(k_m l_1\right)\cos\left(k_m l_2\right)\sin\left(k_m l_3\right)\\&-\alpha\sin\left(k_m l_1\right)\cos\left(k_m l_2\right)\cos\left(k_m l_3\right)\\&-\alpha^2\cos\left(k_m l_1\right)\sin\left(k_m l_2\right)\cos\left(k_m l_3\right)=0\end{aligned} \tag{6.77}$$

Using trigonometric manipulations for Eqs. (6.76) and (6.77) give

RPR:
$$\begin{aligned}&\sin\left(k_m L\right)\\&-\frac{\left(1-\alpha\right)}{\left(1+\alpha\right)}\sin\left(k_m\left(l_1-l_2-l_3\right)\right)\\&+\frac{\left(1-\alpha\right)}{\left(1+\alpha\right)}\sin\left(k_m\left(l_1+l_2-l_3\right)\right)\\&-\frac{\left(1-\alpha\right)^2}{\left(1+\alpha\right)^2}\sin\left(k_m\left(l_1-l_2+l_3\right)\right)=0\end{aligned} \tag{6.78}$$

and

VPV:
$$\begin{aligned}&\sin\left(k_m L\right)\\&+\frac{\left(1-\alpha\right)}{\left(1+\alpha\right)}\sin\left(k_m\left(l_1-l_2-l_3\right)\right)\\&-\frac{\left(1-\alpha\right)}{\left(1+\alpha\right)}\sin\left(k_m\left(l_1+l_2-l_3\right)\right)\\&-\frac{\left(1-\alpha\right)^2}{\left(1+\alpha\right)^2}\sin\left(k_m\left(l_1-l_2+l_3\right)\right)=0\end{aligned}\quad, \tag{6.79}$$

respectively. Note that the second to fourth terms in Eq. (6.78) and Eq. (6.79) represents the effect of the blockage. In fact, for $\alpha=1$, those terms vanish and Eq. (6.78) and Eq. (6.79) become identical to the dispersion relation of an intact symmetric pipe system.

Figures 6.20 and 6.21 give the dimensionless eigenfrequency variation with $\eta_3+\eta_2/2$ when $\eta_2=0.15$ for the case of RPR and VPV systems, respectively. As seen for the case of RPV system, the eigenfrequency shift takes positive, negative and zero shift depending on the blockage location. Again, the zero and maximum shift locations change with α.

Figure 6.20 Dimensionless eigenfrequency variation with $\eta_3+\eta_2/2$ for the case of RPR system with interior blockage ($\eta_2=0.15$)

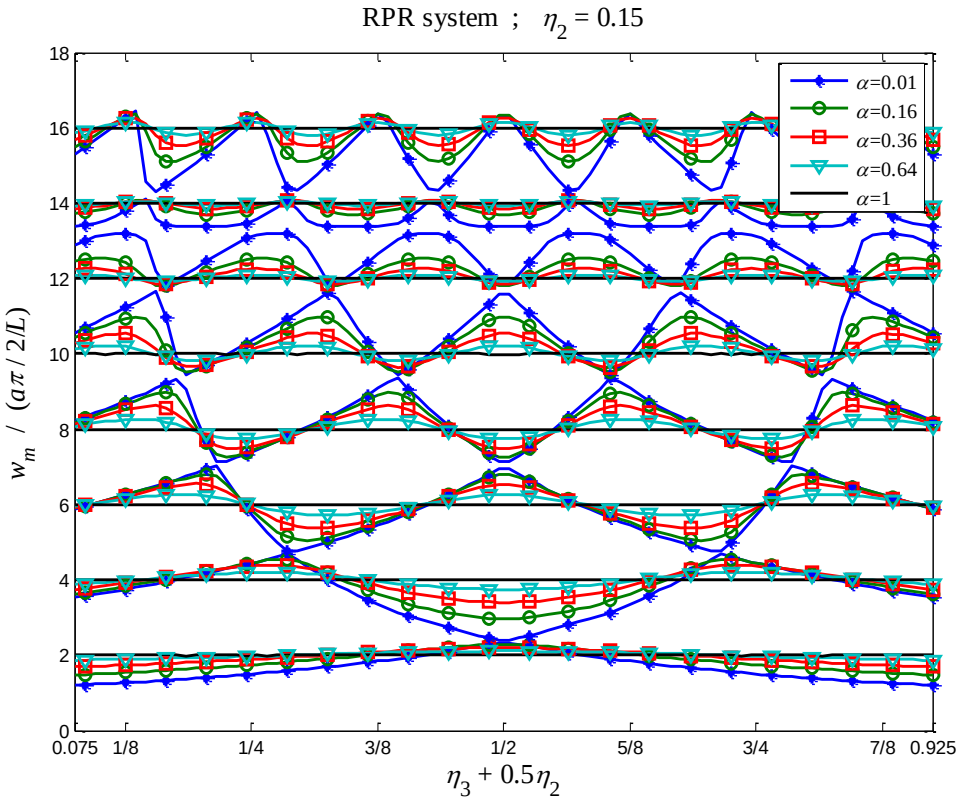

Figure 6.21 Dimensionless eigenfrequency variation with $\eta_3+\eta_2/2$ for the case of VPV system with interior blockage ($\eta_2=0.15$)

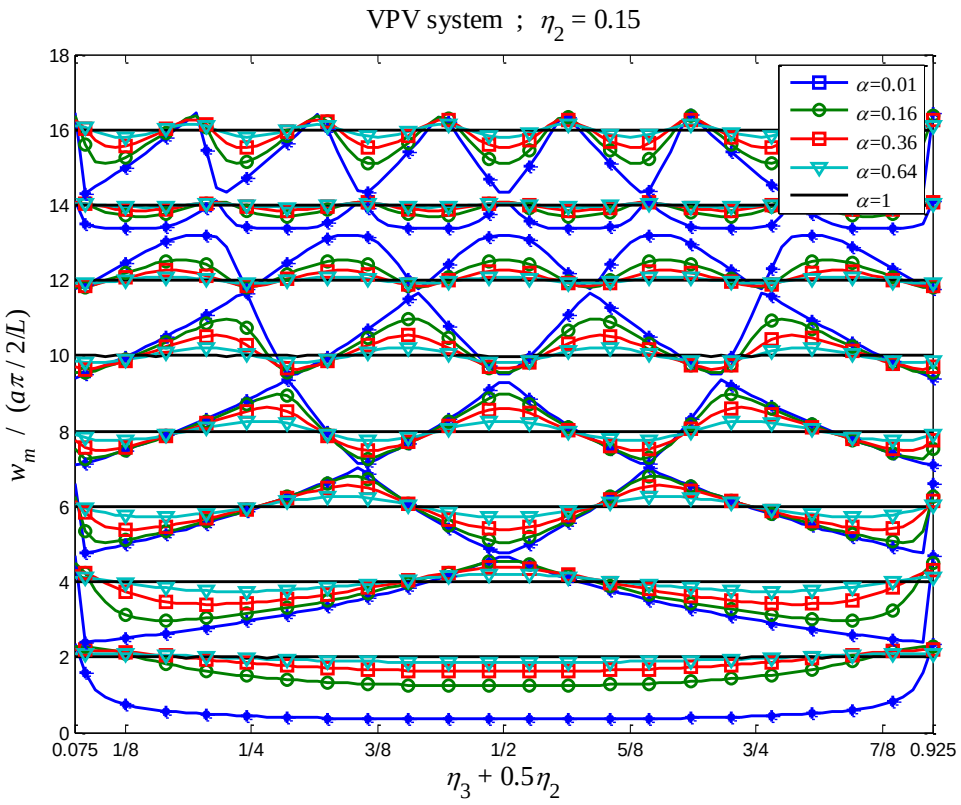

6.6.1. Blockage with small radial protrusion

For the case of blockage with small radial protrusion, the shift equation Equation (5.41) gives the eigenfrequency equations for RPR and VPV systems respectively as follows

RPR:
$$\Rightarrow \frac{\overline{\Delta w_m}}{w_1^0} = -\frac{(1-\alpha)}{\pi}\left[\sin\left(2m\pi\left(\eta_3+\eta_2\right)\right)-\sin\left(2m\pi\eta_3\right)\right]$$
$$= -\frac{2(1-\alpha)}{\pi}\sin\left(2m\frac{\pi}{2}\eta_2\right)\cos\left(2m\pi\left(\eta_3+\frac{\eta_2}{2}\right)\right) \qquad (6.80)$$

and

VPV:

$$\begin{aligned}\Rightarrow \frac{\overline{\Delta w_m}}{w_1^0} &= \frac{(1-\alpha)}{\pi}\left[\sin\left(2m\pi\left(\eta_3+\eta_2\right)\right)-\sin\left(2m\pi\eta_3\right)\right] \\ &= \frac{2(1-\alpha)}{\pi}\sin\left(2m\frac{\pi}{2}\eta_2\right)\cos\left(2m\pi\left(\eta_3+\frac{\eta_2}{2}\right)\right)\end{aligned} \tag{6.81}$$

where the following pressure head and flow harmonic of intact RPR and VPV systems are used

$$\text{RPR}: \begin{cases} h_m\left(x,k_m^0\right) = 2iC\sin\left(k_m^0 x\right) = h_m^{\text{amp}}\sin\left(k_m^0 x\right) \\ q_m\left(x,k_m^0\right) = -2C\frac{g}{a}A_0\cos\left(k_m^0 x\right) = q_m^{\text{amp}}\cos\left(k_m^0 x\right) \end{cases}$$

$$\Rightarrow \begin{cases} \frac{h_m^0}{h_m^{\text{amp}}} = \sin\left(k_m^0 x\right) \\ \frac{\overline{q_m^0}}{\overline{q_m^{\text{amp}}}} = \cos\left(k_m^0 x\right) \end{cases} \tag{6.82}$$

and

$$\text{VPV}: \begin{cases} h_m\left(x,k_m^0\right) = 2C\sin\left(k_m^0 x\right) = -ih_m^{\text{amp}}\sin\left(k_m^0 x\right) \\ q_m\left(x,k_m^0\right) = -2iC\frac{g}{a}A_0\cos\left(k_m^0 x\right) = iq_m^{\text{amp}}\cos\left(k_m^0 x\right) \end{cases}$$

$$\Rightarrow \begin{cases} \frac{h_m^0}{h_m^{\text{amp}}} = -i\sin\left(k_m^0 x\right) \\ \frac{\overline{q_m^0}}{\overline{q_m^{\text{amp}}}} = -i\cos\left(k_m^0 x\right) \end{cases} \tag{6.83}$$

The zero shift locations for both RPR and VPV systems having an interior blockage with small radial protrusion are given by

$$\begin{cases} \eta_2 = \frac{\overline{m}-1}{m} \;\Leftrightarrow\; \frac{w_m^0}{w_{\overline{m}}^T\left(l_2\right)} = 1 \;\Leftrightarrow\; l_2 = \frac{\left(\overline{m}-1\right)}{2}\left[\frac{4L}{2m}\right] \\ \text{or} \\ \eta_3 + \frac{\eta_2}{2} = \frac{2\overline{m}-1}{4m} \Rightarrow \frac{h_m^0}{h_m^{amp}} = \pm\frac{q_m^0}{q_m^{amp}} \end{cases} \tag{6.84}$$

The first equation in Eq. (6.84) corresponds to the case where the frequency is equal to the Bragg resonance frequency of total transmission (Eq. (4.11)). The second equation in Eq. (6.84) corresponds to the case where the blockage mid-length is located at a position of equal pressure head and flow magnitudes.

Taking similar steps to obtain the maximum shift locations for RPV system, the maximum shift for both RPR and VPV systems occur when

$$\begin{cases} \eta_2 = \dfrac{2\overline{m}-1}{2m} \;\Leftrightarrow\; \dfrac{w_m^0}{w_{\overline{m}}^R(l_2)} = 1 \;\Leftrightarrow\; l_2 = \dfrac{\left(2\overline{m}-1\right)}{4}\left[\dfrac{4L}{2m}\right] \\ \text{and} \\ \eta_3 + \dfrac{\eta_2}{2} = \dfrac{\overline{m}'}{2m} \;\Rightarrow\; \dfrac{h_m^0}{h_m^{amp}} = 0 \;\text{ or }\; \dfrac{q_m^0}{q_m^{amp}} = 0 \end{cases} \tag{6.85}$$

The first equation in Eq. (6.85) corresponds to the case where the frequency is equal to the Bragg resonance frequency of maximum reflection (Eq. (4.10)). The second equation in Eq. (6.85) corresponds to the case where the blockage mid-length is located at a position of zero pressure head (pressure node) and or zero flow (stagnation point).

at a given maximum shift location, the blocked RPR and VPV systems have opposite shift sign which is given by

$$\text{sgn}\left[\frac{\partial^2\left(\overline{\Delta w_m}/\left(a\pi/2L\right)\right)}{\partial\left(\eta_3+\eta_2/2\right)^2}\right] = (-1)^{n_T+\overline{m}+n_{sys}} \begin{cases} \text{if } > 0 \;\Rightarrow\; \text{max shift is negative} \\ \text{if } < 0 \;\Rightarrow\; \text{max shift is positive} \end{cases} \tag{6.86}$$

where "sgn" is the sign function; $n_{sys} = 1$ for RPR system and $n_{sys} = 0$ for VPV system; and n_T is an integer that gives the number of modes region between two consecutive Bragg resonance frequencies of total transmission defined as

$$n_T = \text{Floor}\left(m\eta_2\right) + 1 \tag{6.87}$$

6.6.2. Blockage with severe and moderate radial protrusion

For a severe blockage such as α tends to 0, Eqs. (6.76) and (6.79) reduce respectively to

RPR: $$\cos\left(k_m^s l_1\right)\sin\left(k_m^s l_2\right)\cos\left(k_m^s l_3\right)=0 \qquad (6.88)$$

and

VPV: $$\sin\left(k_m^s l_1\right)\sin\left(k_m^s l_2\right)\sin\left(k_m^s l_3\right)=0 \qquad (6.89)$$

The solution to Eqs. (6.88) and (6.89) gives the asymptotic solutions for RPR and VPV systems. Eq. (6.88) shows that the RPR system with severe interior blockage is equivalent to three uncoupled intact subsystems: RPV subsystem with length l_1, and RPR subsystem with length l_2 and RPV subsystem with length l_3. On the other hand, Eq. (6.89) shows that the VPV system with severe interior blockage is also equivalent to three uncoupled intact subsystems: VPV subsystem with length l_1, RPR subsystem with length l_2 and VPV subsystem with length l_3.

The eigenfrequency variation for RPR and VPV systems along with the asymptotic solutions are given in Figures 6.22 and 6.23 when $\eta_2 = 0.15$. Similarly to the RPV case, Figures 6.22 and 6.23 show that the eigenfrequencies approach the asymptotic solution (*i.e.* the decoupling effect increases) at modes with frequencies close to the Bragg resonance frequency of maximum reflection; and become far away from the asymptotic solutions (*i.e.* the decoupling effect decreases) at modes with frequencies close to the Bragg resonance frequency of total transmission.

Inserting the Bragg resonance frequency of total transmission (Eq. (4.11)) into Eqs. (6.76) and (6.77) give $\sin\left(w_m^T L/a\right)=0$ which is the dispersion relation for intact symmetric pipe system with length L.

Similarly, inserting the Bragg resonance frequency of maximum reflection (Eq. (4.10)) into Eqs. (6.76) and (6.77) give

RPR: $$\cos\left(kl_1\right)\cos\left(kl_3\right)-\alpha^2\sin\left(kl_1\right)\sin\left(kl_3\right)=0 \qquad (6.90)$$

and

VPV: $$\cos\left(kl_1\right)\cos\left(kl_3\right)-\frac{1}{\alpha^2}\sin\left(kl_1\right)\sin\left(kl_3\right)=0 \qquad (6.91)$$

Equations (6.90) and (6.91) shows that, at modes with frequencies close to the w_m^R (Eq. (4.10)), the RPR system becomes equivalent to a blocked RPV system with total length l_1+l_3 and having a blockage at the *downstream* boundary with area ratio α^2; and the VPV system becomes equivalent to a blocked RPV system with total length l_1+l_3 and having a blockage at the *upstream* boundary with area ratio α^2.

Similarl to the case of RPV system, the zero and maximum shift locations for the cases of RPR and VPV systems could be obtained which are given by

$$\eta_3+\frac{\eta_2}{2}=\frac{2\bar{m}-\frac{2}{\pi}\arccos\left[\left(-1\right)^{\bar{m}+n_{sys}}\frac{\left(1-\alpha\right)}{\left(1+\alpha\right)}\cos\left(m\pi\eta_2\right)\right]}{4m} \qquad (6.92)$$

and

$$\eta_3+\frac{\eta_2}{2}=\frac{1}{2}-\frac{\bar{m}}{\frac{w_m}{w_1^0/2}}, \qquad (6.93)$$

respectively.

Figure 6.22 Dimensionless eigenfrequency variation along with the asymptotic solutions for RPR system ($\eta_2 = 0.15$).

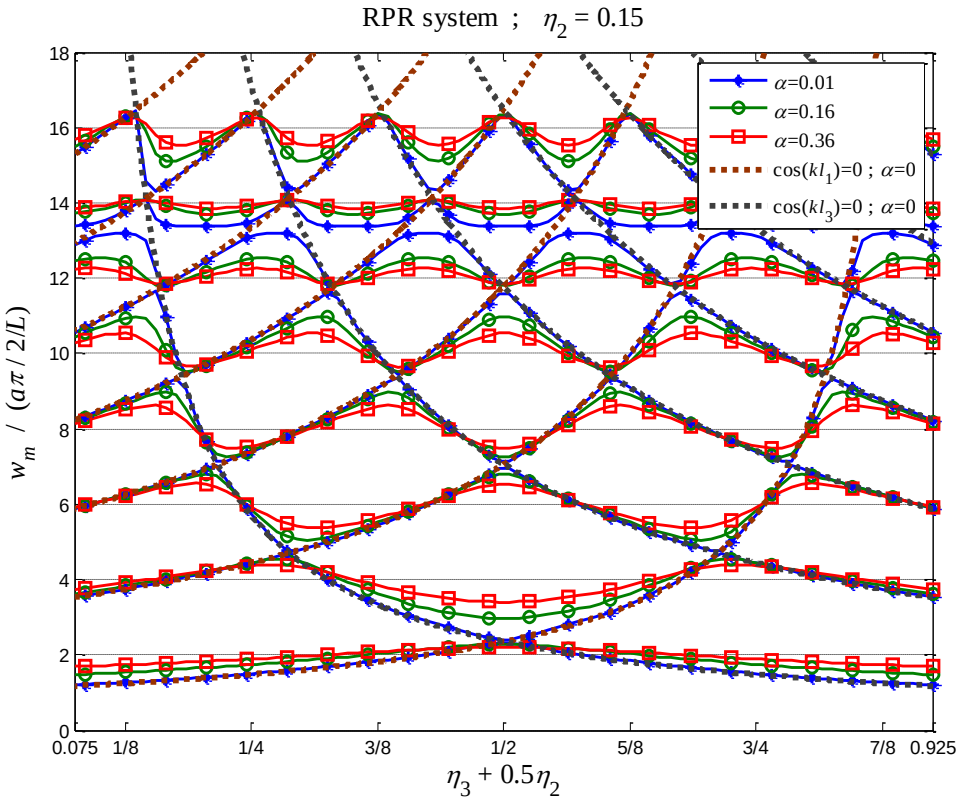

Figure 6.23 Dimensionless eigenfrequency variation along with the asymptotic solutions for VPV system ($\eta_2 = 0.15$).

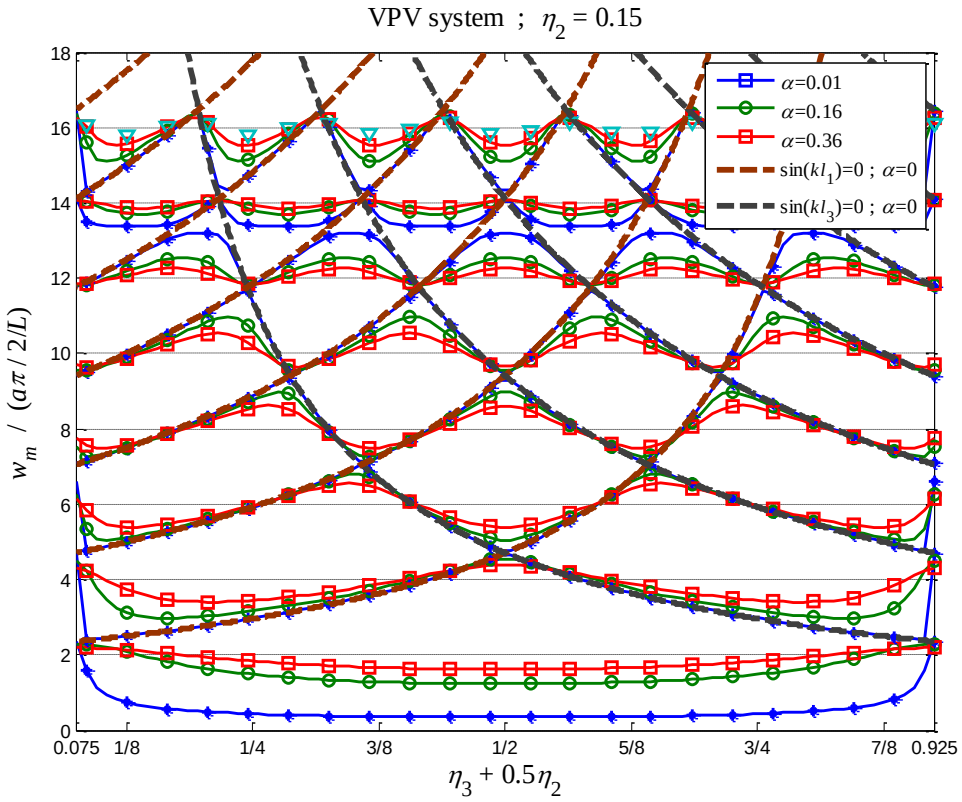

6.7. Application of Bragg resonance and eigenfrequency shift information for TBDDM

6.7.1. Implication to TBDDM

In practice, most transient wave generators transmit narrow frequency bandwidth (FBW). If the FBW is close to w_m^T, then the blockage signature on the transient wave will be negligible (see Figure 4.7) and therefore the blockage will be undetectable. On the other hand, if the FBW is close to w_m^R, the blockage interacts with the wave and its signature becomes clear. In this regards, the injected FBW should be varied for two main advantages. First is to avoid

hidden blockage signature if the FBW is close to a Bragg resonance frequency of total transmission ($w_{\overline{m}}^{T}$). The second advantage is that the sweeping of the injected FBW helps detecting the Bragg resonance frequency. The knowledge of these frequencies gives information about the blockage characteristics. For example, if $w_{\overline{m}}^{R}$ or $w_{\overline{m}}^{T}$ is determined, the blockage length could be obtained from Eq. (4.10) or Eq. (4.11). With the knowledge of the shift sign mechanism, the search domain of the blockage location could be narrowed.

Such FBW sweeping technique was used in Duan, et al. ([36]) to obtain the highest reflection coefficient that leads to accurate detectability of the blockage. In their experiment, Duan, et al. ([36]) found that when the length of the blockage is equal to odd integer multiples of a quarter of the wavelength, the power reflection ratio becomes maximum. This is precisely the condition of Bragg resonance frequency of maximum reflection (Eq. (4.10)).

6.7.2. Experimental investigation

Experimental tests are conducted in order (i) to validate the effect of Bragg resonance in bounded pipe system, and the different features discussed about the eigenfrequency shift mechanism in previous sections; and (ii) to illustrate the potential of using the eigenfrequency shift and Bragg resonance information for blockage detection in bounded pipe system.

6.7.2.1. <u>Description of the experimental setup</u>

The experimental investigation is conducted at the Water Engineering Laboratory located at the University of Perugia-Italy in collaboration with Prof. Bruno Brunone and Prof. Silvia Meniconi. The experimental setup consists of a reservoir-pipe-valve system which contains a single blockage as shown in Figure 6.1. The blockage is modelled as a pipe with length l_2 and a diameter $D_2 < D_0$ where D_0 is the diameter of the intact pipe. The pipe material is high-density polyethylene (HDPE) (viscoelastic pipe) ([86]) and the blockage has the same material as the pipe (i.e., HDPE).. Two tests, each with different blockage length, are conducted. The characteristics of the experimental tests are given in Table 6.1.

Due to the limited space in the laboratory, it was not possible to use a long straight pipe, and therefore a coiled pipe setup was used. A schematic description of the intact pipe system setup (without blockage) used for experimental tests is shown in Figure 6.24, and part of the real pipe setup is given in Figure 6.25.

The flow in the pipe is initially stagnant and pressurized at $P_0 \approx 1 \pm 0.1$ bar. The transient is generated using a portable pressure wave maker (PPWM) (see Figures 6.24, 6.25 and 6.26) which is a small-sized pressurized tank that has a higher pressure ($P_w \approx 4.3 \pm 0.1$ bar) than the initial pressure in the pipe system ($P_0 \approx 1 \pm 0.1$ bar). The PPWM is connected to an initially closed downstream electro-valve that has a diameter $D_v = 1/4$ inch ($= 6.35\ 10^{-3}$ m). The opening and closing of the electro-valve is controlled to generate the desired waveform. In these experimental tests, a square pulse is used as wave from which is created by a rapid opening and closing of the valve. The duration of the pulse is $t_p \approx 50ms$ and the wave form produced is shown in Figure 6.27.

The pressure is measured at three different locations (see points T1, T2 and T3 in Figure 6.24). The distance from the electro-valve to the measurement location T1 is 0.98 m. The measurement location T2 is at 1.26m from the downsteam junction of the blockage location, and the measurement location T3 is at 2.06m to the upstream junction of the blockage. The pressure signal is acquired by piezoresistive transducers with a frequency acquisition of 1,024 Hz.

The blockage (or smaller diameter pipe) is located between the locations T1 and T3. The pressure signals are analysed in the frequency domain after being processed using the Fast Fourier Transform implemented in Matlab 2013a.

The method of characteristic (MOC) is used to simulate the experimental tests. For the numerical simulation, the pressure signal in Figure 6.27 is injected at the downstream valve location.

Notice that Figures 6.12 and 6.14 correspond to the case in test 1 (see Table 6.1), and Figures 6.13, 6.15 and 6.16 correspond to the case in test 2 (Table 6.1). These Figures will be used for later discussion (Sections 6.7.2.2.2 and 6.7.2.2.3).

Table 6.1. Characteristics of the experimental tests

Parameters	Test 1	Test 2
l_1 (m)	52.86	52.86
l_2 (m)	24	3.6
l_3 (m)	76.75	76.75
L (m)	153.61	133.21
$\eta_2 = l_2 / L$	≈ 0.156	≈ 0.027
D_1 (m)	0.0933	0.0933
D_2 (m)	0.0383	0.0383
D_3 (m)	0.0933	0.0933
$\alpha = A_2 / A_1$	0.168	0.168
Pipe thikness (m)	0.0167	0.0167
Wave speed (a) (m/s)	$\approx 355 \pm 15$	$\approx 355 \pm 15$
Pipe material	HDPE	HDPE

Figure 6.24 Schematic description of the intact pipe system setup used for the experimental tests

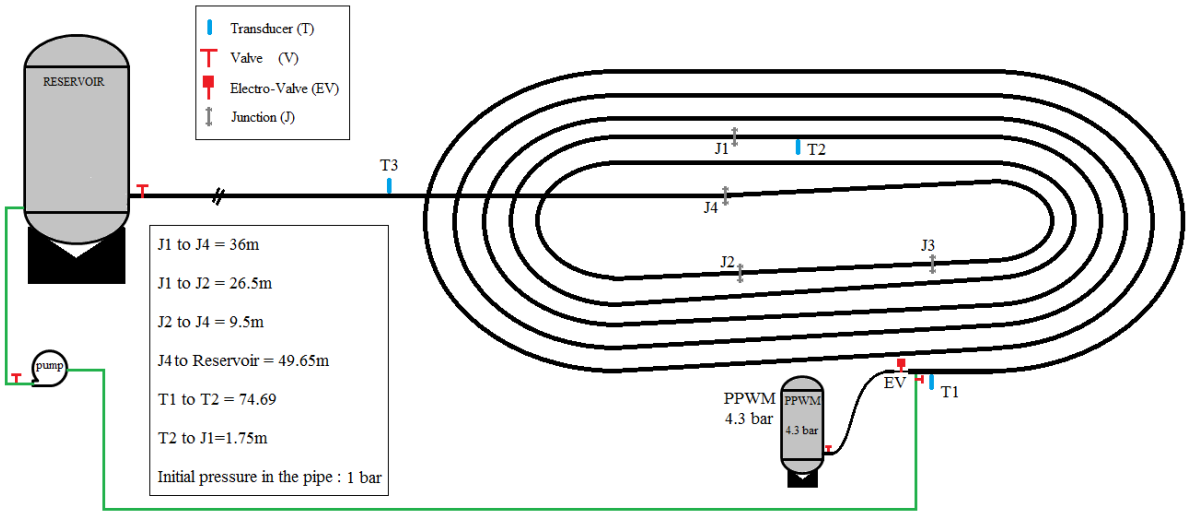

Figure 6.25 Part of the real pipe setup

Figure 6.26 PPWM and its connection to the pipe

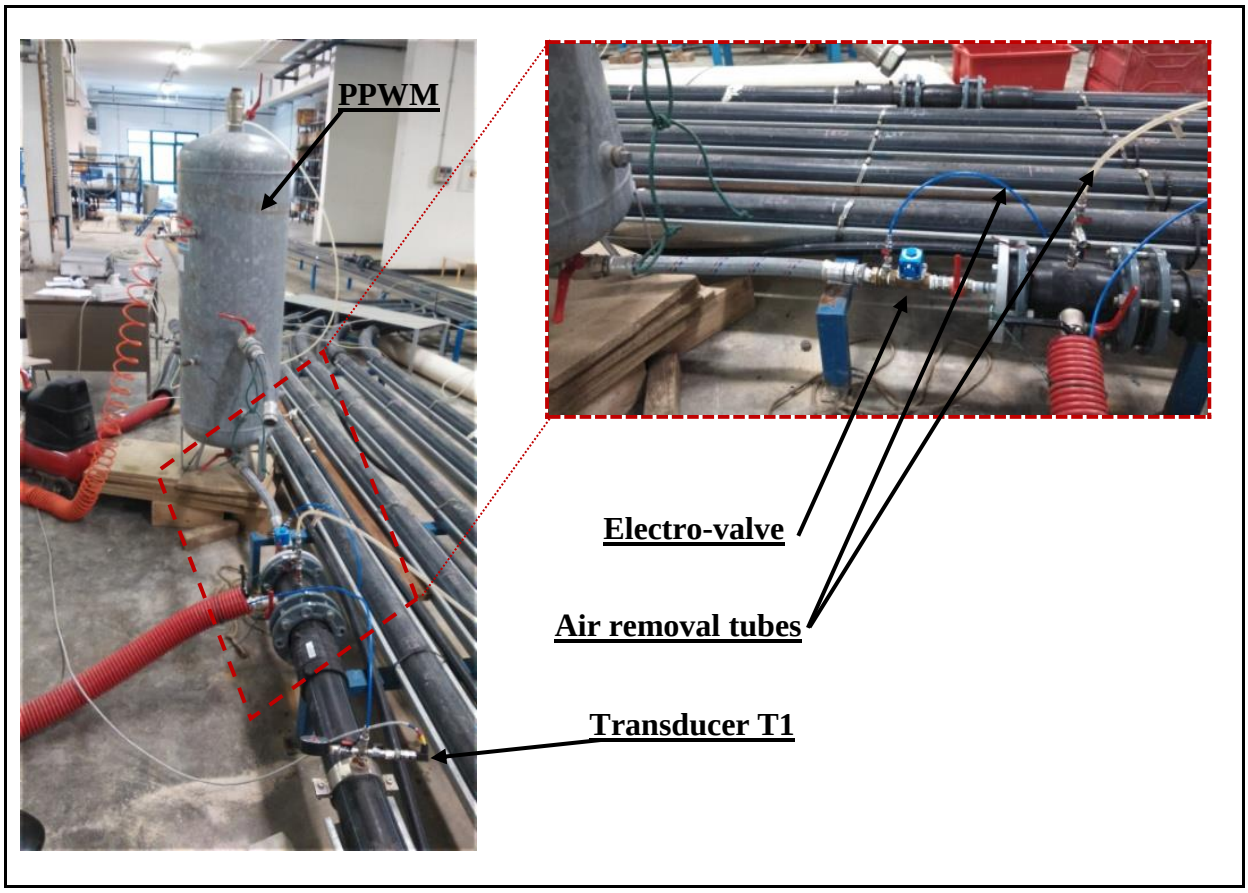

Figure 6.27 Pressure signal in the time domain at T1 and T2 transducers (Test 1).

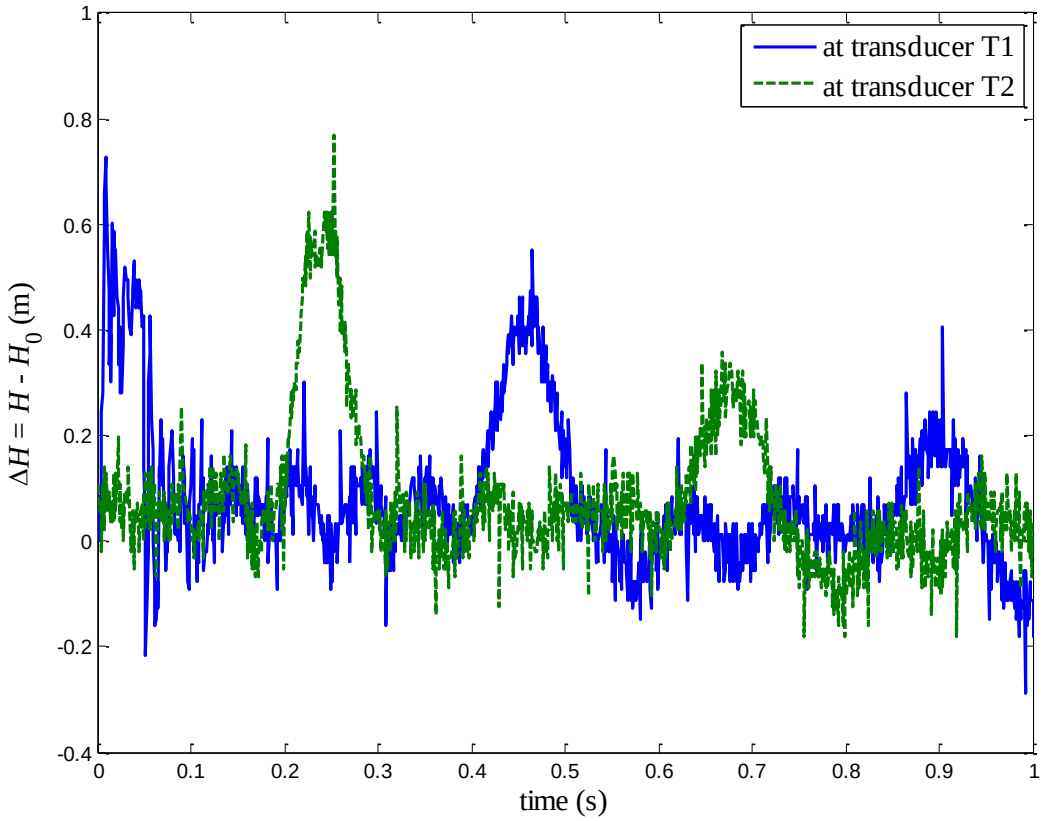

6.7.2.2. Experimental results and discussion

6.7.2.2.1. Discussion on experimental errors

In Figure 6.28, the frequency response function (FRF) of the pressure signal for the test case 1 with blockage length $\eta_2 \approx 0.156$ (see test 1 in Table 6.1) measured at location T1 (downstream boundary) is compared with the numerical test which consider ideal straight pipe. The frequency axis in Figure 6.28 is dimensionlized by the first eigenfrequency for intact RPV system ($w_1^0 = \pi a/2/L$). Figure 6.28 shows that the first seven eigenfrequencies obtained from the measured signal match those from the numerical signal. The mean error between them with respect to w_1^0 is about 5% for the first 5 modes and about 20% for the 6th

and 7th modes. Eigenfrequencies at higher modes (>7) are not reliable because of the noise/errors and the limitation of the frequency bandwidth. The possible sources of errors are the bends effect, anchorage effect and/or measurement errors and noise.

The mean distance between two successive bends is about 10 m. Therefore the effect of the bends may become very apparent at frequencies close to (a/4/10) / $w_1^0 \approx 15$ which may affect eigenfrequency at mode six or higher.

The anchorage effect is most likely to be small because the transient pressure head injected is very small (less than 1m (see Figure 6.27)), and therefore the pipe displacement is very small too.

The most probable source of error affecting the experimental result is the measurement error especially for determining the wave speed. For example, it is found that an error of 4% in wave speed produces an error in the eigenfrequency that increases almost linearly from 4% at the 1st mode to 63% at the 7th mode; whereas an error of 1% in wave speed produces an error in the eigenfrequency that increases almost linearly from 0.9% at the 1st mode to 14% at the 7th mode. The mean wave speed in Table 6.1 (355m/s) is based on the average of 16 repeated experiments; and the error in wave speed in Table 6.1 (15m/s) is based on the standard deviation.

Figure 6.28 Frequency response function (FRF) of the pressure signal measured at T1 for the test case with blockage length $\eta_2 \approx 0.156$ (test 1 in Table 6.1 with *a* = 355 m/s): Comparison between experimental and numerical results.

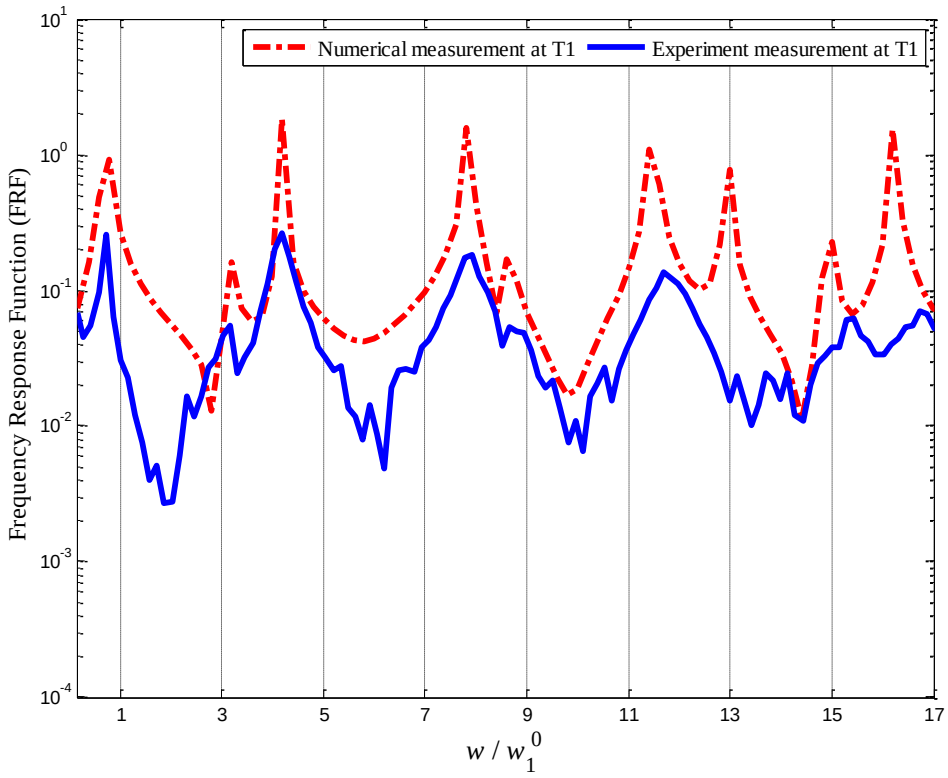

6.7.2.2.2. Test 1: extended blockage

Figure 6.29 gives the frequency FRF of the pressure signal for the case of blockage length $\eta_2 \approx 0.156$ (see test 1 in Table 6.1) measured at location T1 (downstream boundary). Figure 6.29a indicates the location of maximum reflection frequencies (w_n^R) and total transmission frequencies (w_n^T) (see Eq. (4.10) and Eq. (4.11)); and Figure 6.29b indicates the location of the uncoupled eigenfrequencies for subsystem 1 (RPV system with length l_1) and subsystem 3 (VPV system with length l_3) (see Eqs. (6.28) and (6.30) and Figure 6.9). Figure 6.29b shows that the 3rd , 4th and 5th resonant frequencies, located respectively at $w/w_1^0 \approx 4.2$, $w/w_1^0 \approx 8$ and $w/w_1^0 \approx 8.65$, almost coincides with the uncoupled eigenfrequencies. This is because these eigenfrequencies are close to the first Bragg

resonance frequency of maximum reflection ($w_1^R / w_1^0 \approx 6.4$) (see Figure 6.29a) where the eigenfrequency variations approaches the asymptotic solutions (see Figures 6.14 and 6.12). On the other hand, the 6th and 7th eigenfrequencies, located respectively at $w/w_1^0 \approx 11.6$ and $w/w_1^0 \approx 13.1$, are close to the first Bragg resonance frequency of total transmission ($w_1^T / w_1^0 \approx 12.8$) (see Figure 6.29a), and therefore, do not coincide with the uncoupled eigenfrequencies (see Figure 6.29b) as expected from Figures 6.14 and 6.12. Moreover, the 3rd, 4th and 5th eigenfrequencies, which are near the first Bragg resonance frequency of maximum reflection, are largely shifted with respect to the eigenfrequencies of the intact pipe case, whereas the 7th eigenfrequency shift is zero. This is as expected from Figures 6.14 and 6.12.

Two special cases occurred in Figure 6.29. The first special case is that the 2nd eigenfrequency, although close enough to the first Bragg resonance frequency of maximum reflection, is not shifted with respect to the 2nd eigenfrequency of the intact pipe case. This is because the blockage is placed at a zero shift location (see Eq. (6.45)). In fact, $\eta_3 + \eta_2/2 = (76.75+24/2)/153.61 = 0.5778$ which is very close to the second shift location given by Eq. (6.45) as follows

$$\eta_3 + \frac{\eta_2}{2} = \{0.1048 \quad \text{or} \quad 0.5619 \quad \text{or} \quad 0.7715\} \qquad (6.94)$$

If Eq. (6.48), which gives the zero shift locations for shallow blockage case, is used instead of Eq. (6.45), the following possible blockage locations become

$$\eta_3 + \frac{\eta_2}{2} = \{0.1667 \quad \text{or} \quad 0.5000 \quad \text{or} \quad 0.8333\} \qquad (6.95)$$

The difference between Eq. (6.94) and Eq. (6.95) gives an error of about 6%.

The second special case is that the 5th eigenfrequency is not very clear. This is because the blockage is located where the frequencies of uncoupled subsystem 1 (Eq. (5.68)) and subsystem 2 (Eq. (5.69)) are almost equal (see Figures 6.14 and 6.12 and Figure 6.29). At this special location, the two consecutive eigenfrequencies (4th and 5th eigenfrequency in this case) experience almost similar shift magnitude but with opposite signs (see

Figures 6.14 and 6.12 and Figure 6.29). Therefore, the eigenfrequencies are very close to each other, and this is probably why the 5th eigenfrequency is not very clear.

Figure 6.29 shows that significant shifts occur at the 3rd and 4th eigenfrequencies with the 3rd eigenfrequency shift being positive and the 4th eigenfrequency shift being negative. In these cases, assuming that those shifts correspond to maximum shifts, Eqs. (6.60) and (6.25) for maximum shift locations could be applied which give

$$\eta_3 + \frac{\eta_2}{2} \in \{0.1414 \ ; 0.6195\} \quad ; \quad w_3/w_1^0 = 4.18 \qquad (6.96)$$

and

$$\eta_3 + \frac{\eta_2}{2} \in \{0.31 \ ; \ 0.5633 \ ; \ 0.8165 \ \} \quad ; \quad w_4/w_1^0 = 7.9 \qquad (6.97)$$

Equations (6.96) and (6.97) show that the blockage location, which is actually at $\eta_3 + \eta_2/2 = 0.5778$, is close to the 2nd negative maximum shift location of the 3rd mode and near the 2nd positive maximum shift location of the 4th mode. This shows that, although a significant shift is used which is not necessary a maximum shift, Eqs. (6.60) and (6.25) could give quite accurate approximation for the blockage location with an error of about 1.4% to 4.2%.

A relatively significant shift is observed at the first eigenfrequency in Figure 6.29 where $w_1/w_1^0 = 0.72$. In this case, Eq. (6.70), for low frequency approximation, could be used to approximate the first eigenfrequency which gives

$$\frac{w_1}{w_1^0} \approx \frac{2}{\pi}\sqrt{\frac{\alpha}{\eta_2\eta_3}} = \frac{2}{\pi}\sqrt{\frac{0.168}{0.156\times 0.5}} = 0.9343 \qquad (6.98)$$

There is a large difference between the experimental and the approximated values (21.4% error). Even based on the numerical results which give $w_1/w_1^0 = 0.8$, the difference is still large (13% error). Therefore, Eq. (6.70) does not provide accurate approximation. However, if Eq. (6.69) is used instead of Eq. (6.70), the first eigenfrequency is

$$\frac{w_1}{w_1^0} \approx \frac{2}{\pi}\sqrt{\frac{\alpha}{\alpha^2\eta_1\eta_2 + \alpha\eta_1\eta_3 + \eta_2\eta_3}} \approx 0.83 \qquad (6.99)$$

which gives about 50% better accuracy (11% error). Consequently, Eq. (6.70) is probably not reliable for real applications, whereas Eq. (6.69) might gives enough accuracy since it produces an error relatively close to the measurement error.

In Chapter 4, it is shown that the knowledge of Bragg resonance frequency could inform on the blockage characteristics (e.g. blockage length). However, it may not be trivial to identify the Bragg resonance frequencies from the FRF. Nevertheless, Bragg resonance frequency of maximum reflection could be approximated to be the intact pipe system's eigenfrequency at the mode where the first significant positive shift occurs. This is because, as discussed in Section 6.5.4, positive shift is small at low modes and become large only near Bragg resonance frequency of maximum reflection. For example, Figure 6.29 shows that a significant positive shift occurs at the 4th mode ($w_4/w_1^0 = 7.9$). Therefore, the 4th eigenfrequency of the intact pipe system (w_4^0) could approximated to be the Bragg resonance frequency of maximum reflection. In fact, inserting w_4^0 into Eq. (4.10) give

$$\eta_2 = \frac{1}{w_4^0/w_1^0} = \frac{1}{7} = 0.1425 \approx 0.156 \qquad (6.100)$$

which is very close to the true blockage length with about (0.156–0.1425)×100 = 1.36% error.

Moreover, in Section 6.5.2 it is shown that at modes with eigenfrequency close to the Bragg resonance frequency of maximum reflection, the blocked pipe system becomes equivalent to a junction pipe system (where the blockage is placed at either boundary of the pipe system) with squared blocked area ratio (α^2). Therefore, if a maximum shift at such modes is measured, then Eq. (5.65) could be used to determine the area ratio (α) as follow

$$\sin\left(\frac{w_m^{\max}}{w_1^0}\frac{\pi}{2}\right) \pm \frac{1-\alpha^2}{1+\alpha^2} = 0 \Rightarrow \alpha = \sqrt{\frac{1 \mp \sin\left[\frac{w_m^{\max}}{w_1^0}\frac{\pi}{2}\left(1-\eta_2\right)\right]}{1 \pm \sin\left[\frac{w_m^{\max}}{w_1^0}\frac{\pi}{2}\left(1-\eta_2\right)\right]}} \le 1, \qquad (6.101)$$

For example, using the significant positive shift observed at the 4th mode ($w_4/w_1^0 = 7.9$) (see Figure 6.29), Eq. (6.101) gives

$$\alpha = \sqrt{\frac{1+\sin\left[7.9\pi/2\left(1-0.1425\right)\right]}{1-\sin\left[7.9\pi/2\left(1-0.1425\right)\right]}} = 0.1792 \approx 0.168 \qquad (6.102)$$

which is very close to the true area ratio with about (0.1792–0.168)×100 = 1.12% error.

Figure 6.29 Frequency response function (FRF) of the pressure signal measured at T1 for the test case with blockage length $\eta_2 \approx 0.156$ (test 1 in Table 6.1 with *a* = 355 m/s) where the Bragg resonance frequencies and the uncoupled subsystems eigenfrequencies are included.

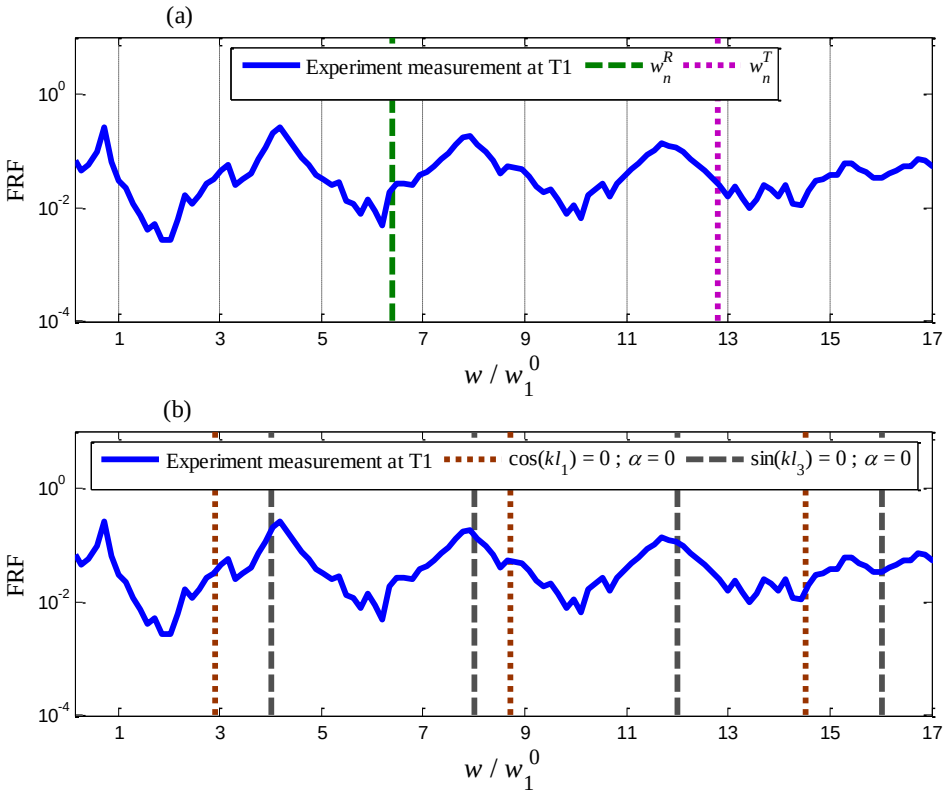

(a) Top **Indicates the location of maximum reflection (w_n^R) and total transmission frequencies (w_n^T) (Eq. (4.10) and Eq. (4.11)).**

(b) Bottom **Indicates the location of the eigenfrequencies of uncoupled subsystem 1 and subsystem 3 (see Eqs (6.28) and (6.30) and Figure 6.9)**

6.7.2.2.3. Test 2: short blockage

Figure 6.30 gives the FRF of the pressure signal measured at location T1 (downstream boundary) for the test case with blockage length $\eta_2 \approx 0.027$ (see test 2 in Table 6.1). Figure 6.30a gives a comparison between experimental and numerical results and shows relatively good fitting between both of them. Figure 6.30b shows the experimental results with the eigenfrequencies of the uncoupled subsystems (see Eqs (6.28) and (6.30) and Figure 6.9). In this case, the Bragg resonance frequencies are too high ($w_1^R / w_1^0 = 37$) to be observed in the frequency domain due to the limitation of the injected frequency bandwidth (FBW).

Conversely to the test case 1 discussed above (see Figure 6.29), Figure 6.30b shows that the eigenfrequencies at low modes do not coincide with the uncoupled frequencies (see first five eigenfrequencies in Figure 6.30b) as expected from Figures 6.13, 6.15 and 6.16. Notice that the 4th eigenfrequency, although at low enough mode, is close the eigenfrequency of the uncoupled subsystem 3. This is because the blockage is located near a zero shift position of the 4th mode as shown in Figure 6.30. A quick calculation shows that $\eta_3 + \eta_2/2$ = (76.75+3.6/2)/133.21 = 0.5035, whereas the zero shift locations at the 4th mode from Eq. (6.45) are

$$\eta_3 + \frac{\eta_2}{2} = \left\{ \begin{matrix} 0.0371\ ;\ 0.2486\ ;\ 0.3228\ ;\ 0.5343\ ; \\ 0.6085\ ;\ 0.8201\ ;\ 0.8942 \end{matrix} \right\} \qquad (6.103)$$

showing that the blockage mid-length is located near the 4th zero shift position of the 4th mode.

Although the first Bragg resonance frequencies of maximum reflection occur at high frequency ($w_1^R / w_1^0 = 37$), Figure 6.30b shows that the 6th and higher eigenfrequencies get close to the eigenfrequencies of the uncoupled subsystems. This is because for severe-short blockages (which is the case for test 2), the Bragg resonance effect of maximum reflection affects large frequency bandwidth as shown in Figure 4.3 and 4.4; and therefore the

decoupling effect is enhanced at frequencies much lower than the Bragg resonance frequency of maximum reflection (see Figures 6.13, 6.15 and 6.16).

Notice that all eigenfrequency shifts in Figure 6.30b are negative which is as expected from Eq. (6.66) where the zero shift locations approaches the maximum positive shift locations and therefore, preventing positive shift to occur at modes much lower than the mode with eigenfrequency close to the first Bragg resonance frequency of maximum reflection.

Figure 6.30 shows that significant negative shifts occur at the 3rd and 5th eigenfrequencies. Assuming that those shifts correspond to maximum shifts, then Eqs. (6.60) and (6.25) could be applied and give

$$\eta_3 + \frac{\eta_2}{2} \in \{0.1629 \ ; \ 0.6124\} \quad ; \quad w_3 / w_1^0 = 4.45 \qquad (6.104)$$

and

$$\eta_3 + \frac{\eta_2}{2} \in \{0.08 \ ; \ 0.32 \ ; \ 0.56 \ ; \ 0.8\} \quad ; \quad w_5 / w_1^0 = 8.33 \qquad (6.105)$$

Equations (6.104) and (6.105) show that the blockage location, which is actually at about $\eta_3 + \eta_2/2$ = 0.59, is close to the 2nd and 3rd negative maximum shift location of the 3rd and 5th modes with an error of about 2.2% and 3%, respectively. Again, this shows that Eqs. (6.60) and (6.25) could give quite accurate approximation for the blockage location based on a significant shift magnitude which may not be necessary the exact maximum shift magnitude.

Figure 6.30 Frequency response function (FRF) of the pressure signal measured at T1 for the test case with blockage length $\eta_2 \approx 0.027$ (test 2 in Table 6.1 with *a* = 370 m/s)

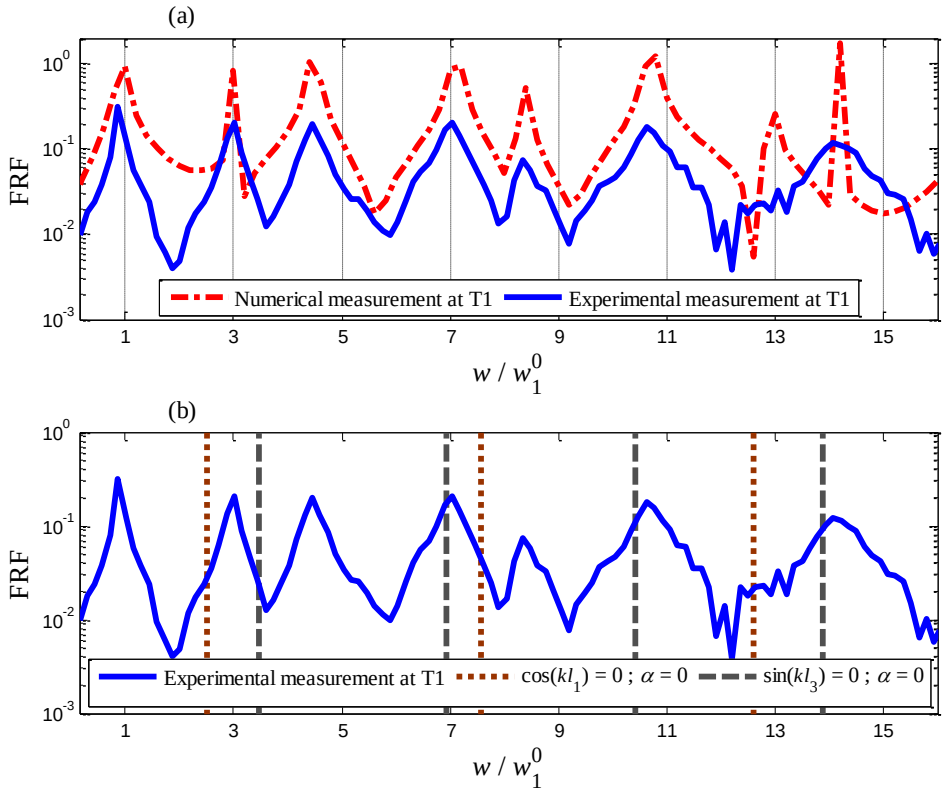

(a) Top **Comparison between experimental and numerical results**

(b) Bottom **Indicates the location of the eigenfrequencies of uncoupled subsystem 1 and subsystem 3 (see Eqs. (6.28) and (6.30) and Figure 6.9)**

6.7.2.3. Potential of using of Bragg resonance and frequency shift mechanism information for blockage detection

The purpose of this work is to study the blockage-wave interaction in pipe system and not to establish new transient-based blockage defect detection method. Nevertheless, it is instructive to show the potential of using the understanding gained form studying wave-blockage interaction and eigenfrequency shift mechanisms for blockage detection. Recently, Duan, et al. ([32]) used the dispersion relation (Eq. (5.1)) for blockage detection. For

example, denoting the dispersion relation equation for the case of blocked RPV system with interior blockage by

$$F_{dis}\left(k_m,\eta_2,\eta_3,\bar{\alpha}\right)=\begin{Bmatrix}\cos\left(k_mL\right)\\+\bar{\alpha}\cos\left(k_mL\left(1-\left(2\eta_3+\eta_2\right)-\eta_2\right)\right)\\-\bar{\alpha}\cos\left(k_mL\left(1-\left(2\eta_3+\eta_2\right)+\eta_2\right)\right)\\-\bar{\alpha}^2\cos\left(k_mL\left(1-2\eta_2\right)\right)\end{Bmatrix}=0 \quad , \qquad (6.106)$$

$$=\begin{Bmatrix}\cos\left(k_mL\right)\\+2\bar{\alpha}\sin\left(k_mL\left(1-\left(2\eta_3+\eta_2\right)\right)\right)\sin\left(k_mL\eta_2\right)\\-\bar{\alpha}^2\cos\left(k_mL\left(1-2\eta_2\right)\right)\end{Bmatrix}=0$$

where

$$\bar{\alpha}=\frac{\left(1-\alpha\right)}{\left(1+\alpha\right)}, \qquad (6.107)$$

Duan, et al. ([32]) used inverse optimization techniques such as genetic algorithm to minimize the flowing equation

$$\sum_m\left|F_{dis}\left(w_m^{mes},l_2,l_3,\alpha\right)\right|=\min \qquad (6.108)$$

where w_m^{mes} is the m^{th} measured eigenfrequency. Such techniques requires a search on all possible combinations of $\{l_2,l_3,\alpha\}$ which gives a very large search domain. This section shows how the use of Bragg resonance and eigenfrequency shift mechanism could reduce significantly the search domain.

The procedure to reduce the search domain is to use the equations of zero shift locations (Eq. (6.45)) and maximum shift locations (Eq. (6.60)) whenever a zero or maximum shift is observed. The zero and maximum shift equations for RPV system are respectively repeated here for convenience

$$\eta_3+\frac{\eta_2}{2}=\frac{2\bar{m}-\frac{2}{\pi}\arccos\left[(-1)^{\bar{m}}\frac{(1-\alpha)}{(1+\alpha)}\cos\left((2m-1)\frac{\pi}{2}\eta_2\right)\right]}{2(2m-1)};\quad \bar{m}\le 2m-1 \tag{6.109}$$

$$\eta_3+\frac{\eta_2}{2}=\frac{1}{2}\left[1-\frac{2(m-\bar{m})-1}{w_m^{\max}/w_1^0}\right];\ \text{with}\ \begin{cases}\frac{\eta_2}{2}<\eta_3+\frac{\eta_2}{2}<1-\frac{\eta_2}{2}\\ \bar{m}=1,2,\ldots\le 2m\end{cases} \tag{6.110}$$

Equations (6.109) and (6.110) are discrete at any given mode *m*. This means if a zero or maximum shift occurs at a mode *m*, then there exist at most 2*m*−1 possible blockage locations. Notice that the lower the mode where a zero or maximum shift is observed, the narrower the search domain becomes. At relatively high modes (*m* > 2), Eqs. (6.52) and (6.53) show that Eq. (6.109) could approximated by the equation of zero shift location for shallow blockage case as follows

$$\eta_3+\frac{\eta_2}{2}=\frac{2\bar{m}-1}{2(2m-1)};\quad \bar{m}\le 2m-1 \tag{6.111}$$

with a maximum error of

$$\text{err}(m)=\frac{(-1)^{\bar{m}}}{2(2m-1)}, \tag{6.112}$$

Equations (6.110) and (6.111) give different sets of multiple solutions for the blockage location (see Eqs. (6.95), (6.96) and (6.97)), which would require a *position recognition algorithm* to identify the possible blockage position. This identification is possible by selecting different possible combination of blockage locations where each combination must include one possible location from each set; and imposing the maximum error (Eq. (6.112)) on the zero shift locations and assuming a maximum error for the maximum shift locations which must be located between two consecutive zero locations. Such identification process could converge if enough sets are used. If the sets are not enough to obtain convergence towards unique possible location, then a probabilistic approach could be applied based on the minimum error in each combination. For example, the sets of possible locations given by Eqs. (6.95), (6.96) and (6.97) show that the combination of {0.5 ; 0.6195 ; 0.5633} has the

minimum error. An approximation of the blockage location could be obtain by an average of this combination as follows

$$\eta_3 + \frac{\eta_2}{2} = \frac{\left(0.5 + 0.6195 + 0.5633\right)}{3} = 0.561 \qquad (6.113)$$

which is close to the exact solution $\eta_3 + \eta_2/2 = 0.5778$ (see test 1 in Table 6.1).

Furthermore, Eq. (6.110) could be inserted into the dispersion relation (Eq. (6.106)) to simplify the equation and reduce the search domain. If a significant shift occurs at the m^{th} eigenfrequency, then Eq. (6.110) is inserted into Eq. (6.106) which gives

$$F_{dis}\left(w_m, \eta_2, \bar{m}, \bar{\alpha}\right) = \left\{ \begin{array}{l} \cos\left(\dfrac{w_m}{w_1^0}\dfrac{\pi}{2}\right) \\ +2\bar{\alpha}\left(-1\right)^{m-\bar{m}+1}\sin\left(\dfrac{w_m}{w_1^0}\dfrac{\pi}{2}\eta_2\right) \\ -\bar{\alpha}^2\cos\left(\dfrac{w_m}{w_1^0}\dfrac{\pi}{2}\left(1-2\eta_2\right)\right) \end{array} \right\} = 0 \qquad (6.114)$$

For example, Figure 6.29, which gives the FRF for test 1 (see Table 6.1), shows a significant negative shift occuring at the 3rd eigenfrequency and a significant positive shift occuring at the 4th eigenfrequency. Therefore, one could write the following equations

$$F_{dis}\left(w_3, \eta_2, \bar{m}, \bar{\alpha}\right) = \left\{ \begin{array}{l} \cos\left(\dfrac{w_3}{w_1^0}\dfrac{\pi}{2}\right) \\ -2\bar{\alpha}\sin\left(\dfrac{w_3}{w_1^0}\dfrac{\pi}{2}\eta_2\right) \\ -\bar{\alpha}^2\cos\left(\dfrac{w_3}{w_1^0}\dfrac{\pi}{2}\left(1-2\eta_2\right)\right) \end{array} \right\} \approx 0 \;\; ; \;\; \bar{m} = 1,3,5 \qquad (6.115)$$

$$F_{dis}\left(w_4,\eta_2,\bar{m},\bar{\alpha}\right)=\left\{\begin{array}{l}\cos\left(\dfrac{w_4}{w_1^0}\dfrac{\pi}{2}\right)\\ -2\bar{\alpha}\sin\left(\dfrac{w_4}{w_1^0}\dfrac{\pi}{2}\eta_2\right)\\ -\bar{\alpha}^2\cos\left(\dfrac{w_4}{w_1^0}\dfrac{\pi}{2}\left(1-2\eta_2\right)\right)\end{array}\right\}\approx 0\ \ ;\ \ \bar{m}=2,4,6,8 \qquad (6.116)$$

If a unique blockage position is obtained through a location recognition algorithm, then Eqs. (6.115) and (6.116) depend only on the blockage length (η_2) and severeness (α). Inserting Eqs. (6.115) and (6.116) into Eq. (6.108) for inverse optimization process gives narrower search domain and better accuracy to obtain the blockage characteristics. The pipe length constraint imposes a condition on the blockage length that helps narrowing the search domain. This condition is given by

$$\begin{cases}\eta_2\le\eta_3+\eta_2/2 & ;\ \text{if}\quad \eta_3+\eta_2/2\le 0.5\\ \eta_2\le 1-\left(\eta_3+\eta_2/2\right) & ;\ \text{if}\quad \eta_3+\eta_2/2\ge 0.5\end{cases} \qquad (6.117)$$

Moreover, if Bragg resonance frequency is determined, then the blockage length could be obtained from Eq. (4.10). In addition, it is shown (see Section 6.5.2) that at modes with eigenfrequencies close to the Bragg resonance frequency of maximum reflection, the blocked pipe system becomes equivalent to a junction pipe system (where the blockage is placed at either boundary of the pipe system) with squared blocked area ratio (α^2). If maximum shift is measured at such modes, then Eq. (5.56) or Eq. (5.65) could be used to determine the area ratio (α). For RPV system, Eq. (5.65) could be used and gives

$$\sin\left(k_m^{\max}L\right)\pm\frac{1-\alpha^2}{1+\alpha^2}=0\Rightarrow\alpha=\sqrt{\frac{1\mp\sin\left[k_m^{\max}L\left(1-\eta_2\right)\right]}{1\pm\sin\left[k_m^{\max}L\left(1-\eta_2\right)\right]}}\,, \qquad (6.118)$$

whereas for RPR and VPV systems, Eq. (5.56) is used and gives

$$\cos\left(k_m^{\max}L\right)\pm\frac{1-\alpha^2}{1+\alpha^2}=0\Rightarrow\alpha=\sqrt{\frac{1\mp\cos\left[k_m^{\max}L\left(1-\eta_2\right)\right]}{1\pm\cos\left[k_m^{\max}L\left(1-\eta_2\right)\right]}} \qquad (6.119)$$

and

$$\cos\left(k_m^{\max}L\right)\pm\frac{1-\left(\frac{1}{\alpha}\right)^2}{1+\left(\frac{1}{\alpha}\right)^2}=0\Rightarrow\alpha=\sqrt{\frac{1\pm\cos\left[k_m^{\max}L\left(1-\eta_2\right)\right]}{1\mp\cos\left[k_m^{\max}L\left(1-\eta_2\right)\right]}},\qquad(6.120)$$

respectively. Bragg resonance frequency of maximum reflection may not be trivial to identify in the frequency response; however, it could be approximated to be the intact pipe system's eigenfrequency at the mode where the first significant positive shift occurs. This is because, as discussed in Section 6.5.4, positive shift is small at low modes and become significant only near Bragg resonance frequency of maximum reflection. If such positive shift is measured, then the area ratio and blockage length could be obtained as given in Eqs. (6.100) and (6.102).

Another possible way to identify the Bragg resonance frequency is to use signal correlation techniques in the frequency domain. This is because, as shown from the results in Chapter 4 (see Figures 4.10 and 4.11), there exists regularity (periodicity) in the distribution of the Bragg resonances frequency bands which related to the pipe system's characteristic lengths. However, this technique may require a large FBW. To understand this technique, assume that the eigenfrequency shift has the following form

$$\frac{\overline{\Delta w_m}}{w_1^0}=\sum_i \mathrm{B}_i\left(\alpha\right)\sin\left[\left(2m-1\right)\pi\Im_i\left(\eta_1,\eta_2,\eta_3\right)+\Phi_i\right]\qquad(6.121)$$

where $\Im_i\left(\eta_1,\eta_2,\eta_3\right)$ is a combination of the characteristic lengths of the pipe system (e.g. $\Im_i=\eta_2$ or $\Im_i=\eta_3$ or $\Im_i=\eta_2+\eta_3$ or $\Im_i=\eta_1+\eta_3$); $\mathrm{B}_i\left(\alpha\right)$ is a coefficient depending in the area ratio (α), Φ_i is representing a phase. The choice of the shift equation form in Eq. (6.121) is based on the shift equation form for shallow blockage (Eq. (6.10)) and the form of the dispersion relation (Eq. (6.2)). Applying Fourier transform on the shift equation in Eq. (6.121) with respect to the mode number gives the

$$\wp\left(\frac{\overline{\Delta w_m}}{w_1^0}\right)\left(\eta\right)=\sum_i \overline{\mathrm{B}_i}\exp\left(i\overline{\Phi_i}\right)\delta\left(\eta,\Im_i\right)\qquad(6.122)$$

where $\wp$ refers to discrete Fourier transform (DFT); $\overline{\mathrm{B}_i}$ is amplitude; $\overline{\Phi_i}$ is phase; η the characteristic length variable; and $\delta(\eta, \Im_i)$ is the Kronecker delta function. Eq. (6.122) shows that, if the shift has the form in Eq. (6.121), the Furrier transform of the eigenfrequency shift with respect to the mode number would indicate the characteristic lengths of the pip system ($\Im_i$). To verify this, Figure 6.31a gives the exact eigenfrequency shifts at the first 40 modes corresponding to the experimental test 1 (see Table 6.1). The DFT of the eigenfrequency shift (Figure 6.31a) with respect to the mode number is given in Figure 6.31b. The observed peaks in Figure 6.31b are given at $\eta = 0.15$, $\eta = 0.35$ and $\eta = 0.5$ which correspond approximately to the blockage length ($\eta_2 = 0.156$), the length $\eta_1 = 52.86/153.61 = 0.344$. and $\eta_1 + \eta_2 = 0.5$.

Figure 6.31 Eigenfrequency shift variation with mode number and its DFT corresponding to test 1 in Table 6.1.

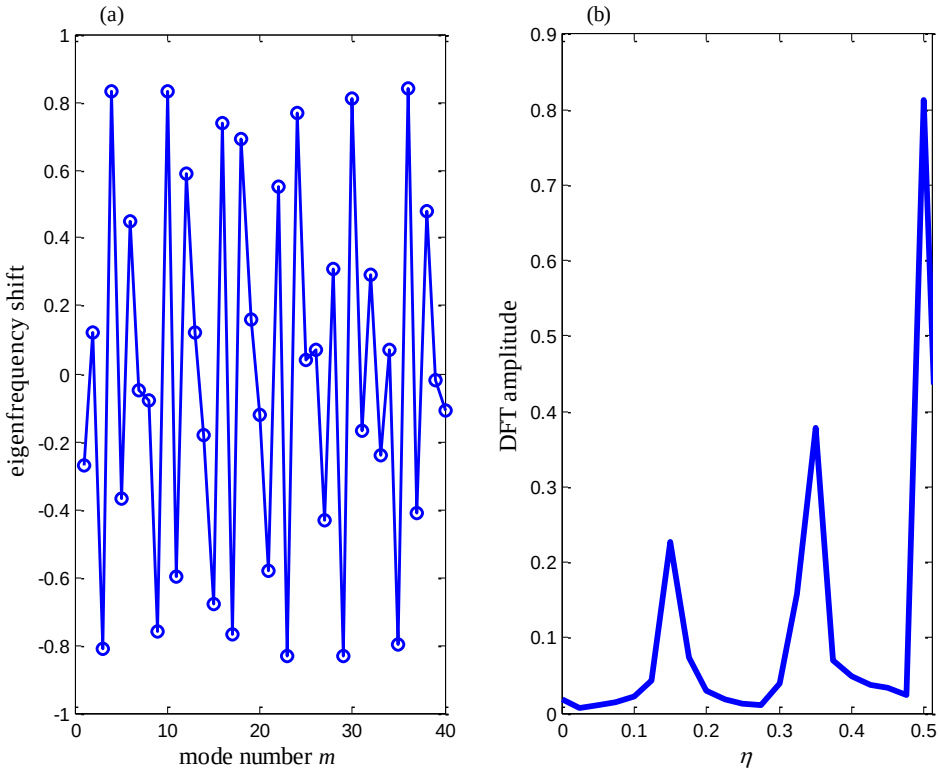

(a) Left **Eigenfrequency shift variation with mode number**

(b) Right **DFT of the eigenfrequency shift**

Similarly, the DFT of the eigenfrequency shift is carried for four different blocked pipe systems in Figure 6.32. The sets of lengths and area ratio ($\{\eta_1, \eta_2, \eta_3, \alpha\}$) for the four different tests are given in Table 6.2 which correspond to the test cases in Figure 6.32a-d, respectively.

Figure 6.32a , which is similar to the experimental test 2 in Table 6.1, shows that the observed peaks are given at $\eta = 0.025$, $\eta = 0.175$ and $\eta = 0.4$ which correspond approximately to the blockage length (η_2 = 0.027), $\eta_3 - \eta_1$ = 0.1794 and η_1 =0.3968. One more unclear peak in Figure 6.32a is shown in circle which as at $\eta = 0.425$ and corresponds approximately to the $\eta_1 + \eta_2$ = 0.4238. Figure 6.32b shows that the three peaks correspond to η_1, η_2 and η_3, whereas Figure 6.32c shows that the three peaks correspond to η_1, η_3 and $\eta_1 + \eta_3$. The area ratio in these two last tests is $\alpha = 0.5$ showing that the DFT of the shift is not affected by the area ratio, which means that it is not affected by the shift magnitude. In fact Figure 6.32d gives a test case with $\alpha = 0.8$ and shows that the peaks are clear and correspond to η_2, η_1 and η_3.

The characteristic lengths appearing in DFT the shift are restricted by the Nyquist frequency which states that the characteristic lengths are less than $\Delta m/2$ = 1/2 to remove any aliases. It is this condition which makes the apparent characteristic lengths varies for different pipe system cases. To understand this better, Eq. (6.10) given the shift for shallow blockage case is recalled here

$$\begin{aligned}\frac{\overline{\Delta w_m}}{w_1^0} &= \frac{(1-\alpha)}{\pi}\left[\sin\left((2m-1)\pi\eta_1\right) - \sin\left((2m-1)\pi\left(\eta_1+\eta_2\right)\right)\right] \\ &= \frac{(1-\alpha)}{\pi}\left[\sin\left((2m-1)\pi\left(\eta_3+\eta_2\right)\right) - \sin\left((2m-1)\pi\eta_3\right)\right]\end{aligned} \qquad (6.123)$$

and shows that the shift could be written in terms of different characteristic lengths. The DFT select the ones restricted by the Nyquist frequency.

Table 6.2. Sets of lengths and area ratio for the test examples in Figure 6.32

#	a	b	c	d
η_1	0.3968	0.22	0.14	0.34
η_2	0.027	0.36	0.58	0.12
η_3	0.5762	0.42	0.28	0.54
α	0.168	0.5	0.5	0.8

Figure 6.32 DFT of eigenfrequency shift corresponding to the test cases in Table 6.2.

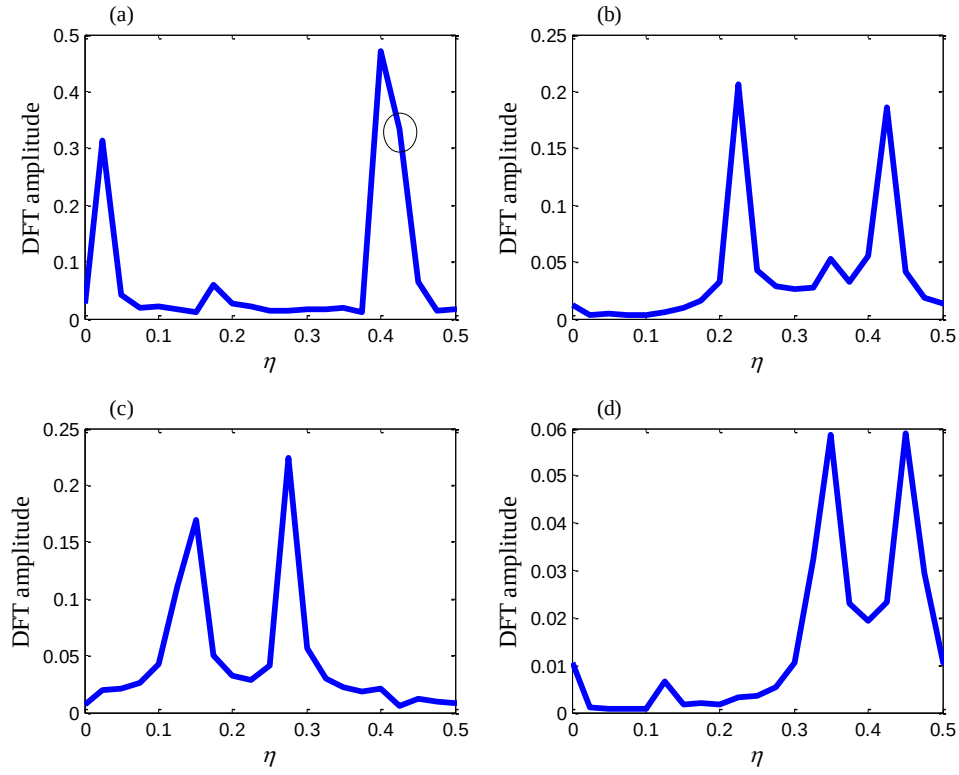

(a) Top left **Test case number a in Table 6.2**

(b) Top right **Test case number b in Table 6.2**

(c) Bottom left **Test case number c in Table 6.2**

(d) Bottom right **Test case number d in Table 6.2**

The clarity of the peaks in the DFT of the shift depends on the frequency bandwidth. For example, Figure 6.33 gives the DFT of the shift at the first seven modes for the case corresponding to the experimental test 1 (Table 6.1) and compares the exact and experimental results. First, Figure 6.33 shows that the experimental and exact results are similar. Second, although the peaks are not as clear as for the case using 40 modes (see Figure 6.31b), the peak observed in Figure 6.33 give an estimate of the blockage length with about 1.31% error. On the other hand, Figure 6.33 compares the exact and experimental results of the DFT of the shift at the first seven modes for test 2 (Table 6.1) and shows no clear peaks. The higher amplitude at low characteristic length (η) may be an indication that a small length scale is involved. This shows that small scale blockages requires larger FBW, and therefore, higher injected frequencies.

Although not shown here, but it is found that Eqs. (6.121) and (6.122) could be applied for multi-blockages case.

Figure 6.33 DFT of eigenfrequency shift corresponding to test 1 in Table 6.1 using only the first seven modes. A comparison between experimental and exact results.

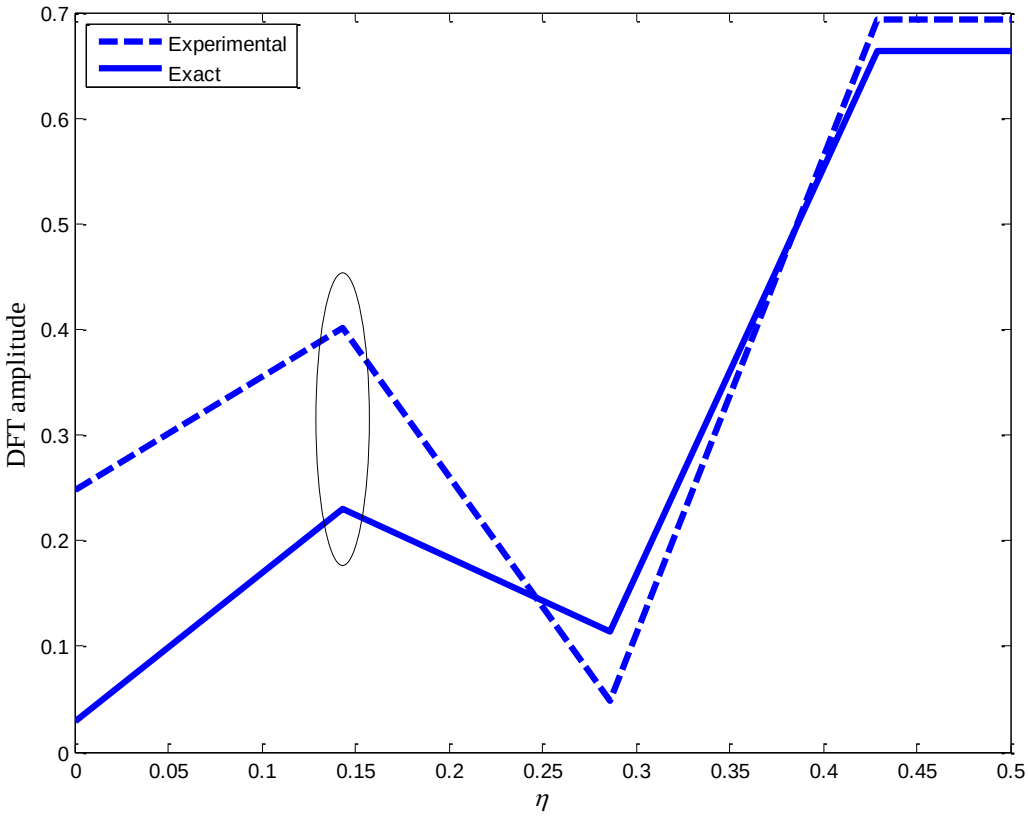

Figure 6.34 DFT of eigenfrequency shift corresponding to test 2 in Table 6.1 using only the first seven modes. A comparison between experimental and exact results.

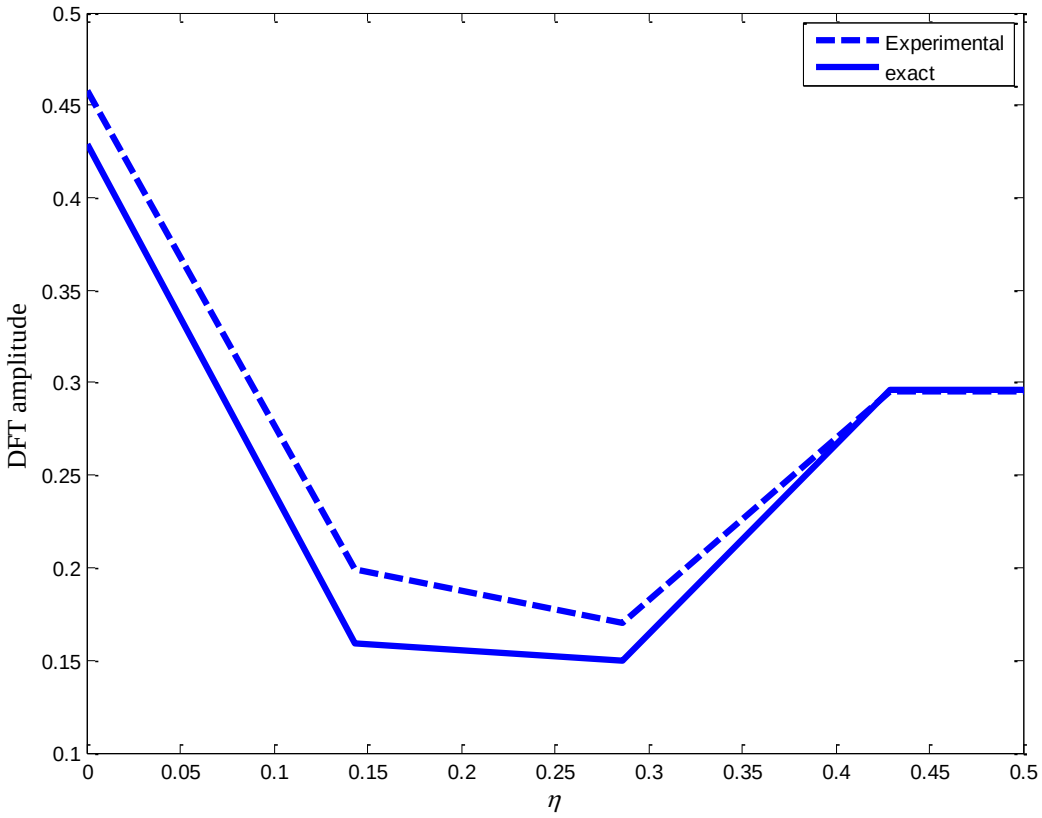

6.8. Summary

This chapter studied the eigenfrequency shift due to an interior blockage in bounded pipe system with the primary goal being to understand and describe the mechanisms that cause such eigenfrequency shift. The key findings are summarized below:

(i) The eigenfrequency shift variation caused by a shallow blockage in a conduit is analyzed by studying the variation of the work of radiation pressure at the blockage boundaries. It is found that if the works at the blockage boundaries are equal in magnitude and sign, then the eigenfrequency shift is zero. This case occurs under two conditions: The first condition is when the blockage length is a multiple of half wavelength of the m^{th} mode harmonic, and therefore, the eigenfrequency corresponds to the Bragg resonance frequency of total transmission. Under such condition, the shift is zero for any blockage location. The second condition states that, at a given mode *m*, the shift is zero when the blockage mid-length is located at a position of equal pressure and flow magnitudes. On the other hand, maximum shift occur if the work at the blockage boundaries are equal in magnitude but with opposite sign. There are two mechanisms governing the maximum shift. The first mechanism is for a given resonant mode *m* and states that the shift is maximum if the blockage mid-length is located at a position of either a pressure node or stagnation point. The second mechanism describes the variation of the maximum shift magnitude with mode number and shows that the largest magnitude of maximum shift occurs at modes with eigenfrequency close to the Bragg resonance frequencies of maximum reflection. Positive and negative shifts depend on which work is higher at the blockage boundaries.

(ii) Similarly to the case of blockage at the boundary, an interior severe blockage decouples the pipe system into independent intact subsystems with different lengths. The eigenfrequencies of these subsystems defines the asymptotic solutions of the eigenfrequency variations at the limit of most severe blockage cases $\alpha \to 0$. This decoupling effect is governed by two mechanisms depending on either the

change of the blockage location at a given mode or the change in mode number. The first mechanism is for a given resonant mode and states that the decoupling effect is weakened when the blockage location is such that the eigenfrequencies of the subsystems are close or equal to each other. When this occurs, waves in the subsystems act as forcing functions for one to another which drives the whole pipe system at or near resonance. The fact that subsystems are driving one another at or near resonance is what brings about the coupling even for a very severe blockage. The second mechanism describes the variation of the maximum shift magnitudes with mode number and shows that as the eigenfrequency mode number varies, the coupling/decoupling mechanism is governed by the Bragg resonance effect studied in Chapter 4. In fact, it is shown that most decoupling effect occurs at modes with eigenfrequencies close or at the Bragg resonance frequencies of maximum reflection. This is because the more reflections are from the blockage, the more the upstream and downstream regions of the blockage become decoupled. Conversely, maximum coupling effect occurs at modes with eigenfrequencies close or at the Bragg resonance frequencies of total transmission where the eigenfrequency shift is zero for any blockage location.

(iii) The assumption of shallow blockage (with small radial protrusion) is applicable when the blockage occupies 35% of the pipe's area or less. The assumption of severe blockage is applicable when the blockage occupies 35% of the pipe's area or more provided that the eigenfrequencies of the asymptotic subsystems are not equal or close to each others.

(iv) At modes close to the Bragg resonance frequency of maximum reflection, the blocked pipe system with interior blockage behaves as a blocked pipe system with blockage at the boundary.

(v) Experimental tests are conducted validating the effect of Bragg resonance in bounded pipe system as well as the different features discussed about the eigenfrequency shift mechanism. Experimental and numerical tests showed that the eigenfrequency mechanism has potential to improve blockage detection techniques in pipe system. For example, if a zero or maximum shift is measured, a narrow solutions set of blockage location could be obtained which reduces the search domain for inverse techniques used in TBDDM. Moreover, knowledge of the Bragg resonance

frequencies allows the determination of blockage characteristics such as its length and area.

(vi) The injected FBW should be varied through a range of frequencies inversely proportional to the blockage length scale in target for detection. This avoid hidden blockage signature and helps detecting the Bragg resonance frequencies from which the blockage characteristics could be obtained.

(vii) The smaller the blockage length is, the smaller the shifts at low modes are. This is because, for short (discrete) blockages, the Bragg resonant frequencies becomes at high resonant modes (high frequencies). Therefore, if the injected FBW contains only low frequencies, the blockage signature becomes unclear. The FBW should be either large enough or swept to include frequencies close to the Bragg resonance frequency of maximum reflection. However, severe-short blockages induce large Bragg resonance frequency bandwidth of maximum reflection which increases the shift at low modes.

Localisation of small scale blockages could require the use of high frequency waves (HFW) to obtain better resolution and clear blockage signature. However, plane wave assumption, on which all one dimensional models are based, fails if the injected frequency FBW exceeds the cut-off frequencies of high radial and/or azimuthal modes. Next chapter studies the behaviour of HFW in water-filled pipe flow using a high order two dimensional numerical scheme (see Chapter 3) and gives some initial conclusions on the different aspects that practitioners must take into account if HFW are to be used for TBDDM.

CHAPTER 7

BEHAVIOUR OF HIGH FREQUENCY ACOUSTIC WAVES IN PRESSURIZED CONDUIT

7.1. Introduction

In the past, the condition that the frequency of the transient is smaller than a/D, and by implication the classical water-hammer (WH) theory, has never been challenged because WH waves are generated by mechanical devices such as valves and pumps whose frequency is far below 1 kHz. Recent research showed that the accuracy of transient based defect detections methods (TBDDM) increases with higher frequencies of the injected wave signal ([71], [79]). This is natural given that higher frequencies (*i.e.*, shorter wavelength) provide higher resolution of defect detection and are better at localizing multi-defects with multi-scales. However, the use of high frequency waves excites radial and azimuthal waves and renders the classical one-dimensional WH theory invalid. Unlike classical WH theory, the resulting wave field is highly dispersive.

Although the theory of high frequency waves (HFW) in water supply system (WWS) has not received much attention, the physics of acoustic waves in gas/air flows is well advanced and is founded on early notable works (e.g. [5], [55], [93], [94], [95], [42] and [109]). A good summary of key analytical treatment of acoustic wave propagation in cylindrical gas-filled tubes is given in Tijdeman ([124]). Moreover, HFW have been widely used in underwater acoustics applications (e.g. [67], [1], [84], [24], [46], [47], [49], [61] and [66]), but rarely in the study of pipe transient flows.

Recently, Kondis ([69]) studied the propagation of acoustic waves in water-filled pipes and provided an algorithm that advises under which circumstances the simplified model of the rigid pipe should be used versus the more complete model, which includes pipe wall

impedance and takes the pipe surroundings into account. At the same time and in a related work by Kondis ([69]), an experiment was conducted by Kokossalakis ([68]) with the purpose of communication system design for an in-pipe wireless sensor network where high frequency waves were injected and collected in separate locations using different pipes setups. Although the experiment was conducted in air-filled pipes, all the parameters in the experiment were scaled to mimic the wave propagation in water-filled pipe.

Metje et al. ([90]) gave initial results of a proof-of-concept prototype smart pipe system. Their work consisted of designing a sensor-communication system for a prototype water pipe network which was built and buried in the summer of 2009 on the University of Birmingham, UK campus, where different commercial MEMS (Micro-Electro-Mechanical System) sensors are tested. They provided initial results of the research carried out on communication, power and miniaturisation of the sensors even though much research is still required for individual components of the system.

Lee's group at the University of Canterbury, NZ, has recently developed and employed a piezoelectric generator capable of generating signals with frequencies as high as 1 MHz in water pipes. Furthermore, this work is part of a theme-based research project at HKUST ([121]) led by the advisor of the author of this thesis that aims to use high frequency (2 kHz-100 kHz) waves to detect defects in WSS. Currently, the research group at HKUST is conducting preliminary transient tests generated by piezoelectric actuators with a frequency band that goes up to 100 kHz.

In aeroacoustic applications, where most of the focus is on sound intensity and propagation, analytical solutions are available because the sound sources are usually not complex and can be represented by simple models (monopoles, dipoles and quadripoles) ([78], [23]), and the acoustic analogy ([45]) can be applied to project the sound solution in the far field. However if high frequency waves (HFW) are to be used in WWS, specific probing wave sources are generated at the boundaries, and analytical solutions for such applications are not straightforward.

In this chapter, the behaviour of high frequency waves (non-plane and dispersive waves) in water-filled pipe is studied numerically using higher-order numerical scheme (see

Chapter 3). The study gives some initial conclusions on the different aspects that practitioners must take into account if high frequency waves are to be used for TBDDM.

7.2. Study of high frequency waves behaviour in unbounded pipe system

In this section, the behaviour of high frequency waves in fluid in a pipe is studied numerically. The second and fifth order numerical schemes developed in Chapter 3 are used to solve the two dimensional axi-symmetric Navier-Stokes equations (Eq. (2.56)). In some test cases, where comparison with the 2D wave theory properties is made and where wave dispersion is solely studied, only inviscid flow will be considered. The test rig of unbounded pipe system is depicted in Figure 7.1, where a wave is generated from a source located at $x = L$ and only the left going waves are considered. The waveform at the source is given by Eq. (3.42) (see Figures 3.8 and 3.9). In what follows the zeroth, first and second modes are referred as M0, M1 and M2, respectively.

Figure 7.1 Sketch of unbounded pipe system

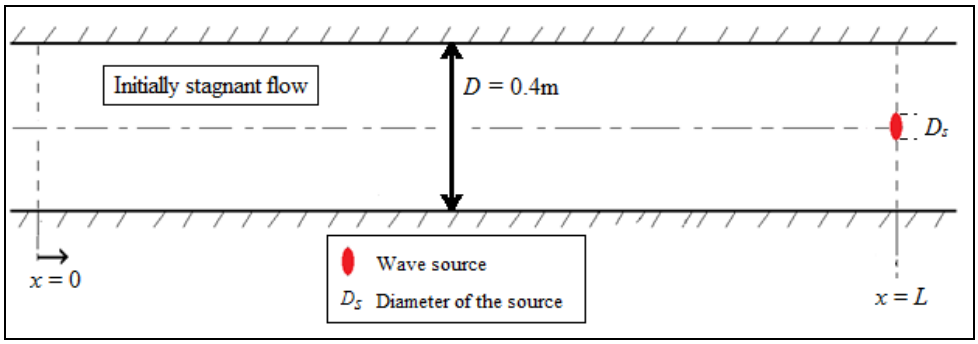

7.2.1. High frequency waves behaviour under resonating probing source

In this section, the frequency bandwidth (FBW) is chosen so as to include the cut-off frequencies of the excited high modes. In this way, the resonant response is studied and

results could be compared to the properties of the 2D inviscid wave theory (Chapter 2 Section 2.6) where the natural cut-off frequencies are well defined. The test rig is a pipe with diameter D=0.4m and length L (Figure 7.1). In this section, the flow is considered inviscid and initially stagnant. The source has a cylindrical shape with diameter denoted by D_s and located at the pipe centreline (r = 0) and at $x = L$ (Figure 7.1). The input signal has a FBW within [0.5f_c to 1.5f_c] corresponding to $\beta = 16\pi$ (Figure 3.8) where f_c is the central frequency corresponding to the angular frequency $w_c = 2\pi f_c$.

7.2.1.1. Dispersion and behaviour of high modes

Three tests are conducted using three different central frequencies f_c=1000Hz, 3000Hz and 5000Hz and using a source diameter D_s=0.1D. The upper bound frequency content (UBFC) in these three test cases are 1500Hz, 4500Hz and 7500Hz, respectively. The results are given in Figures 7.2 and 7.3 which show the time and the frequency domains of the pressure at x=9m and x=0m along the pipe centreline, respectively. The dashed lines in Figure 7.3 indicate the cut-off frequencies of the higher modes. Figure 2.11 plots the group velocity (Eq. (2.120)) for the first four modes and will aid later discussions. According to Eq. (2.115) and Figure 2.11, if the frequency is higher than f_1=3050Hz, the first higher mode (M1) is excited and the classical 1D WH theory is no longer valid. This is in good agreement with the numerical tests in Figures 7.2 and 7.3 where the signals with f_c=3000Hz and f_c=5000Hz are dispersive and do not conform to the classical 1D WH theory as the wave form of the signal is distorted due to the dispersion of the signal (Figures 7.2b and 7.2c). On the other hand, the signal with f_c=1000Hz (Figures 7.2a and 7.3a) is non-dispersive and behaves according to the classical 1D WH theory. The frequency axis in Figure 7.3a is extended to show that no higher modes are excited. Figure 7.3b (f_c=3000Hz) shows that both M0 and M1 are excited, which is in agreement with Eq. (2.115). In Figure 7.3c (f_c=5000Hz), the second mode (M2) is also excited as predicted from Eq. (2.116).

Figure 7.2 Dimensionless pressure variation with time measured near the source and at 7m away from the source and at the pipe centreline. For all cases D_s=0.1D and L=10m.

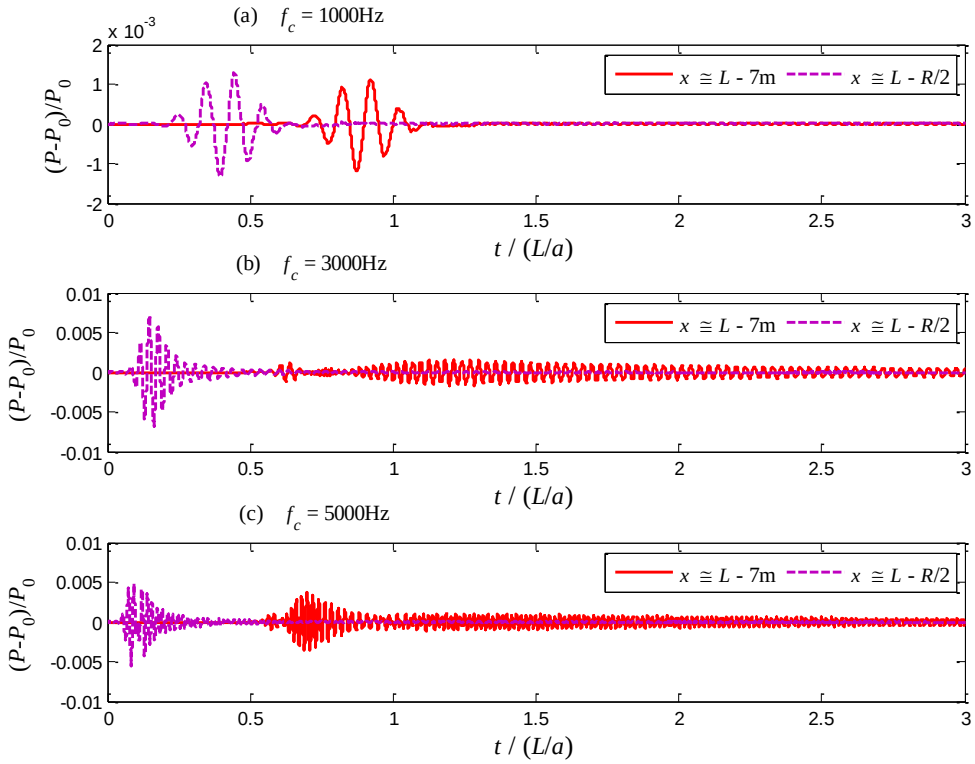

(a) Top f_c**=1000Hz**

(b) Middle f_c**=3000Hz**

(c) Bottom f_c**=5000Hz**

Figure 7.3 Amplitude in the frequency domains corresponding to the pressure signals in Figure 7.2 measured near the source and at 7m away from the source and at the pipe centreline. For all cases D_s=0.1D and L=10m.

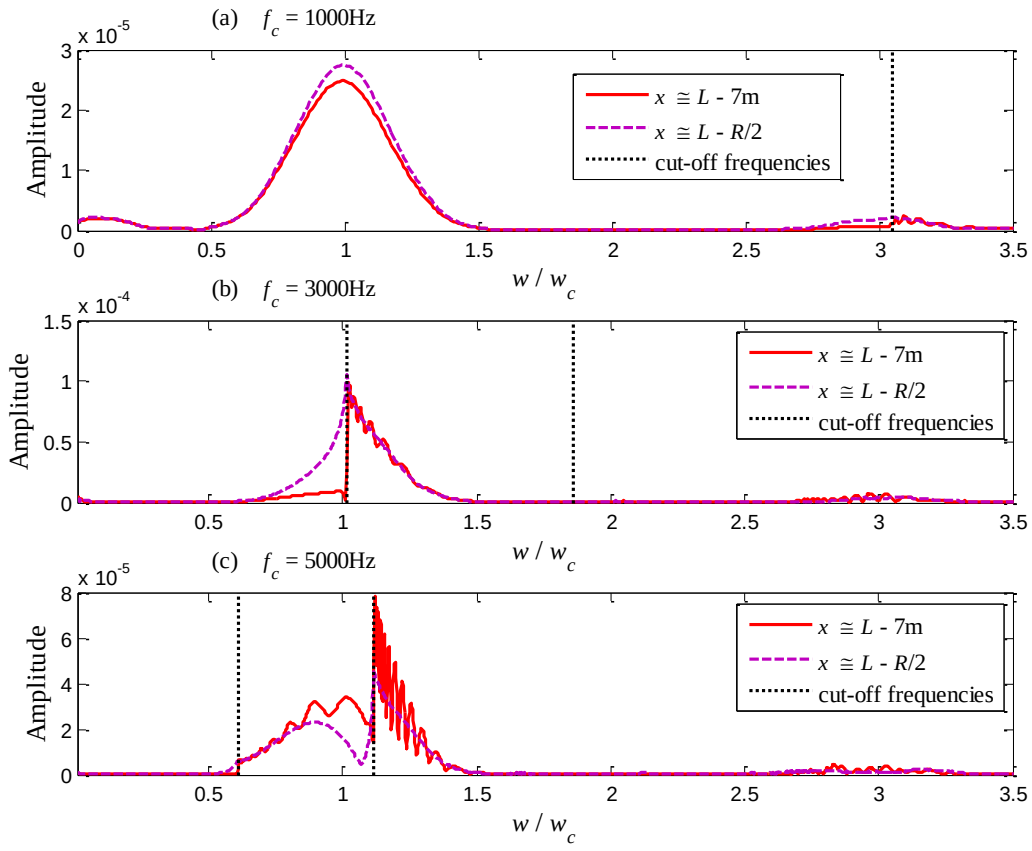

(a) Top **f_c=1000Hz**

(b) Middle **f_c=3000Hz**

(c) Bottom **f_c=5000Hz**

The dispersion of the waves along the pipe is associated with radial waves. It is, therefore, important to analyze the behaviour of these radial waves. Figure 7.4 shows the surface plot (along r and x) of the pressure of the three tests conducted in Figure 7.2 for which the central frequencies are f_c=1000Hz, 3000Hz and 5000Hz, and each test is plotted at different times $t = t_{wave} = 8/f_c$, $t = 0.66L/a$ and $t = 0.9L/a$ (see Figure 7.4) with L=50m in these cases. As discussed earlier, for the case where f_c=1000Hz (UBFC<f_1), the classical 1D WH theory

is held (Figures 7.4a, 7.4b and 7.4c). However, for the case where f_c=3000Hz (see Figures 7.4d, 7.4e and 7.4f), both M0 and M1 are excited, but the amplitude of M0 is much smaller than M1 (see arrow in Figure 7.4f). In addition to M0 and M1, M2 is excited for the case f_c=5000Hz shown in Figures 7.4g-i and Figures 7.5 which is an enlarged version of Figure 7.4i for better visualization. In this case, it is first noticed that there exist a region (see arrows in Figure 7.5) where M2 is developed. It is clear that M2 propagates at slower speed than the two other modes as it is lagging behind M1 and M0 which is as expected from Eq. (2.120) and Figure 2.11 showing that the speed at which M2 propagates is slower. Second, it is seen that M1 spreads over a longer region for the case with f_c=5000Hz case (Figure 7.4i) than for the case with f_c=3000Hz (Figure 7.4f). This is because, from Figure 2.11, the UBFC of f_c=5000Hz case excites much faster M1 waves than for the case of f_c=3000Hz. A quick check using Figure 7.4h (f_c=3000Hz) shows that the leading M1 wave propagates at a speed of $0.65/(0.9/a) \approx 722$m/s. On the other hand, Figure 7.4i (f_c=5000Hz) shows that the leading M1 wave travels at $0.81/(0.9/a) \approx 900$m/s. Both speeds agree well with the theoretical speeds read from Figure 2.11 for which the speeds of leading M1 waves for the cases f_c=3000Hz (UBFC=1.5*3000=4500Hz) and f_c=5000Hz (UBFC=1.5*5000=7500Hz) are 735m/s and 913m/s, respectively. The agreement between computed and analytical group velocities testify to the fact that the scheme has little numerical dispersion. Such conclusion is key for the remaining analysis.

Figure 7.4 Surface plot of the pressure in the *r*-*x* surface plane when different central frequencies are used showing the behaviour of the excited high modes. For all cases D_s=0.1*D* and *L*=50m.

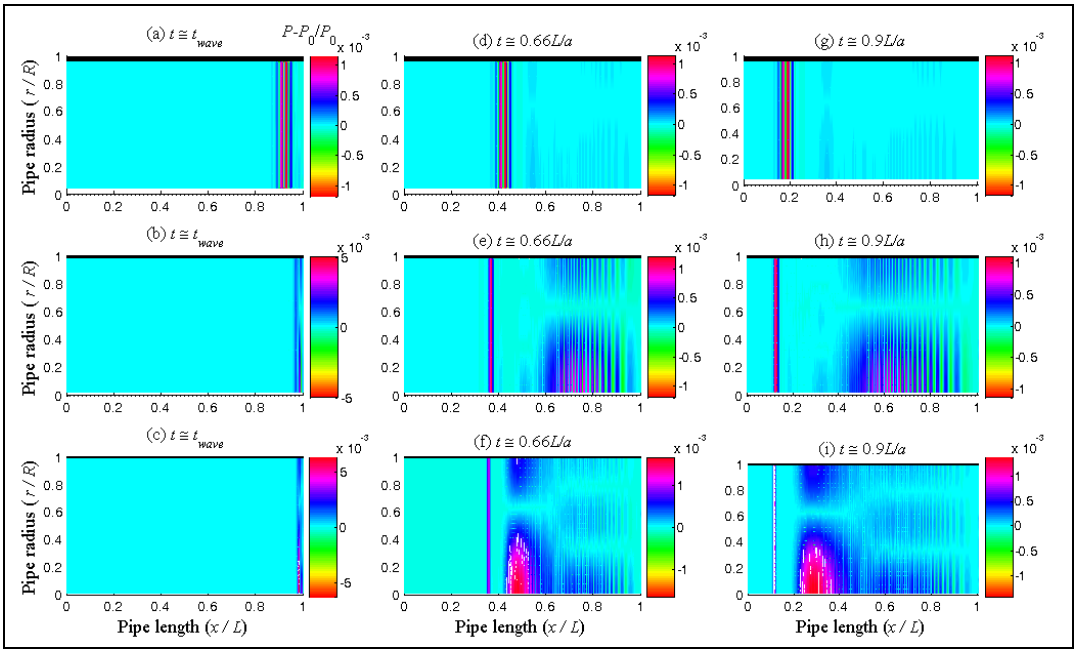

(a) Top left f_c=1000Hz ; $t \approx t_{wave}$

(b) Middle left f_c=3000Hz ; $t \approx t_{wave}$

(c) Bottom left f_c=5000Hz ; $t \approx t_{wave}$

(d) Top middle f_c=1000Hz ; $t \approx 0.66\ L/a$

(e) Middle middle f_c=3000Hz ; $t \approx 0.66\ L/a$

(f) Bottom middle f_c=5000Hz ; $t \approx 0.66L/a$

(g) Top right f_c=1000Hz ; $t \approx 0.9\ L/a$

(h) Middle right f_c=3000Hz ; $t \approx 0.9\ L/a$

(i) Bottom right f_c=5000Hz ; $t \approx 0.9\ L/a$

The analytical solution (Eq. (2.111)) shows that at any given x, the n-th mode (n = 1, 2,…) is standing radial wave with nodes located at $J_0(k_{rn}r)=0$. For example, M1 has one node at $k_{r1}r \approx 2.4048$ which gives $r \approx 0.627R$. In addition, M2 has two nodes: one at $r \approx 0.3427R$ and the other at $r \approx 0.787R$. These nodes are clearly shown in Figure 7.5. Figure 7.5 shows that there is a region where the node of M1 is clear which implies that M2 is negligible in this region.

Similarly, there is a region where the nodes of M2 are clear which implies that M1 is negligible in that region. Knowledge of the locations of these nodes could have important implications in locating sensors for transient-based defect detection methods (TBDDM). For example, locating a sensor at the nodes of M1 would mean that this sensor cannot provide information about this mode. Results of this nature are important to the theme-based project ([121]) led by the advisor of the author of this thesis.

Figure 7.5 An enlarged figure of Figure 7.4i which gives the case of pressure distribution in the *r*-*x* space plane when f_c=5000Hz, D_s=0.1*D* and *t*=0.9*L*/*a* to show in more details the pressure nodes and the mode forms.

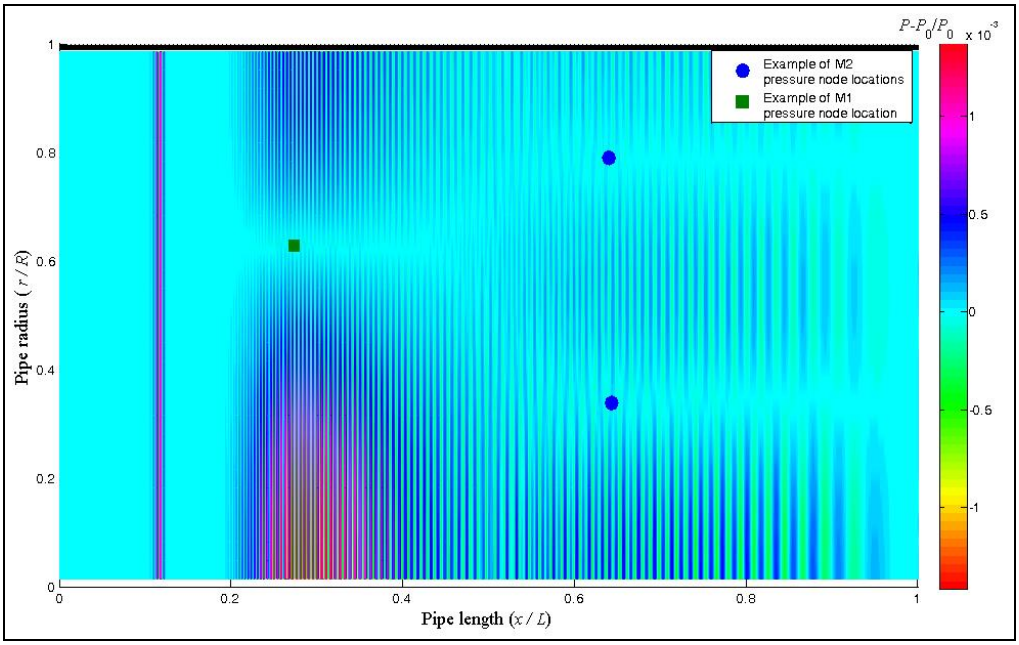

7.2.1.2. *Multi-path effect*

Figure 7.6 shows the energy flux with time at three different locations along the pipe ($x \approx L$-0.5m, $x \approx L/2$, $x \approx 0$) where f_c=3000Hz, the frequency band is [1500Hz, 4500 Hz] and D_s=0.1*D*. Waves with frequency in the range [1500 Hz to 3050 Hz (=f_1) [are WH waves and

propagate with speed of 1000m/s (see Figure 2.11). Frequencies in the range [3050Hz (=f_1) to 4500Hz] excite both M0 and M1 waves, where the group (energy) velocity of the M0 is 1000 m/s (Figure 2.11) while that of the M1 varies continuously from 0 to about 700m/s with frequency (see Figure2.11). That is, the energy of M0 leads that of the M1 when the frequency is in the range [3050Hz (=f_1) to 4500Hz]. The spatial separation between the fast propagating energy of M0 and the slow propagating energy of M1 is small near the wave source (Figure 7.6a) and grows with distance from the source (Figures 7.6b and 7.6c). In addition, due to the variation of the propagation angle of M1 waves (Eq. (2.122) and Figure 2.13), and by consequences their group velocity (Figure 2.11), with frequency, these waves experience significant spatial spread with time (Figures 7.6b and 7.6c). This spreading is due to the fact that M1 waves travel along zig-zag path (Figure 2.12) where waves at frequencies near f_1 (cut-off frequency of the first high mode) taking much longer path than those travelling at high frequencies. The fact that different wave modes acquire different paths is referred to as multipath process and is the reason why these waves are dispersive ([108]).

In practice, if one is interested in using high frequency waves for defect detection by injecting these waves in one location and collecting pressure measurement in another location, it is important to know how this multipath process influences measured signals. Therefore, the multipath effect is further analysed. Figure 7.6a shows that, close to the source location, most of the energy is propagating as unit (see also Figure 7.4d). However, in Figures 7.6b and 7.6c, the energy gets distributed with a pronounced tail and such tail grows longer and gets more uniform with distance from the source. It is observed from Figures 2.11 and 2.13 that for a given mode, the farthest away are the frequencies from the cut-off frequency, the more uniform are the group velocity and the propagation angle, respectively. In the frequency region where the group velocity does not vary much with the frequency, the energy at different frequencies travels at nearly the same speed (Figures 7.6b and 7.6c). However, as time increases considerably while waves are propagating, even small variations in group velocity could lead to significant spread of energy along the pipe. By consequences, the wave magnitude gets reduced with time and could eventually become of the same order as noise or even lower. Therefore, it is crucial that measurements are taken (i)

over a long enough time to ensure that the whole wave passes through and (ii) not too far away from the source to ensure that they do not become "buried under noise".

Figure 7.6 Energy flux computed numerically for the case of f_c=3000Hz and D_s = 0.1D showing how energy spreads with distance from the source. For all cases L=10m.

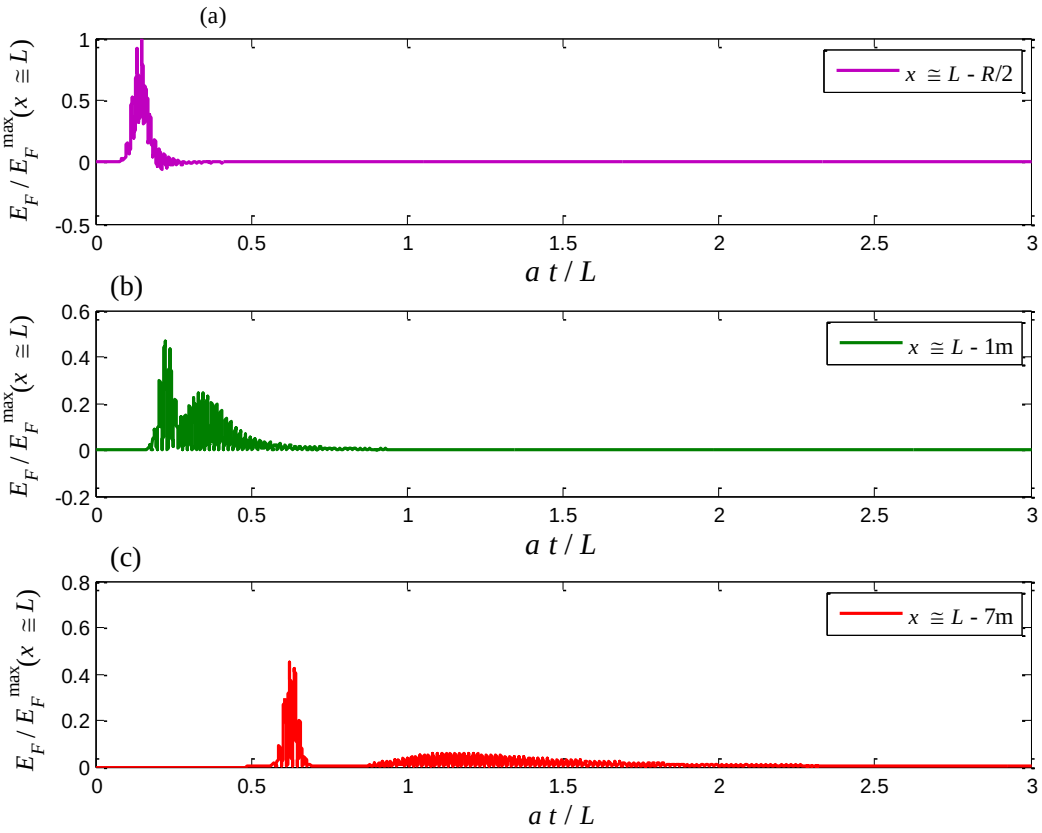

(a) Top **At near the source (at x=L–R/2)**

(b) Middle **At 1m away from the source**

(c) Bottom **At 7m away from the source**

7.2.1.3. *Effect of the transient source size*

In all the previous test cases, the source diameter was fixed at D_s=0.1D. In what follows, the effect of the source size on the wave dispersion behaviour is studied. This is an important parameter in the selection of a wave generator. In Figures 7.7 and 7.8 three tests are conducted each with different source diameter D_s=D, 0.5D and 0.1D. The central frequency is fixed to f_c=3000Hz. The total energy (potential and kinetic) along the pipe for these tests is given in Figure 7.9. The results show that when D_s=D (Figure 7.7a and 7.8a), the signal propagates as a plane wave (M0) despite the fact that the waves with frequencies in the range [f_1=3050Hz, 4500Hz] all exceed f_1. The reason is that the wave generator, having the same diameter as the pipe, transmits signals that are independent of radius; thus, radial waves are not excited. However, if the M0 waves with frequencies higher than f_1 meet any non-uniformity in the pipe, M1 gets excited. For the cases where D_s=0.5D and D_s=0.1D (see Figures 7.7b and 7.7c and Figures 7.8b and 7.8c), M1 is excited. However, in the D_s=0.5D case, more energy is carried by M0 (Figure 7.9b) in comparison with the D_s=0.1D case (Figure 7.9c). Therefore, the magnitude of the radial scale of the wave source has significant influence on how the input energy gets distributed over the different excited modes. Figure 7.9 shows that the smaller the source diameter, the less energy is carried by M0. In fact, as seen from Figures 7.10a and 7.10b, which are magnified versions of Figures 7.7b and 7.7c, M0 gets separated from M1 as it propagates at a faster speed (Eq. (2.120)), and it is very clear that the amplitude of M0 is much smaller for the D_s=0.1D case (Figure 7.10b) in comparison with the D_s=0.5D case (Figure 7.10a).

This could be important since previous work on TBDDM were based on plane wave assumption ([32], [35], [70]; [79]). If one is able to develop TBDDM based on the measurement of M0 waves alone, the use of small sized source will make the amplitude of M0 waves very small, making these waves susceptible to turbulence dissipation, and thus, undetectable. A discussion of the propagation range of HFW modes is given in later discussion where viscous laminar flow is considered.

As the injected FBW contains the cut-off frequency of the excited high mode, the tail of energy of the high mode extends from the source location to the measurement location

(Figure 7.8) because the group velocity at the cut-off frequency is zero (Figure 2.11). In this case, it takes, theoretically, infinite time to measure all the energy at a location away from the source (Figure 7.6). The case where the FBW does not contain the cut-off frequency of the excited high mode is discussed later (see Section 7.2.2).

Figure 7.7 Dimensionless pressure variation with time measured near the source and at 7m away from the source and at the pipe centreline. For all cases f_c=3000Hz, $r \approx 0$ and L=10m.

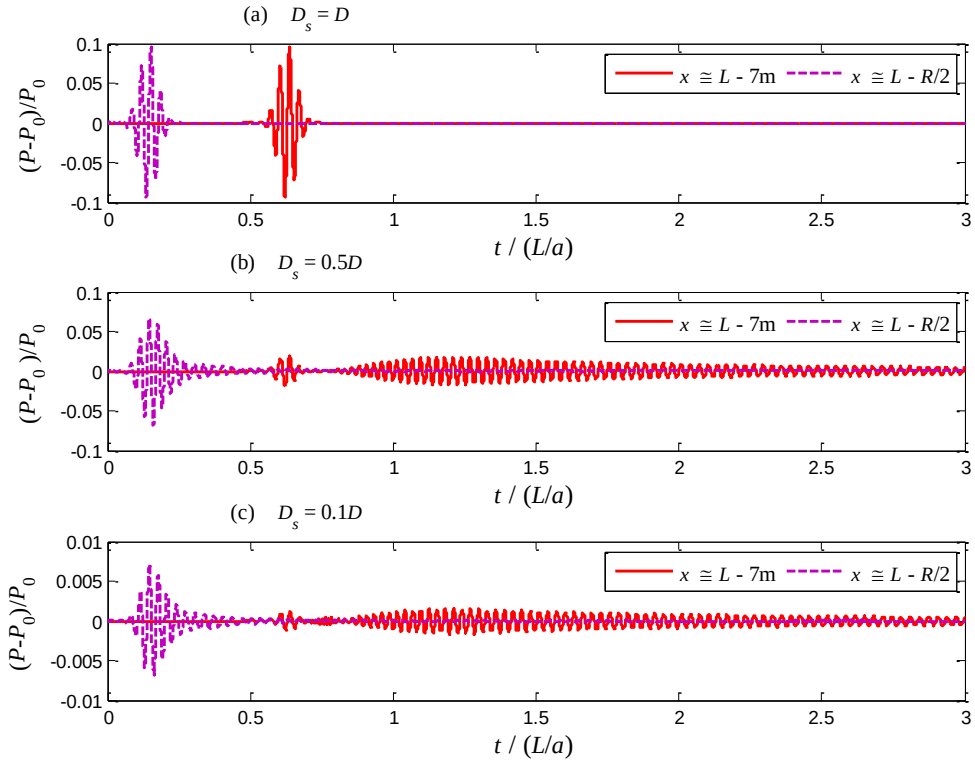

(a) Top $D_s = D$

(b) Middle $D_s = 0.5D$

(c) Bottom $D_s = 0.1D$.

Figure 7.8 Amplitude in the frequency domains corresponding to the pressure signals in Figure 7.7 measured near the source and at 7m away from the source and at the pipe centreline. For all cases f_c=3000Hz, $r \approx 0$ and L=10m.

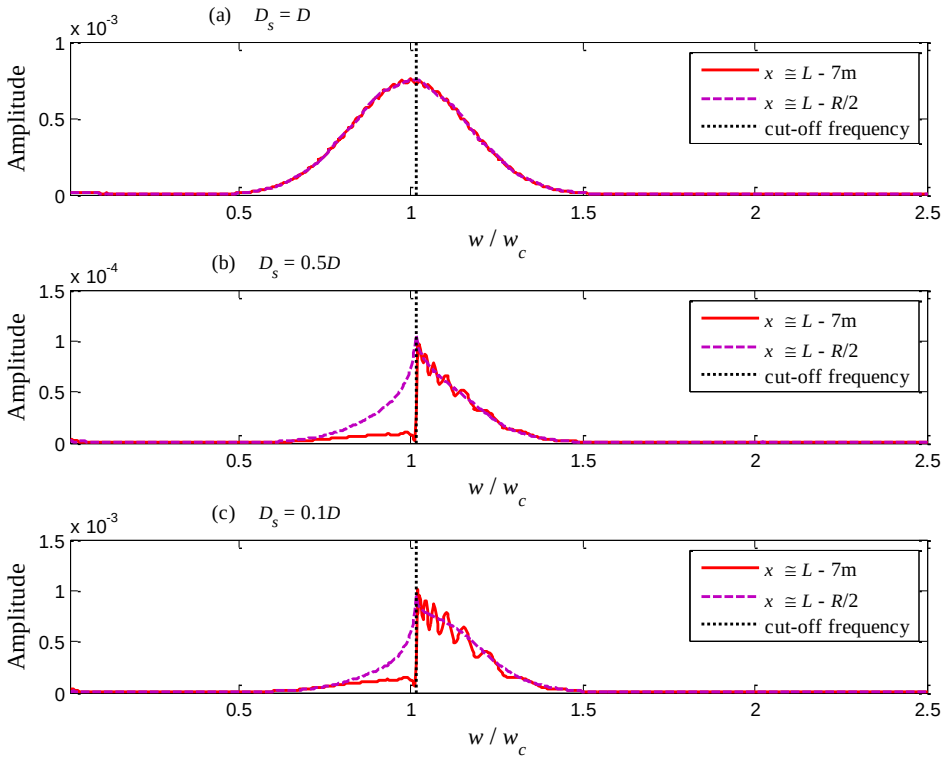

(a) Top $D_s = D$

(b) Middle $D_s = 0.5D$

(c) Bottom $D_s = 0.1D$.

Figure 7.9 Dimensionless energy distribution along the pipe axis for different source. For all cases f_c=3000Hz and L=10m.

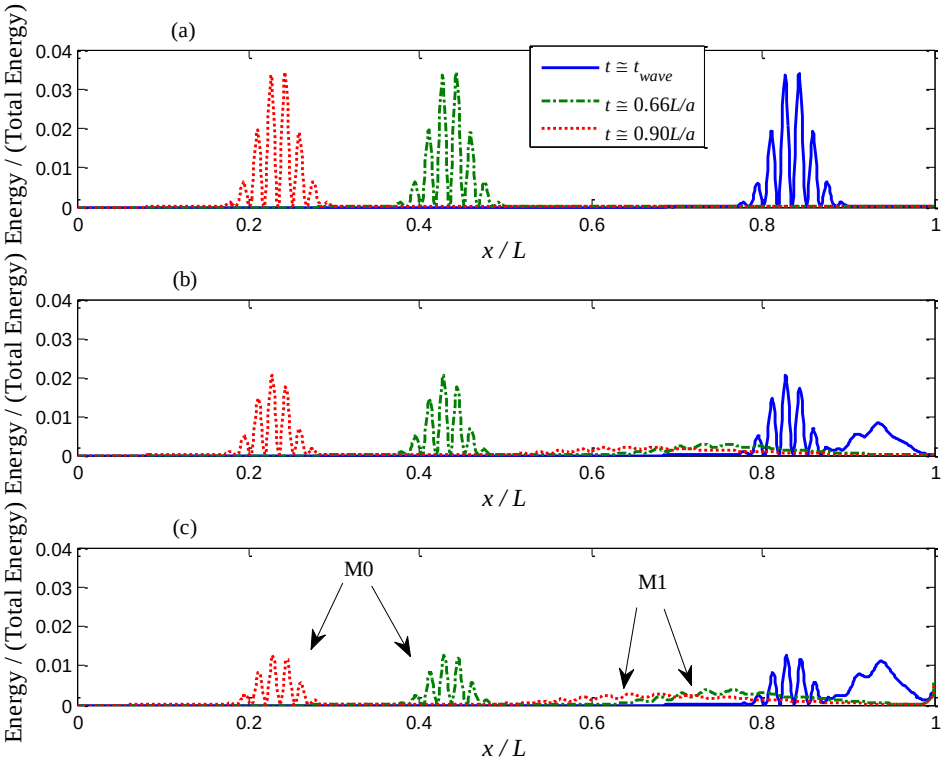

(a) Top $D_s = D$

(b) Middle $D_s = 0.5D$

(c) Bottom $D_s = 0.1D$.

Figure 7.10 Magnified versions of Figures 7.7b and 7.7c showing the separation of the plane mode (fundamental mode M0) from the higher mode at about 7m away from the source.

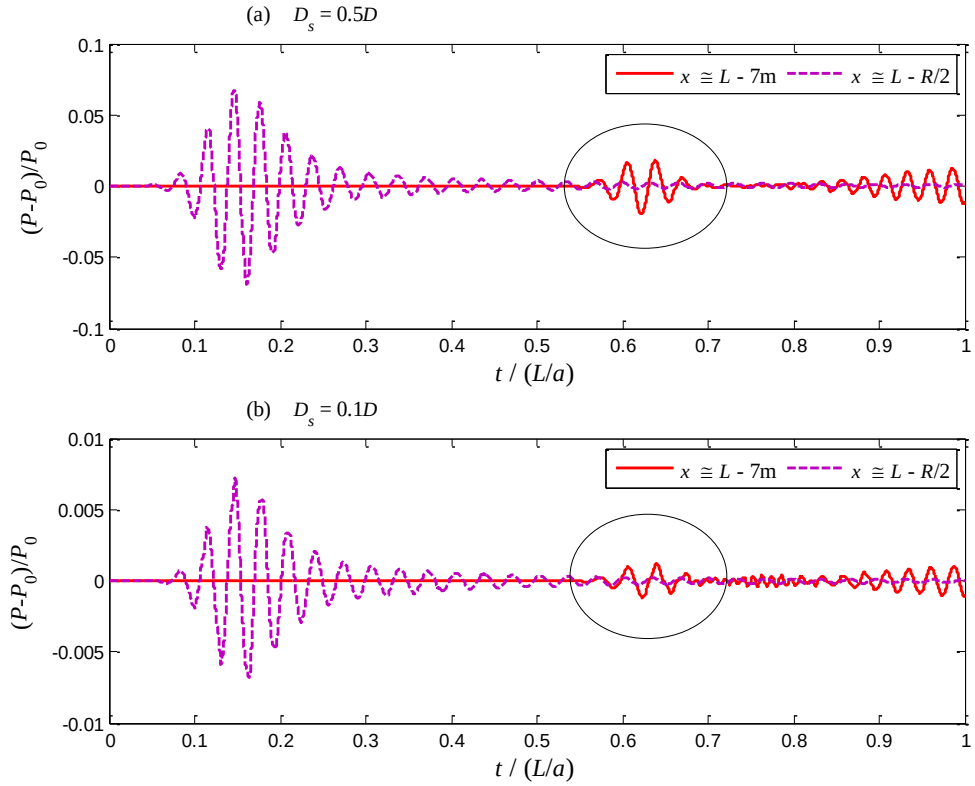

(a) Top **D_s = 0.5D**

(c) Bottom **D_s = 0.1D.**

7.2.2. High frequency waves behaviour under non-resonating probing source

In previous test cases, the FBW included the cut-off frequencies at which resonance occurs. Their inclusion helped to validate the physical behaviour of the numerically-modelled high frequency waves where resonance occurs (see Figures 7.3 and 7.8). However in practice, the FBW should not include the resonant frequencies to avoid damage to pipes. In this section, similar numerical tests as presented above are studied but with narrower FBW of an injected waveform that does not include any cut-off frequency. Such waveform and FBW are shown

in Figure 3.9 where $\beta = 80\pi$ and shows that the FBW is within about [0.9f_c to 1.1f_c]. Two central frequency cases are considered: (i) f_c=6800Hz which excites three modes (M0, M1 and M2) (see Figure 2.11), and (ii) f_c=4000Hz which excite only two modes (M0 and M1) (see Figure 2.11).

The plane wave mode propagates at the acoustic wave speed a=1000m/s. However, the energy of high mode waves travel at the group velocity (see Figure 2.11) which is bounded within the interval [$V_{gn}^{\min}$, $V_{gn}^{\max}$] where $V_{gn}^{\min}$ and $V_{gn}^{\max}$ are the minimum and maximum group velocity of the n-th excited high mode. The maximum and minimum group velocities could be determined from Eq. 2.120 or Figure 2.11 using the lower and upper bound of the FBW, respectively. For f_c=4000Hz, the M1 group velocity varies within [$V_{g_1}^{\min}$ = 532m/s , $V_{g_1}^{\max}$ = 721m/s], whereas for f_c=4000Hz, M1 and M2 group velocity varies within [$V_{g_1}^{\min}$ = 867m/s , $V_{g_1}^{\max}$ = 913m/s] and [$V_{g_2}^{\min}$ = 411m/s , $V_{g_2}^{\max}$ = 666m/s], respectively.

The pipe diameter D is fixed to 0.4m whereas the pipe length L is 100m for the cases of f_c=6800Hz and 180m for f_c=4000Hz case. The source has a cylindrical shape with diameter D_s=0.2D located at the pipe centreline (r = 0) and at $x = L$ (see Figure 7.1).

For some test cases, viscous flow is considered but only at laminar regime (Reynolds number R_e <1300) to study the effect of multi-path on dissipation. Note, unless explicitely stated, the fluid is assumed inviscid.

7.2.2.1. Modes separations

Figure 7.11 shows the pressure variation with time for f_c=6800Hz where M0, M1 and M2 are excited as expected from Figure 2.11. Due to the group velocity difference at different modes (Figure 2.11), separations of these modes occur as shown in Figure 7.11. The position at which the n-th mode separates from all other excited modes is given as follows:

$$\frac{x_n^s}{V_{g_n}^{\max}} = \left(\frac{x_n^s}{V_{g_{n-1}}^{\min}} + t_{wave} \right) \qquad (7.1)$$

which states that the slowest propagating wave of the (n–1)-th mode catches up with the fastest propagating wave of the n-th mode arrive at x_n^s. Equation (7.1) leads to

$$x_n^s = \frac{t_{wave}}{\left(\frac{1}{V_{g_n}^{\max}} - \frac{1}{V_{g_{n-1}}^{\min}} \right)} \qquad (7.2)$$

where x_n^s is the position at which the modes n and (n-1) get separated; and t_{wave} (see Eq. (3.42)) is the duration of the injected transient wave at the source which is about 0.005s when measured from Figure 3.9. Applying Eq. (7.2) to M2 gives x_2^s=0.005/(1/666–1/867) ≈ 14.3m, and this is why in Figure 7.11a, M2 looks separated from M0 and M1 at about 15m away from the source. For M1 case, Eq. (7.2) gives x_1^s = 0.005/(1/913–1/1000) ≈ 52.5m which agrees with Figure 7.11b which shows that M1 gets separated from M0 at about 50m away from the source.

Figure 7.12 gives the total area-averaged energy distribution along the pipe at the time t=0.7L/a (Figure 7.12a) and the energy flux variation with time for the case of f_c = 6800Hz measured at 50m away from the source (Figure 7.12b). Figure 7.12a shows that the energy distribution of the n-th excited mode is bounded by the location where the fastest and slowest waves at the n-th mode, travelling respectively at $V_{gn}^{\max}$ and $V_{gn}^{\min}$, are located at a given time. Figure 7.12b shows that it takes a finite time to measure the whole injected energy at a given location away from the source which depends on the time it takes for the slowest wave at the highest excited mode to reach the measurement location. Such time is given by $x^{mes} / V_{gn_h}^{\min}$ where x^{mes} is the measurement location away from the source and n_h is the highest excited mode number. For f_c=6800Hz case, the highest excited mode is M2 and therefore the whole injected energy is measured at 50m away from the source within 50/411/(L/a) ≈ 1.22 L/a as shown in Figure 7.11c and Figure 7.12b. This is in contrast with the case of resonating

probing wave (see Section 7.2.1) where the tail of the energy extends from the source location to the measurement location (Figure 7.8) because the group velocity near cut-off frequency is too small and zero at the cut-off frequency (Figure 2.11), and where it takes, theoretically, infinite time to measure all the energy flux at a location away from the source (Figure 7.6).

Notice in Figure 7.11 that M2 waveform is more elongated to the right hand side (slower waves) than to the left hand side (faster waves) whereas M0 and M1 waveforms are not. Since the waveform symmetry is with respect to the central frequency f_c, therefore, this deformation feature of the waveform is due to the difference between the rates of dispersion of the waves travelling at frequencies higher than f_c (fast propagating waves) and those travelling at frequencies lower than f_c (slow propagating waves) (see Figure 2.11). To explain this feature, a magnified portion of Figure 2.11 is shown in Figure 7.13 which gives the group velocity variation with the non-dimensional frequency (f / f_c; where f_c=6800Hz). Approximating the variation of group velocity to the left and to the right side of the central frequency by an average linear variation, Figure 7.13 shows that the slope of M2 group velocity is steeper to the left side of the central frequency than to the right side, whereas the variation in slope of the group velocity is almost the same for M1. The slope of the group velocity of the fast propagating waves (to the right of the central frequency (see Figure 7.13)) dictate the rate at which a high mode separate from M0. The difference between the group velocity slopes of the fast propagating M1 and M2 waves dictates the rate at which these two modes separate.

If the central frequency of the injected wave is reduced to a region where M1 group velocity varies more non-linearly (see Figure 2.11), M1 waveform would undergo severe distortion. For example, Figure 7.14 gives the case of for f_c=4000Hz where only M0 and M1 are excited and shows that, similarly to M2 waveform, M1 waveform is deformed and no longer symmetric (see Figure 7.11c and Figure 7.14c).

Figure 7.11 Variation of the pressure signal at the centreline with time for the case f_c=6800Hz where M0, M1 and M2 are excited.

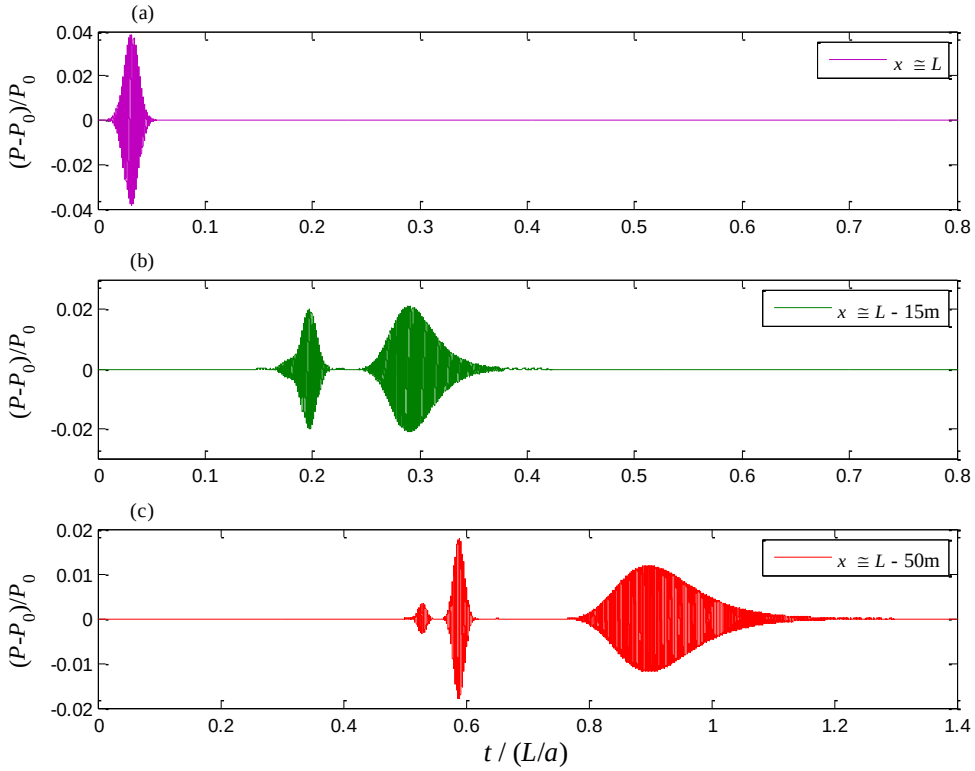

(a) Top **At $x \approx L$ (near the source)**

(b) Middle **At 10m away from the source**

(c) Bottom **At 50m away from the source**

Figure 7.12 Distribution of the area-averaged energy along the pipe and the variation of energy flux with time for the case f_c=6800Hz.

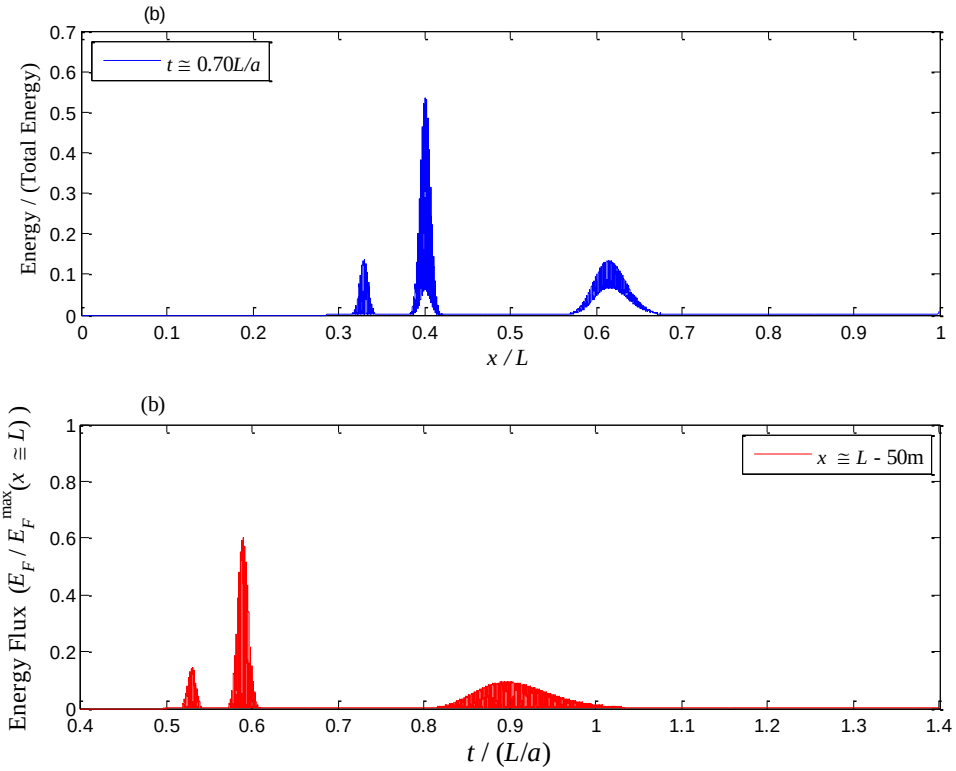

(a) Top **Total area-averaged energy distribution along pipe at the time t=0.7L/a**

(b) Bottom **Energy flux variation with time for the case of f_c = 6800Hz measured at 50m away from the source.**

Figure 7.13 Group velocity variation with the non-dimensional frequency (f / f_c; where f_c=6800Hz) showing how the M2 group velocity variation is steeper to the left side of the central frequency than to the right side, whereas the variation slope is almost the same for M1.

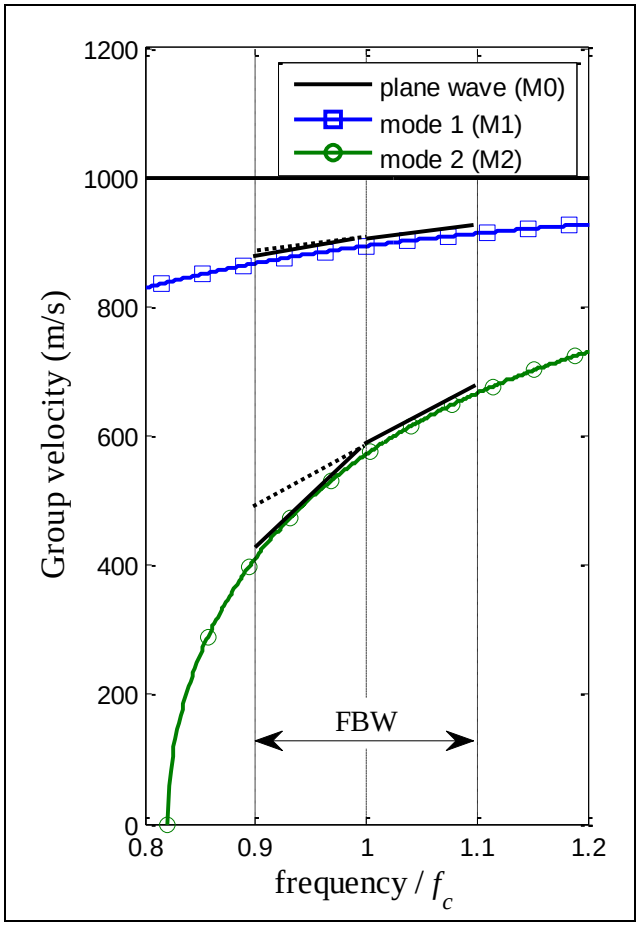

Figure 7.14 Variation of the pressure signal at the centreline with time for the case f_c=4000Hz where only M0 and M1 are excited.

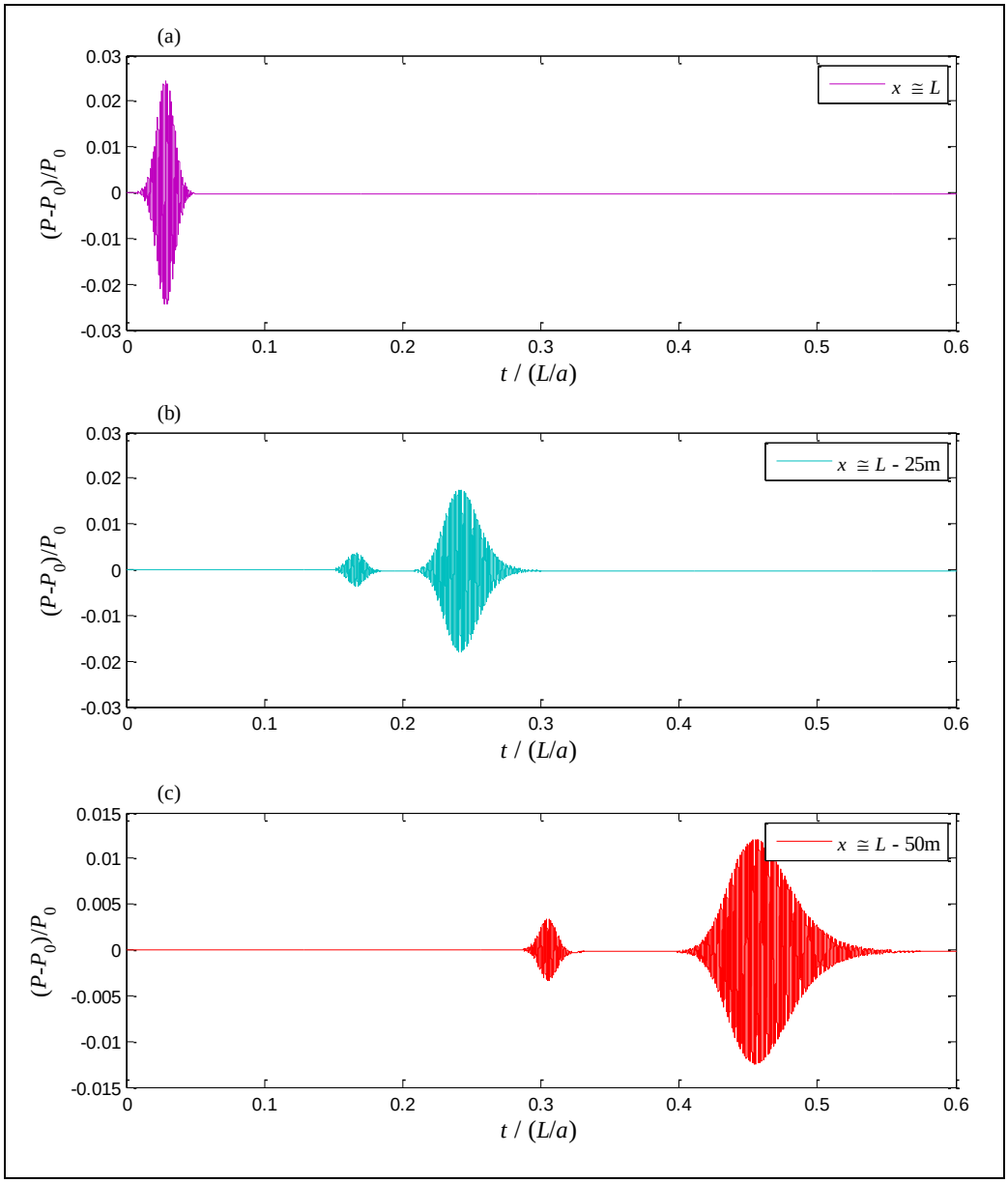

(a) Top **At $x \approx L$ (near the source)**

(b) Middle **At 25m away from the source**

(c) Bottom **At 50m away from the source**

7.2.2.2. *Energy propagation range of high modes*

Figure 7.15 gives the area-averaged energy flux variation with time at 15m (Figure 7.15a) and 50m (Figure 7.15b) away from the source for f_c=6800Hz case. Figure 7.15b shows that the injected energy is carried by three propagating modes. The energy distribution among the different modes is affected by the source size (D_s) (see Section 7.2.1.3). The energy conveyed by M0, M1 and M2 are about 8%, 42.3% and 47.22% of the total injected energy, respectively. This shows how most of the energy is conveyed by the high modes. However, since high modes are dispersive, the farther away from the source, the more the energy is spread (Figure 7.15 and Figure 7.6). The combined effect of energy spreading with time and energy conservation means that the maximum energy amplitude (MEA) decreases with distance from the source (see Figure 7.15).

Although almost half of the energy is conveyed by M2, because of its high dispersion rate, Figure 7.15 shows that the M2 MEA reduces severely and becomes smaller than that of M0 at 50m away from the source (see Figure 7.15b). On the other hand, even though M1 conveys almost the same amount of energy carried by M2, but since its dispersion rate is lower (ses previous section), its energy spreads less than M2 energy does at a given location away from the source (Figure 7.15b). As a result, the M1 MEA is higher than that of M2 (Figure 7.15b), and therefore, M1 waves are able to propagate over larger range.

Since M0 is non-dispersive, its propagation range could only be affected by the presence of viscous dissipation. However, the propagation ranges of high modes are affected by both dispersion and viscous dissipation. It is therefore important to know at which measurement location away from the source the MEAs of an excited high mode and M0 would have similar order of magnitude. This and the knowledge of the rate of viscous dissipation, would allow predicting which high modes could propagate farther than M0 and which does not. Such predictions could help in designing the location of measurements.

Figure 7.15 Energy flux variation with time for the case of f_c = 6800Hz

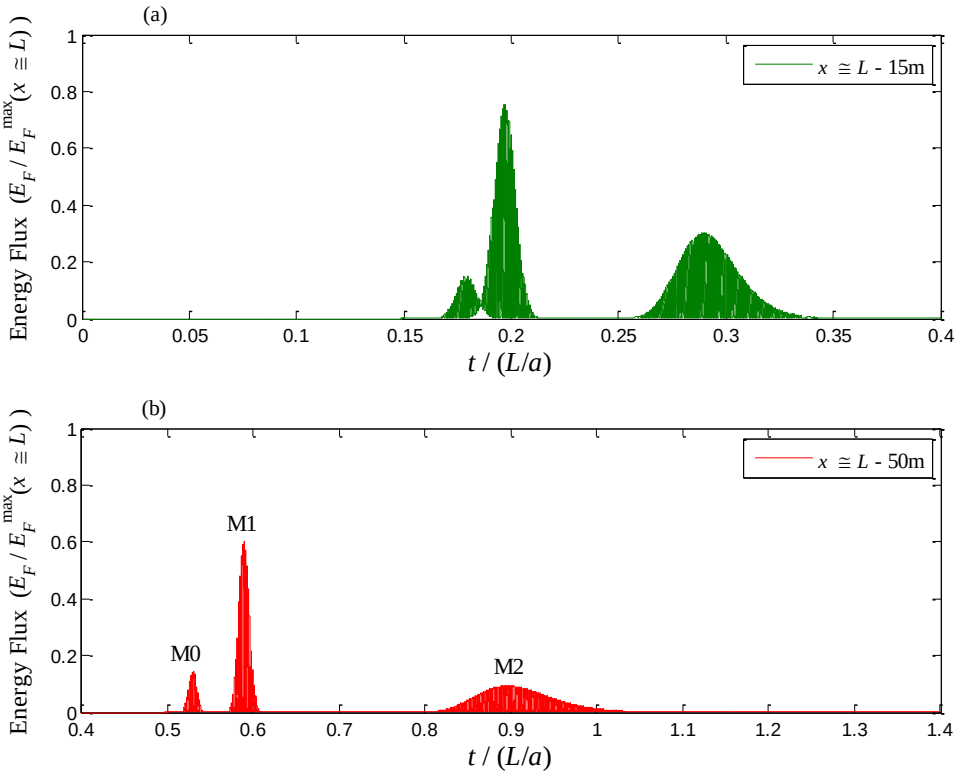

(a) Top **At 15 away from the source**

(b) Bottom **At 50m away from the source**

For this reason, the propagation range of a given *n*-th high mode with respect to M0 is defined by the location away from the source at which MEA of M0 and the *n*-th high mode are the same. Denoting by Ψ_n the ratio of MEA between the *n*-th high mode and M0 measured at the location x_n^s (see Eq. (7.2)). To obtain an approximate order of magnitude of the position x_n^r away from the source where the MEAs of the *n*-th high mode and M0 have about the same magnitude, energy conservation requires that the energy spreads by a similar factor Ψ_n. That is:

$$\left(\frac{x_n^r}{V_{g_n}^{\min}}-\frac{x_n^r}{V_{g_n}^{\max}}\right)=\Psi_n t_n^s=\Psi_n\left(\frac{x_n^s}{V_{g_n}^{\min}}-\frac{x_n^s}{V_{g_n}^{\max}}\right) \quad (7.3)$$

where t_n^s denote the spreading time of the energy flux of the n-th high mode at x_n^s. Equation (7.3) leads to

$$x_n^r=\frac{\Psi_n t_n^s}{\left(\frac{1}{V_{g_n}^{\min}}-\frac{1}{V_{g_n}^{\max}}\right)}=\Psi_n x_n^s \quad (7.4)$$

Applying Eq. (7.4) to M2 in Figure 7.15a gives

$$x_2^r=\Psi_2 x_2^s\approx 2.48\times 14.3\approx 35.5\text{m} \quad (7.5)$$

Figure 7.16 gives the total energy (integrated with respect to the cross sectional area) distribution along the pipe at the time when M0 and M2 have about the same MEAs and shows that M2 waveform is centred at about 38.5m which is close to what was predicted from Eq. (7.5). Applying Eq. (7.4) to M1 in Figure 7.15b gives

$$x_1^r=\Psi_1 x_1^s\approx 4.18\times 52\approx 220\text{m} \quad (7.6)$$

where Ψ_1 is measured from Figure 7.15b. In this case x_1^r =220m > L=100m and it is computationally very time consuming to simulate very long pipe using high frequencies. Therefore, it is difficult to check the approximated x_1^r for f_c=6800Hz case. In order to study the dispersion of M1, the test case with f_c=4000Hz and pipe length L=180m is used where only M0 and M1 are excited. Figure 7.17 gives the energy flux variation with time at different locations for the case of f_c=4000Hz. Figure 7.17c shows that the MEAs of M0 and M1 becomes of same magnitude at about 80m. Applying Eq. (7.4) for this case gives

$$x_1^r=\Psi_1 x_1^s\approx 3\times 23.2\approx 70\text{m} \quad (7.7)$$

Although x_1^r is lower than 80m, but Figure 7.17b shows that at x_1^r = 70m away from the

source, the M1 and M0 MEA have about the same order of magnitude. The reason why x_n^r does not give the exact value where a given high mode has the same MEA of that of M0, is because Eq. (7.4) assumes linear spreading whereas the true spreading is not linear (see Figure 2.11 and Figure 7.13). The difference between the assumed and the true spreading is sketched in Figure 7.18. However, Eq. (7.4) gives reliable and quick estimate of the energy amplitude with time.

Figure 7.16 Total energy (integrated with respect to the cross sectional area) distribution along pipe axis at the time when M0 and M2 have the same MEA.

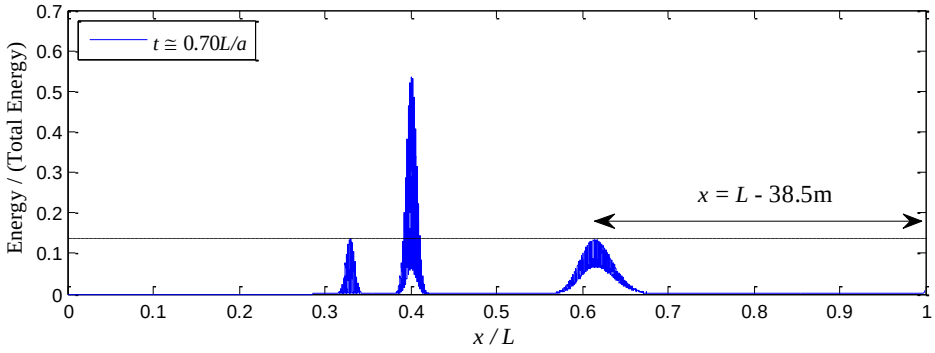

Figure 7.17 Energy flux variation with time for the case of f_c = 4000Hz and L=180m.

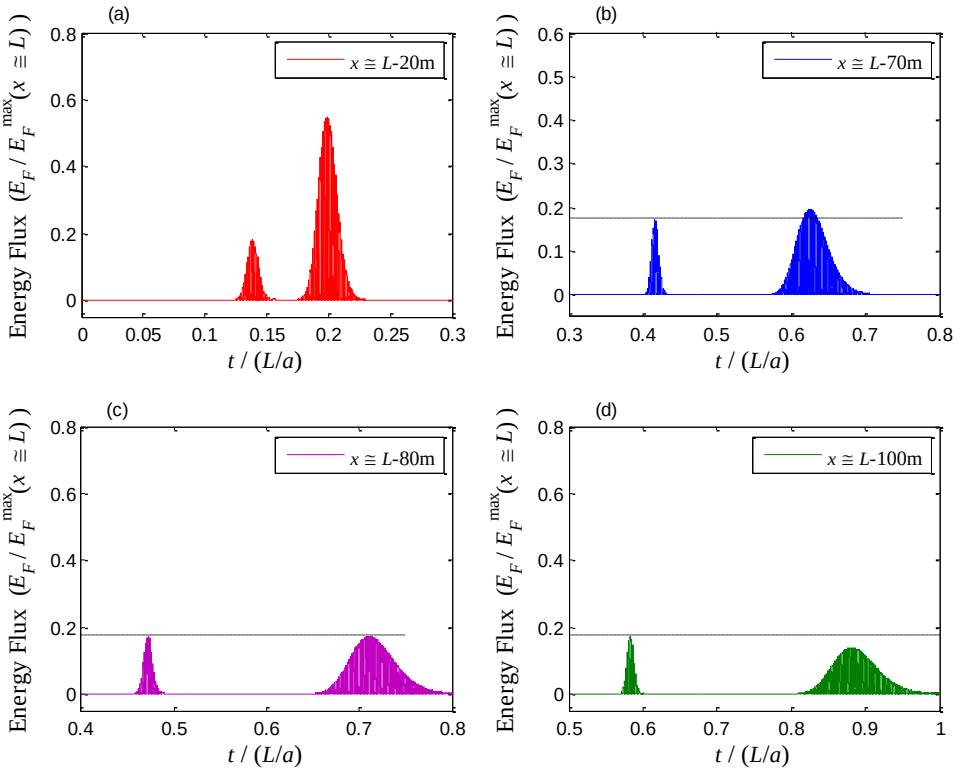

(a) Top left **At 20m away from the source**

(b) Top right **At 70m away from the source**

(c) Bottom left **At 80m away from the source**

(d) Bottom right **At 100m away from the source**

Figure 7.18 Comparison between the true spreading behaviour and the linear spreading assumed in Eq. (7.4).

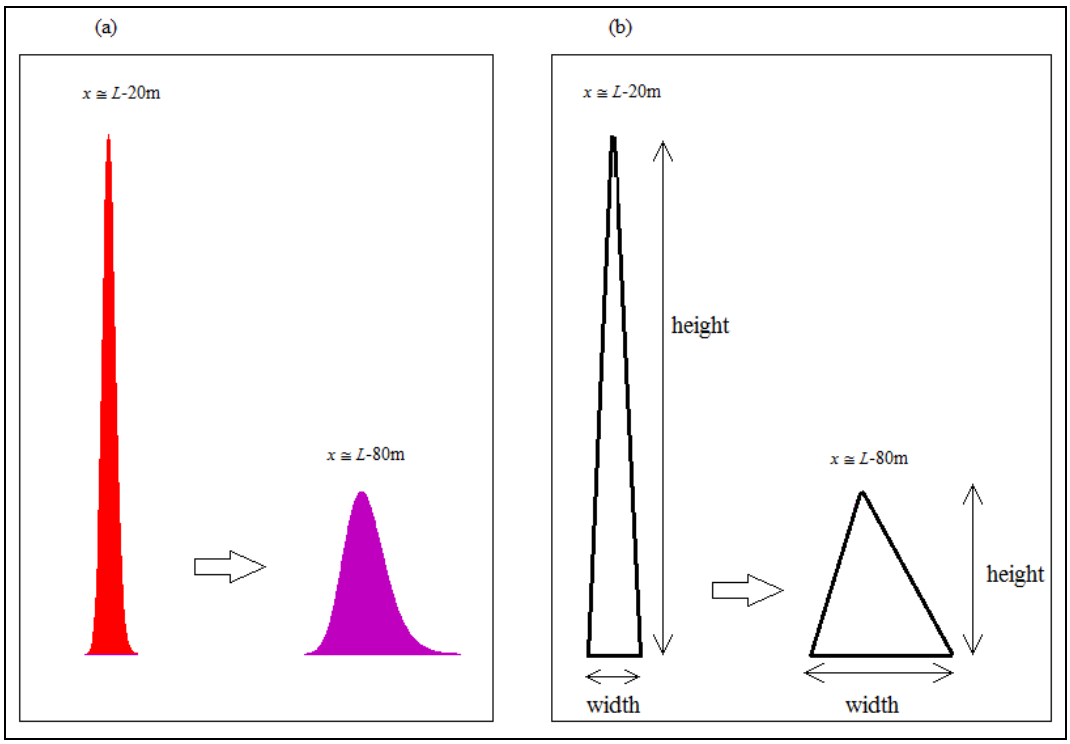

(a) Top **M1 energy flux spreading from measurement at 20m to 80m from the source (f_c=6800Hz)**

(b) Bottom **Sketch of linear spreading assumption**

7.2.2.3. Effect of multi-path on dissipation

Waves at higher modes take longer paths to traverse a given section of a pipe than waves at lower modes. This is the multi-path process discussed earlier in this chapter. Naturally, one should expect that waves which take longer paths to traverse a given section of a pipe would exhibit more energy losses due to friction. It is noted that this effect is found to be important in the field of ocean acoustics (e.g. [24], [46], [47], [49], [61] and [66]). To investigate this phenomena in water supply systems, a viscous fluid is considered in this section where viscosity is treated as a parameter. For stagnant flow (e.g., state of the flow late at night), the

viscosity is $\nu = 10^{-6}$ m^2/s. For normal operating condition where the flow is turbulent, the eddy viscosity is of the order of $(f_v / 8)^{0.5} VD$ in which f_v is the friction factor, D is the pipe diameter and V is the average water speed along the pipe. For typical values of f_v, D and V, the eddy viscosity varies from about $\nu = 10^{-3}$ m^2/s to about $\nu = 10^{-2}$ m^2/s. These ranges are investigated in this section.

Figure 7.19 gives the energy flux variation with time for the case of viscous flow, f_c = 4000Hz, L = 180m. In this case, the kinematic viscosity is $\nu = 10^{-3}$ (m^2/s). Figure 7.19 shows that M0 and M1 have similar MEA at 70m from the source which implies that weak viscous effect ($\nu \le 10^{-3}$ (m^2/s)) does not change too much the range of propagation. However, Figure 7.20 gives the case for $\nu = 10^{-2}$ (m^2/s) and shows that the two modes have similar MEA at about x = 45m away from the source which is almost half the distance for the inviscid case (Figure 7.20c). In fact, using the MEA ratio (Ψ_1) between M0 and M1 for the case of viscous flow with $\nu = 10^{-2}$ (m^2/s) gives $x_1^r = \Psi_1 x_1^s \approx 1.9 \times 23.2 \approx 44$m which shows that Eq. (7.4) is still approximately valid for viscous (laminar) cases.

Figures 7.20c and 7.20d show that at either 70m (Figure 7.20c) or 80m (Figure 7.20d) away from the source, M1 MEA is much smaller than M0. This demonstrates that as the viscous effect increases, it affects the propagation ranges of higher modes more than lower modes. For example, for the case of $\nu = 10^{-2}$ (m^2/s), D_s = 0.2D and f_c=4000Hz (see Figure 7.20), the computed viscous dissipation rate of the total energy carried by both M0 and M1 is about 21% at 10m away from the source. However, if instead, the total energy is carried by M0 only (considering D_s=D case), the computed viscous dissipation rate of the total energy is found to be only about 13.2% at 10m away from the source. This difference in dissipation rate is because high modes take longer path than lower modes, and therefore, dissipate more energy. To quantitatively explain the dissipation rate difference, denote by t_n^E the time at which the n-th mode energy reaches a measurement location x_n^{mes} which is given as follows

$$t_n^E = \frac{x^{mes}}{V_{gn}} \qquad (7.8)$$

and using Eqs. (2.120) and (2.122), yields

$$t_n^E = \frac{x^{mes}}{a}\frac{1}{\cos(\theta_{kn})} = t_0^E \frac{1}{\cos(\theta_{kn})} \qquad (7.9)$$

Eq. (7.9) shows how high modes energy propagate over longer time due to the longer path it takes with respect to the M0 energy path. Assuming that the difference in energy dissipation rate is only due to the propagation time ratio from Eq. (7.9), the viscous dissipation rate of the n-th mode ς_n is given by

$$\varsigma_n = \frac{\tau_\nu}{\cos(\theta_{kn})} \qquad (7.10)$$

where τ_ν denote the viscous dissipation rate of the plane wave mode. Using, Eq. (7.10), the total energy dissipation (E_ν) is

$$E_\nu = \sum_n \varsigma_n E_n = \tau_\nu \sum_n \frac{E_n}{\cos(\theta_{kn})} \qquad (7.11)$$

Applying Eq. (7.11) to the case of $\nu = 10^{-2}$ (m^2/s), D_s=0.2D and f_c=4000Hz (see Figure 7.20), and assuming that, on average, the whole energy is propagating at the central frequency for which the M1 propagation angle is $\theta_{k1}^c \approx 5\pi/18$ degrees, gives

$$\frac{E_\nu}{E_T} = \left[\frac{E_0}{E_T} + \frac{E_1/E_T}{\cos(\theta_{k1}^c)}\right]\tau_\nu \qquad (7.12)$$

where E_T is the total injected energy from the source. The energy carried by M0 (E_0) and M1 is (E_1) are obtained from the inviscid flow case (see Figure 7.17) which are E_0 =16.75% and E_1 =83.25% of the total energy, respectively. Inserting these M0 and M1 energy values into Eq. (7.12) to compute the dissipation for the viscous case with $\nu = 10^{-2}$ (m^2/s), gives

$$\frac{E_\nu}{E_T} = \left[0.1675 + \frac{0.8325}{\cos(5\pi/18)}\right]0.132 = 19.3\% \qquad (7.13)$$

which is very close to the above 21% energy dissipation measured for the case in Figure 7.20.

Figure 7.19 Energy flux variation with time for the case of viscous flow with kinematic viscosity $\nu = 10^{-3}\left(\mathrm{m}^2/\mathrm{s}\right)$, f_c = 4000Hz, L=180m.

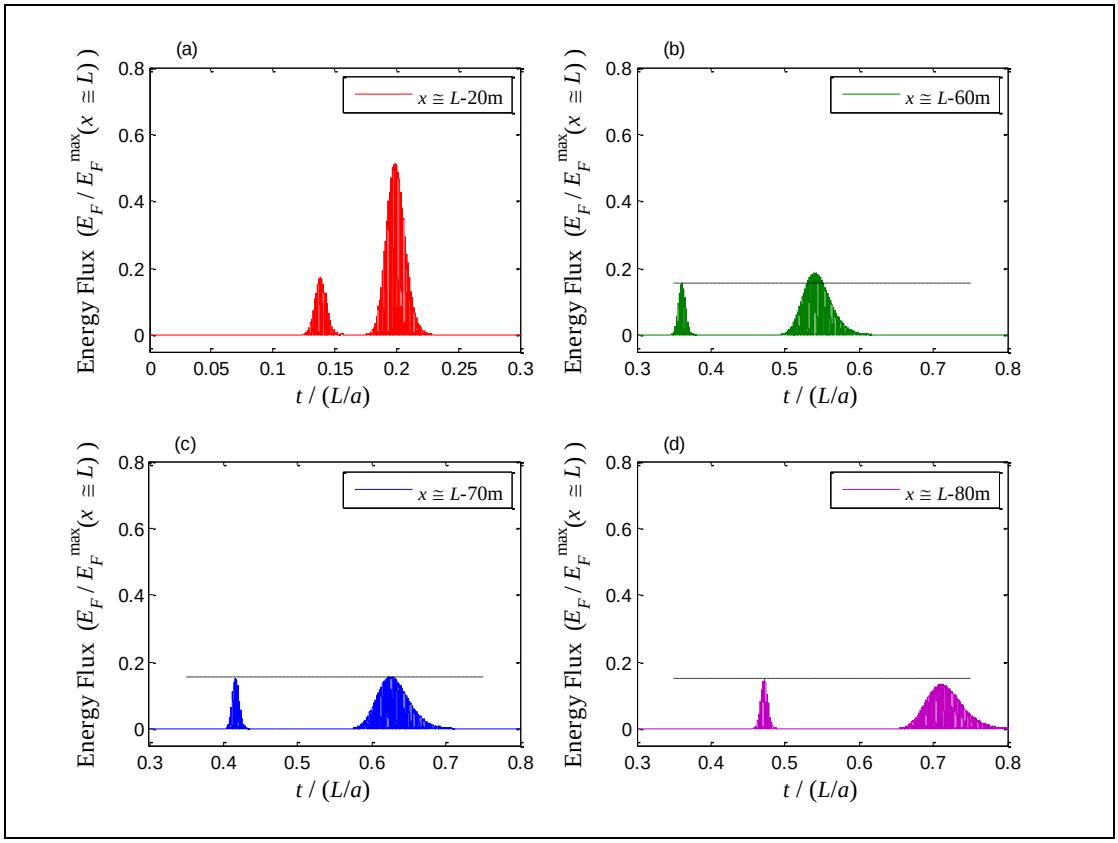

(a) Top left **At 20m away from the source**

(b) Top right **At 60m away from the source**

(c) Bottom left **At 70m away from the source**

(d) Bottom right **At 80m away from the source**

Figure 7.20 Energy flux variation with time for the case of viscous flow with kinematic viscosity $\nu = 10^{-2}$ (m²/s), f_c = 4000Hz, L=180m.

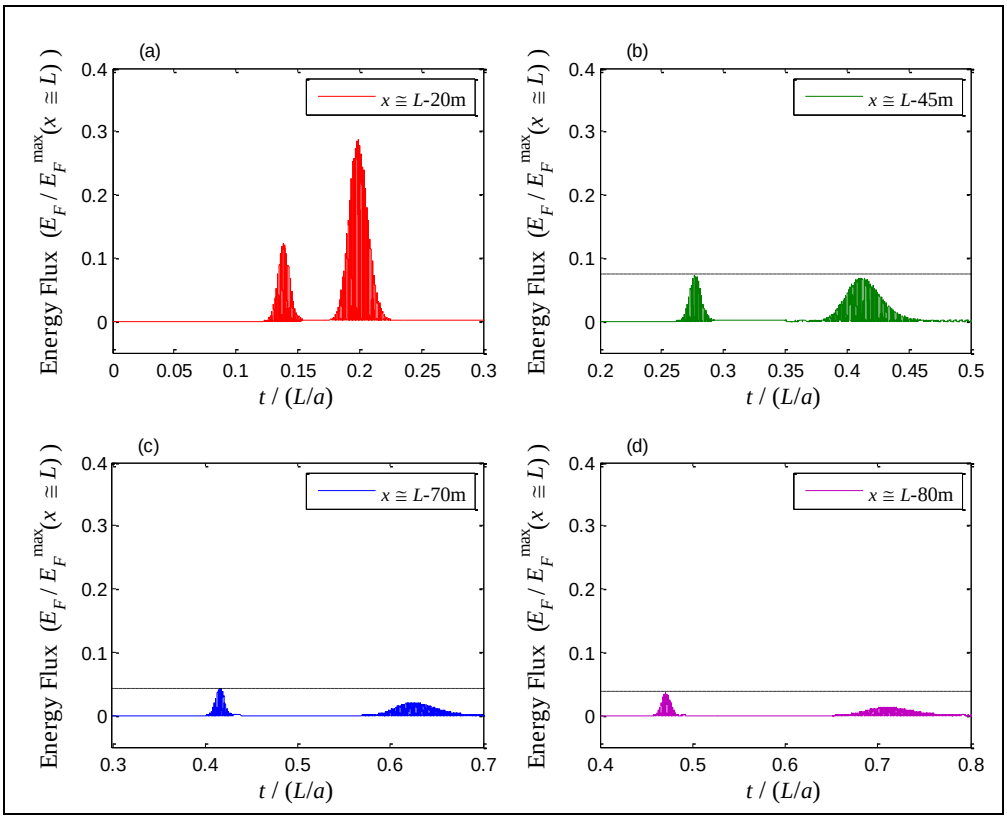

(a) Top left **At 20m away from the source**

(b) Top right **At 45m away from the source**

(c) Bottom left **At 70m away from the source**

(d) Bottom right **At 80m away from the source**

7.2.2.4. Effect of energy radial distribution

So far, the energy propagation is studied by computing the energy through integration over the cross sectional area of the pipe, and therefore, the energy variation along the radial direction was not considered. Figure 7.21 gives the pressure distribution in the *r-x* space plane for the case of f_c=6800 at time $t \approx 0.7L/a$ and shows clear separation of the three modes. The Modes are distinct by their pressure nodes along the radial axis where M2 include two

pressure nodes and M1 include only one pressure node. Figure 7.22 gives the vector velocity field (VVF) in the *r*-*x* space plane for the case of f_c=6800 at time $t \approx 0.7L/a$. Figure 7.22 shows that, at the pressure node locations, the flow is radial with zero axial velocity and maximum radial velocity. For the case of f_c = 6800Hz and inviscid flow, Figure 7.23 gives the distribution in the *r*-*x* space plane of total energy (Figure 7.23a), the potential energy (U) (Figure 7.23b), the kinetic energy due to axial velocity only (T_x) (Figure 7.23c) and the kinetic energy due to radial velocity only (T_r) (Figure 7.23d). The energy plotted in Figure 7.23 are non-dimensionlized by the maximum total energy. Figure 7.23 shows that most of the energy of the high modes is trapped near the pipe centreline and the energy magnitude decreases towards the pipe wall. Figure 7.23 also shows that, at the pressure node, only T_r is present and it takes maximum values. This section studies in more details the properties of the energy radial distribution and its effects on the propagation range.

Figure 7.24 gives the energy and pressure distribution along the pipe when M0 and M2 have the same MEA. Figures 7.24a and 7.24b show that, at the pipe centreline, the M2 maximum pressure amplitude (MPA) and MEA are much larger than those of M0. However, Figures 7.24b and 7.24d show that, at the pipe wall, M2 and M0 have about the same MPA and MEA. Similar results were observed for the case of f_c=4000Hz with comparison between M0 and M1. The variation of the length-averaged energy and the time-averaged energy flux along the radial direction in dimensionless form are given respectively by (Chapter 2 Section 2.6.5)

$$\frac{E_n^r}{\frac{\varphi_n^2}{4\rho a^2}} = \left[1+\cos^2\left(\theta_{kn}\right)\right] J_0^2\left(\alpha_{rn}\frac{r}{R}\right) + \sin^2\left(\theta_{kn}\right) J_1^2\left(\alpha_{rn}\frac{r}{R}\right) \qquad (7.14)$$

and

$$\frac{E_{Fn}^r}{\frac{\varphi_n^2}{2\rho a^2}V_{gn}} = J_0^2\left(\alpha_{rn}\frac{r}{R}\right) \qquad (7.15)$$

where

$$E_n^r = \frac{1}{\lambda_n}\int_0^{\lambda_n}\frac{1}{2}\left(\rho V_{xn}^2 + \rho V_{rn}^2 + \frac{P_n^2}{\rho a^2}\right)dx \text{ and } E_{Fn}^r = \frac{1}{t_p}\int_0^{t_p}\left(P_n \cdot V_{xn}\right)dt \qquad (7.16)$$

The maximum energy is given at the pipe centreline where Eqs. (7.14) and (7.15) gives

$$E_n^0 = E_n^{\max} = \left[1+\cos^2\left(\theta_{kn}\right)\right]\frac{\varphi_n^2}{4\rho a^2} \text{ (at } r = 0) \qquad (7.17)$$

and

$$E_{Fn}^0 = E_{Fn}^{\max} = \frac{\varphi_n^2}{2\rho a^2}V_{gn} \text{ (at } r = 0) \qquad (7.18)$$

and therefore, when Eqs. (7.14) and (7.15) are dimensionlized by their corresponding maximum energy in Eqs. (7.17) and (7.18), yields

$$\frac{E_n^r}{E_n^{\max}} = J_0^2\left(\alpha_{rn}\frac{r}{R}\right) + \frac{\sin^2\left(\theta_{kn}\right)}{1+\cos^2\left(\theta_{kn}\right)}J_1^2\left(\alpha_{rn}\frac{r}{R}\right) \qquad (7.19)$$

and

$$\frac{E_{Fn}^r}{E_{Fn}^{\max}} = J_0^2\left(\alpha_{rn}\frac{r}{R}\right) \qquad (7.20)$$

Figure 7.25 gives the M1 and M2 energy and energy flux distributions along the pipe radius computed from Eqs. (7.19) and (7.20). The results are compared with the numerical solution (Figure 7.15b) and show excellent agreement. Figure 7.25 illustrates how most of the energy is trapped near the pipe centreline, and that the energy decreases with distance from the centreline. The energy takes minimum values at the pressure nodes where only the kinetic energy due to the radial velocity (T_r) is present (see Figure 7.23), but this radial velocity is small.

At the pipe wall, the dimensionless energy flux from Eq. (7.20) is $J_0^2\left(\alpha_{rn}\right)$ and the averaged dimensionless energy flux over the cross sectional area is also $J_0^2\left(\alpha_{rn}\right)$ (Eq. (2.137)) showing why Eq. (7.4) holds for energy measured at the pipe wall as shown in Figure 7.24b.

At a given location and time, the pressure magnitude is (Eq. (2.123))

$$\left|\frac{P_n}{P_n^{\max}}\right| = \left|J_0\left(\alpha_{rn}\frac{r}{R}\right)\right| = \sqrt{\frac{E_{Fn}^r}{E_{Fn}^{\max}}} \qquad (7.21)$$

with $$P_n^{\max} = \varphi_n \exp\left(ik_{xn}\, x^{mes} - iwt\right) \qquad (7.22)$$

Notice from Eqs. (7.20) and (7.21) that the magnitude of the dimensionless pressure is the square root of the dimensionless energy flux at any radial location. Moreover, Eqs. (7.19) and (7.21) show that the magnitude of the dimensionless pressure becomes also the square root of the dimensionless energy magnitude at the pipe wall and centreline. That is, the energy propagation range (Eq. (7.4)) discussed above is also valid for the pressure propagation range at the wall as shown in Figure 7.24d.

For a given mode, the magnitude ratio between measurements at the pipe wall and the pipe centreline is $1/J_0^2\left(\alpha_{rn}\right)$ for the energy and $1/J_0\left(\alpha_{rn}\right)$ for the pressure which increases for higher modes. For example, the energy ratios for M1 and M2 are about 6.16 and 11.1, respectively. The M1 and M2 energy ratios measured from Figures 7.24a and 7.24b are respectively about 6 and 10 which are very close to the analytical values. Theoretically, the M1 and M2 pressure ratios are $\sqrt{6.16} = 2.48$ and $\sqrt{11.1} = 3.33$ which are close to 2.49 and 3.37 ratios measured from Figures 7.24c and 7.24d, respectively. The small differences between the numerical and analytical values are probably due to numerical boundary conditions errors and that the measurements are taken slightly above the centreline and slightly below the pipe wall.

The radial distribution of pressure and energy has profound implications in practice. For example, pressure measurements are generally taken at or near the pipe wall. However, the results show that the pressure magnitude at the wall of M1 is only 40% of the of the maximum pressure, and that of M2 is only 30% of the maximum pressure. If many modes are excited, then the higher the modes are, the lower their pressure magnitudes at the wall. If one relies only on measuring the pressure at the pipe wall only, it may mislead the analyst to believe that the energy is highly dissipated and/or attenuated.

It is shown above that measurement at the wall gives the averaged energy flux, and therefore, Eq. (7.4) could predict the range of propagation with respect to M0 at the wall, but not near the centreline. However, using the ratio of $1/\left|J_0\left(\alpha_{rn}\right)\right|$ between magnitudes at the centreline and at the wall, one could predict the range of propagation of high modes with respect to M0 at the pipe centreline which is

$$x_n^c = \frac{x_n^r}{\left|J_0\left(\alpha_{rn}\right)\right|} = \frac{\Psi_n x_n^s}{\left|J_0\left(\alpha_{rn}\right)\right|} \qquad (7.23)$$

To check this, consider the case of viscous flow ($\nu = 10^{-2}$ (m^2/s)) and f_c=4000Hz shown in Figure 7.20 where it is found that M0 and M1 have the same MEA at about 45m from the source. Equation (7.23) predicts that the propagation range of M1 waves at the pipe centreline with respect to M0 is 45×2.48=111m. Figure 7.26 gives the pressure variation near the pipe wall and near the centreline measured at 45m (Figures 7.26a and 7.26c) and 110m (Figures 7.26b and 7.26d) form the source. Figure 7.26b shows that at 110m from the source, M0 and M1 have similar pressure amplitude as predicted from Eq. (7.23).

Figure 7.21 Dimensionless pressure distribution in the *r*-*x* space plane for the case f_c=6800Hz at time $t/(L/a) \approx 0.7$.

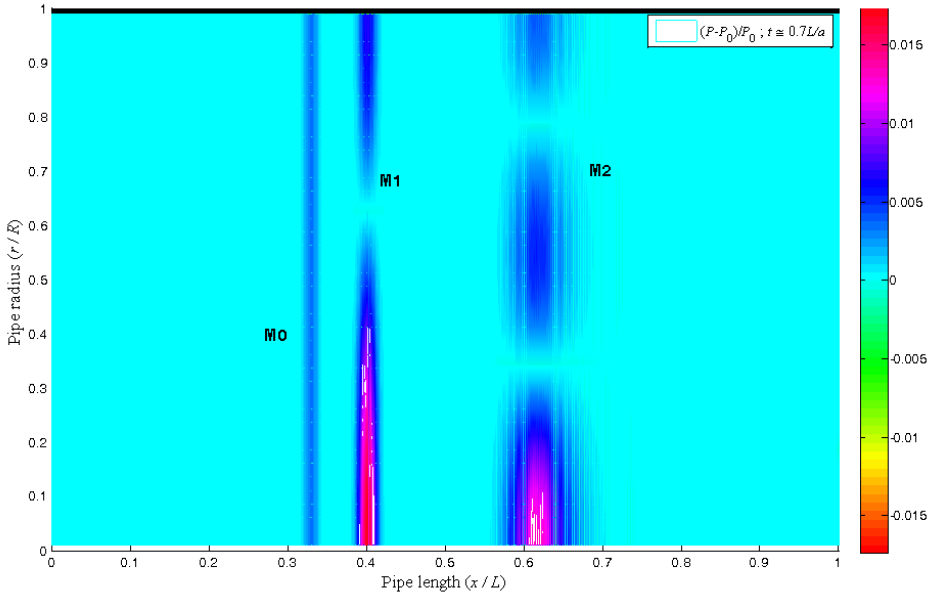

Figure 7.22 Vector velocity field (VVF) distribution in the *r*-*x* space plane for the case f_c=6800Hz at time $t/(L/a) \approx 0.7$.

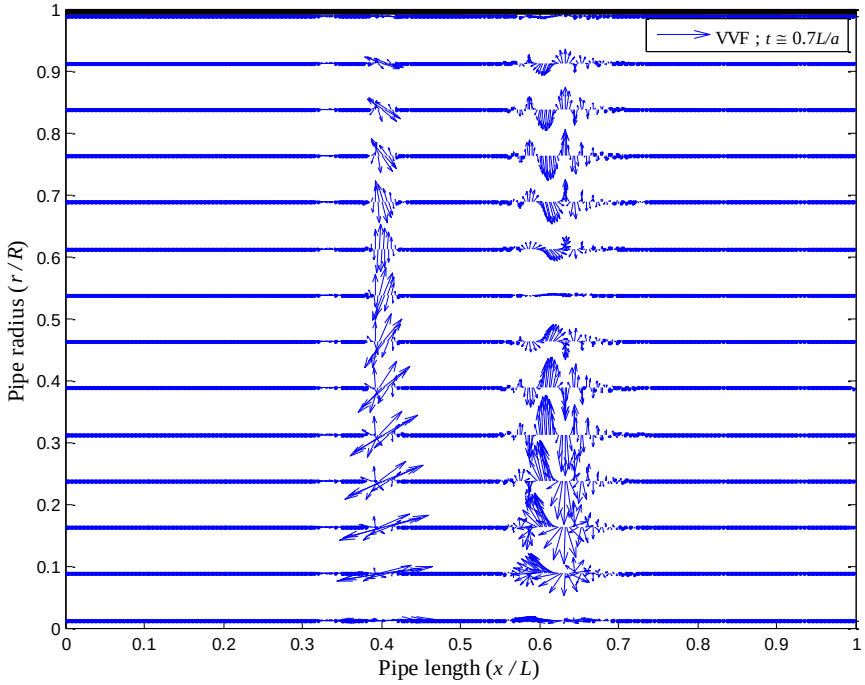

Figure 7.23 Energy distribution in the *r*-*x* space plane for the case of inviscid flow and f_c = 6800Hz at time $t/(L/a) \approx 0.7$.

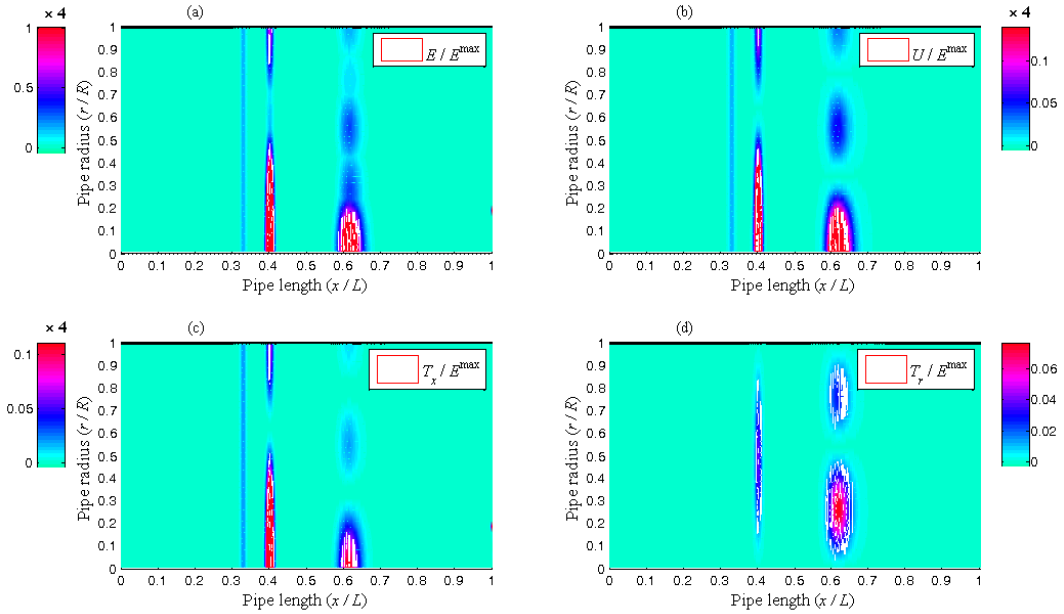

(a) Top left **Total energy**

(b) Top right **Potential energy**

(c) Bottom left **Kinetic energy due to axial velocity**

(d) Bottom right **Kinetic energy due to radial velocity**

Figure 7.24 Energy and pressure distributions along the pipe axis for the case of inviscid flow and f_c = 6800Hz at time $t/(L/a) \approx 0.7$

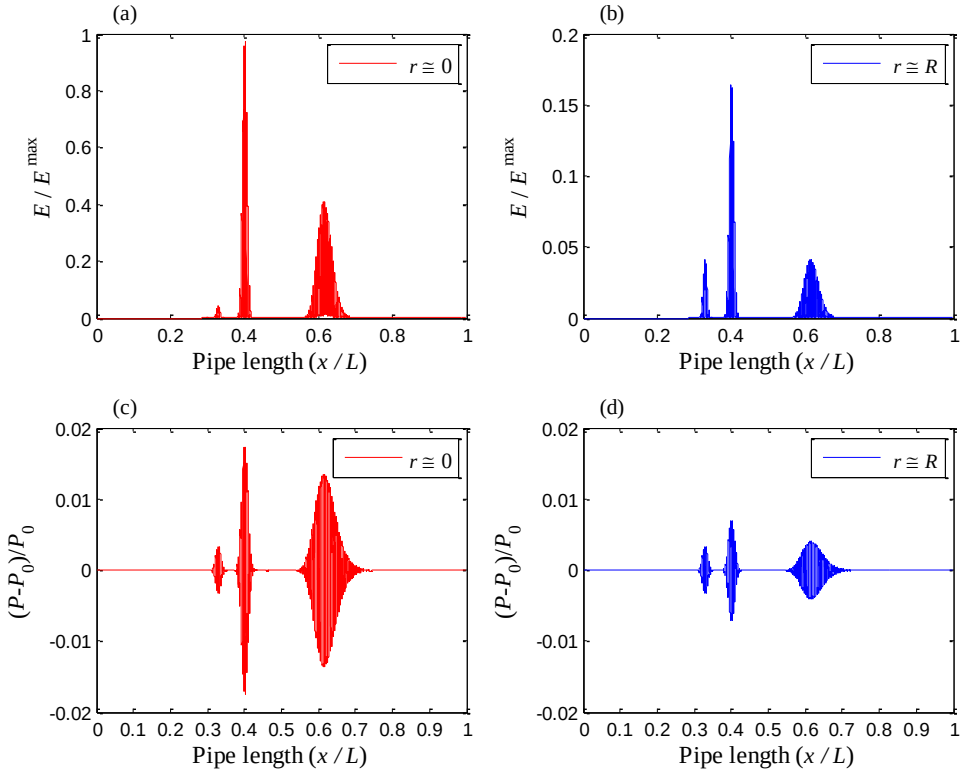

(a) Top left **Energy at the pipe centreline**

(b) Top right **Energy at pipe wall**

(c) Bottom left **Pressure at the pipe centreline**

(d) Bottom right **Pressure at pipe wall**

Figure 7.25 Dimensionless energy and energy flux variations along the pipe radius and comparison with the numerical result for the case of inviscid flow and f_c = 6800Hz at time $t/(L/a) \approx 0.7$.

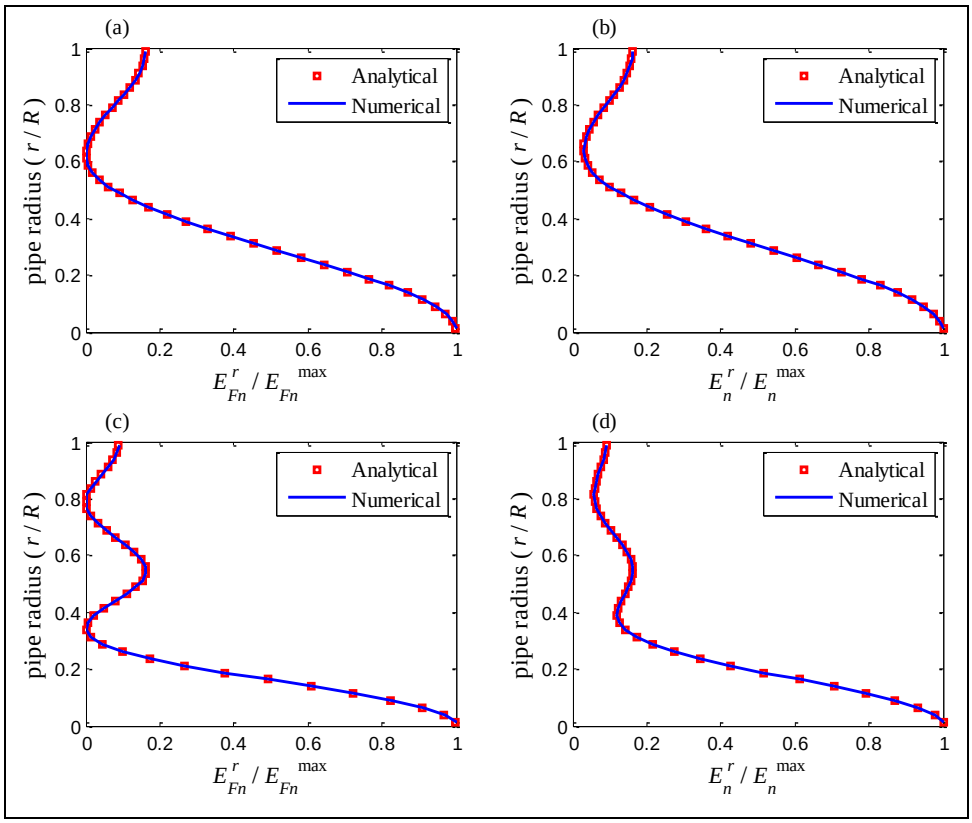

(a) Top left **M1 energy flux**

(b) Top right **M1 energy**

(c) Bottom left **M2 energy flux**

(d) Bottom right **M2 energy**

Figure 7.26 Pressure variation with time for the case of viscous flow ($\nu = 10^{-2}$ (m^2/s)), f_c=4000Hz and L=180m.

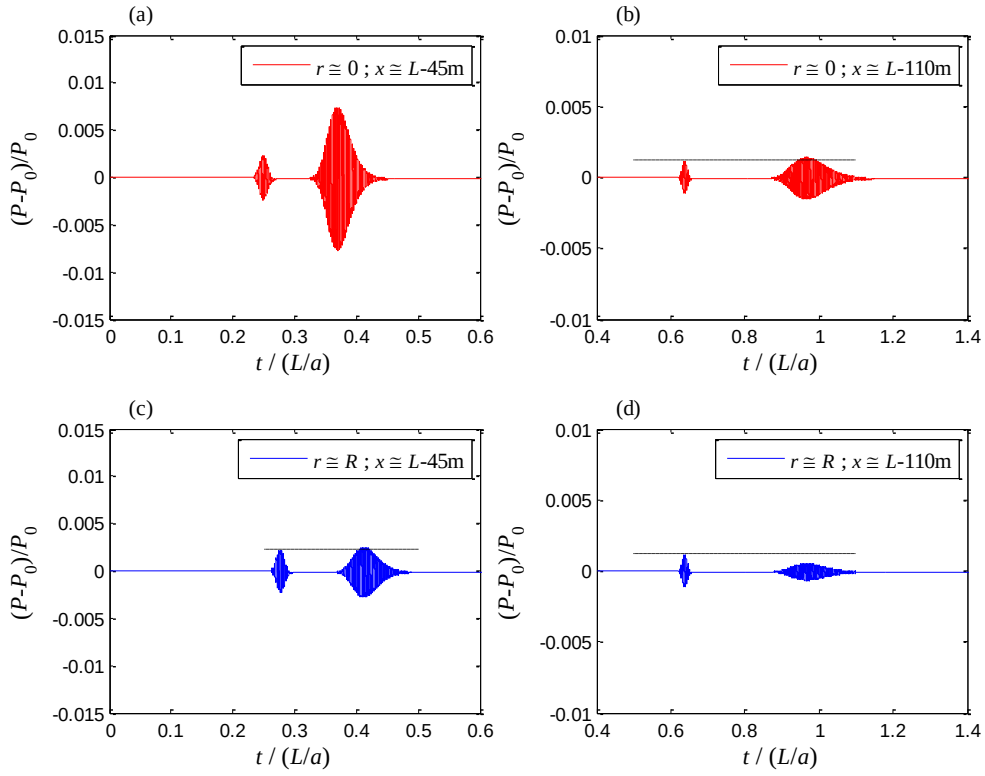

(a) Top left **At the pipe centreline and x=L-45m**

(b) Top right **At the pipe centreline and x=L-110m**

(c) Bottom left **At the pipe wall and x=L-45m**

(d) Bottom right **At the pipe wall and x=L-110m**

7.2.3. High frequency waves in blocked pipe system

At a junction of two pipe segments (see Appendix A), an incident wave is scattered into reflected and transmitted modes such that the continuity of pressure and velocity is satisfied, and by consequences, the energy is conserved. This section studies numerically the scattering behaviour of high frequency wave due to blockage in an unbounded pipe, where the blockage is modeled as a pipe segment (Figure 7.27).

The three pipe segments in Figure 7.27 are defined as pipe 1 with length extending from negative infinity to junction 2 and diameter $D_1 = D$; pipe 2 with length l_2 and diameter $D_2 < D$; and pipe 3 with length extending from junction 1 to positive infinity and diameter $D_3 = D$ where D is the intact pipe diameter. It is assumed that the wave speed (a) is not affected by the change in diameter. Two D_2 cases are considered in this section. The first case is D_2 / D=0.8 and it is referred to as shallow blockage case. The second case is D_2 / D=0.4 and is referred to as severe blockage case. The incident wave generated at a source located at x=L has a waveform as shown in Figure 3.9 with central frequency f_c =4000Hz and a narrow FBW [0.9f_c to 1.1f_c] ≡ [3600Hz to 4400Hz].

A long blockage length l_2=100m is first considered so that the interaction of the incident wave with the blockage could be clearly analysed in two parts. The first part considers the wave scattering at junction 1. The second part considers the wave scattering at junction 2.

Figure 7.27 Sketch of blocked pipe system in unbounded pipe.

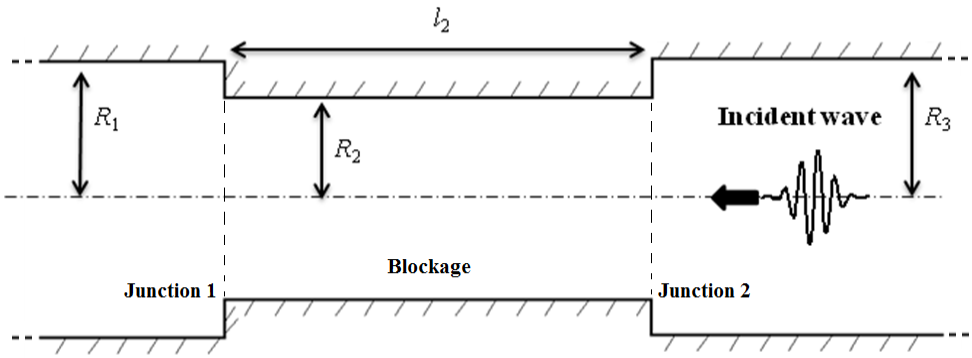

For the shallow blockage case (D_2/D=0.8), Figure 7.28 gives the pressure distribution in the r-x plane where only a plane wave mode is generated at the source (D_s=D). Figure 7.28a is at time before the incident wave reaches the blockage, whereas Figure 7.28b is at time after the incident wave reaches junction 1 but before it reaches junction 2. Figure 7.28b shows that the incident plane wave is scattered into reflected M0 ($M0_0^R$) and M1 ($M1_0^R$) and into

transmitted M0 ($M0_0^T$) and M1 ($M1_0^T$). However, in Figure 7.29 which shows the severe blockage case (D_2/D=0.4), only M0 is transmitted through the blockage. The reason for this is that the M1 cut-off frequency in pipe 2 (*i.e.* blockage) for the shallow blockage case is (see Eq. (2.115)) $f_1 = \alpha_{r1}/\pi \times a/D_2 \approx$ 3800Hz which means that waves propagating at frequencies within [3800Hz to 4400Hz] excite M1. However, the M1 cut-off frequency in pipe 2 for the severe blockage case is $f_1 = \alpha_{r1}/\pi \times a/D_2 \approx$ 7600Hz which is higher than the upper bound frequency content (UBFC) 4400Hz of the incident signal. Therefore M1 in the blockage does not get excited.

Figure 7.28 Dimensionless pressure distribution in the *r-x* space plane for shallow blockage case where only M0 is injected. (f_c=4000Hz and L=200m; l_2=100m and l_3=50m).

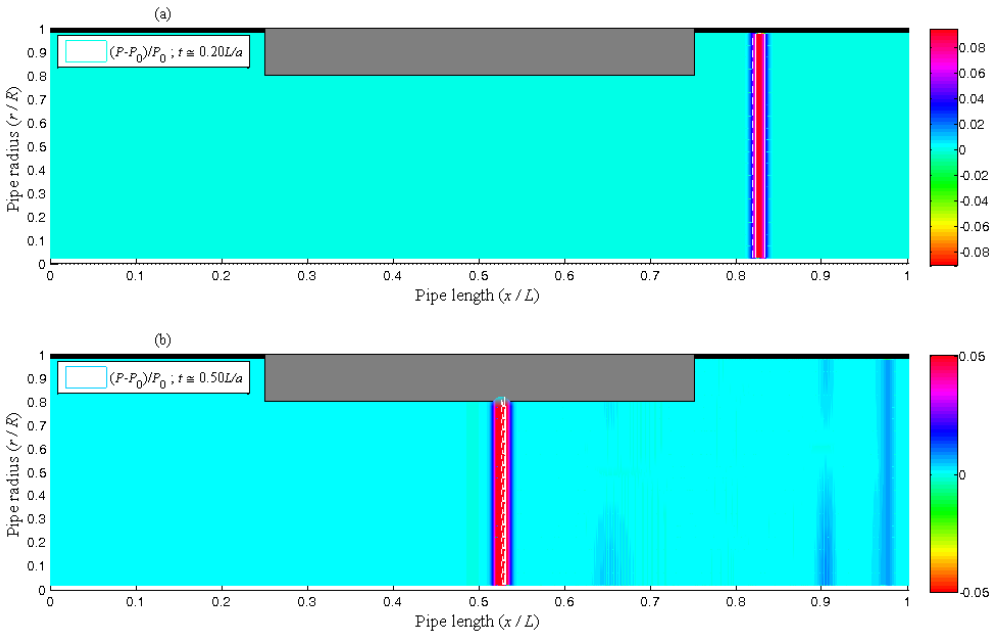

(a) Top **At time $t \approx 0.2L/a$: before the incident waves reach the blockage**

(b) Bottom **At time $t \approx 0.5L/a$: after the incident waves reach the blockage**

Figure 7.29 Dimensionless pressure distribution in the *r*-*x* space plane for severe blockage case where only M0 is injected. (f_c=4000Hz and L=200m; l_2=100m and l_3=50m).

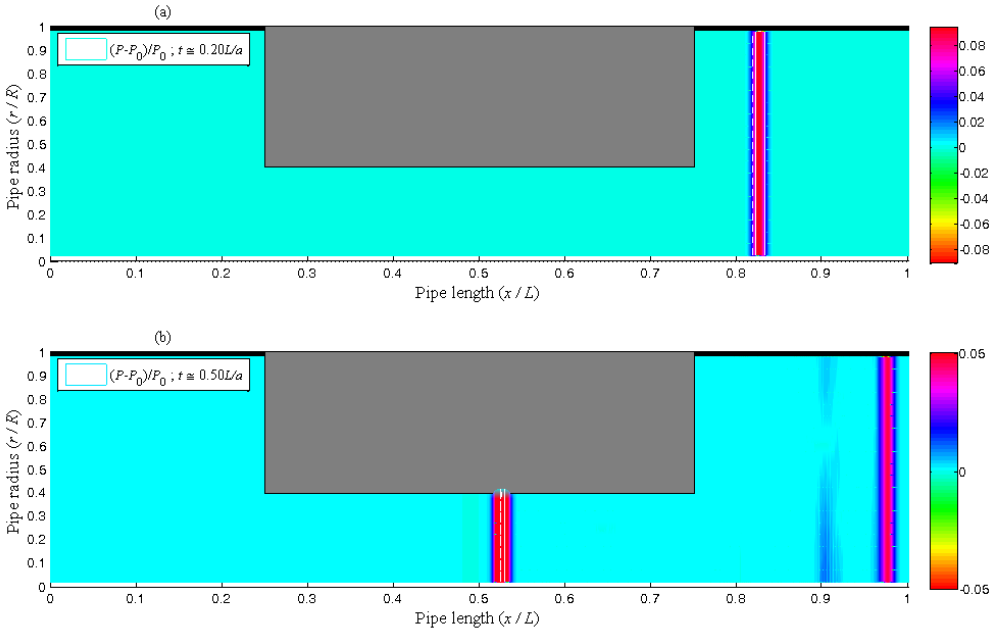

(a) Top **At time $t \approx 0.2L/a$: before the incident waves reach the blockage**

(b) Bottom **At time $t \approx 0.5L/a$: after the incident waves reach the blockage**

Figure 7.30 gives an enlarged plot of the pressure distribution at the time right after the wave interacts with junction 1. Figure 7.30 shows the presence of M1 and a third high mode just to the left and to the right of junction 1, respectively. These two modes are evanescent that get excited at junction 1 to conserve the continuity of pressure and velocity but they do not propagate along the pipe. They get attenuated over a short range near the junction (see Chapter 2 Section 2.6.3). The scale of attenuation of these evanescent modes is of the order of pipe diameter.

Figure 7.30 Enlarged plot of dimensionless pressure distribution in the *r-x* space plane for severe blockage case where only M0 is injected showing the presence of evanescent modes. (f_c=4000Hz and L=200m; l_2=100m and l_3=50m).

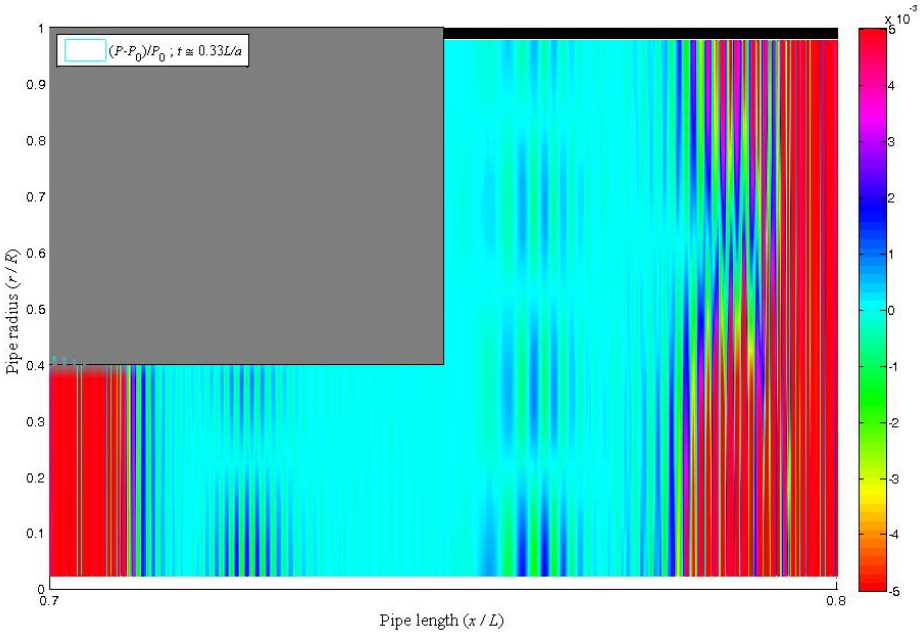

Similarly, Figures 7.31 and 7.32 gives the pressure distribution in the *r-x* plane, respectively, for the case of D_2=0.8D and D_2=0.4D where M1 is excited (D_s=0.2D) and separated from M0 before reaching the blockage (see Figures 7.31a and 7.32a). The M0 waves in Figures 7.31 and 7.32 scatter as discussed above (see Figure 7.28 and 7.29). Figure 7.31b shows that, for the shallow blockage case, M1 is scattered into reflected M0 ($M0_1^R$) and M1 ($M1_1^R$) and into transmitted M0 ($M0_1^T$) and M1 ($M1_1^T$). However, Figure 7.32b shows that, for the severe blockage case, only $M0_1^T$ waves are transmitted through the blockage. This is because, for the shallow blockage case, the transmitted M1 waves at frequencies within [3600 and 3800] are cut-off in pipe 2, whereas M1 waves at frequencies within [3800 and 4400] are cut-on for pipe 1. On the other hand, for the severe blockage case, all transmitted M1 waves are cut-off in pipe 2. Figures 7.33 and 7.34 give the velocity vector field for shallow and severe cases and show the existence of M1 where radial velocity is present.

Notice that in Figures 7.31b and 7.33, the transmitted M1 from the incident M0 ($M1_0^T$) is not clear because it carries little energy (see Figure 7.28) and it is located where $M0_1^T$ is dominant.

Figure 7.31 Dimensionless pressure distribution in the *r*-*x* space plane for shallow blockage case where M0 and M1 are injected. (f_c=4000Hz and L=200m; l_2=100m and l_3=50m).

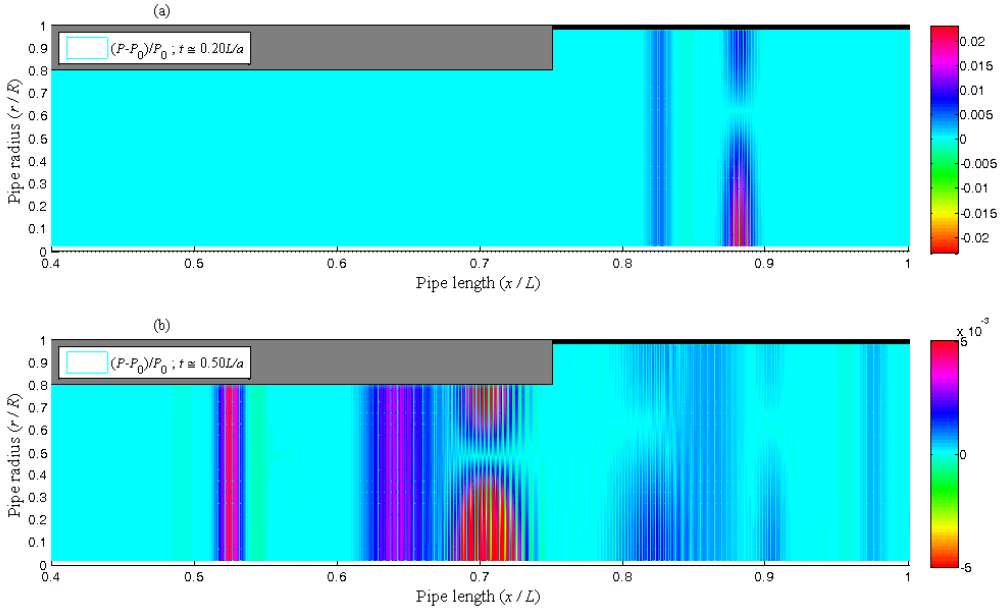

(a) Top **At time $t \approx 0.2L/a$: before the incident waves reach the blockage**

(b) Bottom **At time $t \approx 0.5L/a$: after the incident waves reach the blockage**

Figure 7.32 Dimensionless pressure distribution in the *r*-*x* space plane for severe blockage case where M0 and M1 are injected. (f_c=4000Hz and L=200m; l_2=100m and l_3=50m).

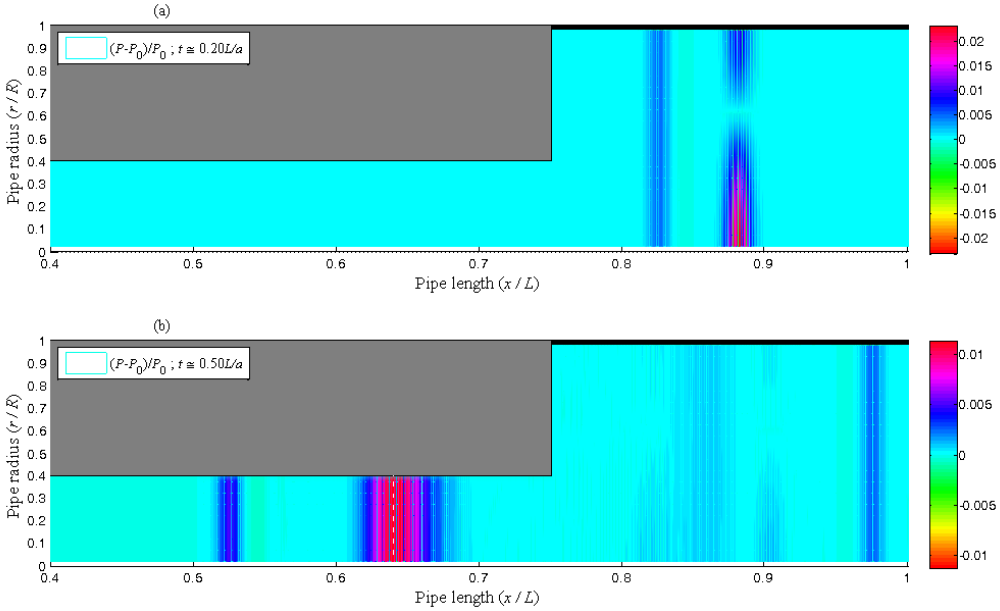

(a) Top **At time $t \approx 0.2L/a$: before the incident waves reach the blockage**

(b) Bottom **At time $t \approx 0.5L/a$: after the incident waves reach the blockage**

Figure 7.33 Vector velocity field (VVF) distribution in the *r*-*x* space plane at time $t \approx 0.5L/a$ for shallow blockage case where M0 and M1 are injected. (f_c=4000Hz and L=200m; l_2=100m and l_3=50m).

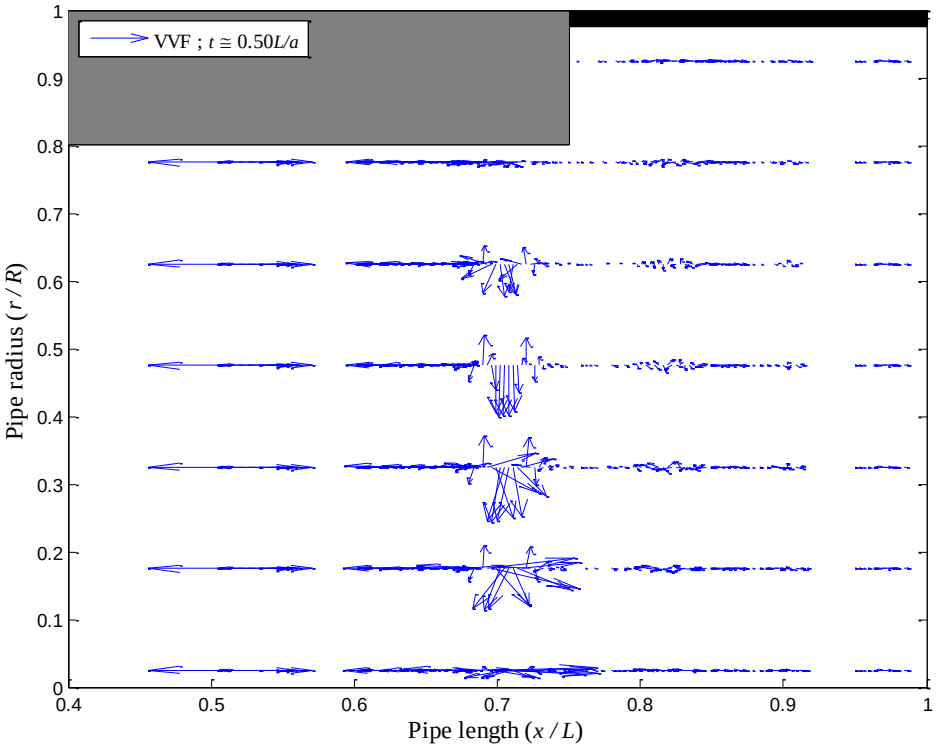

Figure 7.34 Vector velocity field (VVF) distribution in the *r*-*x* space plane at time $t \approx 0.5L/a$ for severe blockage case where M0 and M1 are injected. (f_c=4000Hz and L=200m; l_2=100m and l_3=50m).

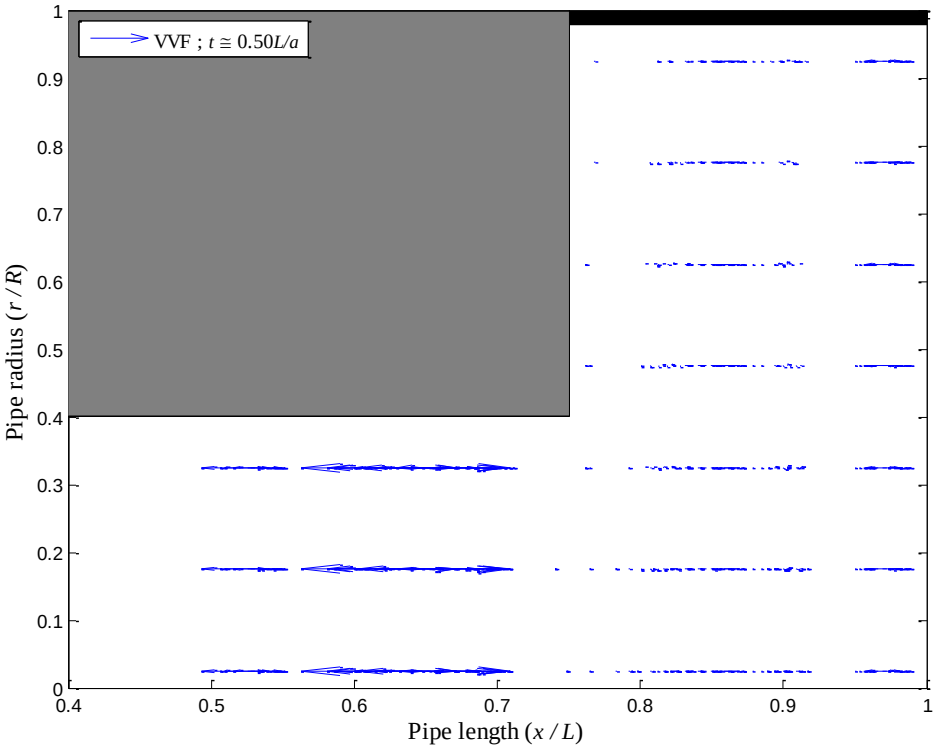

The scattered incident wave distributes it energy into the transmitted and reflected modes such that the continuity of pressure and velocity at the discontinuity is satisfied. Figures 7.35a and 7.35b gives the energy distribution for shallow and severe blockage corresponding to the cases shown in Figures 7.31b and 7.32b, respectively. Figures 7.35a and 7.35b show that the reflected and transmitted energy from the incident M0 is very different for severe and shallow blockage cases where severe blockage reflects much more of M0 energy than shallow blockage. However, the amount of energy reflected from the incident M1 is similar for both severe and shallow blockage cases. One reason for this is that most of M1 energy is trapped near the pipe centreline and therefore it does not interfere much with the blockage in comparison with M0 (see Figure 7.23a).

Figure 7.35 Dimensionless area-averaged energy variation along the pipe at time $t \approx 0.5L/a$ where M0 and M1 are injected. (f_c=4000Hz and L=200m; l_2=100m and l_3=50m).

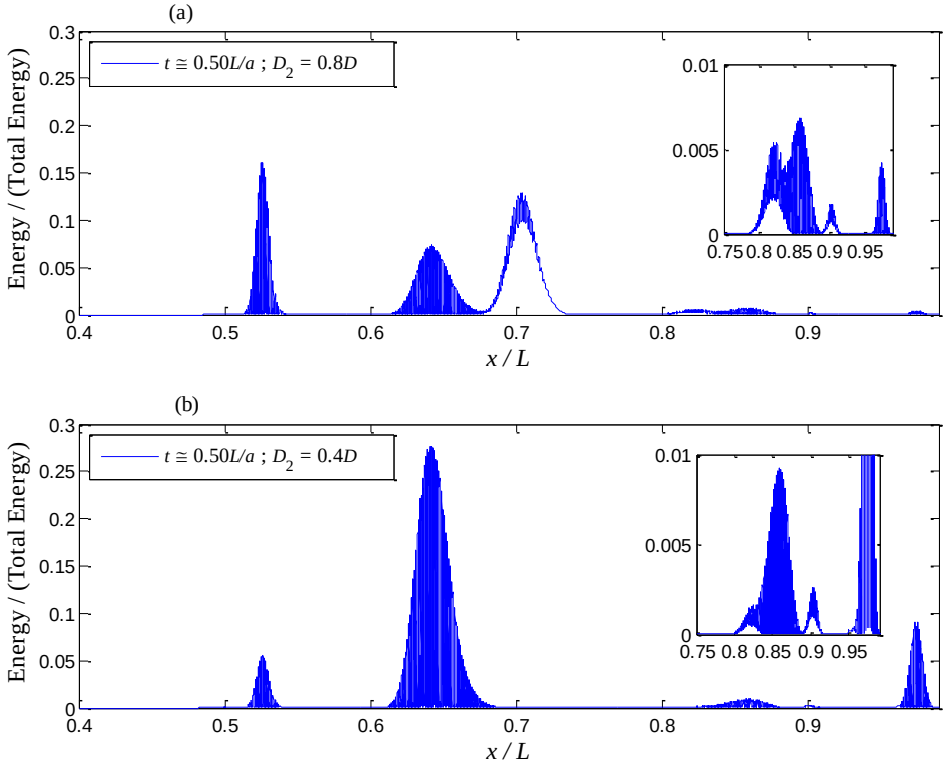

(a) Top **Shallow blockage case**

(b) Bottom **Severe blockage case**

To discuss the wave scattering at junction 2, the pressure distribution in the *r-x* plane where only M0 is injected is given in Figures 7.36 and 7.37 respectively for the case of shallow and severe blockage cases. Figures 7.36a and 7.37a are given at the time before the incident M0 exits the blockage, whereas Figures 7.36b and 7.37b are given at the time after the incident M0 exits the blockage. Figures 7.36b shows that the incident M0 wave is scattered into transmitted M0 and M1 and into reflected M0 and M1 for the case of shallow blockage. However, Figures 7.37b shows that, for the case of severe blockage, the incident M0 wave in the blockage and incident on junction 2 gets scattered into transmitted M0 and M1 and into only reflected M0. The absence of a reflected wave from junction 2 is due to the fact that M1

is cut-off in pipe 2 (*i.e.* blockage) for severe blockage as discussed above. Figures 7.36b and 7.37b show two main features of plane wave scattering at junction 2. First, more wave reflections is induced for the case of shallow blockage than for the case of severe blockage. Second, most of the transmitted energy from a shallow blockage is carried by the transmitted M0 waves rather than by M1 waves. Conversely, most of the transmitted energy from a severe blockage is carried by the transmitted M1 waves rather than by M0 waves. This shows how different blockages induces different signature on the injected signal. It is these differences that could be exploited in using high frequency waves for blockage detection.

Figure 7.36 Dimensionless pressure distribution in the *r-x* space plane for shallow blockage case where only M0 is injected. (f_c=4000Hz and L=200m; l_2=100m and l_1=50m).

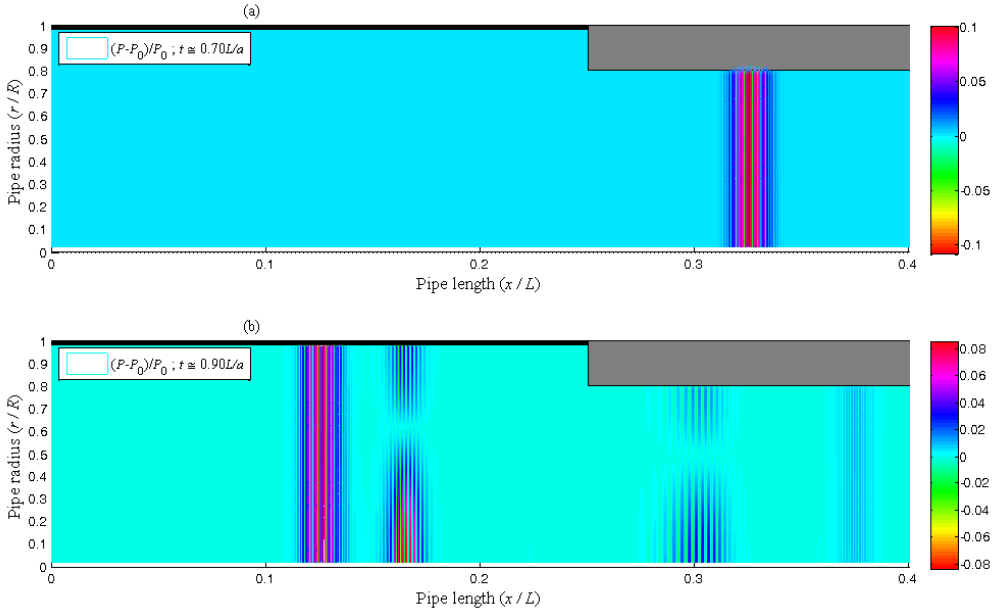

(a) Top **At time $t \approx 0.7L/a$: before the incident waves exits the blockage**

(b) Bottom **At time $t \approx 0.9L/a$: after the incident waves exited the blockage**

Figure 7.37 Dimensionless pressure distribution in the *r-x* space plane for severe blockage case where only M0 is injected. (f_c=4000Hz and L=200m; l_2=100m and l_1=50m).

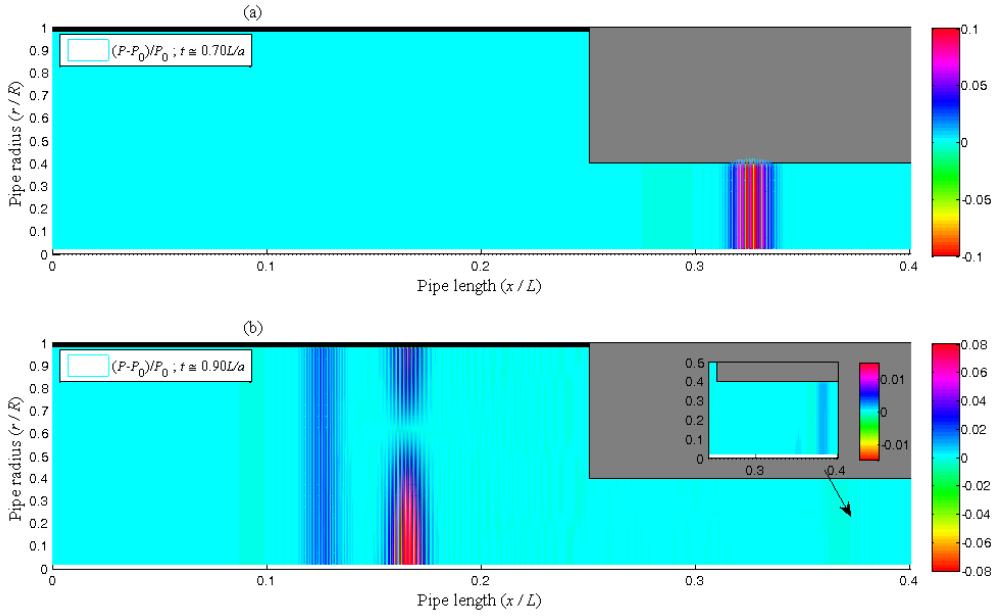

(a) Top **At time $t \approx 0.7L/a$: before the incident waves exits the blockage**

(b) Bottom **At time $t \approx 0.9L/a$: after the incident waves exited the blockage**

A smaller blockage with length l_2=5m is considered to discuss the overall pressure field induced from a wave-blockage interaction. Figures 7.38 and 7.39 give the pressure distribution in the *r-x* plane, where M0 and M1 are injected for the case of shallow and severe blockage cases, respectively. Figures 7.38a and 7.39a are given at the time before the incident waves reach the blockage (*i.e.* junction 1), whereas Figures 7.38b and 7.39b are given at the time after the incident waves are scattered from junction 1. Figures 7.38b and 7.39b show that each incident mode is scattered into transmitted M0 and M1 and into reflected M0 and M1. Figures 7.40a and 7.40b give the area-averaged energy

along the pipe at the time after the incident waves are scattered from the blockage for the shallow and severe blockage cases, respectively. Figures 7.38b and 7.40a show that most of M0 energy (97%) is transmitted through the shallow blockage, whereas Figures 7.39b and 7.40b show that about only half of M0 energy is transmitted through the severe blockage. On the other hand, Figures 7.38b, 7.39b and 7.40, show that most of M1 energy is transmitted through both severe and shallow blockages except that shallow blockage induces slightly extra reflections which could be observed within [x/L=0.55 to x/L=0.65] in Figures 7.38b and 7.40a. The reason that shallow blockage reflect slightly more M1 waves than the severe blockage is because at junction 2, shallow blockage reflects part of its energy whereas severe blockage transmits most of its energy as shown in Figures 7.36b and 7.37b. Figures 7.38b and 7.39b show that wave scattering increases the dispersion and distortion of the waves. Because the energy of the incoming waves is distributed into multiple transmitted and reflected modes, the maximum pressure and energy magnitudes decreases severely. Therefore, if there exist multiple non-uniformities in the pipe cross sectional area (such as junctions, partially closed valve, bends…etc), the attenuation of the pressure signal due to scattering would increase severely and would reduce the range of propagation of high frequency waves.

Figure 7.38 Dimensionless pressure distribution in the *r*-*x* space plane for shallow blockage case where M0 and M1 are injected. (f_c=4000Hz and L=205m; l_2=5.1m and l_1=99.9m).

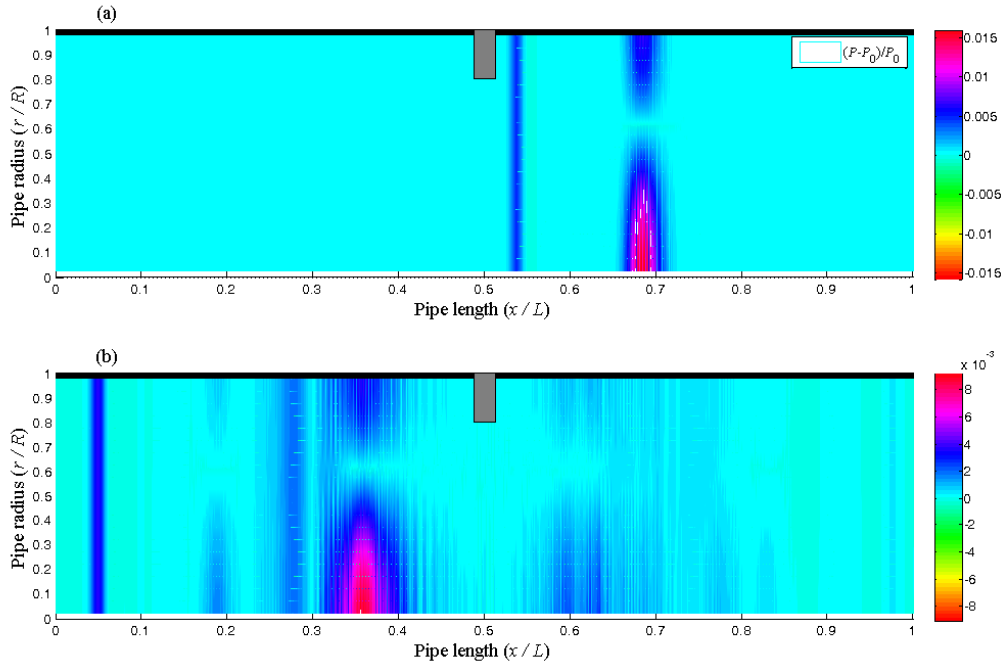

(a) Top **At time $t \approx 0.49L/a$: before the incident waves reach the blockage**

(b) Bottom **At time $t \approx 0.97L/a$: after the incident waves are scattered from the blockage**

Figure 7.39 Dimensionless pressure distribution in the *r*-*x* space plane for severe blockage case where M0 and M1 are injected. (f_c=4000Hz and L=205m; l_2=5m and l_1=99.9m).

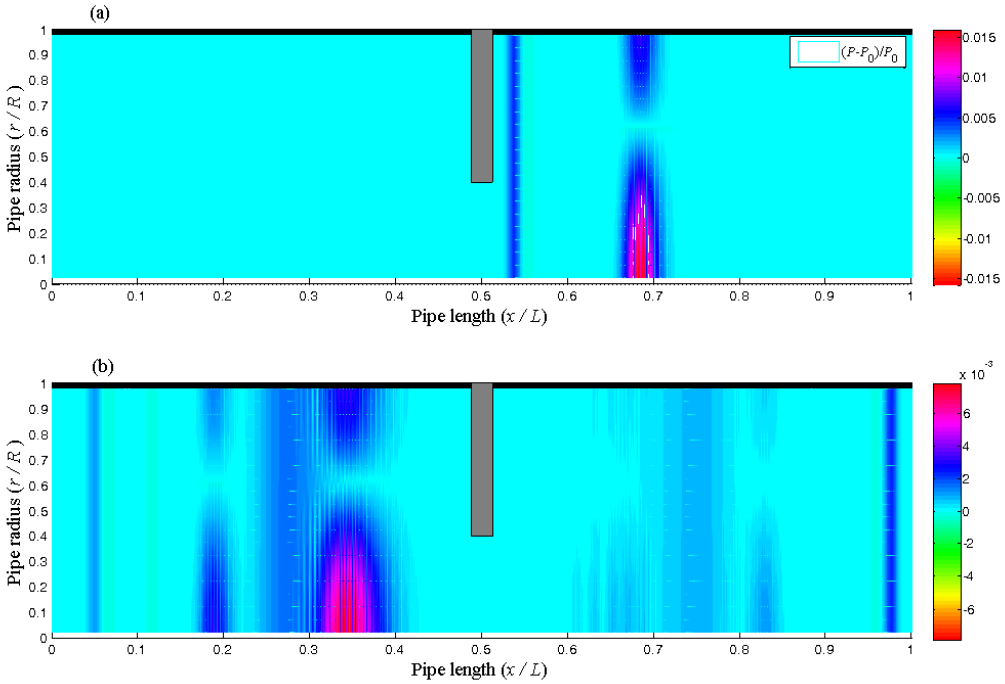

(a) Top **At time $t \approx 0.7L/a$: before the incident waves reach exits the blockage**

(b) Bottom **At time $t \approx 0.9L/a$: after the incident waves exited the blockage**

Figure 7.40 Dimensionless area-averaged energy variation along the pipe at $t \approx 0.97L/a$ where M0 and M1 are injected. (f_c=4000Hz and L=205m; l_2=5.1m and l_1=99.9m).

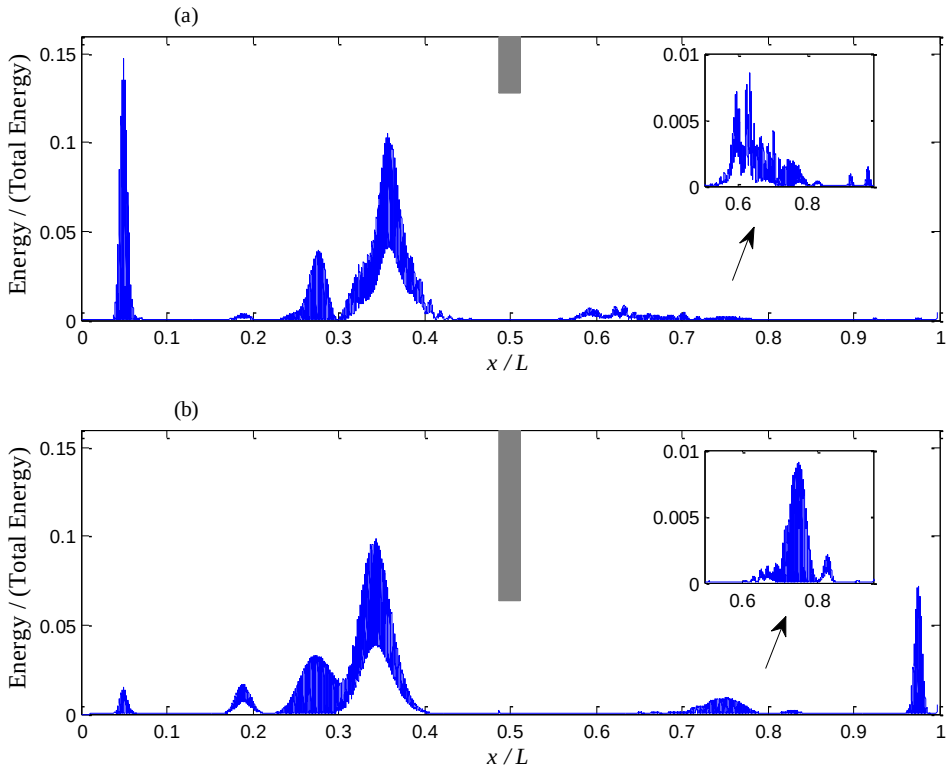

(a) Top **Shallow blockage case**

(b) Bottom **Severe blockage case**

7.3. Classical water-hammer test case: rapid valve closure in a RPV system

This section considers a classical test case for WH application which consists of a rapid valve closure in RPV system with initial Poiseuille flow. The pipe system and boundary conditions for this test case are given in Chapter 3-Section 3.2.7.5. This test case was first considered by Mitra and Rouleau ([96]) to study radial waves in liquid transmission lines numerically. Usually radial waves are not considered in WH models because WH waves are generated by mechanical devices such as valves and pumps whose frequency is far below the cut-off frequency of any high mode. However, Mitra and Rouleau ([96]) considered an ideal

sudden valve closure which induces a broad band signal (with large FBW) that excites high modes, and yet they reported that radial pressure waves are only large near the valve and decay rapidly with distance from the valve. The reason is that the numerical scheme used by Mitra and Rouleau ([96]) was implicit in time and with low accuracy, therefore the numerical dissipation is too high for simulating accurately HFW. This work uses the developed high order explicit scheme to study the radial wave's propagation due to sudden valve closure.

Figure 7.41 gives the dimensionless pressure variations with time at the valve. Figure 7.41a shows that the pressure at the pipe centreline is twice as large as the Joukowsky pressure. This is because the maximum velocity at the centerline is twice the average velocity for a steady state pipe Poiseuille flow (Eq. (3.58)). In fact Figure 7.41b gives the pressure at the pipe wall and shows that pressure oscillates slightly around the Joukowsky pressure. The pressure signal at the pipe wall in Figure 7.41b up to $t = L/a$ is shown in Figure 7.42a and it is transformed into the frequency domain shown in Figure 7.42b. Figure 7.42b shows that the pressure oscillations observed in Figure 7.41 are due to the radial waves excited by the sudden valve closure where f_n ($n = 1,\ldots 5$) in Figure 7.42b are the cut-off frequencies of the first five high modes (Eq. (2.117)).

Figure 7.41 Dimensionless pressure variation at the valve with time

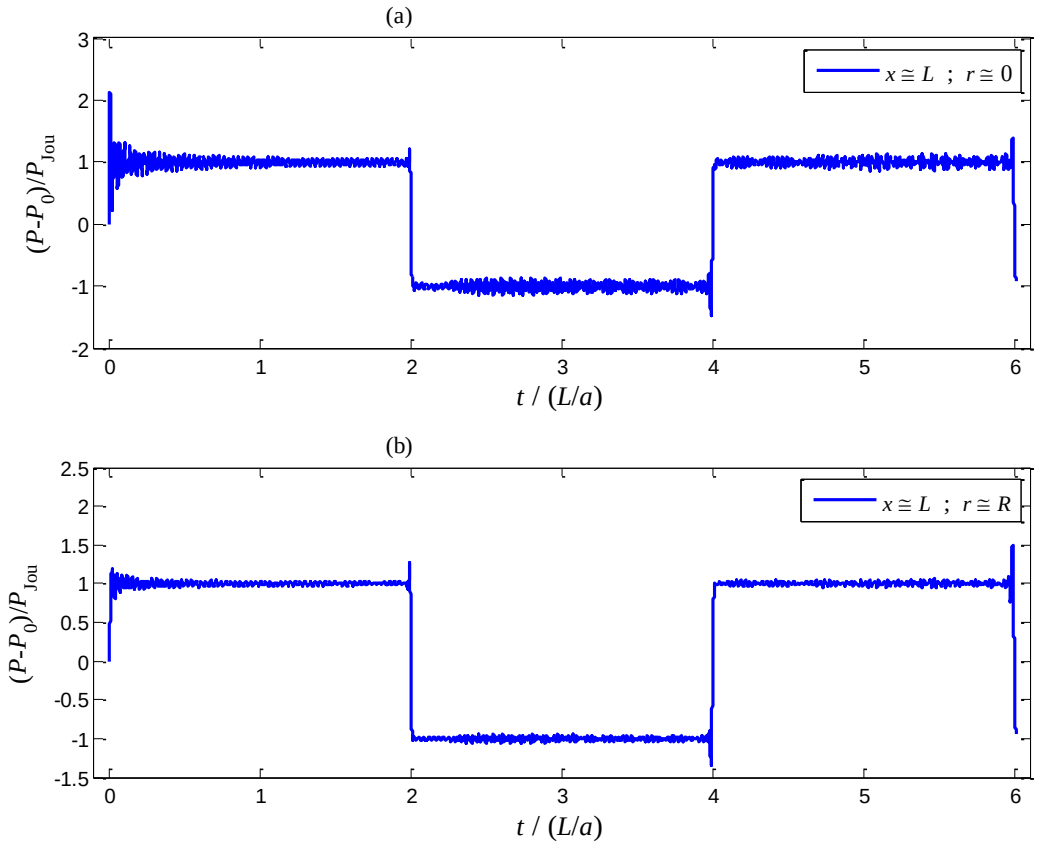

(a) Top **At pipe centreline**

(b) Bottom **At pipe wall**

Figure 7.42 Dimensionless pressure variation at the valve and at the pipe wall for a period of *L*/*a* and its frequency domain transformation

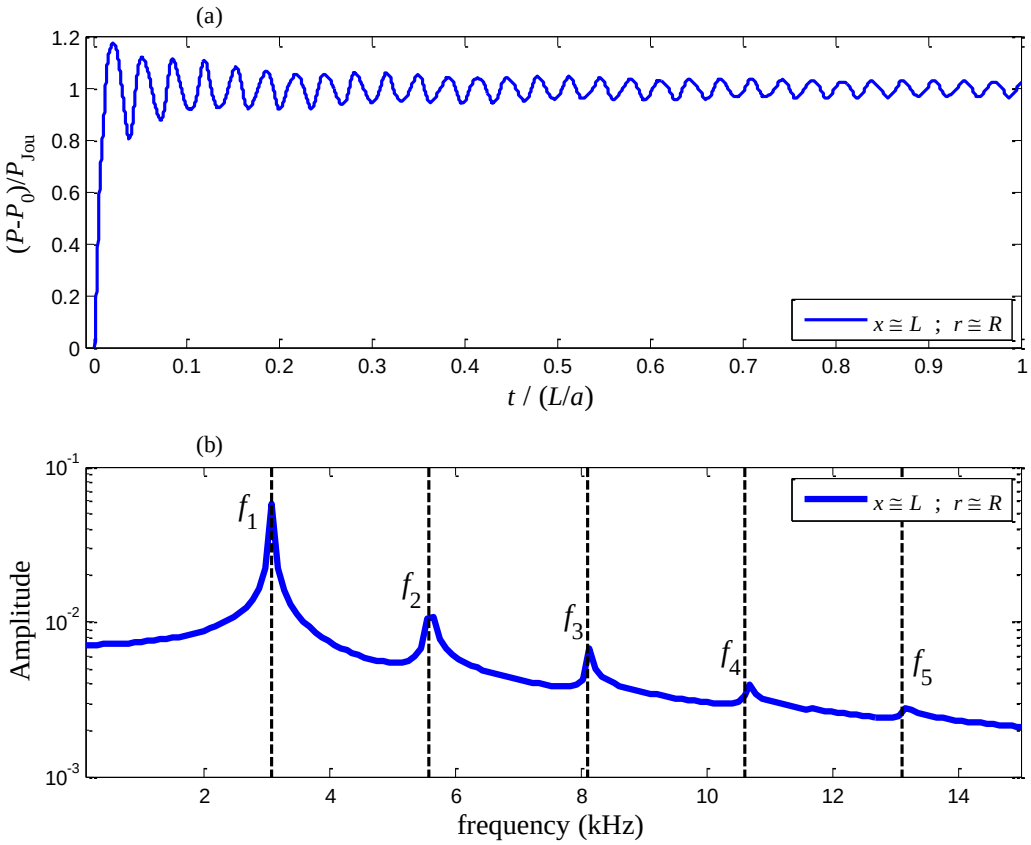

(a) Top **Dimensionless pressure variation with time (normalized by Joukowsky pressure ($P_{Jou} = \rho_0 V_x^0 a$))**

(b) Bottom **Frequency domain**

Figure 7.43 gives the dimensionless pressure distribution in *r*-*x* plane for different times and shows the propagation of M0 and M1 along the pipe. Although higher modes ($n > 1$) are excited (see Figure 7.42b), M1 is dominant and carry most of the energy as shown in Figure 7.42b. As shown in Figure 2.11, waves close to the cut-off frequency propagate at very low speed. These waves are observed in Figure 7.43 near the valve location. The fastest waves are propagating at the highest injected frequency for which the group velocity

approaches the M0 acoustic speed (Figure 2.11). These fast waves are located right behind the plane waves (see Figure 7.43). Figure 7.43 shows that the slower the waves are, the higher their spreading is. This is because, as explained previously form Figure 7.13, the group velocity variation with frequency (see Figure 7.13 and Figure 2.11) is steeper near the cut-off frequency and becomes more uniform away from the cut-off frequency.

Figure 7.43 Dimensionless pressure distribution in the *r-x* space plane for the case of sudden valve closure in a RPV system with initial Poiseuille flow at different times.

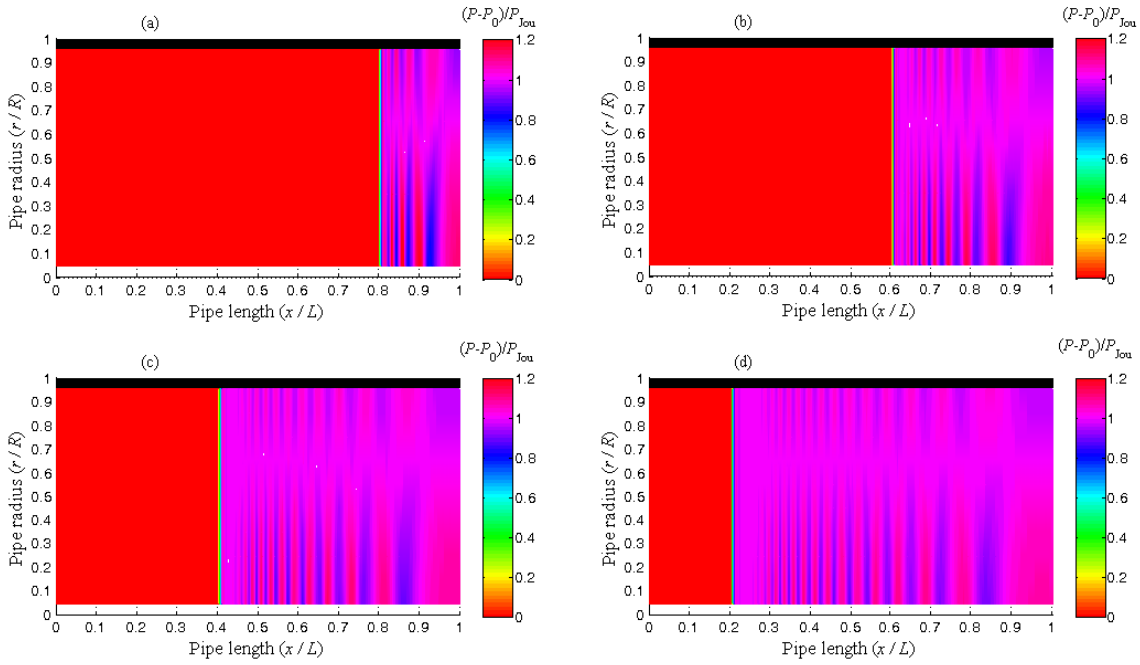

(a) Top left **At time $t = 0.2L/a$**

(b) Top right **At time $t = 0.4L/a$**

(c) Bottom left **At time $t = 0.6L/a$**

(d) Bottom right **At time $t = 0.8L/a$**

7.4. Summary

Although, the physics of acoustic wave behaviour in ducts containing gas/air is well advanced, there is little literature relevant to high frequency waves in water-filled pipes. In this chapter, the behaviour of high frequency waves (non-plane and dispersive waves) in water-filled pipe is studied. The study is conducted numerically using high order numerical scheme (see Chapter 3) and discusses the dispersion behaviour of HFW under resonating probing source (*i.e.* the injected FBW contains the cut-off frequencies of high modes) and non-resonating probing source (*i.e.* the injected FBW does not contain any cut-off frequency) as well as their scattering behaviour due to the presence of a blockage in the conduit. The key conclusions of this study are given below:

(i) Riemann solver scheme preserves the physical dispersion of high frequency waves.

(ii) The resonant response of high frequency waves is studied and the results agree well with the analytical solution.

(iii) At a given location x, the pressure nodes of standing radial wave located at $J_0(k_{rn}r)=0$ were accurately observed from the numerical results. At these pressure nodes, the pressure is constant, the wave-induced axial velocity is zero and the wave-induced radial velocity is maximum, but still small. Knowledge of the locations of these nodes could have important implications in locating sensors for TBDDM.

(iv) The numerical results show that the magnitude of the radial scale of the wave source has significant influence on how the input energy gets distributed over the different excited modes. It is found that small sized source reduces the amplitude of the M0 waves. When high frequency waves are used for TBDDM, and if these methods rely on measuring the plane (M0) waves, then the design of the source size plays significant role.

(v) The dispersion and multipath effect of high modes is analysed. It is shown that the energy contained in high modes gets distributed along the pipe in the form of a tail of energy that grows longer and more uniform with distance from the source. Moreover, if the injected FBW contain the cut-off frequency of a given mode n, the tail of energy of the n-th mode becomes infinite because the group velocity near cut-off frequency is too small and it is zero at the cut-off frequency. However,

when the injected FBW does not contain any cut-off frequency, each excited mode get separated from all other excited modes with finite tail of energy, and their spatial spreading with distance from the source depends on the slope of the group velocity with respect to frequency over the range of injected frequencies. As a result, the measurement locations of HFW should neither be far away from the source locations where wave amplitude becomes very small due to dispersion, nor very close to the source so that the modes get separated, and thus, are easily analyzed. Simple and reliable expressions to determine the waves propagation range and the separation locations of different modes are proposed.

(vi) It is found that the energy of radial modes is trapped near the centreline and decreases with distance from the centreline. This is a result of no flux boundary at the pipe wall. The energy at the pipe wall gives the magnitude of the area-averaged energy. The *n*-th energy magnitude at the pipe centreline is proportional to the magnitude at the pipe wall by the factor $1/J_0^2(\alpha_{rn})$ where $J_0^2(\alpha_{rn})<1$. The pressure magnitude has similar feature except that the proportionality factor is $1/\left|J_0(\alpha_{rn})\right|$. This is important in practice because, usually, the pressure measurements are taken at the pipe wall. If many modes are excited, the higher the modes are, the lower the pressure magnitudes are measured at the pipe wall. If one relies only on measuring the pressure at the pipe wall without taking into account the radial distribution of the high modes, it could mislead to believe that the energy is highly dissipated and/or attenuated.

(vii) Viscous effect affects the propagation ranges of higher modes more than lower modes. This is because high modes take longer path than lower modes, and therefore, they dissipate over a longer time. Knowing the dissipation rate for plane wave, the additional dissipation of high modes due to multi-path effect could be determined from the ratio between the plane wave path and high modes paths which is given by the propagation angle.

(viii) Scattering of high frequency waves due to the presence of a blockage is studied. It is shown that each incident mode is scattered into multiple of reflected and transmitted modes. The plane wave mode is highly affected by the severity of area

reduction. The more severe the reduction is, the more energy of a plane wave is reflected. However, high radial modes have little interaction with the blockage and transmit most of their energy through both severe and shallow blockage. This is because most of the high radial modes energy is trapped near the pipe centreline. This work considered only axi-symetric pipe system, and therefore, blockages are assumed axi-symmetric.

CHAPTER 8

CONCLUSIONS

8.1. Overall conclusions

As stated in the introduction chapter, the objective of this thesis is to shed greater light on the forward problem of wave-blockage interaction in WSS under a wide range of frequencies. In particular,

(i) The eigenfrequency shift mechanism induced by wave-blockage interaction is investigated theoretically, numerically and experimentally. The underlying physics of the frequency shift is clrafied.

(ii) HFW in water-filled pipe and how they interact with blockages is investigated.

These aims have been addressed in this research and the results and conclusion are given below.

This work uses analytical, numerical and experimental means to investigate the wave-blockage interaction in a conduit. This investigation is accomplished in a two-pipe system case scenarios discussed in Chapter 4, Chapter 5 and Chapter 6. In Chapter 4, an unbounded pipe system is considered which allows examination of the direct interaction between waves and blockages without interference from other effects. Such analysis established the existence of Bragg-type resonance in conduits where wave reflections are enhanced at certain frequency bands and wave transmissions are enhanced at other frequency bands. The Bragg resonce conditions are derived in this thesis.

A bounded pipe system (e.g. reservoir-pipe-valve (RPV) system) is considered in Chapter 5 and Chapter 6. Chapter 5 studied the case where the blockage is located one end of the pipe, whereas Chapter 6 studied the case of interior blockage. The eigenfrequency shift mechanism is investigated for both blockage cases.

It is found that the eigenfrequency shift caused by shallow blockages (with small radial protrusion) could be explained either by the variation of the change of kinetic and potential in the blocked area, or by the change of the difference in work of the radiation pressure at the blockage boundaries. Both approaches lead to an analytical equation of the eigenfrequency shift for the case of shallow blockage. In particular, the shallow blockage assumption shows that zero shifts occur under two conditions. The first condition is when the blockage length is a multiple of the half wavelength of the m^{th} mode harmonic. At these modes, the eigenfrequency corresponds to the Bragg resonance frequency of total transmission. Under this condition, the shift is zero for any blockage location. The second condition states that, at a given mode *m*, the shift is zero when the blockage mid-length is located at a position of equal pressure and flow magnitude. Furthermore, maximum shifts are governed by two mechanisms. The first mechanism is for a given mode *m* and states that the shift is maximum if the blockage mid-length is located at a position of either a pressure node or stagnation point. The second mechanism describes the variation of the maximum shift magnitude with mode number and shows that the largest magnitude of the maximum shift occurs at modes with eigenfrequencies close to the Bragg resonance frequencies of maximum reflection. The assumption of shallow blockage is found to remain applicable when the blockage occupies 35% of the pipe area, or less.

Severe and moderate blockages decouple the pipe system into independent intact subsystems with different lengths and diameters corresponding to the blocked and intact regions (pipe sections). The eigenfrequencies of these subsystems define the asymptotic solutions of the eigenfrequency variations at the limit of the most severe blockage case ($\alpha \to 0$). This decoupling effect is governed by two mechanisms, depending on either the change of the blockage location at a given mode or the change in eigenfrequency mode number. The first mechanism is for a given resonant mode and states that the decoupling effect is weakened when the blockage location is such that the eigenfrequencies of the subsystems are close or

equal to each other. As a result, waves in one subsystem acts as forcing to other subsystems. The fact that subsystems are driving one another at or near resonance is what brings about the coupling, even for a very severe blockage. The second mechanism describes the variation of the shift magnitudes with mode number and shows that as the eigenfrequency mode number varies, the coupling/decoupling mechanism is governed by the Bragg resonance effect discussed in Chapter 4. In fact, it is shown that modes with eigenfrequencies close to or at the Bragg resonance frequencies of maximum reflection experience the largest shift magnitude. To explain, the more the reflections are from the blockage, the more the upstream and downstream regions of the blockage become decoupled. Conversely, modes with eigenfrequencies close to or at the Bragg resonance frequencies of total transmission experience zero shifts for any blockage location.

The Bragg resonance effects, as well as the different features of the eigenfrequency shift, are investigated using experimental tests conducted at the Water Engineering Laboratory in the University of Perugia-Italy in collaboration with Prof. Bruno Brunone and Prof. Silvia Meniconi. Reasonable agreement and consistency between the experimental and numerical Bragg resonance and eigenfrequency shift is found. In addition, it is shown that the eigenfrequency and Bragg resonance can be exploited in the development of for blockage detection techniques in pipe systems. In particular, the relation between Bragg-type resonance and eigenfrequency shift allows the identification of the blockage characteristics (*i.e.* blockage's length and area) from the frequency response function. Moreover, simple equations that link the measured zero shifts as well as maximum shifts (*i.e.* significant shifts) to discrete sets of possible blockage locations are proposed, which improves the inverse optimization techniques for blockage detection in pipe systems.

The behaviour of HFW are studied numerically in Chapter 7. Second, third and fifth (for smooth waves) order finite volume schemes based on the approximate Riemann solver are developed. The details and accuracy of these schemes are given in Chapter 3. The second order accuracy is achieved by using the MUSCL–Hancock approach. The third and fifth order accuracy for smooth wave propagation is achieved by using a weighted essentially non-oscillatory (WENO) reconstruction. Prior to using the developed schemes to conduct numerical experiments, their accuracy, efficiency and robustness were tested. The results

show that second and third order schemes could be used for simulating wave propagation at frequencies less than 1000Hz. However, for frequencies higher than 1 kHz, higher order schemes are needed to minimize the numerical dissipation at low computational time. Numerical experiments reveal that for frequencies ranging from 5 kHz to 100 kHz, the required order of accuracy increases from 5 to 8.

Plane waves propagate at the acoustic wave speed (a). However, dispersive waves at high modes propagate at the group velocity which is the speed at which the energy propagates. The group velocity is smaller than the acoustic wave speed (a) and varies with the frequency. Therefore at high modes, the energy of waves with different frequencies propagates at different speeds. The fact that different wave modes acquire different paths is referred to as a multipath process and is the reason why HFW are dispersive.

The dispersion and multipath effect of the high modes is analysed. It is shown that the energy contained in high modes gets distributed along the pipe in the form of a tail of energy that grows longer and more uniform with distance from the source. Moreover, if the injected FBW contain the cut-off frequency of a given mode n, the tail of the energy of the n-th mode becomes infinite because the group velocity near the cut-off frequency is too small and it is zero at the cut-off frequency. However, when the injected FBW does not contain any cut-off frequency, each excited mode get separated from all other excited modes with a finite tail of energy, and the spatial spreading with distance from the source depends on the slope of the group velocity with respect to frequency over the range of injected frequencies. As a result, the measurement locations of HFW should not be far away from the source location where the wave amplitude becomes very small due to dispersion, or very close to the source so that the modes get separated, and thus, are easily analyzed. Simple and reliable expressions to determine the waves propagation range and the separation locations of different modes are proposed.

It is found that the energy of the radial modes is trapped near the centreline and decreases with distance from the centreline. This is a result of "no flux" boundary at the pipe wall. The energy at the pipe wall gives the magnitude of the area-averaged energy. The n-th energy magnitude at the pipe centreline is proportional to the magnitude at the pipe wall by the

factor $1/J_0^2(\alpha_{rn})$, where $J_0^2(\alpha_{rn})<1$. The pressure magnitude has a similar feature except that the proportionality factor is $1/|J_0(\alpha_{rn})|$. This is important in practice because, the pressure measurements are usually taken at the pipe wall. If many modes are excited, the higher the modes are, the lower the pressure magnitudes measured at the pipe wall. If one relies only on measuring the pressure at the pipe wall without taking into account the radial distribution of the high modes, it could be misleading to believe that the energy is highly dissipated and/or attenuated.

The viscous effect affects the propagation ranges of the higher modes more than lower modes. This is because the high modes take longer paths than the lower modes, and therefore, they dissipate over a longer time. Knowing the dissipation rate for a plane wave, the additional dissipation of the high modes due to multi-path effect could be determined from the ratio between the plane wave path and the high modes paths which is given by the propagation angle.

Scattering of high frequency waves due to the presence of a blockage is studied. It is shown that each incident mode is scattered into a multiple of reflected and transmitted modes. The plane wave mode is highly affected by the severity of the area reduction. The more severe the reduction, the more the energy of a plane wave is reflected. However, high radial modes have little interaction with the blockage and transmit most of their energy through both severe and shallow blockages. This is because most of the high radial modes energy is trapped near the pipe centreline. This research considered only axi-symetric pipe systems, and therefore, blockages are assumed to be axi-symmetric.

8.2. Future work

This research assumes that fluid is inviscid, the flow is initially at rest, the pipe system is relatively simple and the wave siganls are free of noise. However, WSS are highly complex, the flows in them are turbulent and subjected to a myriad of noise sources (e.g. vibrations of

mechanical devices, traffic noise, etc). To advance and extend the research of this thesis to more practical applications, below are some recommendations for future work regarding one dimensional analysis:

(i) Conduct a sensitivity analysis of the wave signals to noise and develop ways to maximize signal to noise ratio. In this regard, the HKUST research group working on the theme-based project led by the advisor of the author of this thesis ([121]) has started conducting experimental field tests to obtain initial information on the noise level and characteristics in HK WSS.

(ii) Initial results showed that the Bragg resonance effects, where wave reflections are enhanced for certain frequency bands and weakened for other bands, occurs in the case of multi-blockages. An understanding of the mechanisms describing the relation between these Bragg resonance frequency bands and the blockage characteristics could open the doors to new techniques for processing the data in the frequency domain. In particular, it would be very important if such an understanding could lead to prior knowledge of the blockage number in the pipe. In fact, current solutions of inverse problems require that the number of blockages is known a priori, which leads to unrealistic computational time for practical applications. Preliminary results with multi-blockages showed that regularity exists in the distribution of the Bragg resonances frequency bands. Therefore, it could be possible to use signal correlation techniques in the frequency domain to identify the Bragg resonance frequency bands which leads to inform on the blockage characteristics.

(iii) Leak detection is a major problem for WSS. A study similar to the one conducted in this thesis but for the case of leak-wave interaction would contribute greatly to the understanding of how waves scatter from a leak and would form the pre-requisite for the development of reliable leakage detection in WSS.

(iv) The pipe system used for the experimental investigation in this work includes bends, and it is found that that these bends may influence the eigenfrequency shift. Yet, the phenemomna of bend-wave interaction is not yet understood and should be

addressed in the future especially that most laboratory pipe systems are coiled due to space limitation.

The HFW research in this thesis considers only a simple pipe configuration where the pipe flow is assumed either inviscid or viscous but laminar. In addition, the flow is assumed axi-symetric. Prior to using HFW for TBDDM, the following researches need to be conducted in the future:

(i) This thesis shows that wave dispersion spreads the energy in space and could easily be misconstrued as damping. Future work should seek to understand the reduction in amplitude of HFW as they propagate and how much of this reduction is due to dissipiation, how much is due to dispersion and how much is due to fluxes of energy from the fluid to the pipe wall. This requires numerical and experimental investigation of HFW under more realistic conditions. In addition, models that incorporate the interaction between the pipe wall and the fluid will need to be developed for the case of HFW.

(ii) Numerical results in this thesis show that the size of the radial scale of the wave source has significant influence on how the input energy is distributed over the different excited modes. Therefore, further study on the influence of the source size should be undertaken in future work. This would help in designing an appropriate transient source and give control on the energy field injected into the pipe system.

(iii) In current practice, transients are typically generated from a side discharge valve and the pipe wall is the easiest and most practical spot for implementing wave generators. This causes flow asymmetry; as a consequence, azimuthal waves (that travel in a helicoidal motion) are generated and could excite the natural azimuthal modes of the pipe system. Therefore, the dispersion effect studied in this thesis could become more pronounced; leading to increased distortion of the pressure signal. As a result, it is expected that the energy dispersion gets intensified. These processes are currently not understood and need to be invrestigated in the future.

(iv) The current study analyzes an idealized blockage (*i.e.* axi-symmetrical shape, pipe junctions with different diameter). More realistic blockage shapes will need to be investigated in the future.

(v) WSS flows are highly turbulent. The effect of turbulent noise and nonlinearity on the high frequency waveform and transformation need to be investigated.

(vi) The current thesis focuses on blockages and a follow up study that investigates the interaction between leaks and HFW would be interesting and important.

BIBLIOGRAPHY AND REFERENCES

[1] Akyildiz, I. F., Pompili, D., & Melodia, T. (2005). Underwater acoustic sensor networks: *Research challenges. Ad Hoc Networks*, 3(3), 257-279.

[2] Allen, M., Preis, A., Iqbal, M., Srirangarajan, S., Lim, H. B., Girod, L., & Whittle, A. J. (2011). Real-time in-network distribution system monitoring to improve operational efficiency. *Journal American Water Works Association (AWWA), 103*(7), 63-75.

[3] American Society of Civil Engineers 2009 Report Card on Infrastructure. http://ascelibrary.org/doi/book/10.1061/9780784410370

[4] American Society of Civil Engineers 2013 Report Card on Infrastructure.

[5] Anderson, D., & Barnes, C. (1953). The dispersion of a pulse propagated through a cylindrical tube. *The Journal of the Acoustical Society of America, 25*(3), 525-528.

[6] Beyer, R. T. (1978). Radiation pressure--the history of a mislabeled tensor a). *J.Acoust.Soc.Am, 63*(4), 4.

[7] Borgnis, F. E. (1953). Acoustic radiation pressure of plane compressional waves *Reviews of Modern Physics, 25*(3), 653 <last_page> 664. doi:10.1103/RevModPhys.25.653

[8] Brunone, B. (1999). Transient test-based technique for leak detection in outfall pipes. *Journal of Water Resources Planning and Management,*

[9] Brunone, B., & Ferrante, M. (2001). Detecting leaks in pressurised pipes by

means of transients. *Journal of Hydraulic Research, 39*(5), 539-547.

[10] Brunone, B., Ferrante, M., & Meniconi, S. (2008). Discussion of "detection of partial blockage in single pipelines" by PK Mohapatra, MH Chaudhry, AA Kassem, and J. Moloo. *Journal of Hydraulic Engineering, 134*(6), 872-874.

[11] Casper, J. (1991). Finite-volume application of high-order ENO schemes to two-dimensional boundary-value problems. *29th AIAA Aerospace Sciences Meeting, , 1.*

[12] Casper, J., & Atkins, H. (1993). A finite-volume high-order ENO scheme for two-dimensional hyperbolic systems. *Journal of Computational Physics, 106*(1), 62-76.

[13] Chaudhry, M. H. (2014). *Applied Hydraulic Transients*. 3rd ed., springer. New York.

[14] Chaudhry, M. H., & Hussaini, M. Y. (1985). Second-order accurate explicit finite-difference schemes for waterhammer analysis. *Journal of Fluids Engineering, 107*(4), 523-529.

[15] Chen, S., & Doolen, G. D. (1998). Lattice boltzmann method for fluid flows Annual Review of Fluid Mechanics, 30(1), 329 <last_page> 364. doi:10.1146/annurev.fluid.30.1.329.

[16] Cockburn B., Karniadakis G.E., & Shu C.W. (2000). *The development of discontinuous Galerkin methods*. Springer, Berlin.

[17] Coelho, B., & Andrade-Campos, A. (2014). Efficiency achievement in water supply systems—A review *Renewable and Sustainable Energy Reviews, 30*, 59.

[18] Colombo, A. F., & Karney, B. W. (2002). Energy and costs of leaky pipes:

Toward comprehensive picture. *Journal of Water Resources Planning and Management, 128*(6), 441-450.

[19] Colonius, T. (2004). Modeling artificial boundary conditions for compressible flow. Annu.Rev.Fluid Mech., 36, 315-345.

[20] Congressional Budget office (CBO) report (2015). "*Public Spending on Transportation and Water Infrastructure, 1956 to 2014"*.

[21] Covas, D., Ramos, H., & De Almeida, A. B. (2005). Standing wave difference method for leak detection in pipeline systems. *Journal of Hydraulic Engineering, 131*(12), 1106-1116.

[22] Covas, D., Ramos, H., Brunone, B., & Young, A. (2004). Leak detection in water trunk mains using transient pressure signals: Field tests in scottish water. *International Conference on Pressure Surges,*

[23] Curle N., (1955). *The influence of solid boundaries upon aerodynamic sound*, Proc. Roy. Soc. A **231**, 505 – 514.

[24] Dashen, R., Flatté, S. M., Munk, W. H., Watson, K. M., & Zachariasen, F. (2010). *Sound transmission through a fluctuating ocean* Cambridge University Press.

[25] De Salis, M. H. F., & Oldham, D. J. (1999). Determination of the blockage area function of a finite duct from a single pressure response measurement. *Journal of sound and vibration*, *221*(1), 180-186.

[26] Deane, A. (1986). *Time domain work on brass instruments* (PhD). Available from University of Surrey.

[27] Domis M. A. (1979). Acoustic resonances as a means of blockage detection in sodium cooled fast reactors. *Nuclear Engineering and Design*, *54*, 125-147.

[28] Domis M. A. (1980). Frequency dependence of acoustic resonances on blockage Position in a fast reactor subassembly wrapper. *Journal of sound and vibration*, *72*(4), 443-450.

[29] Domis, M., & Butterfield, M. (1979). The transmission of sound waves through water in a PFR subassembly wrapper. *Journal of Sound and Vibration*, *63*(2), 247-258.

[30] Duan, H., Ghidaoui, M., Lee, P. J., & Tung, Y. (2010). Unsteady friction and visco-elasticity in pipe fluid transients. *Journal of Hydraulic Research*, *48*(3), 354-362.

[31] Duan, H., Lee, P. J., Ghidaoui, M. S., & Tung, Y. (2010). Essential system response information for transient-based leak detection methods. *Journal of Hydraulic Research*, *48*(5), 650-657.

[32] Duan, H., Lee, P. J., Ghidaoui, M. S., & Tung, Y. (2011). Extended blockage detection in pipelines by using the system frequency response analysis. *Journal of Water Resources Planning and Management*,

[33] Duan, H., Lee, P. J., Ghidaoui, M. S., & Tung, Y. (2012a). Leak detection in complex series pipelines by using the system frequency response method. *Journal of Hydraulic Research*, *49*(2), 213-221.

[34] Duan, H., Lee, P. J., Ghidaoui, M. S., & Tung, Y. (2012b). System response Function–Based leak detection in viscoelastic pipelines. *Journal of Hydraulic Engineering*, *138*(2), 143-153.

[35] Duan, H., Lee, P. J., Kashima, A., Lu, J., Ghidaoui, M., & Tung, Y. (2013). Extended blockage detection in pipes using the system frequency response: Analytical analysis and experimental verification. *Journal of Hydraulic Engineering*, *139*(7), 763-771.

[36] Duan, W., Kirby, R., Prisutova, J., & Horoshenkov, K. V. (2015). On the use of power reflection ratio and phase change to determine the geometry of a blockage in a pipe. *Applied Acoustics, 87*, 190-197.

[37] Ehrenfest, P. (1916). On Adiabatic Changes of a System in Connection with the Quantum Theory. *Proceedings of the Amsterdam Academy*, *19*, 576-597.

[38] Eichinger, P., & Lein, G. (1992). The influence of friction on unsteady pipe flow. *Unsteady Flow and Fluid Transients, ,* 41-50.

[39] El-Rahed M. & Wagner P. (1982). Acoustic propagation in rigid ducts with blockage. *Journal of the Acoustical Society of America, 12*, 1046- 1055.

[40] envirofluid.com, ' How to remove Limescale from Pumps & Pipes', 2014. [Online]. Available: https://envirofluid.com/case-studies/how-to/how-to-remove-limescale-pumps-pipes. [Accessed: 23- May- 2016].

[41] Fant, G. (1975). Vocal-Tract Area and Length Perturbations. *STL-QPSR*, 16(4), 1-14.

[42] Felsen, L. B., & Yee, H. Y. (1968). Ray Method for Sound-Wave Reflection in an Open-Ended Circular Pipe. *The Journal of the Acoustical Society of America, 44*(4), 1028-1039.

[43] Ferrante, M., & Brunone, B. (2003a). Pipe system diagnosis and leak detection by unsteady-state tests. 1. harmonic analysis. *Advances in Water Resources, 26*(1), 95-105.

[44] Ferrante, M., & Brunone, B. (2003b). Pipe system diagnosis and leak detection by unsteady-state tests. 2. wavelet analysis. *Advances in Water Resources, 26*(1), 107-116.

[45] Ffowcs J.E.Williams and D.L. Hawkings, 1969, *Sound generation by turbulence and surfaces in arbitrary motion*, Phil. Trans. Roy. Soc. (London)

Ser. A, 264, 321 – 342.

[46] Fink, M. (2002). *Imaging of complex media with acoustic and seismic waves* Springer Science & Business Media.

[47] Flatte, S. M. (1983). Wave propagation through random media: Contributions from ocean acoustics. *Proceedings of the IEEE, 71*(11), 1267-1294.

[48] Fletcher, R., & Chandrasekaran, M. (2008). SmartBall™: A new approach in pipeline leak detection. *2008 7th International Pipeline Conference,* 117-133.

[49] Fouque, J., Garnier, J., Papanicolaou, G., & Solna, K. (2007). *Wave propagation and time reversal in randomly layered media* Springer Science & Business Media.

[50] Ghidaoui, M. S. (2004). On the fundamental equations of water hammer. *Urban Water Journal, 1*(2), 71-83.

[51] Ghidaoui, M.S., Mansour, S. and Zhao, M., (2002). Analysis of quasi-two-dimensional water-hammer models. J. Hydraulic Eng., 128, 917 – 924.

[52] Gill, J. R., Fattah, R., & Zhang, X. (2015). Evaluation and development of non-reflective boundary conditions for aeroacoustic simulations. 21st AIAA/CEAS Aeroacoustics Conference, 2677.

[53] Goodwin, J. (1981). *Relations between the geometry and acoustics of brass instruments* (PhD). Available from University of Surrey.

[54] Harten A., Enqguist B., Osher S., & Chakravarthy S. (1987). Uniformly high-order essentially non-oscillatory schemes III, *J. Comput. Phys. 71*, 231–303.

[55] Hartig, H. E., & Swanson, C. E. (1938). " Transverse" acoustic waves in rigid tubes. *Physical Review, 54*(8), 618.

[56] Heinz, J. (1967). Perturbation Functions for the Determination of Vocal-Tract Area Functions from Vocal-Tract Eigenvalues. *STL-QPSR, 8*(1), 1-14.

[57] Hirsch, C. (1988a). Numerical computation of internal and external flows. volume 1: Fundamental of numerical discretization. Chichester [England]: Wiley.

[58] Hirsch, C. (1988b). Numerical computation of internal and external flows. volume 2: Computational method for inviscid and viscous flows. Chichester (England): Wiley.

[59] Hirsch, C. S. (Ed.). (2007). *Numerical computation of internal and external flows: Fundamentals of computational fluid dynamics* (2nd ed.). Amsterdam: Elsevier, Butterworth-Heinemann.

[60] Hong Kong Water Supplies Department (WSD), private communication.

[61] Howe, M. (1973). Multiple scattering of sound by turbulence and other inhomogeneities. *Journal of Sound and Vibration*, *27*(4), 455-476.

[62] Hunaidi, O. (2000). Detecting Leaks in Water-Distribution Pipes. *Construction Technology Update*, *40*, 6.

[63] Jeffrey, A., & Dai, H. H. (2008). *Handbook of mathematical formulas and integrals* Academic Press.

[64] Jiang G., & Shu, C.W. (1996). Efficient implementation of weighted ENO schemes, *J. Comput. Phys. 126*, 202–228.

[65] Karney, B. W. (1990). Energy relations in transient closed-conduit flow. *Journal of Hydraulic Engineering*, *116*(10), 1180-1196.

[66] Katz, E. J. (1967). Effect of the propagation of internal water waves on underwater sound transmission. *The Journal of the Acoustical Society of America, 42*(1), 83-87.

[67] Kilfoyle KB, & Baggeroer AB (2000). The state of the art in underwater acoustic telemetry, *IEEE J Oceanic Eng*, 25(1), 4-27.

[68] Kokossalakis, G. (2006). *Acoustic data communication system for in-pipe wireless sensor networks* (PhD). Available from Massachusetts Institute of Technology.

[69] Kondis, A. (2005). *Acoustical wave propagation in buried water filled pipes* (MSc thesis). Available from Massachusetts Institute of Technology.

[70] Lee, P. J., Duan, H. F., Ghidaoui, M., & Karney, B. (2013). Frequency domain analysis of pipe fluid transient behaviour. *Journal of hydraulic research, 51*(6), 609-622.

[71] Lee, P. J., Duan, H., Tuck, J., & Ghidaoui, M. (2014). Numerical and experimental study on the effect of signal bandwidth on pipe assessment using fluid transients. *Journal of Hydraulic Engineering, 141*(2), 04014074.

[72] Lee, P. J., Lambert, M. F., Simpson, A. R., Vítkovský, J. P., & Liggett, J. (2006). Experimental verification of the frequency response method for pipeline leak detection. *Journal of Hydraulic Research, 44*(5), 693-707.

[73] Lee, P. J., Vítkovský, J. P., Lambert, M. F., Simpson, A. R., & Liggett, J. A. (2008). Discrete blockage detection in pipelines using the frequency response diagram: Numerical study. *Journal of Hydraulic Engineering, 134*(5), 658-663.

[74] León, A. S., Ghidaoui, M. S., Schmidt, A. R., & García, M. H. (2007). An efficient finite-volume scheme for modeling water hammer flows.

[75] Li Q.B., Xu K., & Fu S. (2010). A high-order gas-kinetic Navier-Stokes flow solver. *J. Comput. Phys. 229*, 6715-6731.

[76] Li, J., Li, Q., & Xu, K. (2011). Comparison of the generalized riemann solver and the gas-kinetic scheme for inviscid compressible flow simulations. *Journal of Computational Physics*, 230(12), 5080-5099.

[77] Liggett, J. A., & Chen, L. (1994). Inverse transient analysis in pipe networks. *Journal of Hydraulic Engineering, 120*(8), 934-955.

[78] Lighthill M.J., 1952, *On sound generated aerodynamically*, Proc. Roy. Soc. A, **211**, 564 – 586.

[79] Louati, M, & Ghidaoui, MS (2015). Wave blockage interaction in pipes. *E-proceedings of the 36th IAHR World Congress*, 28 June – 3 July, 2015, The Hague, the Netherlands.

[80] Louati, M. (2013).“On wave-defect interaction in pressurized conduits.”*Proceedings of the 35th IAHR Congress*, Chengdu-China.

[81] Lu, J., Koliskins, A., Ghidaoui, M. S., & Duan, H. (2011). The effect of random inhomogeneities on wave propagation in pipes. *The 34th IAHR Congress, Brisbane Australia,*

[82] Luo J., Xuan L.J., & Xu K. (2013). Comparison of fifth-order WENO scheme and WENO-gas-kinetic scheme for inviscid and viscous flow simulation. *Commun. Comput. Phys*, *14*(3), 599-620, September.

[83] Massari, C., Yeh, T. C. J., Ferrante, M., Brunone, B., & Meniconi, S. (2014). Detection and sizing of extended partial blockages in pipelines by means of a stochastic successive linear estimator. *Journal of Hydroinformatics, 16*(2), 248-258.

[84] Mei, C. C., Stiassnie, M., & Yue, D. K. (2005). *Theory and applications of ocean surface waves* World Scientific.

[85] Meniconi, S., Brunone, B., & Ferrante, M. (2012). Water-hammer pressure waves interaction at cross-section changes in series in viscoelastic pipes. *Journal of Fluids and Structures, 33*, 44-58.

[86] Meniconi, S., Brunone, B., and Ferrante, M. (2011). "In-line pipe device checking by short period analysis of transient tests." *J. Hydraul. Eng*., *137*(7), 713–722.

[87] Meniconi, S., Brunone, B., Ferrante, M., Capponi, C., Carrettini, C., Chiesa, C., Lanfranchi, E. (2015). Anomaly pre-localization in distribution–transmission mains by pump trip: Preliminary field tests in the milan pipe system. *Journal of Hydroinformatics, 17*(3), 377-389.

[88] Meniconi, S., Duan, H., Lee, P., Brunone, B., Ghidaoui, M., & Ferrante, M. (2013). Experimental investigation of coupled frequency and time-domain transient Test–Based techniques for partial blockage detection in pipelines. *Journal of Hydraulic Engineering, 139*(10), 1033-1040.

[89] Mermelstein, P. (1967). Determination of the Vocal-Tract Shape from Measured Formant Frequencies. *J. Acoust. Soc. Am*., *41* (5), 1283-1294.

[90] Metje, N., Chapman, D. N., Cheneler, D., Ward, M., & Thomas, A. M. (2011). Smart Pipes—Instrumented water pipes, can this be made a reality? *Sensors, 11*(8), 7455-7475.

[91] Milenkovic, P. (1984). Vocal Tract Area Functions from Two Point Acoustic Measurements with Formant Frequency Constraints. *Acoustics, Speech and Signal Processing, IEEE Transactions on*, *32*(6), 1122-1135.

[92] Milenkovic, P. (1987). Acoustic Tube Reconstruction from Noncausal *Excitation. Acoustics, Speech and Signal Processing, IEEE Transactions on*,

35(8), 1089-1100.

[93] Miles, J. (1944). The reflection of sound due to a change in cross section of a circular tube. *The Journal of the Acoustical Society of America*, *16*(1), 14-19.

[94] Miles, J. W. (1946a). The analysis of plane discontinuities in cylindrical tubes. part I. *The Journal of the Acoustical Society of America*, *17*(3), 259-271.

[95] Miles, J. W. (1946b). The analysis of plane discontinuities in cylindrical tubes. part II. *The Journal of the Acoustical Society of America*, *17*(3), 272-284.

[96] Mitra, A., & Rouleau, W. (1985). Radial and axial variations in transient pressure waves transmitted through liquid transmission lines. *Journal of Fluids Engineering*, *107*(1), 105-111.

[97] Mohapatra, P., Chaudhry, M., Kassem, A., & Moloo, J. (2006). Detection of partial blockage in single pipelines. *Journal of Hydraulic Engineering*,

[98] Mrayati, M., Carré, R., & Guérin, B. (1988). Distinctive regions and modes: A new theory of speech production. *Speech Communication*, *7*(3), 257-286.

[99] Nixon, W., and Ghidaoui, M. S. (2007). "Numerical Sensitivity Study of Unsteady Friction in Simple Systems with External Flows " *J. Hydraul. Eng.*, 133(7), 736

[100] Ohwada T., Adachi R., Xu K., & Luo J. (2013). On the remedy against shock anomalies in kinetic schemes. *J. Comput. Phys. 255*, 106-129.

[101] Pan L., & Xu K. (2015). A third-order gas-kinetic scheme for three-dimensional inviscid and viscous flow computations. *Computers & Fluids 119*, 250-260.

[102] Pezzinga, G. (1999). Quasi-2D model for unsteady flow in pipe networks. *Journal of Hydraulic Engineering, 125*(7), 676-685.

[103] Pezzinga, G. (2000). Evaluation of unsteady flow resistances by quasi-2D or 1D models. *Journal of Hydraulic Engineering, 126*(10), 778-785.

[104] Puust, R., Kapelan, Z., Savic, D., & Koppel, T. (2010). A review of methods for leakage management in pipe networks. *Urban Water Journal, 7*(1), 25-45.

[105] Qunli, W., & Fricke, F. (1989). Estimation of blockage dimensions in a duct using measured eigenfrequency shifts. *Journal of Sound and Vibration, 133*(2), 289-301.

[106] Qunli, W., & Fricke, F. (1990). Determination of blocking locations and cross-sectional area in a duct by eigenfrequency shifts. *The Journal of the Acoustical Society of America, 87*(1), 67-75.

[107] Richards, S. K., Zhang, X., Chen, X., & Nelson, P. A. (2004). The evaluation of non-reflecting boundary conditions for duct acoustic computation. *Journal of Sound and Vibration*, 270(3), 539-557.

[108] Rienstra, S. W., & Hirschberg, A. (2003). An introduction to acoustics. *Eindhoven University of Technology, 18*, 19.

[109] Rochester, N. (1941). The propagation of sound in cylindrical tubes. *The Journal of the Acoustical Society of America, 12*(4), 511-513.

[110] Roy, C. J. (2003). Grid convergence error analysis for mixed-order numerical schemes. *AIAA Journal*, 41(4), 595-604.

[111] Sattar, A. M., Chaudhry, M. H., & Kassem, A. A. (2008). Partial blockage detection in pipelines by frequency response method. *Journal of Hydraulic Engineering,*

[112] Schroeder, M. R. (1967). Determination of the Geometry of the Human Vocal Tract by Acoustic Measurements. *J. Acoust. Soc. Am.*, *41*(4B), 1002-1010.

[113] Schroeter, J., & Sondhi, M. M. (1994). Techniques for Estimating Vocal-Tract Shapes from the Speech Signal. *Speech and Audio Processing, IEEE Transactions on*, *2*(1), 133-150.

[114] Sharp, D., Myers, A., Parks, R., & Campbell, D. (1995). Bore reconstruction by pulse reflectometry and its potential for the taxonomy of brass instruments. *Proceedings of the 15th International Congress on Acoustics, Trondheim, Norway*, 26-30.

[115] Silva-Araya, W. F., & Chaudhry, M. H. (1997). Computation of energy dissipation in transient flow. *Journal of Hydraulic Engineering*, *123*(2), 108-115.

[116] sites.utexas.edu, 'Defining and Recognizing Open Channel Flow', 2015. [Online]. Available: https://sites.utexas.edu/civ-eng-comm/2015/11/17/defining-and-recognizing-open-channel-flow/. [Accessed: 23- May- 2016].

[117] Sondhi, M. M., & Gopinath, B. (1971). Determination of Vocal-Tract Shape from Impulse Response at the Lips. *J. Acoust. Soc. Am.*, *49*(6B), 1867-1873.

[118] Sondhi, M. M., & Resnick, J. (1983). The Inverse Problem for the Vocal Tract: Numerical Methods, Acoustical Experiments, and Speech Synthesis. *J. Acoust. Soc. Am.*, *73*(3), 985-1002.

[119] Stephens, M., (2008). *Transient response analysis for fault detection and pipeline wall condition assessment in field water transmission and distribution pipelines and networks* (PhD). the University of Adelaide, Australia.

[120] Stevens, K. N. (1998). *Acoustic phonetics*. London, England: MIT press.

[121] Theme based project. "Smart Urban Water Supply System". http://smartuws.ust.hk/.

[122] Thompson, K. W. (1987). Time dependent boundary conditions for hyperbolic systems I. Journal of Computational Physics, 68(1), 1-24.

[123] Thompson, K. W. (1990). Time-dependent boundary conditions for hyperbolic systems, II. Journal of Computational Physics, 89(2), 439-461.

[124] Tijdeman, H. (1975). On the propagation of sound waves in cylindrical tubes. *Journal of Sound and Vibration, 39*(1), 1-33.

[125] Tolstoy, A. (2010). Waveguide monitoring (such as sewer pipes or ocean zones) via matched field processing. *The Journal of the Acoustical Society of America, 128*(1), 190-194.

[126] Toro E. F., Millington R.C., & Nejad L.A.M. (2001). *Towards very high order Godunov schemes*, in: Toro E.F. (Ed.), *Godunov Methods: Theory and Applications*, Kluwer/Plenum Academic Publishers, 2001, 907–940

[127] Toro, E. F. (2009). *Riemann solvers and numerical methods for fluid dynamics: A practical introduction* Springer Science & Business Media.

[128] towerscan.com, 'Pipe Scanning', 2013. [Online]. Available: http://www.towerscan.com/pipe_scanning.htm. [Accessed: 23-May-2016].

[129] USEPA (United States U.S. Environmental Protection Agency) (2013). Drinking water infrastructure needs survey and assessment: Fifth report to congress, http://water.epa.gov/grants_funding/dwsrf/upload/epa816r13006.pdf.

[130] Vardy, A. E., & Hwang, K. (1991). A characteristics model of transient

friction in pipes. *Journal of Hydraulic Research, 29*(5), 669-684.

[131] Vítkovský, J. P., Simpson, A. R., & Lambert, M. F. (2000). Leak detection and calibration using transients and genetic algorithms. *Journal of Water Resources Planning and Management,*

[132] Wang Z.J. (2002). Spectral (finite) volume method for conservation laws on unstructured grids: basic formulation, *J. Comput. Phys. 178*, 210–251.

[133] Wang, X., Lambert, M. F., Simpson, A. R., Liggett, J. A., & V ı´ tkovský, John P. (2002). Leak detection in pipelines using the damping of fluid transients. *Journal of Hydraulic Engineering*, *128*(7), 697-711.

[134] Wang, X.J., Lambert, M.F., & Simpson, A.R. (2005). Detection and location of a partial blockage in a pipeline using damping of fluid transients. *Journal of Water Resources Planning and Management*, ASCE, *131*(3), 244-249.

[135] Wang, Z. J., Fidkowski, K., Abgrall, R., Bassi, F., Caraeni, D., Cary, A., & Kroll, N. (2013). High-order CFD methods: current status and perspective. *International Journal for Numerical Methods in Fluids*, *72*(8), 811-845.

[136] Webster, A. G. (1919). Acoustical impedance and the theory of horns and of the phonograph. *Proceedings of the National Academy of Sciences of the United States of America, 5*(7), 275-282.

[137] Wylie, E. B., Streeter, V. L., & Suo, L. (1993). *Fluid transients in systems* Prentice Hall Englewood Cliffs, NJ.

[138] Xu K., & Li Z.W. (2001). Dissipative Mechanism in Godunov-type Schemes. *Int. J. Numer. Methods in Fluids, 37*, 1-22.

[139] Xu, K. (2014). Direct modeling for computational fluid dynamics: Construction and application of unified gas-kinetic schemes World Scientific.

[140] Zhao, M, Ghidaoui, MS, Louati, M., & Duan, HF (2016). Transient wave and extended blockage interaction in pipe flows. *Journal of Hydraulic Research.*, IAHR, (accepted).

[141] Zhao, M., & Ghidaoui, M. S. (2003). Efficient quasi-two-dimensional model for water hammer problems. *Journal of Hydraulic Engineering*, *129*(12), 1007-1013.

Appendix A

Mode matching at discontinuity

Consider a junction of tow pipes with a discontinuity in diameter at $x = 0$ (Figure A.1) with a radius R along $x < 0$ and a radius R_s along $x > 0$, where $R > R_s$. The subscript "s" denotes the region of incident wave.

Figure A.1 Mode matching at discontinuity

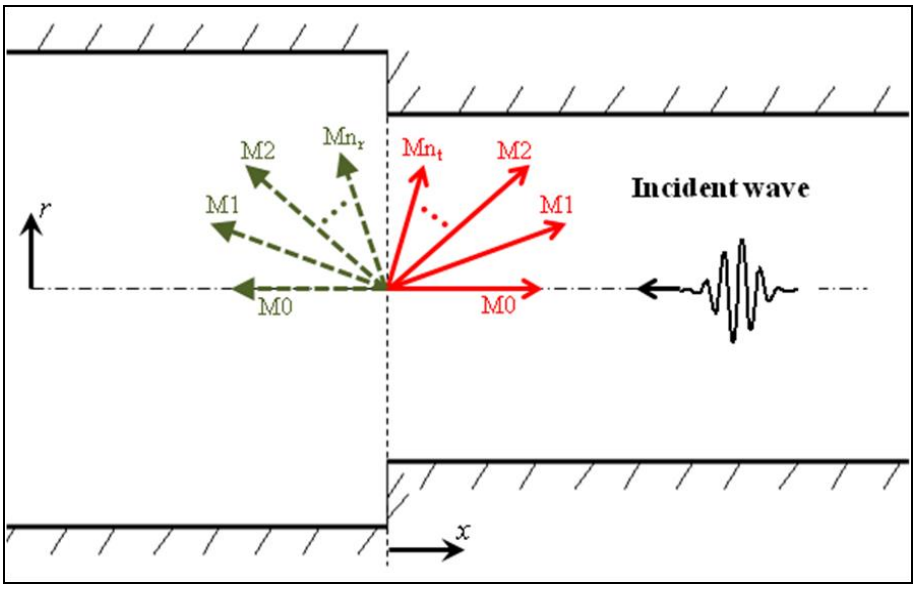

An incident wave from $x = \infty$ given by (see equation Eq. (2.114))

$$P_{in} = \sum_n \varphi_n^s \exp\left(ik_{xn}^s\, x\right)\exp\left(-iwt\right) J_0\left(rk_{rn}^s\right) \tag{A.1}$$

is scattered at x=0 into a reflected wave P_{ref}

$$P_{ref} = \sum_n \gamma_n^s \exp\left(-ik_{xn}^s\, x\right)\exp\left(-iwt\right) J_0\left(k_{rn}^s\right) \tag{A.2}$$

and into a transmitted P_{tr}

$$P_{tr} = \sum_n \varphi_n \exp\left(ik_{xn}\, x\right)\exp\left(-iwt\right) J_0\left(rk_{rn}\right) \tag{A.3}$$

The reflected and transmitted amplitudes could be written as follows

$$\gamma_n^s = \sum_m \Upsilon_{nm}\varphi_m^s \tag{A.4}$$

and

$$\varphi_n = \sum_m \mathrm{T}_{nm}\varphi_m^s \tag{A.5}$$

where Υ_{nm} and T_{nm} are the contributions of the m^{th} mode to reflected and transmitted n^{th} modes, respectively. Υ_{nm} and T_{nm} are also called the reflection and transmission matrices, respectively. Applying the continuity of pressure at x=0, gives

$$\left(P_{in} + P_{ref}\right)_{x=0} = \left(P_{tr}\right)_{x=0} \tag{A.6}$$

$$\Rightarrow \sum_n \left\{\left[\varphi_n^s + \sum_m \Upsilon_{nm}\varphi_n^s\right] J_0\left(rk_{rn}^s\right)\right\} = \sum_n \left\{\left[\sum_m \mathrm{T}_{nm}\varphi_n^s\right] J_0\left(rk_{rn}\right)\right\} \tag{A.7}$$

Considering a single incident mode m=j such that $\varphi_{m\neq j}^s = 0$ and $\varphi_{m=j}^s = \varphi_j^s \neq 0$, yields

$$\varphi_j^s J_0\left(rk_{rj}^s\right) + \sum_n \left\{\Upsilon_{nj}\varphi_j^s J_0\left(rk_{rn}^s\right)\right\} = \sum_n \left\{\mathrm{T}_{nj}\varphi_j^s J_0\left(rk_{rn}\right)\right\} \tag{A.8}$$

$$\Rightarrow J_0\left(rk_{rj}^s\right) + \sum_n \left\{\Upsilon_{nj} J_0\left(rk_{rn}^s\right)\right\} = \sum_n \left\{\mathrm{T}_{nj} J_0\left(rk_{rn}\right)\right\} \tag{A.9}$$

Taking the inner product with $J_0\left(rk_{rn'}\right)r$ and using the Orthogonality of Bessel's function gives:

$$\sum_n \left(\delta_{nj} + \Upsilon_{nj}\right) \int_0^R J_0\left(rk_{rn}^s\right) J_0\left(rk_{rn'}\right) rdr = \sum_n \mathrm{T}_{nj} \int_0^R J_0\left(rk_{rn}\right) J_0\left(rk_{rn'}\right) rdr \tag{A.10}$$

$$\Rightarrow \sum_n \int_0^R J_0\left(rk_{rn}^s\right) J_0\left(rk_{rn'}\right) rdr \left(\delta_{nj} + \Upsilon_{nj}\right) = \mathrm{T}_{n'j} \int_0^R J_0^2\left(rk_{rn'}\right) rdr \tag{A.11}$$

$$\Rightarrow \sum_n \frac{-Rk_{rn}^s J_1\left(Rk_{rn}^s\right) J_0\left(Rk_{rn'}\right)}{\left\{\left[k_{rn'}\right]^2 - \left[k_{rn}^s\right]^2\right\}} \left(\delta_{nj} + \Upsilon_{nj}\right) = \mathrm{T}_{n'j} J_0^2\left(\alpha_{rn'}\right) \frac{R^2}{2} \tag{A.12}$$

where δ_{nj} is the Kronecker delta function. In matrix form, Eq. (A.12) gives

$$\overline{\overline{M}} \left(I + \Upsilon\right) = J_0^2\left(\overline{\overline{\alpha_r}}\right) \mathrm{T} \frac{R^2}{2} \tag{A.13}$$

where

$$\overline{\overline{M}} = \left\{M\right\}_{n'n} \quad ; \quad \Upsilon = \left\{\Upsilon\right\}_{nj} \quad ; \quad T = \left\{T\right\}_{n'j} \quad ; \quad \overline{\overline{\alpha_r}} = \left\{\overline{\overline{\alpha_r}}\right\}_{n'n'} \tag{A.14}$$

and $M_{n'n} = \dfrac{-Rk_{rn}^s J_1\left(Rk_{rn}^s\right) J_0\left(Rk_{rn'}\right)}{\left\{\left[k_{rn'}\right]^2 - \left[k_{rn}^s\right]^2\right\}}$.

Applying the continuity of axial velocity at $x = 0$ gives

$$\left(V_x^{in} + V_x^{ref}\right)_{x=0} = \left(V^{tr}\right)_{x=0} \tag{A.15}$$

This condition can be written in terms of pressure by using the momentum equation as follows

$$\frac{\partial V}{\partial t} = -\frac{1}{\rho}\frac{\partial p}{\partial x} \quad \Rightarrow \quad -iwV = -\frac{1}{\rho}\frac{\partial p}{\partial x} \quad \Rightarrow \quad V = \frac{1}{iw\rho}\frac{\partial p}{\partial x} \tag{A.16}$$

where the convective terms are neglected. Considering only the incident mode *m=j*, leads to

$$\left[k_{xj}^{s}J_0\left(rk_{rj}^{s}\right)-\sum_{n}\left\{k_{xn}^{s}\Upsilon_{nj}J_0\left(rk_{rn}^{s}\right)\right\}\right]=\sum_{n}\left\{k_{xn}T_{nj}J_0\left(rk_{rn}\right)\right\} \tag{A.17}$$

Taking the inner product with $J_0\left(rk_{rn'}^{s}\right)r$ and integrating from 0 to R_s for $x>0$ and from 0 to R for $x<0$, give

$$\begin{aligned}&k_{xn}^{s}\sum_{n}\left\{\delta_{nj}-\Upsilon_{nj}\right\}\int_{0}^{R_s}J_0\left(rk_{rn}^{s}\right)J_0\left(rk_{rn'}^{s}\right)rdr\\&=\sum_{n}k_{xn}\mathrm{T}_{nj}\int_{0}^{R}J_0\left(rk_{rn}\right)J_0\left(rk_{rn'}^{s}\right)rdr\end{aligned} \tag{A.18}$$

$$\Rightarrow k_{xn'}^{s}\int_{0}^{R_s}J_0^2\left(rk_{rn'}^{s}\right)rdr\left\{\delta_{n'j}-\Upsilon_{n'j}\right\}=\sum_{n}\int_{0}^{R}J_0\left(rk_{rn'}^{s}\right)J_0\left(rk_{rn}\right)rdrk_{xn}\mathrm{T}_{nj} \tag{A.19}$$

$$\Rightarrow k_{xn'}^{s}J_0^2\left(\alpha_{rn'}\right)\left\{\delta_{n'j}-\Upsilon_{n'j}\right\}\frac{R_s^2}{2}=\sum_{n}\frac{-Rk_{rn'}^{s}J_1\left(Rk_{rn'}^{s}\right)J_0\left(Rk_{rn}\right)}{\left[k_{rn}\right]^2-\left[k_{rn'}^{s}\right]^2}k_{xn}\mathrm{T}_{nj} \tag{A.20}$$

Equations (A.12) and (A.20) are combined into a system of equations as follows

$$\begin{cases}\sum_{n}M_{n'n}\left(\delta_{nj}+\Upsilon_{nj}\right)=\mathrm{T}_{n'j}J_0^2\left(\alpha_{rn'}\right)\dfrac{R^2}{2}\\k_{xn'}^{s}J_0^2\left(\alpha_{rn'}\right)\left\{\delta_{n'j}-\Upsilon_{n'j}\right\}\dfrac{R_s^2}{2}=\sum_{n}M_{nn'}k_{xn}\mathrm{T}_{nj}\end{cases} \tag{A.21}$$

In matrix form, Eq. (A.21) becomes

$$\begin{cases}\overline{\overline{M}}\left(\delta+\Upsilon\right)=J_0^2\left(\overline{\overline{\alpha_r}}\right)\mathrm{T}\dfrac{R^2}{2}\\\mathrm{K}_x^{s}J_0^2\left(\overline{\overline{\alpha_r}}\right)\left(\delta-\Upsilon\right)\dfrac{R_s^2}{2}=\overline{\overline{M}}^{tr}\mathrm{K}_x\mathrm{T}\end{cases} \tag{A.22}$$

where

$$\mathrm{K}_x^{s}=\left\{k_x^{s}\right\}_{n'n}\ \ ;\ \ \mathrm{K}_x=\left\{k_x\right\}_{n'n}\ \ ;\ \ \overline{\overline{\delta}}=\left\{\delta\right\}_{nj} \tag{A.23}$$

which leads to

$$\Upsilon = \left[\mathrm{K}_x^s + \overline{\overline{M}}_u^{tr} \mathrm{K}_x \overline{\overline{M}}_u \right]^{-1} \left[\mathrm{K}_x^s - \overline{\overline{M}}_u^{tr} \mathrm{K}_x \overline{\overline{M}}_u \right] \overline{\delta} \tag{A.24}$$

and

$$\mathrm{T} = \frac{R_s}{R} \overline{\overline{M}}_u \left[\mathrm{K}_x^s + \overline{\overline{M}}_u^{tr} \mathrm{K}_x \overline{\overline{M}}_u \right]^{-1} \left[2\mathrm{K}_x^s \right] \overline{\delta} \tag{A.25}$$

where $\overline{\overline{M}}_u = \frac{2}{RR_s} J_0^2 \left(\overline{\overline{\alpha}}_r \right)^{-1} \overline{\overline{M}}$ and $M_u|_{n'n} = \frac{-2\alpha_{rn} J_1 \left(\alpha_{rn} R / R_s \right)}{R_s^2 \left\{ \left[k_{rn'} \right]^2 - \left[k_{rn}^s \right]^2 \right\} J_0 \left(\alpha_{rn'} \right)}$.

The transmitted and reflected modes from the discontinuity must satisfy the energy conservation as follows:

$$E_{tr} + E_{ref} = E_{in} \Rightarrow \sum_{n_t} E_{n_t} + \sum_{n_r} E_{n_r} = E_{in} \tag{A.26}$$

where n_t are the transmitted modes numbers; n_r are the reflected mode numbers; E_{tr}, E_{ref} and E_{in} are the transmitted, reflected and incident energy, respectively. Using Eq. (2.136) yields

$$\sum_{n_t} \frac{\varphi_{n_t}^2 \pi R^2}{2\rho a^2} J_0^2 \left(\alpha_{rn_t} \right) + \sum_{n_r} \frac{\gamma_{n_r}^2 \pi R_s^2}{2\rho a^2} J_0^2 \left(\alpha_{rn_r} \right) = \frac{\left(\varphi_j^s \right)^2 \pi R_s^2}{2\rho a^2} \tag{A.27}$$

$$\Rightarrow \frac{R^2}{R_s^2} \sum_{n_t} \mathrm{T}_{n_t j}^2 J_0^2 \left(\alpha_{rn_t} \right) + \sum_{n_r} \Upsilon_{n_r j}^2 J_0^2 \left(\alpha_{rn_r} \right) = 1 \tag{A.28}$$

Appendix B

Solution of cos(*x*) = –y

The solution of $\cos(x) = -y$ is

$$\begin{cases} x = \pi + \arccos(y) + 2(\bar{m} - 1)\pi \\ x = \pi - \arccos(y) + 2(\bar{m} - 1)\pi \end{cases}; \quad \bar{m} = 1, 2... \tag{B.1}$$

$$\Rightarrow \begin{cases} x = \arccos(y) + (2\bar{m} - 1)\pi \\ x = -\arccos(y) + (2\bar{m} - 1)\pi \end{cases} \tag{B.2}$$

Using $$\begin{cases} \arccos(y) = \pi - \arccos(-y) \\ -\arccos(y) = \arccos(-y) - \pi \end{cases}, \tag{B.3}$$

$$\Rightarrow \begin{cases} x = \pi - \arccos(-y) + (2\bar{m} - 1)\pi \\ x = \arccos(-y) - \pi + (2\bar{m} - 1)\pi \end{cases} \Rightarrow \begin{cases} x = -\arccos(-y) + 2\bar{m}\pi \\ x = \arccos(-y) + 2\bar{m}\pi \end{cases} \tag{B.4}$$

which leads to

$$x = \arccos\left[(-1)^{\bar{m}}\, y\right] + (\bar{m} - 1)\pi \quad \text{or} \quad x = -\arccos\left[(-1)^{\bar{m}+1}\, y\right] + \bar{m}\pi \tag{B.5}$$